UNIVERSITÀ DEGLI STUDI DI PAVIA
DOTTORATO DI RICERCA IN FISICA – XXXII CICLO

Nucleon polarizabilities from Compton scattering data

Stefano Sconfietti

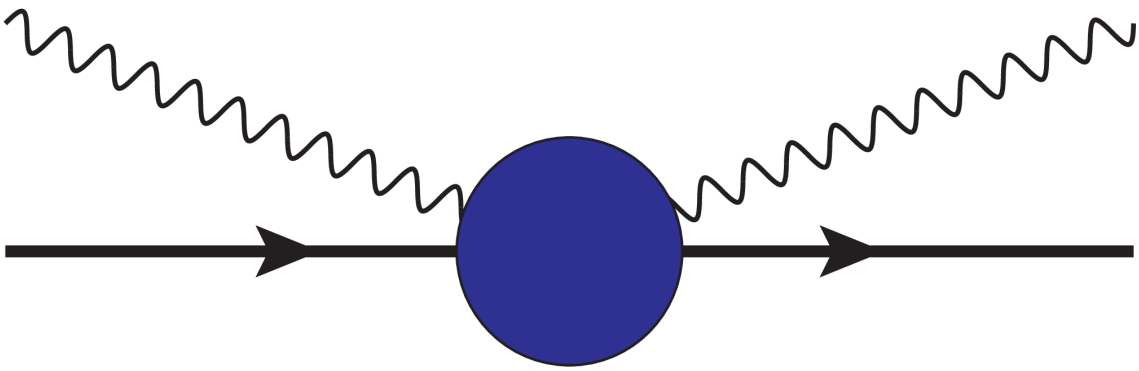

Tesi per il conseguimento del titolo

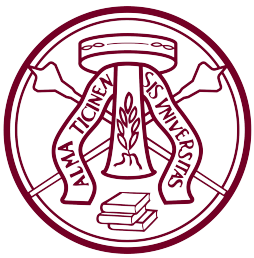

Università degli Studi di Pavia
Dipartimento di Fisica

DOTTORATO DI RICERCA IN FISICA – XXXII CICLO

Nucleon polarizabilities from Compton scattering data

Stefano Sconfietti

Submitted to the Graduate School of Physics
in partial fulfillment of the requirements for the degree of
DOTTORE DI RICERCA IN FISICA
DOCTOR OF PHILOSOPHY IN PHYSICS
at the
University of Pavia

Supervisors: Prof. Barbara Pasquini, Prof. Paolo Pedroni

Cover: *graph of the real Compton scattering process*
Nucleon polarizabilities from Compton scattering data
Sconfietti Stefano
PhD Thesis - University of Pavia
Pavia, Italy, October 2019

To my daughter, Mia.

Contents

Chapter 1

Introduction

In basic tests of Physics, the scattering of photons has been widely used to investigate both the structure of matter and the nature of light. The identification of the light with electromagnetic waves is based on the experiments performed by Faraday and the theoretical studies driven by Maxwell. The Compton effect [1], i.e. the wavelength shift of light scattered off an electron, contributed in establishing the particle-wave duality and at the same time opened the way to study the internal structure of composite particles.

On the heels of the discovery of the four fundamental interactions and the consequent investigation of the sub-nucleon structure, Compton scattering re-confirmed itself as a very clean process to study this structure, both theoretically and experimentally. The connection that can be established, thanks to the optical theorem, between scattering of photons at low frequency and absorption of photons of high frequencies, stresses once more the universality of photons as probes of nucleon structure. This connection links the nucleon photo-absorption spectrum with low-energy coefficients that represent the response of the nucleon to the quasi-static electromagnetic field, i.e. the polarizabilities, and gives rise to a variety of sum rules [2–5].

The nucleon polarizabilities have been studied within different theoretical frameworks, mainly chiral perturbation theory (χPT) [6–10] and fixed-t dispersion relations (DRs) [11–18]. In this work, we focus on the fixed-t subtracted DRs, which are derived from the properties of analyticity, causality and unitarity of the Compton scattering amplitude.

1.1 The analytical structure of the scattering amplitude

The dispersive approach requires the knowledge of the analyticity properties of the scattering amplitudes. Some generic results can be deduced by considering that real Compton scattering (RCS) off the nucleon is a $2 \to 2$ process, as described in Fig. 1.1. In order to define the correct number of independent

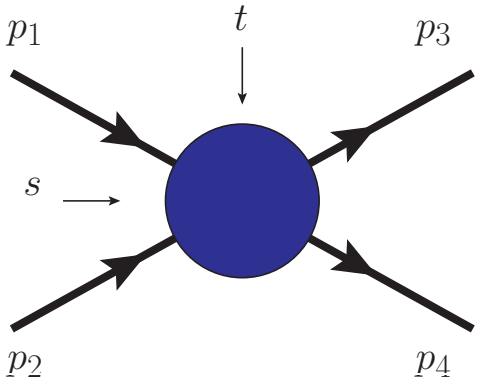

Figure 1.1: Graph of a generic $2 \to 2$ process. The s- and t-channels are indicated by the arrows.

Lorentz invariant variables for the description of the process, we follow the simple scheme given in Ref. [19]. Due to momentum conservation, we have three independent four-momenta (12 components), four on-mass-shell conditions ($p_i^2 = m_i^2$), and three rotations and three Lorentz boosts that characterize the choice of the reference frame and cannot affect the scattering invariant amplitude. Thus, we are left with $12 - 4 - 6 = 2$ independent variables and a very convenient choice is given by the usual Mandelstam variables, i.e.

$$\begin{aligned} s &= (p_1 + p_2)^2 = (p_3 + p_4)^2, \\ t &= (p_1 - p_3)^2 = (p_2 - p_4)^2, \\ u &= (p_1 - p_4)^2 = (p_2 - p_3)^2, \end{aligned} \tag{1.1}$$

which are not independent from each other, but are constrained by the relation

$$s + t + u = \sum_{i=1}^{4} m_i^2. \tag{1.2}$$

In the RCS process, the incoming and outgoing photons are real, i.e. their four-momenta squared are identically 0. The constraint in Eq. (1.2) is simplified as $s + t + u = 2M_N^2$, where M_N is the nucleon mass. Furthermore, we can introduce the crossing-symmetric variable ν as

$$\nu = \frac{s - u}{4M_N}, \tag{1.3}$$

thus identifying (ν, t) as the two independent variables for the description of the process. The boundaries of the physical regions in the s-, u- and t-channel [17] are determined by the zeros of the Kibble function $\Phi(s, t, u)$, i.e.

$$\Phi(s, t, u) = t(us - M_N^4) = 0, \tag{1.4}$$

and correspond to kinematical regions that are practically accessible, as shown in Fig. 1.2.

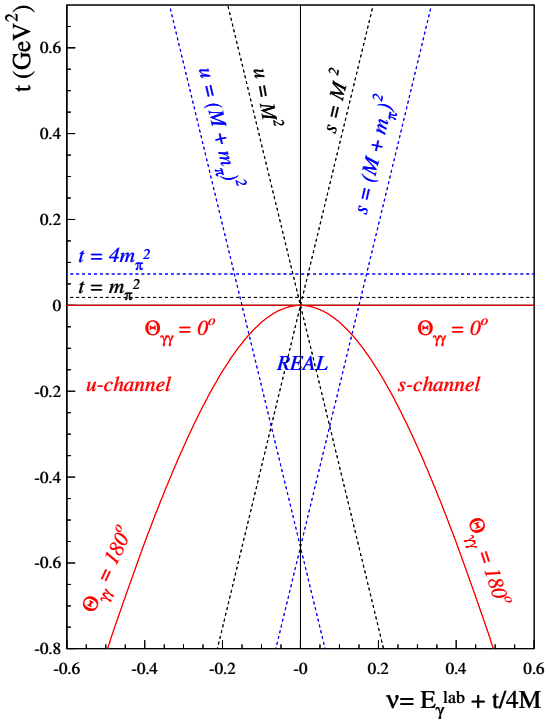

Figure 1.2: Mandelstam plane for the RCS process. The dashed-blue lines represent the particle-production thresholds, the black-dashed lines are in correspondence of the poles, while the red solid curves delimit the physical region of the s- and u-channels.

Moreover, the general theory of scattering (see Ref. [19], for instance), states that as soon as the threshold for particle production is reached in one channel, a branch cut appears in the complex plane of the corresponding Mandelstam variable. Thus, the kinematic constraints and the intermediate states involved in RCS determine the analytical structure of the amplitudes that will be used for the description of this scattering process. For instance, by looking at Fig. 1.2, we can easily identify the branch cuts in the ν variable, that are related to the s and u channel intermediate states of RCS. At fixed values of t, they run along the lines $|\nu| \geq \nu_{thr}$, where ν_{thr} is the threshold of inelastic channels of the RCS process. In Ch. 3, we will start from this analytical structure that leads to the dispersion relations of the RCS amplitudes.

1.2 Real Compton scattering and the nucleon polarizabilities

The analysis of the real Compton scattering can give us a very clean access to the properties related to the internal structure of the nucleon. The RCS

amplitude can be separated into a Born contribution, describing the scattering off a point-like nucleon with anomalous magnetic moment, and a structure-dependent part, referred as non-Born term. The non-Born contribution is parametrized by polarizabilities, which describe the response of the nucleon's internal degrees of freedom to an external electromagnetic field. In the low-energy expansion (LEX) of the non-Born amplitudes, the leading-order effects are given by static polarizabilities, that are defined in the limit of zero frequency of the photon field and therefore measure the response to a static external electromagnetic field. The leading-order spin-independent polarizabilities are the scalar dipole electric and magnetic polarizabilities, α_{E1} and β_{M1}, respectively, while four spin-dependent polarizabilities appear at the next order and involve the nucleon-spin degrees of freedom. They have been the subject of intense research both experimentally and theoretically [12, 13, 17, 18, 20, 21]. In this thesis, we will mainly focus on the extraction of α_{E1} and β_{M1} from the RCS experimental data.

Apart from the key role that the scalar dipole static polarizabilities have in the study of the internal structure of the nucleon, they also enter in other processes that are sensitive to the nucleon structure. For example, the magnetic polarizability gives one of the main contributions to the hadronic corrections in the muonic-hydrogen determination of the proton charge radius (see Refs. [22, 23] and references therein). Moreover, it plays a big role in the electromagnetic contribution to the proton-neutron mass shift [24], expressed by the Cottingham's sum rule [25]. Also for these reasons, a very accurate measurement of α_{E1} and β_{M1} is in order.

If we want to generalize the description of the nucleon response to an external electromagnetic field of arbitrary energy, we have to introduce the dynamical polarizabilities that encode an explicit energy dependence of the response of the internal degrees of freedom of a composite object. This is well known from many branches of Physics (see Refs. [26–28], for instance). The dynamical polarizabilities of the RCS process have been studied in different theoretical frameworks, using dispersion relations or effective field theories [9, 29–32]. In this thesis, we will focus on the extraction of the dipole scalar dynamical polarizabilities (DDPs) from the available RCS experimental data below pion production threshold.

1.3 A new approach for the fit

In the last 30 years, a large number of extractions of the scalar polarizabilities have been performed on RCS data, using both the DR approach (see, for instance, Refs. [33–36] or χPT (see, for instance, Refs. [8, 37, 38]). In this thesis, we present our contribution, introducing a fitting technique that has never been applied before in the analysis of Compton data.

The traditional fitting technique is based on the least square method, i.e. on

the minimization of the χ^2 function, defined as:

$$\chi^2 = \sum_i \left(\frac{E_i - T_i}{\sigma_i} \right)^2 . \tag{1.5}$$

Here, T is the prediction given by the model and the index i runs over the number of data points, whose measured values and statistical uncertainties are labeled as E and σ, respectively. The minimum of this function is assumed to follow a χ^2 distribution, from which the statistical significance of the fit results is computed. However, this assumption is rigorously true only if all the terms in round brackets of Eq. (1.5) are independent Gaussian variables.

If the experimental points are affected by both statistical and systematic uncertainties, some correlation terms arise among the E_i value. Thus, the $(E_i - T_i)/\sigma_i$ terms are neither Gaussian distributed, nor independent variables. As an important consequence, the goodness-of-fit distribution cannot be a χ^2, thus making necessary the development of a method that is able to provide the correct statistical significance for the fit results. To this aim, we will apply a Monte-Carlo fitting method, based on the parametric bootstrap [39]. As a result of our analysis, we will be able to recover the correct goodness-of-fit probability distribution in all those cases where the traditional χ^2 approach fails.

1.4 Outline of the thesis

In this thesis, we show our extraction of both the static and the dynamical scalar dipole polarizabilities of the proton from the unpolarized differential cross section RCS data below the pion-production threshold.

In Ch. 2, we give a comprehensive description of the RCS process, introducing the formalism adopted for the description of the scattering amplitudes, such as the low-energy expansion, which allows us to obtain the expression of the scattering amplitudes in terms of the static polarizabilities. Furthermore, we introduce the definition of the dynamical polarizabilities from a multipole expansion of the scattering amplitudes and we derive a convenient parametrization of the dynamical polarizabilities from the LEX, to be used in the fit to the RCS data.

In Ch. 3, we introduce the DR formalism, in the fixed-t unsubtracted and subtracted variant. We show how to derive dispersion integrals from the Cauchy's theorem, thus relating the real and imaginary part of the scattering amplitudes. The dispersion integrals can be evaluated, through the optical theorem and the unitarity relation, from known information on other scattering processes (e.g., pion-photoproduction). Furthermore, the DRs applied to forward RCS allow us to define a variety of sum rules that all relate a measured electromagnetic structure quantity to an integral over a photo-absorption cross section on the nucleon, which is linked to the forward RCS through the optical theorem.

In Ch. 4, we describe the fitting technique that is adopted for the extraction of the polarizabilities from the proton RCS data. The algorithm itself is based on the parametric bootstrap, which is a Monte-Carlo method that can be successfully applied in the presence of correlated and/or systematic errors. We develop a toy model, simulating random data from a Breit-Wigner (BW) distribution, which is then used to rigorously analyze the features of the fitting technique. Then, we derive for the first time the goodness-of-fit distribution, even for those situations in which the standard χ^2 distribution would not be applicable.

In Ch. 5, we make some sensitivity tests, to infer which of the static polarizabilities can be extracted with good accuracy from the RCS unpolarized cross section data. Moreover, we discuss the statistical significance of the RCS data base, making several tests that let us to conclude that no clear outliers are present in the current data set. On the basis of all these tests, we perform the extraction of the dipole scalar static polarizabilities, α_{E1} and β_{M1}, also considering the propagation of the uncertainties of all the polarizabilities that are not taken as fit parameters, as well as the systematic errors of the experimental data. The statistical significance of the fit results is obtained from the bootstrap method.

In Ch. 6, we show our results of the first extraction of the scalar dipole dynamical polarizabilities from the proton RCS data below pion-production threshold. We again apply the fitting technique described in Ch. 4, which allows us to obtain a realistic uncertainty band from the propagation of the systematic uncertainties of the experimental data.

In Ch. 7, we perform some sensitivity tests to the static polarizabilities on recent data for the RCS beam asymmetry [40]. We also combine these data with the unpolarized cross section measurements, with the goal of obtaining a more precise extraction of the magnetic polarizability β_{M1}. Furthermore, we look at forward RCS, evaluating three well known sum rules from the total photo-absorption cross section data: the Baldin sum rule [3] (involving the sum of the electric and magnetic polarizabilities), the Gerasimov [4], Drell and Hearn [5] (GDH) sum rule (involving the nucleon anomalous magnetic moment) and the Gell-Mann, Goldberger and Thirring [2, 41] (GGT) sum rule (for the forward spin polarizability). We perform a preliminary analysis of these sum rules by evaluating the integrals directly from the available experimental data, without using any phenomenological parametrization. The aim is to develop a new method of analysis that allows one to obtain a more realistic evaluation of the error bands. Being a preliminary evaluation, only the pure statistical fluctuations of the experimental data are included in the analysis, while the systematic errors are neglected.

In Ch. 8, we draw our conclusions and we also outline possible future strategies for a better determination of the scalar polarizabilities as well as of the spin polarizabilities.

Chapter 2

Compton scattering off the nucleon

Compton scattering off the nucleon is a valuable tool to investigate the electromagnetic internal structure of the nucleon. In this chapter, we describe the real Compton scattering process, where both the incoming and the outgoing photons are real, and we introduce the physical meaning of the photon-nucleon interaction through an effective Hamiltonian description. We then discuss some of the observables that can be experimentally measured and that can provide relevant information on the electromagnetic structure of the nucleon.

2.1 Introduction

Real Compton scattering (RCS), i.e. the elastic scattering of a real photon off the nucleon, is a physical process that can give a clean access to the internal structure of the nucleon. At very low energy, the incoming photon carries a quasi-static electromagnetic field and the response of the nucleon can be parametrized in terms of static polarizabilities. This is a reflection of the composite structure of the nucleon: the nucleon system cannot be described as a point-like particle characterized by only its static properties (mass, electric charge and anomalous magnetic moment), but its internal constituents cause the appearance of a collective response to the external field. As soon as the incoming photon energy increases, the nucleon becomes sensitive to the temporal and spatial variation of the external field. In this framework, relaxation mechanisms, baryonic resonances and meson production thresholds of the nucleon give rise to dispersive corrections to the static polarizabilities, and the nucleon response is conveniently described in terms of dynamical polarizabilities, i.e. polarizabilities with an explicit dependence on the incoming photon energy.

In this work, we will discuss a new extraction of both the static and dynamical scalar dipole polarizabilities, using a new statistical technique applied to

the available RCS data below the pion production threshold and a theoretical framework based on fixed-t dispersion relations. The nucleon polarizabilities from RCS data have been widely analyzed in the literature, mainly adopting two different theoretical frameworks: (I) fixed-t dispersion relations (DRs), in the unsubtracted [11–13] and subtracted [14–18] formalism, and (II) chiral perturbation theory (χPT) with explicit nucleons and Deltas, in the variant of heavy-baryon χPT (HBχPT) [6–8] and manifestly covariant [9, 10] χPT (BχPT). Some alternative approaches can be found in Ref. [42] ("dressed K matrix") and in Ref. [43] (chiral Lagrangian approach with constraints from unitarity and analyticity), but they have never been used for a fit of the polarizabilities to the RCS data.

Such a high number of models and theories provides a very important benchmark for the theoretical framework and allow us to better control the model dependence in the extraction of the nucleon polarizabilities from RCS data.

In this chapter, we will discuss the RCS amplitude, how it can be parametrized and how the polarizabilities enter the physical observables.

2.2 Real Compton scattering

Real Compton scattering off the nucleon corresponds to the reaction:

$$\gamma(q) + N(p) \to \gamma(q') + N(p'),$$

where the four-momenta of the participating particles are in brackets and both the incoming and the outgoing photons are real, i.e. $q^2 = q'^2 = 0$. The reaction is shown in Fig. 2.1. The RCS amplitude T_{fi} is defined by

$$\langle f|S-1|i\rangle = i(2\pi)^4\delta^4(q+p-q'-p')T_{fi}, \tag{2.1}$$

and it is related to the differential cross section $d\sigma/d\Omega$ through the following relation

$$\frac{d\sigma}{d\Omega} = \Phi^2|T_{fi}|^2, \tag{2.2}$$

where the phase factor Φ is given by

$$\Phi \equiv \begin{cases} \frac{1}{8\pi M_N}\frac{E'_\gamma}{E_\gamma} & \text{lab frame,} \\ \frac{1}{8\pi\sqrt{s}} & \text{c.m. frame} \end{cases}. \tag{2.3}$$

The labels "lab frame" and "c.m. frame" stand for laboratory and center-of-mass reference frames, respectively. Here, $E_\gamma = q_0$, $E'_\gamma = q'_0$ are the incident and outgoing photon energies in the lab frame, respectively. Being a $2 \to 2$ process, RCS can be described by two independent kinematic invariants. Using the usual Mandelstam variables with their constraints, i.e.

$$\begin{aligned} s &= (p+q)^2 = (p'+q')^2, \quad t = (p-p')^2 = (q-q')^2, \\ u &= (p-q')^2 = (q-p')^2, \quad s+t+u = 2M_N^2, \end{aligned} \tag{2.4}$$

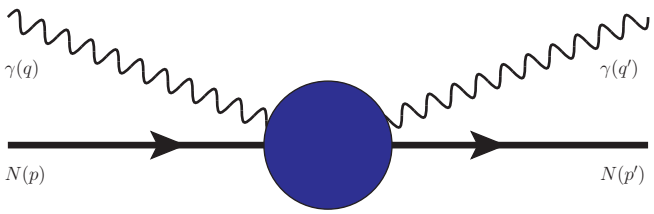

Figure 2.1: Graph of the RCS process.

we can define the crossing symmetric variable ν as

$$\nu = \frac{s-u}{4M_N}. \tag{2.5}$$

The two independent invariants are then chosen to be ν and t, which are expressed in the lab reference frame as

$$\nu = \frac{1}{2}(E_\gamma + E'_\gamma), \quad t = -2E_\gamma E'_\gamma(1-z), \tag{2.6}$$

where $z = \cos\theta_{\rm lab}$ and the scattered photon energy E'_γ can be written as

$$E'_\gamma \equiv E_\gamma + \frac{t}{2M_N} = E_\gamma \left[1 + \frac{E_\gamma}{M_N}(1-z)\right]^{-1}. \tag{2.7}$$

In the most generic form, the scattering amplitude for the RCS process can be formally decomposed as

$$T_{fi} = \bar{u}(p')\epsilon'^{*\mu}\mathcal{C}_{\mu\nu}\epsilon^\nu u(p), \tag{2.8}$$

where $\epsilon^\nu = (0, \boldsymbol{\epsilon})$ and $\epsilon'^\mu = (0, \boldsymbol{\epsilon}')$ are the polarization[1] four-vectors of the incoming and outgoing photon, respectively, while $u(p)$ is the Dirac nucleon spinor with momentum p and $\mathcal{C}_{\mu\nu}$ is the tensor that describe the electromagnetic interaction of the nucleon with the incoming and outgoing photons. In Sec. 2.3, we will show two possible parameterizations for the $\mathcal{C}_{\mu\nu}$ tensor in terms of invariant amplitudes.

2.2.1 Effective Hamiltonian description

If we want to describe the RCS process in terms of low-energy effective Hamiltonians [9, 15], to lowest order in energy, i.e. when the wavelength of the photons is much larger than the size of the target, one has

$$\mathcal{H}^{(0)} = \frac{(\boldsymbol{p} - e\boldsymbol{A})^2}{2M_N}, \tag{2.9}$$

[1]The photon polarization vector $\boldsymbol{\epsilon}$ is chosen in the radiation gauge, i.e. $\boldsymbol{\epsilon}\cdot\boldsymbol{q} = 0$.

where $\boldsymbol{p}$ is the momentum operator and $\boldsymbol{A}$ is the vector potential. This term contributes at $\mathcal{O}(\omega_B^0)$ in the scattering amplitude of RCS[2] and correspond to the well-known Thomson term, i.e.

$$T_{fi}^{Thomson} = -2e^2 q^2 \boldsymbol{\epsilon} \cdot \boldsymbol{\epsilon}', \tag{2.10}$$

completely determined by the charge of the nucleon[3], as well as by the photon polarization vectors. As the energy of the incoming photon increases, the nucleon structure becomes visible and the photon wavelength is short enough to probe it. The corresponding effective Hamiltonian needs to fulfill some constraints: (I) it must be quadratic in the fields, (II) it has to be gauge invariant and (III) it must be a rotational scalar and invariant under parity (P) and time reversal (T) transformations. The simplest form is

$$\mathcal{H}^{(2)} = -\frac{1}{2} 4\pi \left(\alpha_{E1} \boldsymbol{E}^2 + \beta_{M1} \boldsymbol{H}^2 \right), \tag{2.11}$$

where $\boldsymbol{E}$ and $\boldsymbol{H}$ are the static electric and magnetic fields, respectively. This contribution enters the RCS amplitudes at $\mathcal{O}(\omega_B^2)$. With the definitions of the electric and magnetic dipole moments,

$$\boldsymbol{p}_{el} = -\frac{\delta H^{(2)}}{\delta \boldsymbol{E}} = 4\pi \alpha_{E1} \boldsymbol{E}, \quad \boldsymbol{\mu}_{mag} = -\frac{\delta H^{(2)}}{\delta \boldsymbol{H}} = 4\pi \beta_{M1} \boldsymbol{H}, \tag{2.12}$$

we recognize the proportionality constants α_{E1} and β_{M1} in Eq. (2.11) as the electric and magnetic polarizabilities, respectively. In a naive picture of the nucleon, when the external electric field is applied, the charge distribution of the nucleon is stretched by the external field, thus causing the appearance of an electric polarization vector $\boldsymbol{p}_{el}$, which is proportional to the photon electric field via the electric polarizability α_{E1}. Since the resulting electric polarization is along the direction of the external field, the polarizability α_{E1} is positive[4]. The external quasi-static photon also brings a magnetic field that causes two effects in the magnetic polarization $\boldsymbol{\mu}_{mag}$: (I) a paramagnetic effect due to the alignment of the spin magnetic moments of the internal constituents of the nucleon in the direction of $\boldsymbol{H}$ and (II) a diamagnetic effect due to the pion induced currents that, according to Lenz's law, tend to generate a magnetic field opposite to the external one. As a result, we expect the magnetic polarizability β_{M1} to be small, being determined by two contributions of opposite sign[5].

If the energy of the incoming photon becomes larger (i.e., its wavelength becomes smaller), one finds four possible interaction terms that obey the requirements of gauge, P and T. The corresponding effective Hamiltonian at

[2]Here and in the following, the subscript B stands for the Breit reference frame.

[3]$e^2 \simeq 4\pi/137$ and $q = 0(1)$ for the neutron (proton).

[4]This is not always true: for instance, χPT predicts $\alpha_{E1} < 0$ for the neutral pion π^0 [44].

[5]This picture does not hold in general for the hadrons. For instance, chiral perturbation theory predicts $\beta_{M1} \approx -\alpha_{E1}$ for pions [44].

$\mathcal{O}(\omega_B^4)$ is

$$\mathcal{H}^{(4)} = -\frac{1}{2}4\pi\left(\alpha_{E1,\nu}\dot{\boldsymbol{E}}^2 + \beta_{M1,\nu}\dot{\boldsymbol{H}}^2\right) - \frac{1}{12}4\pi\left(\alpha_{E2}E_{ij}^2 + \beta_{M2}H_{ij}^2\right), \quad (2.13)$$

where

$$E_{ij} = \frac{1}{2}(\nabla_i E_j + \nabla_j E_i), \quad H_{ij} = \frac{1}{2}(\nabla_i H_j + \nabla_j H_i). \quad (2.14)$$

In Eq. (2.13), one becomes sensitive to the spatial and time variations of the electromagnetic field. The parameters α_{E2} and β_{M2} represent quadrupole polarizabilities and measure the electric (Q_{ij}) and magnetic (M_{ij}) quadrupole moments induced in a system in the presence of an applied field gradient via

$$Q_{ij} = \frac{\delta\mathcal{H}^{(4)}}{\delta E_{ij}} = \frac{1}{6}4\pi\alpha_{E2}E_{ij}, \quad M_{ij} = \frac{\delta\mathcal{H}^{(4)}}{\delta H_{ij}} = \frac{1}{6}4\pi\beta_{M2}H_{ij}. \quad (2.15)$$

On the other hand, the quantities $\alpha_{E1,\nu}$, $\beta_{M1,\nu}$ represent the dispersive correction to the lowest order static polarizabilities α_{E1} and β_{M1} or, equivalently, the response of the nucleon to the external time-dependent fields, i.e.

$$\begin{aligned} \boldsymbol{p}_{el}(\omega_B) &= 4\pi\alpha_{E1}(\omega_B)\boldsymbol{E}(\omega_B) \\ &= 4\pi(\alpha_{E1} + \alpha_{E1,\nu}\omega_B^2 + \mathcal{O}(\omega_B^4))\boldsymbol{E}(\omega_B), \quad (2.16) \\ \boldsymbol{\mu}_{mag}(\omega_B) &= 4\pi\beta_{M1}(\omega_B)\boldsymbol{H}(\omega_B) \\ &= 4\pi(\beta_{M1} + \beta_{M1,\nu}\omega_B^2 + \mathcal{O}(\omega_B^4))\boldsymbol{H}(\omega_B). \quad (2.17) \end{aligned}$$

From Eqs. (2.16) and (2.17) we learn that, if we consider a time-dependent electromagnetic field, the polarizabilities need to become energy dependent, thus making the definition of the dynamical polarizabilities, $\alpha_{E1}(\omega_B)$ and $\beta_{M1}(\omega_B)$ (i.e. with an explicit energy-dependence) necessary. We will come back to this point in Ch. 6, where we will fit the scalar dipole dynamical polarizabilities to the RCS proton data.

Up to now we have neglected the spin-dependence of the nucleon: the first spin-dependent contribution in the Hamiltonian appears at $\mathcal{O}(\omega_B^3)$ as

$$\begin{aligned} \mathcal{H}^{(3)} &= -\frac{1}{2}4\pi\Big[\gamma_{E1E1}\boldsymbol{\sigma}\cdot\boldsymbol{E}\times\dot{\boldsymbol{E}} + \gamma_{M1M1}\boldsymbol{\sigma}\cdot\boldsymbol{H}\times\dot{\boldsymbol{H}} \\ &- 2\gamma_{M1E2}E_{ij}\sigma_i H_j + 2\gamma_{E1M2}H_{ij}\sigma_i E_j\Big], \quad (2.18) \end{aligned}$$

where the four $\gamma_{...}$ are the so-called spin polarizabilities. The γ_{E1E1} and γ_{M1M1} polarizabilities describe the spin-dependence of the dipole electric and magnetic photon scattering ($E1 \to E1$ and $M1 \to M1$). On the other hand, γ_{E1M2} describes the dipole electric to quadrupole magnetic transition of the photon field due to the spin-dependent interaction with the nucleon. Similarly, γ_{M1E2} corresponds to the spin-dependent response of the nucleon to an incoming dipole magnetic field that is scattered in a quadrupole electric field in the final state. Also the spin polarizabilities, as the electric and magnetic

polarizabilities, show dispersive corrections due to the time-dependence of the electromagnetic field. At $\mathcal{O}(\omega_B^5)$ the effective interaction reads

$$\begin{aligned}\mathcal{H}^{(5)} &= -\frac{1}{2}4\pi\Big[\gamma_{E1E1,\nu}\boldsymbol{\sigma}\cdot\dot{\boldsymbol{E}}\times\ddot{\boldsymbol{E}}\gamma_{M1M1,\nu}\boldsymbol{\sigma}\cdot\dot{\boldsymbol{H}}\times\ddot{\boldsymbol{H}} \\ &\quad -2\gamma_{M1E2,\nu}\sigma_i\dot{E}_{ij}\dot{H}_j+2\gamma_{E1M2,\nu}\sigma_i\dot{H}_{ij}\dot{E}_j+4\gamma_{E2E2}\epsilon_{ijk}\sigma_iE_{jl}\dot{E}_{kl} \\ &\quad +4\gamma_{M2M2}\epsilon_{ijk}\sigma_iH_{jl}\dot{H}_{kl}-6\gamma_{M2E3}\sigma_iE_{ijk}H_{jk}+6\gamma_{E2M3}\sigma_iH_{ijk}E_{jk}\Big],\end{aligned} \tag{2.19}$$

where

$$\begin{aligned}E_{ijk} &= \frac{1}{3}\left[\nabla_i\nabla_jE_k+\nabla_i\nabla_kE_j+\nabla_j\nabla_kE_i\right] \\ &- \frac{1}{15}\left[\delta_{ij}\nabla^2E_k+\delta_{jk}\nabla^2E_i+\delta_{ik}\nabla^2E_j\right],\end{aligned} \tag{2.20}$$

and similarly for H, are the spherical tensor gradient of the electric and magnetic fields, respectively. In Eq. (2.19), four polarizabilities (the ones labeled with the subscript ν) are dispersive corrections to the $\mathcal{O}(\omega_B^3)$ polarizabilities defined in Eq. (2.18). The remaining polarizabilities are new structure constants that probe the octupole excitation of the system.

2.3 Invariant amplitudes of the real Compton scattering

As shown in Ref. [12] and references therein, starting from a basis of independent and orthogonal four-vectors, we can parametrize the scattering amplitude T_{fi} through six invariant functions T_i:

$$\begin{aligned}T_{fi} &= \bar{u}(p')\epsilon'^{*\mu}\Big[-\frac{P'_\mu P'_\nu}{P'^2}(T_1+\gamma\cdot KT_2) \\ &- \frac{N_\mu N_\nu}{N^2}(T_3+\gamma\cdot KT_4)+i\frac{P'_\mu N_\nu-P'_\nu N_\mu}{P'^2K^2}\gamma_5T_5 \\ &+ i\frac{P'_\mu N_\nu+P'_\nu N_\mu}{P'^2K^2}\gamma_5\gamma\cdot KT_6\Big]\epsilon^\nu u(p),\end{aligned} \tag{2.21}$$

where γ_5 is conventionally defined as $\gamma_5\equiv\begin{pmatrix}0&1\\1&0\end{pmatrix}$.
The four-vectors P, P', K and N are defined as

$$\begin{aligned}P^\mu &= \frac{1}{2}(p+p')^\mu, \qquad P'^\mu = P^\mu - K^\mu\frac{P\cdot K}{K^2}, \\ K^\mu &= \frac{1}{2}(q+q')^\mu, \qquad N^\mu = \varepsilon^{\mu\alpha\beta\gamma}P'_\alpha Q_\beta K_\gamma,\end{aligned}$$

where Q is given by

$$Q^\mu = \frac{1}{2}(p-p')^\mu = \frac{1}{2}(q'-q)^\mu, \tag{2.22}$$

and the antisymmetric tensor $\varepsilon^{\mu\alpha\beta\gamma}$ is fixed by the condition $\varepsilon^{0123} = -1$. The T_i amplitudes are functions of ν and t and are free from kinematic singularities but can be affected by kinematic constraints arising from the denominators of Eq. (2.21), that can vanish in the limit of forward or backward scattering. To circumvent this problem, we work with the tensorial basis proposed in Ref. [11], resulting in the set of amplitudes

$$\begin{aligned}
A_1 &= \frac{1}{t}[T_1 + T_3 + \nu(T_2 + T_4)], & A_2 &= \frac{1}{t}[2T_5 + \nu(T_2 + T_4)], \\
A_3 &= \frac{1}{\eta}[T_1 - T_3 - \frac{t}{4\nu}(T_2 - T_4)], & A_4 &= \frac{1}{\eta}[2M_N T_6 - \frac{t}{4\nu}(T_2 - T_4)], \\
A_5 &= \frac{1}{4\nu}(T_2 + T_4), & A_6 &= \frac{1}{4\nu}(T_2 - T_4),
\end{aligned} \tag{2.23}$$

where η is defined as

$$\eta \equiv 4\nu^2 + t - \frac{t^2}{4M_N^2} = 2E_\gamma E'_\gamma(1 + z). \tag{2.24}$$

Like the T_i amplitudes, the A_i do not have any kinematic singularities: in addition, they are free from any kinematic constraints and are symmetric under crossing:

$$A_i(\nu, t) = A_i(-\nu, t), \qquad i = 1, \ldots, 6. \tag{2.25}$$

These properties turn out to be very useful in the dispersion relation (DR) approach, as described in Ch. 3.

The scattering amplitude T_{fi} can thus be conveniently expressed in terms of the invariant amplitudes A_i as [12]

$$\begin{aligned}
T_{fi} &= \frac{1}{N(t)} \Bigg\{ 2M_N \boldsymbol{\epsilon}'^* \cdot \boldsymbol{\epsilon} E_\gamma E_\gamma \left[\left(1 - \frac{t}{4M_N^2}\right)(-A_1 - A_3) - \frac{\nu^2}{M_N^2} A_5 - A_6 \right] \\
&+ 2M_N \boldsymbol{s}'^* \cdot \boldsymbol{s} E_\gamma E'_\gamma \left[\left(1 - \frac{t}{4M_N^2}\right)(-A_1 - A_3) + \frac{\nu^2}{M_N^2} A_5 - A_6 \right] \\
&- 2i\boldsymbol{\sigma} \cdot \boldsymbol{\epsilon}'^* \times \boldsymbol{\epsilon} \nu E_\gamma E'_\gamma (A_5 + A_6) + 2i\boldsymbol{\sigma} \cdot \boldsymbol{s}'^* \times \boldsymbol{s} \nu E_\gamma E'_\gamma (A_5 - A_6) \\
&+ i\boldsymbol{\sigma} \cdot \hat{\boldsymbol{q}} \boldsymbol{s}'^* \cdot \boldsymbol{\epsilon} E_\gamma^2 E'_\gamma \left[A_2 + \left(1 - \frac{E'_\gamma}{M_N}\right) A_4 + \frac{\nu}{M_N} A_5 + A_6 \right] \\
&- i\boldsymbol{\sigma} \cdot \hat{\boldsymbol{q}}' \boldsymbol{\epsilon}'^* \cdot \boldsymbol{s} E_\gamma E'^2_\gamma \left[A_2 + \left(1 + \frac{E_\gamma}{M_N}\right) A_4 - \frac{\nu}{M_N} A_5 + A_6 \right] \\
&- i\boldsymbol{\sigma} \cdot \hat{\boldsymbol{q}} \boldsymbol{\epsilon}'^* \cdot \boldsymbol{s} E_\gamma^2 E'_\gamma \left[-A_2 + \left(1 - \frac{E'_\gamma}{M_N}\right) A_4 - \frac{\nu}{M_N} A_5 + A_6 \right] \\
&+ i\boldsymbol{\sigma} \cdot \hat{\boldsymbol{q}}' \boldsymbol{s}'^* \cdot \boldsymbol{\epsilon} E_\gamma E'^2_\gamma \left[-A_2 + \left(1 + \frac{E_\gamma}{M_N}\right) A_4 + \frac{\nu}{M_N} A_5 + A_6 \right] \Bigg\},
\end{aligned} \tag{2.26}$$

where $N(t) = (1 - t/4M_N^2)^{1/2}$ and $\boldsymbol{s}$ and $\boldsymbol{s}'$ are defined as $\boldsymbol{s} = \hat{\boldsymbol{q}} \times \boldsymbol{\epsilon}$ and $\boldsymbol{s}' = \hat{\boldsymbol{q}}' \times \boldsymbol{\epsilon}'$, respectively.

2.3.1 Low energy expansion and static polarizabilities

We first decompose the A_i amplitudes in terms of the Born and non-Born contributions, i.e.

$$A_i(\nu,t) = A_i^B(\nu,t) + A_i^{NB}(\nu,t), \quad (i=1,\ldots,6). \tag{2.27}$$

The Born term is associated with the pole diagrams shown in Fig. 2.2, where a single nucleon is exchanged and the photon-nucleon vertices are in the on-shell regime. It is completely determined by the mass, the electric charge e and the anomalous magnetic moment $e\kappa_N/2M_N$ of the nucleon as [11]

$$A_i^B(\nu,t) = -\frac{4M_N e^2 r_i(t)}{(4M_N\nu - t)(4M_N\nu + t)}, \tag{2.28}$$

where $e^2 \simeq 4\pi/137$. The pole residues $r_i(t)$ are defined as

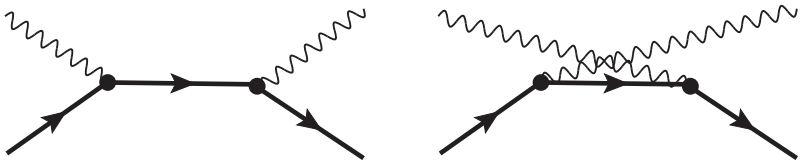

Figure 2.2: The direct (on the left) and crossed (on the right) Born diagrams that contribute to the RCS process.

$$\begin{aligned} r_1 &= -2q^2 + r_3\frac{t}{4M_N^2}, \quad r_2 = 2q\kappa_N + 2q^2 + r_3\frac{t}{4M_N^2}, \\ r_3 &= \kappa_N^2 + 2q\kappa_N, \quad r_4 = \kappa_N^2, \quad r_5 = r_3, \quad r_6 = -2q^2 - r_3. \end{aligned} \tag{2.29}$$

The non-Born contribution subsumes all the structure-dependent information, and can be expanded in a Taylor series of the ν and t variables around the point $\nu = t = 0$, i.e.

$$\begin{aligned} A_i^{NB}(\nu,t) &= A_i^{NB}(\nu,t)|_{(\nu^2=t=0)} + \left.\frac{\partial A_i^{NB}(\nu,t)}{\partial\nu^2}\right|_{(\nu^2=t=0)}\nu^2 \\ &\quad + \left.\frac{\partial A_i^{NB}(\nu,t)}{\partial t}\right|_{(\nu^2=t=0)} t + \mathcal{O}(\nu^4, t^2), \end{aligned} \tag{2.30}$$

thus introducing the low-energy expansion (LEX) of the RCS amplitudes. According to the following definitions,

$$\begin{aligned} a_i &\equiv A_i^{NB}(\nu=0,t=0), \\ a_{i,\nu} &\equiv \left.\frac{\partial A_i^{NB}(\nu,t)}{\partial\nu^2}\right|_{(\nu^2=t=0)}, \\ a_{i,t} &\equiv \left.\frac{\partial A_i^{NB}(\nu,t)}{\partial t}\right|_{(\nu^2=t=0)}, \end{aligned} \tag{2.31}$$

and using the expression given in Eq. (2.6), we can rewrite the non-Born contributions as

$$A_i^{NB}(\nu,t) = a_i + E_\gamma E'_\gamma [a_{i,\nu} - 2(1-z)a_{i,t}] + \dots \tag{2.32}$$

This LEX is equivalent to the low-energy expansion used for the description of the RCS process in terms of an effective Hamiltonian, as shown in Sec. 2.2.1. Thus, we can make a connection between the coefficients of Eq. (2.32) and the static polarizabilities introduced in Sec. 2.2.1. The results, up to the fifth order in energy, are

$$\begin{aligned}
4\pi\alpha_{E1} &= -a_1 - a_3 - a_6, \\
4\pi\beta_{M1} &= a_1 - a_3 - a_6, \\
4\pi\gamma_{E1E1} &= \frac{a_2 - a_4 + 2a_5 + a_6}{2M_N}, \\
4\pi\gamma_{M1M1} &= \frac{-a_2 - a_4 - 2a_5 + a_6}{2M_N}, \\
4\pi\gamma_{M1E2} &= \frac{-a_2 - a_4 - a_6}{2M_N}, \\
4\pi\gamma_{E1M2} &= \frac{a_2 - a_4 - a_6}{2M_N}, \\
4\pi\alpha_{E2} &= -12\,(a_{1,t} + a_{3,t} + a_{6,t}) + \frac{3a_3}{M_N^2}, \\
4\pi\beta_{M2} &= 12\,(a_{1,t} - a_{3,t} - a_{6,t}) + \frac{3a_3}{M_N^2}, \\
4\pi\alpha_{E1,\nu} &= 3a_{1,t} - a_{1,\nu} + a_{3,t} - a_{3,\nu} + a_{6,t} - a_{6,\nu} + \frac{-a_3 - 4a_5}{4M_N^2}, \\
4\pi\beta_{M1,\nu} &= -3a_{1,t} + a_{1,\nu} + a_{3,t} - a_{3,\nu} + a_{6,t} - a_{6,\nu} + \frac{4a_5 - a_3}{4M_N^2}, \\
4\pi\gamma_{E2E2} &= \frac{a_{2,t} - a_{4,t} + 3a_{5,t} + 2a_{6,t}}{6M_N} + \frac{a_2 + 2a_4}{48M_N^3}, \\
4\pi\gamma_{M2M2} &= \frac{-a_{2,t} - a_{4,t} - 3a_{5,t} + 2a_{6,t}}{6M_N} + \frac{2a_4 - a_2}{48M_N^3}, \\
4\pi\gamma_{M2E3} &= \frac{-a_{2,t} - a_{4,t} - a_{6,t}}{3M_N} + \frac{2a_4 - a_2}{24M_N^3}, \\
4\pi\gamma_{E2M3} &= \frac{a_{2,t} - a_{4,t} - a_{6,t}}{3M_N} + \frac{a_2 + 2a_4}{24M_N^3}, \\
4\pi\gamma_{E1E1,\nu} &= \frac{-3a_{2,t} + a_{2,\nu} + a_{4,t} - a_{4,\nu} - 5a_{5,t} + 2a_{5,\nu} - 2a_{6,t} + a_{6,\nu}}{2M_N} \\
&+ \frac{-3a_2 - 2(a_4 - 2a_5)}{16M_N^3}, \\
4\pi\gamma_{M1M1,\nu} &= \frac{3a_{2,t} - a_{2,\nu} + a_{4,t} - a_{4,\nu} + 5a_{5,t} - 2a_{5,\nu} - 2a_{6,t} + a_{6,\nu}}{2M_N}
\end{aligned}$$

$$
\begin{aligned}
&+ \quad \frac{3a_2 - 2\,(a_4 + 2a_5)}{16M_N^3}, \\
4\pi\gamma_{M1E2,\nu} &= \frac{18a_{2,t} - 5a_{2,\nu} + 2a_{4,t} - 5a_{4,\nu} + 10a_{5,t} + 12a_{6,t} - 5a_{6,\nu}}{10M_N} \\
&+ \quad \frac{9a_2 - 2\,(a_4 + 5a_5)}{40M_N^3}, \\
4\pi\gamma_{E1M2,\nu} &= \frac{-18a_{2,t} + 5a_{2,\nu} + 2a_{4,t} - 5a_{4,\nu} - 10a_{5,t} + 12a_{6,t} - 5a_{6,\nu}}{10M_N} \\
&+ \quad \frac{-9a_2 - 2(a_4 - 5a_5)}{40M_N^3}.
\end{aligned} \tag{2.33}
$$

All the static polarizabilities in Eq. (2.33) can be written as $P_{main}/M_N^n + P_{rec}/M_N^{n+2}$, where P_{main} and P_{rec} are linear combinations of the a_i, $a_{i,\nu}$ and $a_{i,t}$ coefficients, with the recoil contributions P_{rec}/M_N^{n+2} being a consequence of the choice of the reference frame[6].

It is also useful to define two combinations of the leading-order spin polarizabilities, which enter in the scattering amplitudes at forward and backward scattering angles. They are the forward spin polarizability, γ_0, and the backward spin polarizability, γ_π, defined as

$$
\begin{aligned}
\gamma_0 &= -\gamma_{E1E1} - \gamma_{M1M1} - \gamma_{M1E2} - \gamma_{E1M2}, \\
\gamma_\pi &= -\gamma_{E1E1} + \gamma_{M1M1} + \gamma_{M1E2} - \gamma_{E1M2}.
\end{aligned} \tag{2.34}
$$

2.3.2 Multipoles decomposition and dynamical polarizabilities

The multipole interactions that have been introduced in Sec. 2.2.1 to define the static polarizabilities can be obtained by performing a multipole expansion of the incoming and outgoing photon fields in the Compton scattering amplitude. Working in the c.m. frame, the scattering amplitude T_{fi} reads [45, 46]:

$$
T_{fi} = 8\pi W \sum_{i=1}^{6} \rho_i R_i(\omega, \theta_{c.m.}). \tag{2.35}
$$

Here $\theta_{c.m.}$ is the photon scattering angle in the c.m. frame, $W = \sqrt{s}$ and

$$
\begin{aligned}
\rho_1 &= \boldsymbol{\epsilon}'^{*} \cdot \boldsymbol{\epsilon}, \quad \rho_2 = \boldsymbol{s}'^{*} \cdot \boldsymbol{s}, \\
\rho_3 &= i\boldsymbol{\sigma} \cdot \boldsymbol{\epsilon}'^{*} \times \boldsymbol{\epsilon}, \quad \rho_4 = i\boldsymbol{\sigma} \cdot \boldsymbol{s}'^{*} \times \boldsymbol{s}, \\
\rho_5 &= i(\boldsymbol{\sigma} \cdot \hat{\boldsymbol{q}} \boldsymbol{s}'^{*} \cdot \boldsymbol{\epsilon} - \boldsymbol{\sigma} \cdot \hat{\boldsymbol{q}}' \boldsymbol{\epsilon}'^{*} \cdot \boldsymbol{s}), \\
\rho_6 &= i(\boldsymbol{\sigma} \cdot \hat{\boldsymbol{q}}' \boldsymbol{s}'^{*} \cdot \boldsymbol{\epsilon} - \boldsymbol{\sigma} \cdot \hat{\boldsymbol{q}} \boldsymbol{\epsilon}'^{*} \cdot \boldsymbol{s}).
\end{aligned} \tag{2.36}
$$

[6]The static polarizabilities are conveniently defined in the Breit frame, as discussed in Sec. 2.2.1.

The relations between the amplitudes R_i and A_i can be found in App. A. Following [11], we can now write the R_i amplitudes through a multipole expansion of the form:

$$\begin{aligned}
R_1 &= \sum_{l\geq 1}\{[(l+1)f_{EE}^{l+}+lf_{EE}^{l-}](lP_l'+P_{l-1}'')-[(l+1)f_{MM}^{l+}+lf_{MM}^{l-}]P_l''\},\\
R_2 &= \sum_{l\geq 1}\left\{[(l+1)f_{MM}^{l+}+lf_{MM}^{l-}](lP_l'+P_{l-1}'')-[(l+1)f_{EE}^{l+}+lf_{EE}^{l-}]P_l''\right\},\\
R_3 &= \sum_{l\geq 1}\left\{[f_{EE}^{l+}-f_{EE}^{l-}](P_{l-1}''-l^2P_l')-[f_{MM}^{l+}-f_{MM}^{l-}]P_l''\right.\\
&+ \left. 2f_{EM}^{l+}P_{l+1}''-2f_{ME}^{l+}P_l''\right\},\\
R_4 &= \sum_{l\geq 1}\left\{[f_{MM}^{l+}-f_{MM}^{l-}](P_{l-1}''-l^2P_l')-[f_{EE}^{l+}-f_{EE}^{l-}]P_l''\right.\\
&+ \left. 2f_{ME}^{l+}P_{l+1}''-2f_{EM}^{l+}P_l''\right\},\\
R_5 &= \sum_{l\geq 1}\{[f_{EE}^{l+}-f_{EE}^{l-}](lP_l''+P_{l-1}''')-[f_{MM}^{l+}-f_{MM}^{l-}]P_l'''\\
&+ f_{EM}^{l+}[(3l+1)P_l''+2P_{l-1}''']-f_{ME}^{l+}[(l+1)P_{l+1}''+2P_l''']\},\\
R_6 &= \sum_{l\geq 1}\{[f_{MM}^{l+}-f_{MM}^{l-}](lP_l''+P_{l-1}''')-[f_{EE}^{l+}-f_{EE}^{l-}]P_l'''\\
&+ f_{ME}^{l+}[(3l+1)P_l''+2P_{l-1}''']-f_{EM}^{l+}[(l+1)P_{l+1}''+2P_l''']\}. \qquad (2.37)
\end{aligned}$$

Here $P_l = P_l(x)$ are the Legendre polynomials of $x = \cos\theta_{c.m.}$, the superscript "′" stands for the derivative and the multipole amplitudes are labeled as $f_{TT'}^{l\pm} = f_{TT'}^{l\pm}(\omega)$, with $T, T' = E, M$, corresponding to transitions $T \to T'$. The superscript $l\pm$ indicates the angular momentum l of the initial photon and the total angular momentum is given by $j = l \pm \frac{1}{2}$. The advantage of the multipole expansion is that all the energy dependence is included in the multipoles $f_{TT'}^{l\pm}(\omega)$, while the angular dependence is described by the Legendre polynomials.

From the multipoles introduced in Eq. (2.37), we can define the dynamical polarizabilities [29, 30], i.e. polarizabilities with an explicit and full dependence on the photon energy ω, as

$$\begin{aligned}
\alpha_{El}(\omega) &= a(l)\frac{(l+1)\bar{f}_{EE}^{l+}+l\bar{f}_{EE}^{l-}}{\omega^{2l}},\\
\beta_{Ml}(\omega) &= a(l)\frac{(l+1)\bar{f}_{MM}^{l+}+l\bar{f}_{MM}^{l-}}{\omega^{2l}},\\
\gamma_{ElM(l+1)}(\omega) &= b(l)\frac{\bar{f}_{EM}^{l+}}{\omega^{2l+1}},\\
\gamma_{MlE(l+1)}(\omega) &= b(l)\frac{\bar{f}_{ME}^{l+}}{\omega^{2l+1}},
\end{aligned}$$

$$\begin{aligned}\gamma_{ElEl}(\omega) &= c(l)\frac{\bar{f}^{l+}_{EE}-\bar{f}^{l-}_{EE}}{\omega^{2l+1}},\\ \gamma_{MlMl}(\omega) &= c(l)\frac{\bar{f}^{l+}_{MM}-\bar{f}^{l-}_{MM}}{\omega^{2l+1}},\end{aligned} \tag{2.38}$$

with $a(l) = (l(2l-1)!!))^2$, $b(l) = 2^{2-l}(2l+1)!!$, $c(l) = (2l-1)$, and the bar indicates the non-Born part of the multipoles.
If we focus only on dipole-dipole and dipole-quadrupole transitions (which is equivalent to fix $l_{max} = 1$ in the multipole expansion), we obtain

$$\begin{aligned}\alpha_{E1}(\omega) &= \frac{2\bar{f}^{1+}_{EE}+\bar{f}^{1-}_{EE}}{\omega^2},\\ \beta_{M1}(\omega) &= \frac{2\bar{f}^{1+}_{MM}+\bar{f}^{1-}_{MM}}{\omega^2},\\ \gamma_{E1M2}(\omega) &= 6\frac{\bar{f}^{1+}_{EM}}{\omega^3},\\ \gamma_{M1E2}(\omega) &= 6\frac{\bar{f}^{1+}_{ME}}{\omega^3},\\ \gamma_{E1E1}(\omega) &= \frac{\bar{f}^{1+}_{EE}-\bar{f}^{1-}_{EE}}{\omega^3},\\ \gamma_{M1M1}(\omega) &= \frac{\bar{f}^{1+}_{MM}-\bar{f}^{1-}_{MM}}{\omega^3}.\end{aligned} \tag{2.39}$$

Inserting these definitions in the $l = 1$ terms of the multipole expansion of Eq. (2.37), we obtain

$$\begin{aligned}R^{NB}_{1,l=1} &= \alpha_{E1}(\omega)\omega^2,\\ R^{NB}_{2,l=1} &= \beta_{M1}(\omega)\omega^2,\\ R^{NB}_{3,l=1} &= [\gamma_{E1E1}(\omega)+\gamma_{E1M2}(\omega)]\omega^3,\\ R^{NB}_{4,l=1} &= [-\gamma_{M1M1}(\omega)+\gamma_{M1E2}(\omega)]\omega^3,\\ R^{NB}_{5,l=1} &= -\gamma_{M1E2}(\omega)\omega^3,\\ R^{NB}_{6,l=1} &= -\gamma_{E1M2}(\omega)\omega^3,\end{aligned} \tag{2.40}$$

from where we can clearly see that the electric (magnetic) dipole-dipole transitions of $R_{1,l=1}$ ($R_{2,l=1}$) are entirely described by $\alpha_{E1}(\omega)$ ($\beta_{M1}(\omega)$). On the other hand, the $R_{3,4,5,6}$ amplitudes depend only on the spin-dependent dynamical polarizabilities. The dynamical polarizabilities of Eq. (2.39), in the limit $\omega \to 0$, reduce to the corresponding static polarizabilities[7].

As a cross-check, we can perform the LEX introduced in Eq. (2.32) of the A_i amplitudes and use the relation between R_i and A_i (see App. A for details),

[7]This is not always true, as discussed in Ref. [9], since the unmixed spin polarizabilities of higher angular momentum, like $\gamma_{E2E2}(\omega)$ and $\gamma_{M2M2}(\omega)$ for instance, diverge in the limit of $\omega \to 0$. This effect is a consequence of the transformations required for the connection between the Breit frame, where the static polarizabilities are defined, and the c.m. frame, where the multipole expansion defining the dynamical polarizabilities is performed.

thus obtaining

$$\begin{aligned}
R^{NB}_{1,l=1} &= \alpha_{E1}\omega^2 + \mathcal{O}(\omega^3),\\
R^{NB}_{2,l=1} &= \beta_{M1}\omega^2 + \mathcal{O}(\omega^3),\\
R^{NB}_{3,l=1} &= (\gamma_{E1E1} + \gamma_{E1M2})\omega^3 + \mathcal{O}(\omega^4),\\
R^{NB}_{4,l=1} &= (-\gamma_{M1M1} + \gamma_{M1E2})\omega^3 + \mathcal{O}(\omega^4),\\
R^{NB}_{5,l=1} &= -\gamma_{M1E2}\omega^3 + \mathcal{O}(\omega^4),\\
R^{NB}_{6,l=1} &= -\gamma_{E1M2}\omega^3 + \mathcal{O}(\omega^4),
\end{aligned} \tag{2.41}$$

We will focus on the proton scalar dipole dynamical polarizabilities (DDPs), $\alpha_{E1}(\omega)$ and $\beta_{M1}(\omega)$, as well as their static partners α_{E1} and β_{M1}, that can be fitted to the RCS unpolarized cross section data. It is convenient to express the DDPs in terms of the A_i amplitudes, which will be adopted in the dispersion relations framework described in Ch. 3. This is schematically done as follows:

1. write Eq. (2.37) as function of dynamical polarizabilities defined in Eq. (2.39);

2. fix a value for l_{max}, i.e. the maximum photon angular momentum for the multipole expansion;

3. compute $R_i^{(k)}(\omega, x) \equiv \frac{\partial^k R_i(\omega,x)}{\partial x^k}$ up to $k = l_{max} - 1$;

4. fix a specific value for $\cos\theta_{c.m.}$, e.g. $x = 0$;

5. invert the obtained results in order to write the dynamical polarizabilities in terms of $R_i^{(k)}$.

Following these prescriptions and restricting ourselves to the DDPs, we obtain

$$\begin{aligned}
\alpha_{E1}(\omega) &= -\frac{-10R_1(\omega,0) - 2R_1^{(2)}(\omega,0) - 5R_2^{(1)}(\omega,0)}{10\omega^2},\\
\beta_{M1}(\omega) &= -\frac{-5R_1^{(1)}(\omega,0) - 10R_2(\omega,0) - 2R_2^{(2)}(\omega,0)}{10\omega^2}.
\end{aligned} \tag{2.42}$$

Using the relation (encoded in Eq. (A.1)) between the A_i and the R_i amplitudes given in App. A, it is finally possible to obtain the DDPs as function of the A_i amplitudes and, once introduced the definition of the static polarizabilities given in Eq. (2.33), we obtain the following expressions for the LEX of the

DDPs:

$$
\begin{aligned}
\alpha_{E1}(\omega) &= \alpha_{E1} + \frac{\beta_{M1}}{M_N}\omega + \left(\alpha_{E1,\nu} + \frac{5\alpha_{E1} - 2\beta_{M1}}{8M_N^2}\right)\omega^2 \\
&+ \left(\frac{8\alpha_{E1,\nu} + \alpha_{E2} + 12\beta_{M1,\nu}}{8M_N} + \frac{\gamma_{M1E2} - \gamma_{M1M1}}{8M_N^2} + \frac{\beta_{M1} - 2\alpha_{E1}}{8M_N^3}\right)\omega^3 \\
&+ [\alpha_4^L + \frac{1}{480M_N^4}(-72\alpha_{E1} - 57\beta_{M1} \\
&+ 6M_N(25\gamma_{E1E1} - 25\gamma_{E1M2} + 39(\gamma_{M1E2} - \gamma_{M1M1})) \\
&+ M_N^2(1248\alpha_{E1,\nu} + 95\alpha_{E2} + 540\beta_{M1,\nu} + 26\beta_{M2}) \\
&- 12M_N^3(15\gamma_{E1E1,\nu} - 15\gamma_{E1M2,\nu} - 69\gamma_{E2E2} + 12\gamma_{E2M3} + 25\gamma_{M1E2,\nu} \\
&- 25\gamma_{M1M1,\nu} - 12\gamma_{M2E3} + 51\gamma_{M2M2}))]\omega^4 \\
&+ [\alpha_5^L + \frac{1}{2400M_N^5}(15\alpha_{E1} \\
&+ 5M_N^2(612\alpha_{E1,\nu} + 38\alpha_{E2} + 1008\beta_{M1,\nu} + 89\beta_{M2}) \\
&- 210\beta_{M1} + 15M_N(-46\gamma_{E1E1} + 46\gamma_{E1M2} + 33(\gamma_{M1M1} - \gamma_{M1E2})) \\
&+ 12M_N^3(55\gamma_{E1E1,\nu} - 55\gamma_{E1M2,\nu} - 6(35\gamma_{E2E2} - 22\gamma_{E2M3} + 5\gamma_{M1E2,\nu} \\
&- 5\gamma_{M1M1,\nu} + 38\gamma_{M2E3}) + 555\gamma_{M2M2}))\omega^5 + \mathcal{O}(\omega^6), \qquad (2.43)
\end{aligned}
$$

$$
\begin{aligned}
\beta_{M1}(\omega) &= \beta_{M1} + \frac{\alpha_{E1}}{M_N}\omega + \left(\frac{5\beta_{M1} - 2\alpha_{E1}}{8M_N^2} + \beta_{M1,\nu}\right)\omega^2 \\
&+ \left(\frac{\alpha_{E1} - 2\beta_{M1}}{8M_N^3} + \frac{8\beta_{M1,\nu} + \beta_{M2} + 12\alpha_{E1,\nu}}{8M_N} + \frac{\gamma_{E1M2} - \gamma_{E1E1}}{8M_N^2}\right)\omega^3 \\
&+ [\beta_4^L + \frac{1}{480M_N^4}(-72\beta_{M1} \\
&+ M_N^2(1248\beta_{M1,\nu} + 95\beta_{M2} + 540\alpha_{E1,\nu} + 26\alpha_{E2}) \\
&- 57\alpha_{E1} + 6M_N(25\gamma_{M1M1} - 25\gamma_{M1E2} + 39(\gamma_{E1M2} - \gamma_{E1E1})) \\
&- 12M_N^3(15\gamma_{M1M1,\nu} - 15\gamma_{M1E2,\nu} - 69\gamma_{M2M2} + 12\gamma_{M2E3} + 25\gamma_{E1M2n} \\
&- 25\gamma_{E1E1,\nu} - 12\gamma_{E2M3} + 51\gamma_{E2E2}))]\omega^4 \\
&+ [\beta_5^L + \frac{1}{2400M_N^5}(15\beta_{M1} \\
&+ 5M_N^2(612\beta_{M1,\nu} + 38\beta_{M2} + 1008\alpha_{E1,\nu} + 89\alpha_{E2}) \\
&- 210\alpha_{E1} + 15M_N(-46\gamma_{M1M1} + 46\gamma_{M1E2} + 33(\gamma_{E1E1} - \gamma_{E1M2})) \\
&+ 12M_N^3(55\gamma_{M1M1,\nu} - 55\gamma_{M1E2,\nu} - 6(35\gamma_{M2M2} - 22\gamma_{M2E3} + 5\gamma_{E1M2,\nu} \\
&- 5\gamma_{E1E1,\nu} + 38\gamma_{E2M3}) + 555\gamma_{E2E2}))\omega^5 + \mathcal{O}(\omega^6). \qquad (2.44)
\end{aligned}
$$

The $\alpha_{4,5}^L$ and $\beta_{4,5}^L$ coefficients takes into account the higher order terms in the multipole expansion and are related to 6^{th}-order polarizabilities, which have never been defined in literature. The expression given in Eqs. (2.43) and (2.44) are an extension of the LEX results given in Ref. [9] up to ω^3.

In the expressions of Eqs. (2.43) and (2.44), the coefficients related to the odd powers of ω are the recoil contributions due to the transformation from the Breit frame to the c.m. frame. In the coefficients of the even powers of ω, we can notice both recoil terms and dispersive corrections.

2.3.3 Real Compton scattering observables

Since the RCS process is described by six complex invariant amplitudes, we expect 11 independent observables[8] that can be expressed in terms of the thirteen independent W_{ij} functions introduced in Ref. [12]. We can distinguish several observables depending on the polarization of the incoming or outgoing photon, as well as of the target or recoil nucleon. Following the notation used in

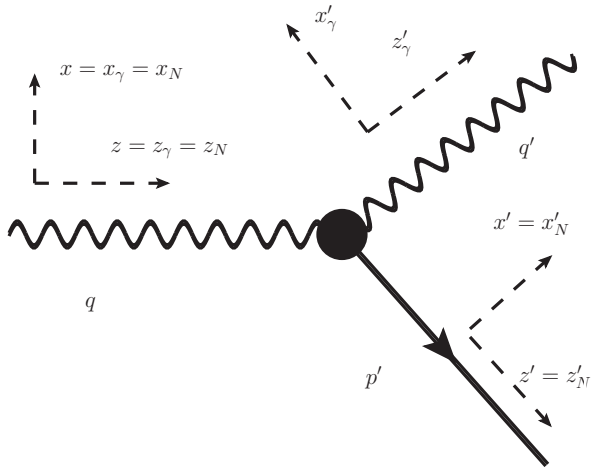

Figure 2.3: Convention for the definition of the polarization in the lab frame, where the y axes point out of the plane.

Fig. 2.3 and the labels used in Ref. [12], it is possible to define the asymmetries Σ_i, Σ_α and $\Sigma_{i\alpha}$, where $i = (1, 2, 3)$ or $(1', 2', 3')$ refers to the photon Stokes parameters that define the incoming or outgoing photon polarization matrix densities[9], while $\alpha = (x_N, y_N, z_N)$ or (x'_N, y'_N, z'_N) refers to the right-hand axes along which the nucleon spin could be aligned. The superscript $'$ in the indices of $\Sigma_{i\alpha}$ refers to the scattered photons or to the recoil nucleons. According to this notation, we can identify 13 independent observables, which can be chosen as in Table 2.1. The full list of polarization observables, also including the ones with the recoil nucleon polarization, can be found in Ref. [12]. We

[8]This number comes from the 12 real functions defining the 6 complex functions A_i minus an overall phase factor.

[9]For the purposes of this chapter, it is sufficient to know that for $i = 1$ the photons are linearly polarized with a $\pi/4$ angle with respect to the scattering plane, for $i = 2$ the photons are circularly polarized and for $i = 3$ the photons are linearly polarized either parallel or perpendicular to the scattering plane. For a comprehensive description we address to Refs. [12, 16]

	photon						
			unpolarized	linear			circular
nucleon	unpolarized		$\boldsymbol{d\sigma/d\Omega}$	x	y	z	
		x		Σ_{1x} , $\Sigma_{1'x}$		$\boldsymbol{\Sigma_3}$	Σ_{2x} , $\Sigma_{2'x}$
	linear	y	Σ_y			Σ_{3y} , $\Sigma_{3'y}$	
		z		Σ_{1z} , $\Sigma_{1'z}$			Σ_{2z} , $\Sigma_{2'z}$
	circular						

Table 2.1: Polarization observables for RCS, classified according to the degree of polarization of the photon or the nucleon. See text for the notation.

focus our attention on two RCS observables: the unpolarized differential cross section $d\sigma/d\Omega$ (neither the nucleons nor the photons are polarized) and the beam asymmetry Σ_3, where the incoming photons are linearly polarized either parallel ($\|$) or perpendicular ($\perp$) to the scattering plane, while the nucleons are unpolarized, i.e.

$$\Sigma_3 = \frac{\sigma^{\|} - \sigma^{\perp}}{\sigma^{\|} + \sigma^{\perp}}.$$

The unpolarized cross section and the beam asymmetry can be written as

$$\frac{d\sigma}{d\Omega} = \Phi^2 W_{00}, \qquad \Sigma_3 = \frac{W_{03}}{W_{00}}, \tag{2.45}$$

where the functions W_{ij} can be expressed in terms of the invariant amplitudes as [12]

$$\begin{aligned}
W_{00}(\nu,t) &= \frac{1}{2}(4M_N^2 - t)(|T_1|^2 + |T_3|^2) - \frac{1}{2}(s - M_N^2)(u - M_N^2)(|T_2|^2 + |T_4|^2) \\
&+ M_N(s-u)\Re(T_1T_2^* + T_3T_4^*) - t|T_5|^2 + (M_N^4 - su)|T_6|^2 \\
&= \frac{1}{4}(4M_N^2 - t)\Big(t^2|A_1|^2 + \eta^2|A_3|^2\Big) - \frac{1}{4}\Big(t^3|A_2|^2 - \eta^3|A_4|^2\Big) \\
&- \nu^2 t\,(t + 8\nu^2)|A_5|^2 \\
&+ \frac{1}{2}\eta\,(t^2 + 2M_N^2\eta)|A_6|^2 + \Re\Big\{2\nu^2t^2(A_1 + A_2)A_5^* \\
&+ \frac{1}{2}\eta^2(4M_N^2A_3 + tA_4)A_6^*\Big\}, \qquad (2.46a) \\
W_{03}(\nu,t) &= \frac{1}{2}(4M_N^2 - t)(|T_1|^2 - |T_3|^2) - \frac{1}{2}(s - M_N^2)(u - M_N^2)(|T_2|^2 - |T_4|^2) \\
&+ M_N(s-u)\Re(T_1T_2^* - T_3T_4^*) \\
&= \frac{\eta t}{2}\Re\Big\{\Big((4M_N^2 - t)A_1 + 4\nu^2A_5\Big)A_3^* + 4M_N^2A_1A_6^*\Big\}, \qquad (2.46b)
\end{aligned}$$

We can now perform a LEX directly on the W_{ij} functions, thus obtaining a LEX on the observables that we are interested in. In order to do so, it is convenient to split the Born part from the non-Born term. Once we define

$r_0 = e^2/4\pi M_N$, the Born contributions of W_{00} and W_{03} read [12]

$$\begin{aligned}\frac{1}{(8\pi M_N)^2}\,W_{00}^{\rm B} &= \frac{r_0^2}{2}\Big\{q^4(1+z^2)+\frac{E_\gamma E_\gamma{}'}{4M_N^2}\Big[4q^3(q+2\kappa_N)(1-z)^2 \\ &+ 2q^2(9-10z+z^2)\kappa_N^2 \\ &+ 4q(3-2z-z^2)\kappa_N^3+(3-z^2)\kappa_N^4\Big]\Big\}, \qquad (2.47)\\ \frac{1}{(8\pi M_N)^2}\,W_{03}^{\rm B} &= -\frac{r_0^2}{2}(1-z^2)\Big[q^4+\frac{E_\gamma E_\gamma{}'}{4M_N^2}(\kappa_N^2+2q\kappa_N)^2\Big], \qquad (2.48)\end{aligned}$$

while the first order in the $E_\gamma E_\gamma{}'$ expansion of the non-Born terms can be written as

$$W_{0k}^{\rm NB} = U_{0k}^{(2)} E_\gamma E_\gamma{}' + U_{0k}^{(4)}(E_\gamma E_\gamma{}')^2 + \mathcal{O}({E_\gamma}^3 {E_\gamma{}'}^3), \qquad (k=0,3). \qquad (2.49)$$

The two first-order terms $U_{00}^{(2)}$ and $U_{03}^{(2)}$ are

$$\begin{aligned}\frac{1}{(8\pi M_N)^2}\,U_{00}^{(2)} &= -r_0 q^2\Big[(1+z^2)\alpha_{E1}+2z\beta_{M1}\Big], \qquad (2.50)\\ \frac{1}{(8\pi M_N)^2}\,U_{03}^{(2)} &= r_0 q^2(1-z^2)\alpha_{E1}, \qquad (2.51)\end{aligned}$$

while the two higher-order terms $U_{00}^{(3)}$ and $U_{03}^{(3)}$ are given in App. B.
The LEX of the non-Born contribution to the unpolarized differential cross section thus reads

$$\begin{aligned}\frac{d\sigma}{d\Omega}^{NB} &= \left(\frac{E'_\gamma}{E_\gamma}\right)^2\Big\{-\frac{e^2q^2}{8\pi M_N}\left[(1+z)^2(\alpha_{E1}+\beta_{M1})\right. \\ &+ \left.(1-z)^2(\alpha_{E1}-\beta_{M1})\right]E_\gamma E'_\gamma + \mathcal{O}(E_\gamma E'_\gamma)^2\Big\}. \qquad (2.52)\end{aligned}$$

We observe that at forward scattering angles ($z=1$) only the sum $\alpha_{E1}+\beta_{M1}$ contributes, while at backward scattering angles ($z=-1$) only the difference $\alpha_{E1}-\beta_{M1}$ contributes.
If we look at the LEX of the beam asymmetry Σ_3 in the Breit frame as performed in Ref. [47], we obtain

$$\Sigma_3^{NB} = -\frac{4M_N\cos\vartheta_B\sin^2\vartheta_B}{\alpha_{em}(1+\cos^2\vartheta_B)^2}\beta_{M1}\omega_B^2 + \mathcal{O}(\omega_B^4), \qquad (2.53)$$

where both the photon energy and the scattering angle are defined in the Breit reference frame as

$$\omega_B = \frac{2-M_N^2+t/2}{\sqrt{4M_N^2-t}}, \quad \vartheta_B = \arccos\left(1+\frac{t}{2\omega_B^2}\right). \qquad (2.54)$$

This means that at the lowest order in ω_B, the non-Born part of Σ_3 depends only on the magnetic polarizability β_{M1}, that could be extracted from the experimental data independently of α_{E1}. In practice, when the photon energy

approaches 80 MeV, the contributions related to the spin polarizabilities and to α_{E1} (which enters at order $\mathcal{O}(\omega_B^4)$) also start being relevant, thus making a simultaneous fit of the polarizabilities necessary. First results of the beam asymmetry with lower statistics [40] provided a proof-of-principle that the scalar polarizabilities can be accessed in this way. Furthermore, new measurement of both the unpolarized cross section and the beam asymmetry have been performed at MAMI with unprecedent precision [48, 49] and hold the promise to provide a more accurate determination of the scalar polarizabilities.

Chapter 3

Dispersion relations and real Compton scattering

In this chapter, we show how the dispersive approach can be conveniently used for the description of the RCS process. We derive the dispersion relations for the Compton invariant amplitudes $A_i(\nu, t)$, starting from the Cauchy formula for the integral of a complex and analytical function. We briefly show how the dispersive integrals are obtained in the RCS framework, using the unitarity constraint, and we discuss, as a particular case, the forward limit of the RCS process, with the derivation of the Baldin and Gerasimov-Drell-Hearn sum rules.

3.1 Introduction

The origin of DRs can be traced back to the classical theory of light dispersion. In the two well-known papers of Kramers [50] and Kronig [51], the authors found out a relation between the real and the imaginary part of the refraction index as a consequence of both causality and unitarity requirements.

The causality constraint, formulated in the quantum mechanical framework, was adopted in the work by Gell-Mann, Goldberger and Thirring [2], where the electromagnetic interaction was described in a perturbative framework, thus leading to DRs for the forward Compton scattering. Later, in Ref. [52], Goldberger went beyond the limits imposed by perturbation theory. On these solid foundations, a number of sum rules could be derived, combining the low-energy theorems [41, 53–55] and DRs for the forward RCS. The most famous sum rules are the ones obtained (I) by Baldin [3] for the sum of the scalar dipole polarizabilities and (II) by Gerasimov-Drell-Hearn (GDH) [4, 5] for the anomalous magnetic moment. These sum rules all relate a measured electromagnetic structure quantity to an integral over a photo-absorption cross section on the nucleon and thus are model-independent relations.

In the 1960s there was a strong effort for the extension of the DR formalism

to non-forward RCS (see Refs. [56–58], for instance), but only recently have high-precision experiments allowed it to become a practicable tool. The most successful application is the extraction of the nucleon static polarizabilities [11–14, 16, 17], analyzing RCS observables from low energies up to the $\Delta(1232)$-resonance. When the polarizabilities acquire an explicit energy dependence, the dynamical polarizabilities are defined [12], as shown in Ch. 2, and can be evaluated in the framework of DRs [17, 30] or chiral perturbation theory (χPT), as in Ref. [9, 29]. In Ref. [59], we extracted for the first time the dipole dynamical polarizabilities from the proton RCS data, as we will discuss in Ch. 6, using the theoretical framework of fixed-t subtracted DRs. In this chapter, we introduce the DR formalism for RCS, following in particular the works of Refs. [14–18].

3.2 The dispersive approach

The dispersion relations provide an integral relation between the real and imaginary part of a complex function. As shown in Eq. (2.26), the RCS scattering amplitude T_{fi} can be written in terms of the amplitudes $A_i(\nu, t)$ introduced in Eq. (2.23), that are complex functions of real variables and, at fixed values of t, can be seen as functions of ν only. Using the Cauchy integral formula for the non-Born part of the A_i amplitudes, one can write

$$A_i^{NB}(\nu + i\epsilon, t) = \frac{1}{2\pi i} \oint \frac{A_i^{NB}(\nu', t)}{\nu' - \nu - i\epsilon} d\nu', \tag{3.1}$$

where

$$A_i^{NB}(\nu, t) = \lim_{\epsilon \to 0} A_i^{NB}(\nu + i\epsilon, t). \tag{3.2}$$

When the pion-production threshold is reached in the s-channel, i.e. $s_{thr} = (M + m_\pi)^2$, the corresponding value of ν reads

$$\nu_{thr}(t) = \frac{s_{thr} - M_N^2}{2M_N} + \frac{t}{4M_N} = m_\pi + \frac{m_\pi^2 + t/2}{2M_N}. \tag{3.3}$$

On the other hand, when the pion-production threshold is reached in the u-channel, the corresponding value of ν is given by $-\nu_{thr}$. Working in the fixed-t framework, we will omit the t dependence in $\nu_{thr}(t)$, thus simply using ν_{thr} from here on.

The A_i amplitudes have two branch cuts on the real axes: the right-hand cut (RHC), which is related to the s channel and lies in the region $[\nu_{thr}, \infty)$, and the left-hand cut (LHC), related to the u-channel and extending in the range $[-\nu_{thr}, -\infty)$. Considering the analyticity properties of the amplitudes A_i^{NB}, we can take the contour of integration in the complex ν plane shown in Fig. 3.1, where the paths along the real axis are shifted by a quantity $\pm i\epsilon'$ and the upper and lower semicircles have radius R. Assuming that the function

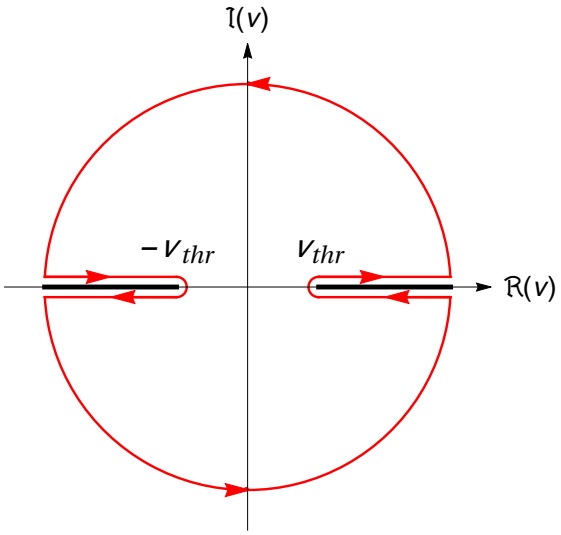

Figure 3.1: Integration contour for the s-channel and the u-channel in the ν complex plane: the black solid lines are the RHC and LHC along the real axes, while the red lines correspond to the integration contour chosen for the Cauchy integral of Eq. (3.1).

decreases fast enough when $\nu \to \infty$, the integrals along the upper and lower semicircles vanish and the Cauchy integral of Eq. (3.1) can be simplified as

$$\begin{aligned} A_i^{NB}(\nu + i\epsilon, t) = \frac{1}{2\pi i} \lim_{\epsilon' \to 0} \Bigg[& \int_{\nu_{thr}}^{\infty} \frac{A_i(\nu' + i\epsilon', t)}{\nu' + i\epsilon' - \nu - i\epsilon} d\nu' \\ & + \int_{\infty}^{\nu_{thr}} \frac{A_i^{NB}(\nu' - i\epsilon', t)}{\nu' - i\epsilon' - \nu - i\epsilon} d\nu' \\ & + \int_{-\infty}^{-\nu_{thr}} \frac{A_i^{NB}(\nu' + i\epsilon', t)}{\nu' + i\epsilon' - \nu - i\epsilon} d\nu' + \int_{-\nu_{thr}}^{-\infty} \frac{A_i^{NB}(\nu' - i\epsilon', t)}{\nu' - i\epsilon' - \nu - i\epsilon} d\nu' \Bigg]. \end{aligned} \tag{3.4}$$

The integral in Eq. (3.1) is thus reduced to the sum of two integrals along the right-hand cut and the left-hand cut, while the two contributions arising from the semicircles of radius ϵ' vanish in the limit of $\epsilon' \to 0$.

Using the Schwartz reflection principle, we obtain

$$\begin{aligned} & \lim_{\epsilon' \to 0} \left[A_i^{NB}(\nu' + i\epsilon', t) - A_i^{NB}(\nu' - i\epsilon', t) \right] \\ & = \lim_{\epsilon' \to 0} \left[A_i^{NB}(\nu' + i\epsilon', t) - A_i^{NB*}(\nu' + i\epsilon', t) \right] = 2i \Im A_i^{NB}(\nu', t). \end{aligned} \tag{3.5}$$

Since $A_i^B(\nu, t)$ are real functions, the imaginary part of A_i^{NB} can be simply written as $\Im A_i(\nu, t)$. Reversing the direction of the integral $\int_{\infty}^{\nu_{thr}} \to -\int_{\nu_{thr}}^{\infty}$, we can combine the two first integrals in Eq. (3.4) to obtain

$$2i \int_{\nu_{thr}}^{\infty} \frac{\Im A_i(\nu', t)}{\nu' - \nu - i\epsilon} d\nu'. \tag{3.6}$$

The integral along the LHC is evaluated in the same way, leading us to the result:

$$A_i^{NB}(\nu + i\epsilon, t) = \frac{1}{\pi} \int_{\nu_{thr}}^{\infty} \Im A_i(\nu', t) \left(\frac{1}{\nu' - \nu - i\epsilon} + \frac{1}{\nu' + \nu + i\epsilon} \right) d\nu'. \quad (3.7)$$

If we recall the identity in Eq. (3.2) and the principle value ($\mathcal{P}$) prescription, i.e.

$$\frac{1}{\nu' \pm \nu - i\epsilon} = \mathcal{P} \left(\frac{1}{\nu' \pm \nu} \right) + i\pi\delta(\nu' \pm \nu), \quad (3.8)$$

we can write

$$\Re[A_i(\nu, t)] = A_i^B(\nu, t) + \frac{2}{\pi} \mathcal{P} \int_{\nu_{thr}}^{\infty} \frac{\nu' \Im[A_i(\nu', t)]}{\nu'^2 - \nu^2} d\nu'. \quad (3.9)$$

The result we just derived in the framework of fixed-t unsubtracted DRs holds if and only if the functions $A_i(\nu, t)$ decrease fast enough for $\nu \to \infty$, in order to ensure that the contributions of the integrals along the upper and lower semicircles are vanishing.

An alternative approach is provided by subtracted dispersion relations (sDRs) that allow us to apply the dispersive formalism to functions that do not decrease fast enough for $\nu \to \infty$ or to just improve the convergence of the integrals. As shown in Ref. [19], using the Cauchy integral definition in Eq. (3.1) for a generic ν_0 value, and performing some algebra, one can rewrite the difference $\Delta_i(\nu, \nu_0) \equiv A_i^{NB}(\nu + i\epsilon, t) - A_i^{NB}(\nu_0 + i\epsilon, t)$ as

$$\Delta_i(\nu, \nu_0) = \frac{\nu - \nu_0}{2\pi i} \oint \frac{A_i^{NB}(\nu', t)}{(\nu' - \nu_0 - i\epsilon)(\nu' - \nu - i\epsilon)} d\nu'. \quad (3.10)$$

The subtraction point ν_0 can be chosen arbitrarily: a convenient choice, driven by the definition of the static polarizabilities in terms of $A_i^{NB}(0, 0)$, is $\nu_0 = 0$, giving for the expression in Eq. (3.10)

$$A_i^{NB}(\nu + i\epsilon, t) = A_i^{NB}(0, t) + \frac{\nu}{2\pi i} \oint \frac{A_i(\nu', t)}{(\nu' - i\epsilon)(\nu' - \nu - i\epsilon)} d\nu'. \quad (3.11)$$

The Cauchy integral is evaluated again along the contour shown in Fig. 3.1: applying the steps described above, we obtain a dispersive integral of the form

$$\Re[A_i^{NB}(\nu, t)] = A_i^{NB}(0, t) + \frac{2}{\pi} \nu^2 \mathcal{P} \int_{\nu_{thr}}^{\infty} \frac{\Im[A_i(\nu', t)]}{\nu'(\nu'^2 - \nu^2)} d\nu'. \quad (3.12)$$

This relation is true only if the integral along the upper and lower semicircles (when $R \to \infty$) in the ν complex plane vanish. As we will see, this is the case for all the six amplitudes A_i, thanks to the extra power in ν' at the denominator of the integral in Eq. (3.13) that improves the fall-off of the integrand function for $\nu' \to \infty$.

The result of Eq. (3.12) is obtained by one subtraction at $\nu = 0$, but the functions $A_i^{NB}(0,t)$ still need to be determined. This can be done using again subtracted DRs, this time in the t-channel, and fixing $t = 0$ as the subtraction point, i.e.

$$\begin{aligned} A_i^{NB}(0,t+i\epsilon) &= A_i^{NB}(0,0) + \left[A_i^{t-pole}(0,t) - A_i^{t-pole}(0,0)\right] \\ &+ \frac{t}{2\pi i}\oint \frac{\Im A_i(0,t')}{(t'-i\epsilon)(t'-t-i\epsilon)}dt', \end{aligned} \tag{3.13}$$

where the t-channel pole contribution A_i^{t-pole} is isolated in order to have an analytical function that satisfies the Cauchy integral formula in the complex t plane [14]. Similarly to Eq. (3.2), we have

$$A_i^{NB}(0,t) = \lim_{\epsilon\to 0} A_i^{NB}(0,t+i\epsilon). \tag{3.14}$$

Unlike for the ν variable, A_i is not even in t and the two branch cuts along

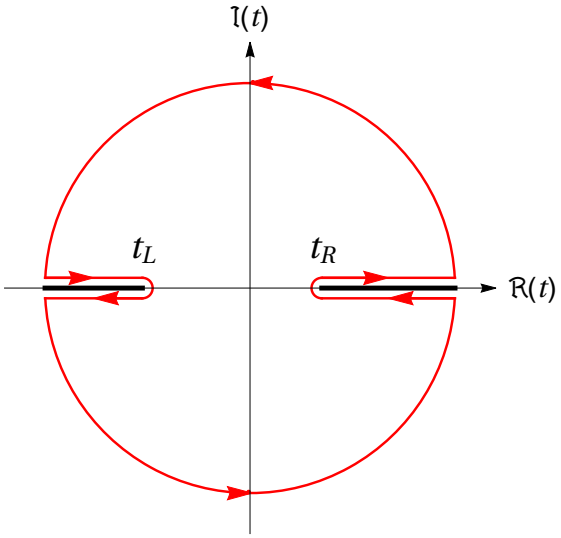

Figure 3.2: t-channel integration contour in the t complex plane: the black solid lines are the RHC and LHC along the real axes, while the red lines are the integration contour for the Cauchy integral in Eq. (3.13).

the real axes are not symmetric. The t RHC starts at the two-pion production threshold ($t_R = 4m_\pi^2$), while the LHC is related to the opening of the s-channel[1] at $\nu = 0$ ($t_L = -2m_\pi^2 - 4M_N m_\pi$). Due to the analytical properties of $A_i^{NB}(0,t)$, a possible contour of integration in the t-complex plane is shown in Fig. 3.2, where the branch cuts are avoided as shown before. In the limit of the radius

[1]The expression for t at $\nu = 0$ reads $t = 2(M^2 - s)$ and at the opening of the s-channel we have $s = (M_N + m_\pi)^2$.

of the semicircle going to infinity, we obtain[2]

$$\begin{aligned} A_i^{NB}(0,t) &= A_i^{NB}(0,0) + \Big[A_i^{t-pole}(0,t) - A_i^{t-pole}(0,0)\Big] \\ &+ \frac{t}{\pi}\int_{t_R}^{\infty} \frac{\Im_t[A_i(0,t')]}{t'(t'-t)}dt' + \frac{t}{\pi}\int_{-\infty}^{t_L} \frac{\Im_t[A_i(0,t')]}{t'(t'-t)}dt'. \end{aligned} \tag{3.15}$$

For the RCS we restrict ourself to small (negative) values of t, well below the opening of the LHC, and then the integral is not evaluated in principal value. Combining Eqs. (3.12) and (3.15), we have the expression for the real part of the A_i amplitudes of RCS in the fixed-t subtracted DRs formalism:

$$\begin{aligned} \Re[A_i(\nu,t)] &= A_i^B(\nu,t) + A_i^{NB}(0,0) + \Big[A_i^{t-pole}(0,t) - A_i^{t-pole}(0,0)\Big] \\ &+ \frac{2}{\pi}\nu^2\mathcal{P}\int_{\nu_{thr}}^{\infty} \frac{\Im_s[A_i(\nu',t)]}{\nu'(\nu'^2-\nu^2)}d\nu' \\ &+ \frac{t}{\pi}\int_{4m_\pi^2}^{\infty} \frac{\Im_t[A_i(0,t')]}{t'(t'-t)}dt' + \frac{t}{\pi}\int_{-\infty}^{-2m_\pi^2-4M_N m_\pi} \frac{\Im_t[A_i(0,t')]}{t'(t'-t)}dt'. \end{aligned} \tag{3.16}$$

In the following sections, we will show how the dispersive integrals in Eq. (3.16) can be evaluated for the RCS process, considering first the forward Compton scattering amplitude, whose imaginary part can be related to the total photo-absorption cross section.

3.2.1 The forward limit and the sum rules

In the forward limit ($t = 0$), the RCS process can be described as a function of ν only. The photon 4-vectors of the momentum $q^\mu = (q_0, \mathbf{q})$ and the polarization $\epsilon_\lambda^\mu = (0, \boldsymbol{\epsilon}_\lambda)$ should satisfy $\epsilon_\lambda \cdot q = 0$ due to the transverse polarization. Labeling with $\hat{\boldsymbol{n}}_{\boldsymbol{x},\boldsymbol{y},\boldsymbol{z}}$ the unit vectors in the x, y, z directions, we can fix the z-axis according to the direction of $\boldsymbol{q} = q_0\hat{\boldsymbol{n}}_{\boldsymbol{z}}$ and the two photon polarization vectors can be accordingly written as

$$\boldsymbol{\epsilon}_\pm = \mp\frac{1}{\sqrt{2}}(\hat{\boldsymbol{n}}_{\boldsymbol{x}} \pm i\hat{\boldsymbol{n}}_{\boldsymbol{y}}), \tag{3.17}$$

that correspond to circularly polarized photons with helicities ± 1 respectively. If we recall that, at $t = 0$, $q_0^{lab} \equiv \nu$, we can write the forward Compton scattering amplitude in the most generic form as

$$T_{fi}(\nu, \theta = 0) = \boldsymbol{\epsilon}'^* \cdot \boldsymbol{\epsilon} f(\nu) + i\boldsymbol{\sigma} \cdot (\boldsymbol{\epsilon}'^* \times \boldsymbol{\epsilon}) g(\nu). \tag{3.18}$$

The expression of Eq. (3.18) is built on the independent vectors $(\boldsymbol{\epsilon}, \boldsymbol{\epsilon}', \boldsymbol{q} = \boldsymbol{q}')$ and the proton spin operator $\boldsymbol{\sigma}$. Furthermore, it is linear in the polarization

[2] Again, the subtraction (at $t = 0$, here) ensure that the integrals on the semicircles vanish as soon as $R \to \infty$.

vectors and obeys the transverse gauge ($\boldsymbol{\epsilon}' \cdot \boldsymbol{q}' = \boldsymbol{\epsilon} \cdot \boldsymbol{q} = 0$). In addition, it is invariant under rotational and parity transformations. Imposing the photon crossing symmetry, the amplitude $T_{fi}(\nu, \theta = 0)$ has to be invariant when $\epsilon' \leftrightarrow \epsilon$ and $\nu \leftrightarrow -\nu$: as a consequence, $f(\nu)$ is an even and $g(\nu)$ an odd function, i.e.

$$f(\nu) = f(-\nu), \quad g(\nu) = -g(-\nu).$$

These two functions can be determined by scattering photons with helicity $\lambda = 1$ off nucleons with helicity $\lambda_N = \pm 1/2$, where the two possible Compton forward amplitudes can be denoted by $T_{1/2}(\nu, \theta = 0)$ and $T_{3/2}(\nu, \theta = 0)$, respectively. The two forward amplitudes can thus be written as

$$f(\nu) = \frac{T_{1/2} + T_{3/2}}{2}, \quad g(\nu) = \frac{T_{1/2} - T_{3/2}}{2}. \tag{3.19}$$

Once defined the unpolarized and the helicity-difference cross sections of total photo-absorption as, respectively,

$$\sigma(\nu) \equiv \frac{1}{2}(\sigma_{3/2} + \sigma_{1/2}), \quad \Delta\sigma(\nu) \equiv (\sigma_{3/2} - \sigma_{1/2}), \tag{3.20}$$

and using the optical theorem, we can write

$$\begin{aligned} \Im f(\nu) &= \frac{\nu}{8\pi}\left[\sigma_{1/2}(\nu) + \sigma_{3/2}(\nu)\right] = \frac{\nu}{4\pi}\sigma(\nu), \\ \Im g(\nu) &= \frac{\nu}{8\pi}\left[\sigma_{1/2}(\nu) - \sigma_{3/2}(\nu)\right] = -\frac{\nu}{8\pi}\Delta\sigma(\nu). \end{aligned} \tag{3.21}$$

We do not consider the pure electromagnetic processes (such as e^+e^- pair production in the Coulomb field of the proton) that enter at higher order in $\alpha_{em} \simeq 1/137$. We shall consider all the couplings of the proton to the hadronic channels, thus starting at the photon energy in the lab frame given by the pion-production threshold at $t = 0$, i.e. $\nu_0 = m_\pi(1 + m_\pi/2M)$.

Applying the steps described in Sec. 3.2, one can write the following DRs for the f and the g functions

$$\Re f(\nu) = f(0) + \frac{\nu^2}{2\pi^2}\mathcal{P}\int_{\nu_0}^{\infty} d\nu' \frac{\sigma(\nu')}{\nu'^2 - \nu^2}, \tag{3.22}$$

$$\Re g(\nu) = -\frac{\nu}{4\pi^2}\mathcal{P}\int_{\nu_0}^{\infty} d\nu' \frac{\nu'\Delta\sigma(\nu')}{\nu'^2 - \nu^2}. \tag{3.23}$$

The integral of Eq. (3.22) is computed in the subtracted DR framework, because the ν dependence of $\sigma(\nu)$ does not guarantee the convergence of the unsubtracted integral[3]. If both the integrals in Eqs. (3.22) and (3.23) exist, we

[3]This is in agreement with the Regge parametrization of the higher-energy behavior of $\sigma(\nu)$ through a soft pomeron exchange mechanism [60], according to which $\sigma \sim W^{0.2}$, where W is the center-of-mass energy.

can perform a Taylor expansion around $\nu = 0$, thus obtaining the results

$$\Re f(\nu) = f(0) + \frac{1}{2\pi^2} \sum_{n=1}^{\infty} \left[\nu^{2n} \int_{\nu_0}^{\infty} d\nu' \frac{\sigma(\nu')}{\nu'^{2n}} \right], \tag{3.24}$$

$$\Re g(\nu) = -\frac{1}{4\pi^2} \sum_{n=1}^{\infty} \left[\nu^{2n-1} \int_{\nu_0}^{\infty} d\nu' \frac{\Delta\sigma(\nu')}{\nu'^{2n-1}} \right]. \tag{3.25}$$

Comparing these expansions with the results given by the low energy theorem of Low [53], Gell-Mann and Goldberger [2], we obtain[4]

$$f(\nu) = -\frac{e^2 q^2}{4\pi M_N} + (\alpha_{E1} + \beta_{M1})\nu^2 + \mathcal{O}(\nu^4), \tag{3.26}$$

$$g(\nu) = -\frac{e^2 \kappa_N^2}{8\pi M_N^2}\nu + \gamma_0 \nu^3 + \mathcal{O}(\nu^5). \tag{3.27}$$

Comparing the expressions in Eqs. (3.24) and (3.26), we can identify the well-known Baldin sum rule [3], i.e. :

$$\alpha_{E1} + \beta_{M1} = \frac{1}{2\pi^2} \int_{\nu_0}^{\infty} d\nu \frac{\sigma(\nu)}{\nu^2}. \tag{3.28}$$

On the other hand, the first two terms in Eqs. (3.25) and (3.27) give

$$I_{GDH} = \int_{\nu_0}^{\infty} d\nu \frac{\Delta\sigma(\nu)}{\nu} = \frac{\pi e^2 \kappa^2}{2M^2}, \tag{3.29}$$

$$\gamma_0 = -\frac{1}{4\pi^2} \int_{\nu_0}^{\infty} d\nu \frac{\Delta\sigma(\nu)}{\nu^3}, \tag{3.30}$$

which define, respectively, the Gerasimov [4], Drell and Hearn [5] (GDH) sum rule involving the nucleon anomalous magnetic moment and the Gell-Mann, Goldberger and Thirring [2, 41] (GGT) sum rule for the forward spin polarizability. We will come back on this point in Ch. 7, where we will give an estimate of these sum rules using the available experimental data of the total photo-absorption cross section as inputs.

3.3 How to evaluate the dispersive integrals

In this section, we show how the dispersive approach can be applied to the RCS invariant amplitudes. We will present both the unsubtracted and subtracted formalism, as described in Sec. 3.2. For a more detailed description of the DR formalisms, we address to Refs. [11, 14].

[4]The predictions given by the LETs assume that the leading terms for $\nu \to 0$ are completely determined by the Born terms.

3.3.1 Unsubtracted dispersion relations

As shown in Eq. (3.9), we can apply the unsubtracted fixed-t DRs approach to the A_i amplitudes that fully describe the RCS process, if and only if the $A_i(\nu, t)$ functions are analytical functions of ν and if they are vanishing fast enough for $\nu \to \infty$. If this last constraint is not fulfilled, the integral along the upper and lower semicircles of radius R do not vanish. The Regge prediction for real Compton scattering [11] at high energy and at fixed-t states that:

$$A_{1,2}(\nu, t) \sim \nu^{\alpha(t)}, \quad A_{3,5,6}(\nu, t) \sim \nu^{\alpha(t)-2}, \quad A_4(\nu, t) \sim \nu^{\alpha(t)-3}, \tag{3.31}$$

where $\alpha(t)$ is the Regge trajectory, with $\alpha(t) \simeq 1$. From Eq. (3.31), we notice that in the high-energy region the integral of Eq. (3.1) for the amplitudes $A_1(\nu, t)$ and $A_2(\nu, t)$ do not converge, thus making the unsubtracted DR not applicable. Instead, one can introduce finite energy sum rule [11], by using a Cauchy loop of finite size, i.e.

$$\Re A_i(\nu, t) = A_i^B(\nu, t) + A_i^{int}(\nu, t) + A_i^{as}(\nu, t), \tag{3.32}$$

where

$$A_i^{int}(\nu, t) = \frac{2}{\pi} \mathcal{P} \int_{\nu_{thr}}^{\nu_{max}} \frac{\nu' \Im A_i(\nu', t)}{\nu'^2 - \nu^2} d\nu' \tag{3.33}$$

is the integral in the s channel from the threshold ν_{thr} to the upper limit of ν_{max} and $A_i^{as}(\nu, t)$ stands for the "asymptotic contribution" corresponding to the integrals along the finite semicircle of radius ν_{max}.

From Eq. (3.31), we know that the $A_{3,4,5,6}$ amplitudes drop fast enough at infinity and satisfy unsubtracted DRs. Accordingly, their asymptotic contributions can be evaluated as

$$A_i^{as}(\nu, t) = \frac{2}{\pi} \int_{\nu_{max}}^{\infty} \frac{\nu' \Im A_i(\nu', t)}{\nu'^2 - \nu^2} d\nu', \quad (i = 3, 4, 5, 6). \tag{3.34}$$

On the other hand, for the $A_{1,2}$ amplitudes the asymptotic contributions are given by the integrals over the upper semicircle, i.e.

$$A_{1,2}^{as}(\nu, t) = \frac{1}{\pi} \Im \int_{\nu' = \nu_{max} e^{i\phi}} \frac{\nu' A_{1,2}(\nu', t)}{\nu'^2 - \nu^2} d\nu', \tag{3.35}$$

with $0 < \phi < \pi$. The $A_{1,2}^{as}$ terms can be seen as the contribution of scalar and pseudo-scalar t-channel exchanges with $J^{PC} = 0^{++}$ and 0^{-+}. Following Ref. [11], they are assumed to be saturated with the lightest scalar and pseudo-scalar particles, corresponding to the π^0-pole for the A_2 amplitude and to an effective σ-meson, representing a correlated pion pair, for the A_1 amplitude.

In detail, the asymptotic part of A_1 is parametrized as:

$$A_1^{as}(\nu, t) \simeq A_1^{\sigma}(t) \approx \frac{F_{\sigma\gamma\gamma} g_{\sigma NN}}{t - m_\sigma^2}, \tag{3.36}$$

where m_σ stands for the mass of the effective σ meson, while $F_{\sigma\gamma\gamma}$ and $g_{\sigma NN}$ are the $\sigma\gamma\gamma$ and σNN couplings, respectively.
The asymptotic contribution A_2^{as} is calculated as

$$A_2^{as}(\nu,t) \simeq A_2^{\pi^0}(t) \approx \frac{F_{\pi^0\gamma\gamma} g_{\pi NN}}{t - m_{\pi^0}^2} \tau_3 F_\pi(t), \tag{3.37}$$

where m_{π^0} is the π^0 mass, $\tau_3 = 1$ (-1) is the isospin factor for the proton (neutron) and the function $F_\pi(t)$ is an off-shell form factor $F_\pi(t) = (\Lambda_\pi^2 - m_\pi^2)/(\Lambda_\pi^2 - t)$, with the cutoff parameter $\Lambda_\pi = 0.7$ GeV determined from the nucleon axial radius and the pion size. The product of the πNN and $\pi^0\gamma\gamma$ couplings is given by [11]

$$F_{\pi^0\gamma\gamma} g_{\pi NN} = -16\pi \sqrt{\frac{g_{\pi NN}^2}{4\pi} \frac{\Gamma_{\pi^0\to\gamma\gamma}}{m_{\pi^0}^3}}. \tag{3.38}$$

While the evaluation of the $A_2^{as}(\nu,t)$ term is well established, being related to the well known π^0 pole, the $A_1^{as}(\nu,t)$ term introduces a quite strong model dependence in the definition of the "σ meson".

As shown in Sec. 3.2, an alternative approach is the subtracted DRs, where the convergence of the integral is guaranteed by the presence of an additional power in ν at the denominator of the integrand. In this framework, sDRs could avoid the dependencies on the effective σ-meson properties and on the choice of ν_{max}.

3.3.2 Subtracted dispersion relations

In order to overcome the non convergence of the dispersion integrals for the $A_{1,2}(\nu,t)$ amplitudes, according to Eq. (3.31), the fixed-t subtracted dispersion relations provide a valid solution. As shown in Eq. (3.16), the subtraction point can be chosen at $(\nu = 0, t = 0)$, thus relating the six subtraction constants to the static polarizabilities α_{E1}, β_{M1} and the four leading-order spin polarizabilities.

In the next subsections, we will briefly show how the integrals in the s- and t-channels are evaluated in the DR framework.

3.3.2.1 s-channel dispersion integrals

The imaginary part of the s-channel Compton scattering amplitude can be determined from the unitarity relation

$$2\Im_s T_{fi} = \sum_X (2\pi)^4 \delta^4(P_X - P_i) T_{Xf}^\dagger T_{Xi}, \tag{3.39}$$

where the sum runs over all the possible intermediate states that can be reached by the initial γN state. Due to the third power of ν' in the denominator of

the integrals in Eq. (3.12), the main contribution is determined by the πN intermediate states, while the contribution from heavier mesons and multi-meson intermediate states is suppressed. In detail, the πN contribution is evaluated through the last updated version of the MAID[5] multipole analysis [63] at energies $E_\gamma \leq 1.5$ GeV, combined with a multipole expansion of the helicity amplitudes[6] up to the maximum angular momentum $j_{max} = 7/2$ in the high energy region ($E_\gamma \geq 400$ MeV) and $j_{max} = 3/2$ in the low energy region ($E_\gamma \leq 400$ MeV). The higher partial waves of the multipole expansion with $j \geq j_{max} + 1$ are evaluated analytically in the one-pion exchange (OPE) approximation. The multi-pion intermediate states are approximated by the inelastic decay channels of the πN resonances: the resulting contribution to $\Im_s A_i$ is

$$[\Im_s A_i]_{N^* \to \pi\pi N, \eta N, \dots} = R[\Im_s A_i]_{N^* \to \pi N}, \tag{3.40}$$

where the ratio R is given by

$$R = \frac{1 - B_\pi}{B_\pi} = \frac{\Gamma_{inel}(W)}{\Gamma_\pi(W)}. \tag{3.41}$$

Here, B_π is the single-pion branching ratio of the resonance N^*, the inelastic widths $\Gamma_{inel}(W)$ of the decays $N^* \to (\pi\pi N, \eta N, \pi\pi\pi N, \dots)$ are parametrized as in Ref. [11], and $\Gamma_\pi(W)$ is the energy-dependent pionic width [64].

In Fig. 3.3 are shown the A_1 and A_2 amplitudes as function of the upper limit ν_{upper} for the integral of Eq. (3.12), as taken from Ref. [14]: unsubtracted DR calculations for one-pion and two-pion channels are compared with the corresponding results from sDRs. In sDRs the sensitivity to the multi-pion channel is very small, while the unsubtracted DRs have a strong dependence on the multi-pion channels, that amounts to nearly 30% in the case of the A_2 amplitude; the sDRs are, on the other hand, saturated already at $\nu_{upper} \sim 0.4$ GeV.

3.3.2.2 t-channel dispersion integrals

In the t-channel, the pole contribution enters the amplitude A_2 and is given by the π^0 exchange as

$$A_2^{\pi^0}(0,t) = \frac{F_{\pi^0\gamma\gamma} g_{\pi NN}}{t - m_\pi^2}, \tag{3.42}$$

where the coupling $F_{\pi^0\gamma\gamma}$ is determined starting from the $\pi^0 \to \gamma\gamma$ reaction as

$$\Gamma_{\pi^0 \to \gamma\gamma} = \frac{1}{64\pi} m_{\pi^0}^3 F_{\pi^0\gamma\gamma}^2, \tag{3.43}$$

[5]Since the available phenomenological analysis for the pion photoproduction channel are given without uncertainties, it is not possible to quantify the corresponding theoretical uncertainties in the dispersion calculation of RCS. However, to control the uncertainties from this channel, different analysis of pion-photoproduction, such as MAID, SAID [61] and the HDT [62] dispersive analysis, have been employed and compared, finding a difference typically less than 1-2% for RCS observables at low energies [16].

[6]We refer to Ref. [15] and to Appendix B and C of Ref. [11] for a more comprehensive description.

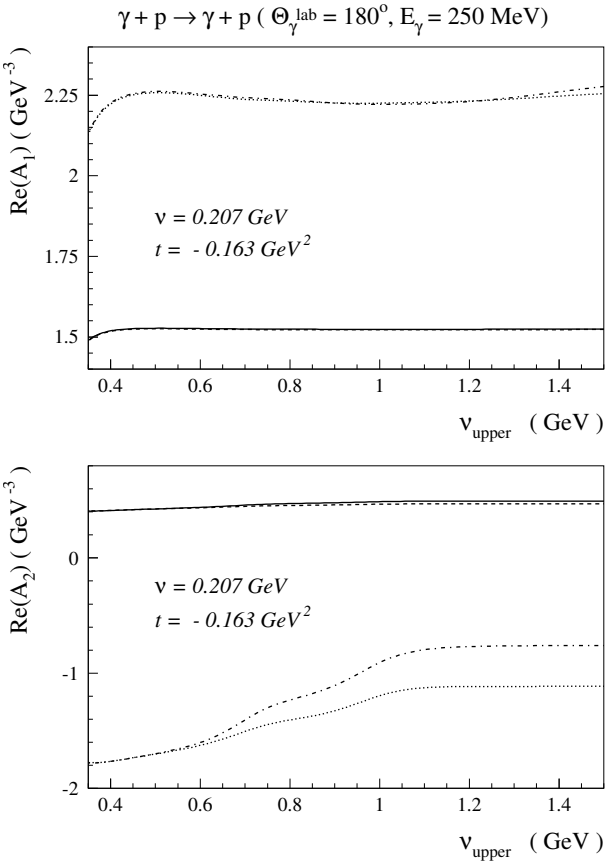

Figure 3.3: Amplitudes A_1 and A_2 as function of the upper limit of integration ν_{upper}: unsubtracted dispersion integral for the one-pion channel (dotted curve) and for the two-pion channel (dashed-dotted curve) compared to subtracted dispersion integral in Eq. (3.16) for the one-pion channel (dashed curve) and for the two-pion channel (solid curve) [14].

using $\Gamma_{\pi^0\to\gamma\gamma} = 7.74$ eV [65] and $g^2_{\pi NN}/4\pi = 13.72$ [66]. The contribution from the RHC in the t-channel in Eq. (3.16) can be computed using the t-channel unitarity relation, taking into account all the possible intermediate states, as shown in Fig. 3.4. For small values of t, well below the $K\bar{K}$ production threshold, the imaginary part is essentially saturated by the $\pi\pi$ intermediate states. For this reason, the imaginary parts in the t-channel from $4m_\pi^2 \to +\infty$ are calculated using the $\gamma\gamma \to \pi\pi \to N\bar{N}$ channel as input. In a first step, a unitarized amplitude for the $\gamma\gamma \to \pi\pi$ subprocess is constructed from available experimental data. This information is then combined with the $\pi\pi \to N\bar{N}$ amplitudes determined by analytical continuation of πN scattering amplitudes [67]. In practice, the upper limit of integration along the positive-t cut is taken equal to $t = 0.78$ GeV^2, which is the highest t value at which the $\pi\pi \to N\bar{N}$ amplitudes are tabulated in Ref. [67]. This serves well for the present purpose, since the subtracted t-channel dispersion integrals show good convergence already below this value. The integrals along

the LHC cut in Eq. (3.16), where the integration variable runs from $-\infty$ to $-2(m_\pi^2 + 2Mm_\pi) \approx -0.56$ GeV^2, lies in the kinematical unphysical region. As long as we stay at small (negative) values of t, this integral is strongly suppressed by the denominator $t'(t'-t)$, and can be approximated by taking the analytical continuations at $\nu = 0$ and negative t of the most important contributions from the $\Delta-$resonance and non-resonant πN in the physical s-channel region.

We address to Ref. [14] for a more detailed description of the evaluation of the t-channel integrals for RCS.

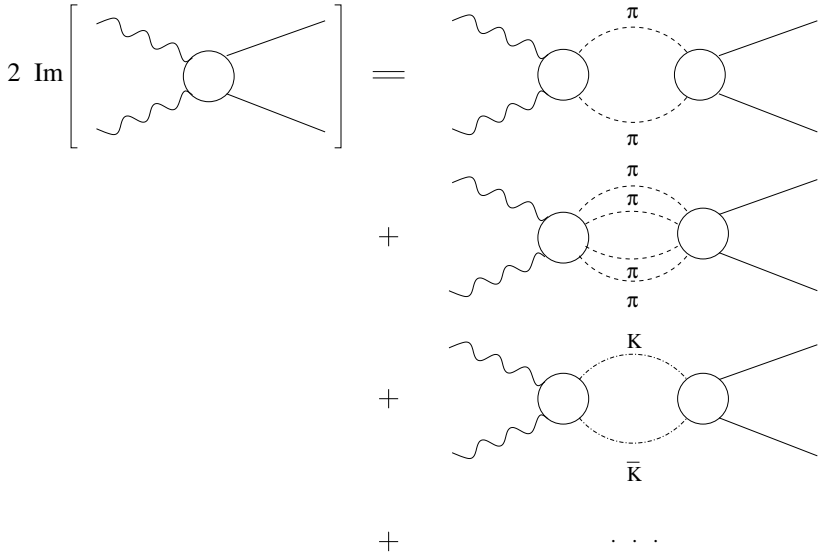

Figure 3.4: t-channel unitarity diagrams for real Compton scattering [14].

Chapter 4

A new bootstrap-based fitting technique

In this chapter, we present a new fitting technique based on the parametric bootstrap method. Its working principle relies on the idea of producing artificial measurements, using the estimated probability distribution of the experimental data. In order to investigate the main properties of this technique, we use a toy model and we analyze several fitting conditions. Then, we compare the results obtained with the new method to the outcome of the standard χ^2 minimization procedure. Furthermore, we analyze the effect of the data systematic uncertainties both on the probability distribution of the fit parameters and on the shape of the goodness-of-fit distribution. Our conclusion is that only the bootstrap procedure is able to provide reliable confidence levels and p-values, when systematic uncertainties are included in the analysis, thus improving the results given by the χ^2 minimization procedure. The results shown here are mainly based on our work of Ref. [68].

In Ch. 5 and Ch. 6 we will extensively use this technique for the fit of the scalar dipole static and dynamical polarizabilities.

4.1 A brief summary of a best-fit procedure

The main goal of a best-fit procedure is the estimate of some unknown parameters, which a given model T depends on and that are collected in an array, $\boldsymbol{\theta}$. The more commonly used algorithm is the so-called least-square method, which is based on the function:

$$\chi^2_{stand}(\boldsymbol{\theta}) = \sum_i \left(\frac{E_i - T_i(\boldsymbol{\theta})}{\sigma_i} \right)^2 , \tag{4.1}$$

where E_i are the experimental values and σ_i are their statistical uncertainty. The minimum of $\chi^2_{stand}(\boldsymbol{\theta})$, i.e.

$$\chi^2_{min} = \sum_i \left(\frac{E_i - T_i(\hat{\boldsymbol{\theta}})}{\sigma_i} \right)^2 . \tag{4.2}$$

is in correspondence to the optimal parameter set $\hat{\boldsymbol{\theta}}$. This procedure is fairly safe when only statistical uncertainties are included in the data analysis. However, as soon as we try to include some systematic errors, the χ^2 minimization method fails and one has to resort to a modification of χ^2_{stand}, by introducing [69]

$$\chi^2_{mod}(\boldsymbol{\theta}) = \sum_i \left(\frac{fE_i - T_i(\boldsymbol{\theta})}{f\sigma_i} \right)^2 + \left(\frac{f-1}{\sigma^{sys}} \right)^2 . \tag{4.3}$$

Here, f is a normalization factor common to all the data that has to be treated as an additional fit parameter, while σ^{sys} is the evaluated systematic uncertainty in root mean square (rms) units. However, if we consider a database composed by many subsets, this solution becomes impractical, since a different normalization factor has to be used for each subset, thus increasing the number of fit parameters. As a matter of fact, the minimization function becomes:

$$\chi^2_{mod}(\boldsymbol{\theta}) = \sum_k \left\{ \left[\sum_{i \in \text{ set k}} \left(\frac{f_k E_i - T_i}{f_k \sigma_i} \right)^2 \right] + \left(\frac{f_k - 1}{\sigma_k^{sys}} \right)^2 \right\} . \tag{4.4}$$

However, Eq. (4.3) holds if and only if the systematic uncertainties are Gaussian distributed, since

$$\chi^2_{mod}(\boldsymbol{\theta}, f) = -2 \ln \mathcal{L}(\boldsymbol{\theta}, f) \ , \tag{4.5}$$

where the Likelihood function $\mathcal{L}(\boldsymbol{\theta}, f)$ is the product of the normal distributions (with mean and standard deviations given by the experimental data) and the normal distribution modeling the common systematic scale uncertainty, i.e.

$$\mathcal{L}(\boldsymbol{\theta}, f) = \prod_i \left[\frac{1}{\sigma_i^2 \sqrt{2\pi}} e^{-\frac{(fE_i - T_i(\boldsymbol{\theta}))^2}{2f\sigma_i^2}} \right] \cdot \frac{1}{\sigma_{sys}^2 \sqrt{2\pi}} e^{-\frac{(f-1)^2}{2\sigma_{sys}^2}} . \tag{4.6}$$

Moreover, also the systematic uncertainty σ^{sys} may change from point to point, thus introducing some correlation terms that are difficult to implement correctly in this framework. Furthermore, in the presence of non-Gaussian (and non-independent) uncertainties, the χ^2_{min} is not distributed according to a standard χ^2 distribution, since it is not the sum of squared independent Gaussian variables. This means that the p-values can not be evaluated from the χ^2 distribution.

An additional complication is given by the uncertainty propagation of the non-fitted parameters $\boldsymbol{\theta}_f$,which the model T could depend on, in addition to

the fitting parameters $\boldsymbol{\theta}$. If we suppose that those additional parameters $\boldsymbol{\theta}_f$ are taken from some experimental evaluation, they should appear in the form

$$\boldsymbol{\theta}_f = \bar{\boldsymbol{\theta}}_f \pm \boldsymbol{\sigma}_f, \tag{4.7}$$

where $\bar{\boldsymbol{\theta}}_f$ and $\boldsymbol{\sigma}_f$ are their estimated values and uncertainties (in rms units), respectively.

Thus, the total uncertainty of the fit parameters should be written as the sum of the pure contribution from the minimization itself and the uncertainty related to the effect caused by $\boldsymbol{\sigma_f}$. This last contribution can be estimated, even if under the linear approximation, from the standard uncertainty propagation, i.e.

$$\delta\hat{\boldsymbol{\theta}}_{extra,ab} \simeq \sum_{cd} \left(\frac{\partial \boldsymbol{\theta}_a}{\partial \boldsymbol{\theta}_{f,c}}\bigg|_{\boldsymbol{\theta}_a=\hat{\boldsymbol{\theta}}_a} \right) \sigma_{f,cd} \left(\frac{\partial \boldsymbol{\theta}_b}{\partial \boldsymbol{\theta}_{f,d}}\bigg|_{\boldsymbol{\theta}_b=\hat{\boldsymbol{\theta}}_b} \right), \tag{4.8}$$

where the indexes a, b run over the components of $\boldsymbol{\theta}$, while c, d on the components of $\boldsymbol{\theta}_f$. The quantity $\delta\hat{\boldsymbol{\theta}}_{extra,ab}$ thus include both the covariances and the variances, obtained when $a \equiv b$. Furthermore, the terms in round brackets are evaluated as

$$\frac{\partial \boldsymbol{\theta}_x}{\partial \boldsymbol{\theta}_{f,y}}\bigg|_{\boldsymbol{\theta}_x=\hat{\boldsymbol{\theta}}_x} = \left[\left(\frac{\partial T}{\partial \boldsymbol{\theta}_x} \right)^{-1} \frac{\partial T}{\partial \boldsymbol{\theta}_{f,y}} \right]_{\boldsymbol{\theta}_x=\hat{\boldsymbol{\theta}}_x}. \tag{4.9}$$

If the analytical structure of the model is strongly non-linear, the derivative term $\frac{\partial T}{\partial \boldsymbol{\theta}_{f,y}}$ could yield to some singularity or, at least, could be hard to be computed, even numerically.

Our new fitting technique that we are going to thoroughly describe in this chapter, is able to provide a valid solution to all these drawbacks. We decided to apply it within the framework of the least square, but it can be used with other minimization schemes, as the Maximum Likelihood (ML) approach.

4.2 Minimization strategies

We will show two well-known minimization methods, which are commonly used in order to find the minimum of the χ^2 function: the *gradient method* and the *simplex method*, which differ for both the working principle and the speed of convergence. As a reference, in this explanation we follow the Minuit manual [70], the minimization package used throughout this work.

4.2.1 The gradient method

We consider a generic function F depending on a variable x. As it is indicated by the name of the method, the minimum value of the function F can be found looking at the gradient and at its speed of descent. This strategy is

called *steepest descent*, because the choice is to follow the direction of the negative gradient vector in order to find the minimum.

The key point is the calculation of n-order derivatives, and it could turn out to be not that easy if the function F is strongly non linear in x. The algorithm computes the derivative by finite differences, namely

$$\left.\frac{\partial F}{\partial x}\right|_{x=x_0} \simeq \frac{F(x_0+d)-F(x_0)}{d}, \tag{4.10}$$

where $d > 0$ and x_0 is the starting value of x in the hunt of the minimum. Using the Taylor expansion,

$$F(x) = F(x_0) + \left.\frac{\partial F}{\partial x}\right|_{x=x_0}(x-x_0) + \frac{1}{2}\left.\frac{\partial^2 F}{\partial x^2}\right|_{x=x_0}(x-x_0)^2 + \ldots, \tag{4.11}$$

we can notice that the gradient method introduces an intrinsic error given by

$$\delta \simeq \frac{d}{2}\left.\frac{\partial^2 F}{\partial x^2}\right|_{x=x_0}. \tag{4.12}$$

The distance d has to be small enough to optimize the algorithm, but still large enough to have a computational error smaller than δ. Unfortunately, there is no possibility to find an algorithm that gives us the optimal value of d, so it has to be found by empirical trials.
The procedure can be refined through the choice of a symmetric interval with respect to x_0, so that the first derivative assumes the form

$$\left.\frac{\partial F}{\partial x}\right|_{x=x_0} \simeq \frac{F(x_0+d)-F(x_0-d)}{2d}, \tag{4.13}$$

and the intrinsic error δ is now proportional to the third derivative $\partial^3 F/\partial x^3$. The price to pay is that for the evaluation of n first derivatives, the function has to be called $2n$ times, assuming that $F(x_0)$ is known. On the other hand, the second derivative is given for free, since we can write

$$\left.\frac{\partial^2 F}{\partial x^2}\right|_{x=x_0} \simeq \frac{F(x_0-d)+F(x_0+d)-2F(x_0)}{d^2}. \tag{4.14}$$

The gradient method works very well for a one dimensional function, even if the starting point x_0 cannot be too far from the $\hat{x}$ value that corresponds to the minimum of F. However, as soon as we increase the dimension of the domain, some complications arise, because we need to fix how to vary the gradient vector. If we change one variable at a time, we could find a local minimum but we would not have any possibility to control it after a change of the values of the remaining variables. For this reason, we have to find a strategy that is able to take into account the reciprocal dependence of all the variables.

To this aim, we have to make a strong approximation, i.e. that the function is completely defined by its first and second derivatives. It is then clear that

this method is not adapted to "hill-behaving" function, with rapid variations. Under this assumption, we have a quadratic form:

$$F(\boldsymbol{x}) = F(\boldsymbol{x}_0) + \boldsymbol{g}^T(\boldsymbol{x} - \boldsymbol{x}_0) + \frac{1}{2}(\boldsymbol{x} - \boldsymbol{x}_0)^T \mathbb{G}(\boldsymbol{x} - \boldsymbol{x}_0), \tag{4.15}$$

where g stands for the gradient (evaluated in x_0) and $\mathbb{G}$ is the second derivative matrix. The minimum is directly determined by

$$\boldsymbol{x}_{min} = \boldsymbol{x}_0 - \mathbb{G}^{-1}\boldsymbol{g} \equiv \boldsymbol{x}_0 - \mathbb{V}\boldsymbol{g}, \tag{4.16}$$

where $\mathbb{V}$, given by the inverse of the second-derivative matrix, is the *covariance matrix*.

The main condition required by this method is that the second-derivative matrix (or, equivalently, the covariance matrix) has to be *positive-definite*, otherwise the minimum is not stable or, even worst, it is not a minimum at all. Some necessary and sufficient conditions for $\mathbb{G}$ to be positive-definite are the following ones:

* the determinants of all the upper left square sub-matrices (square matrices built up starting from the top left element and descending along the diagonal) are positive;
* the scalar number $\boldsymbol{e}^T\mathbb{G}\boldsymbol{e}$ is positive for each vector $\boldsymbol{e}$;
* the covariance matrix $\mathbb{V}$ is positive definite.

4.2.2 The simplex method

A completely different algorithm is the *simplex method*, which is a geometrical technique. The minimum of the generic function F is searched starting from an arbitrary initial set of F values and applying the algorithm for a given number of iterations. Basically, this method is based on *simplex*, defined as a n-dimensional figure determined by its $n+1$ vertexes: a $2d$ simplex is a triangle, a $3d$ simplex is a tetrahedron and so on. The key point is the evaluation of the function at the vertexes of the simplex, and the method can be represented for the bi-dimensional case as in Fig. 4.1. We consider a bi-dimensional domain for F, i.e. $F = F(x_1, x_2)$. In the (x_1, x_2) plane, we define a triangle having vertices P_1, P_2, P_3 and we evaluate the function F in these points. We will find a point (P_L) in which the function has the lowest value and another point (P_H) in which the function has the highest value. Let assume that $P_1 = P_L$, $P_3 = P_H$ and define $\bar{P}$ as the middle point between P_1 and P_2, i.e.

$$\bar{P} = \frac{P_1 + P_2}{2}. \tag{4.17}$$

The basic idea of this method is to replace the "worst" point P_H, thus defining a new simplex at each iteration of the algorithm. The first attempt is to reflect

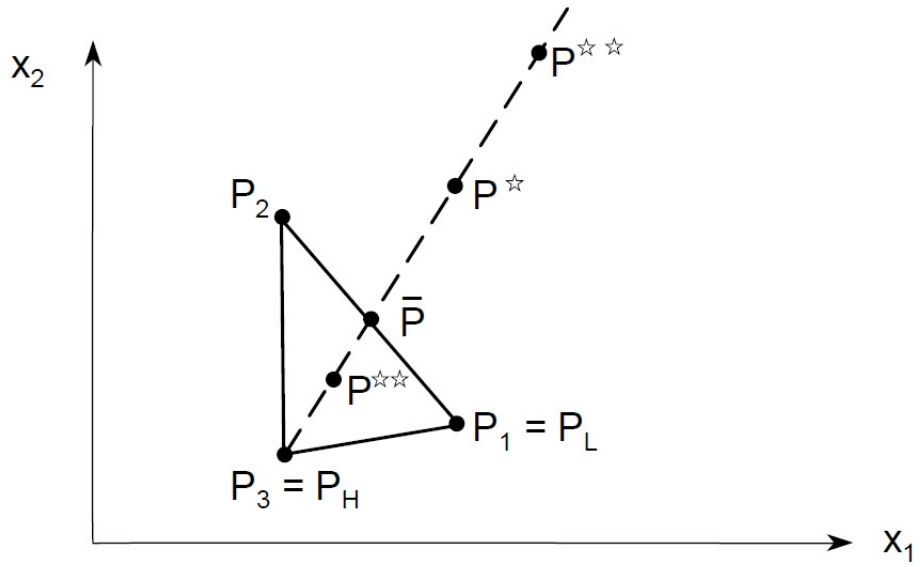

Figure 4.1: Two-dimensional example of the simplex algorithm: the points $P^\star$ and $P^{\star\star}$ stand for the trial points in searching the minimum of the function [70]. See text for explanation.

P_H with respect to $\bar{P}$, finding the point $P^\star = \bar{P} + (\bar{P} - P_H)$: if $F(P^\star) < F(P_L)$ the trial point is replaced with $P^{\star\star} = \bar{P} + 2(\bar{P} - P_H)$, while if $F(P^\star) > F(P_H)$, $P^{\star\star}$ is calculated as $P^{\star\star} = \bar{P} + \frac{1}{2}(\bar{P} - P_H)$. The point $P^{\star\star}$ where the function takes the lowest value will have the role of P_H for the next simplex, while in the case that none of them are useful, a new simplex is built around P_L starting from the original simplex and rescaling it by a factor of 0.5. The algorithm can be modified changing the scaling factor and the contraction/expansion step, but the underlying principle is the same.

Generalizing in more than two dimensions, we can define the point $\bar{P}$ as the "center of mass" of a simplex in which the "worst point" P_H is excluded,

$$\bar{P} = \sum_{i=1}^{n+1} \frac{P_i}{n+1} - P_H, \tag{4.18}$$

and then iterating the simplex method as explained above.

The main advantage of this algorithm is that no calculation of derivatives is required, so it can be performed also in those cases where the algebra is difficult and without the drawback of an intrinsic approximation as in the gradient method. The main disadvantage of this technique is that no estimate is provided for the uncertainties on the variables of the function F. The new technique we propose gives a possible solution to this problem, but still exploiting the advantages of the simplex method.

4.3 Outline of the new method

Our new fitting method is based on the *parametric bootstrap* technique (see, for instance, Ref. [39] and references therein). The underlying idea is to assume that each E_i is the ML estimate of its true (and unknown) value $\mathcal{E}_i$. For fixed value of the kinematical variable x, the true probability distribution $p(x, \mathcal{E}_i)$ is approximated as

$$p(x, \mathcal{E}_i) \simeq p(x, E_i) \tag{4.19}$$

thus replacing the unknown true probability distribution with the (known[1]) probability distribution of the measured value E_i. Then a random bootstrap sample $E_1^b, E_2^b \dots E_n^b$ is generated, for each E_i, according to $p(x, E_i)$, thus determining an estimate of the true model parameters $\boldsymbol{\theta}_1^b$ by the minimization of the standard χ^2 function in Eq. (4.1). Repeating this bootstrap cycle a (very) large number n_b of times, we get a sample $\hat{\boldsymbol{\theta}}_1^b, \hat{\boldsymbol{\theta}}_2^b \dots \hat{\boldsymbol{\theta}}_{n_b}^b$, from which we are finally able to reconstruct the true probability distribution for every fit parameter. For instance, the sample mean and the sample standard deviation are given as

$$\hat{\boldsymbol{\theta}}^b = \frac{1}{n_b} \sum_{i=1}^{n_b} \hat{\boldsymbol{\theta}}_i^b \quad , \quad \sigma_{\hat{\boldsymbol{\theta}}^b} = \left[\frac{1}{n_b - 1} \sum_{i=1}^{n_b} \left(\hat{\boldsymbol{\theta}}_i^b - \hat{\boldsymbol{\theta}}^b \right)^2 \right]^{1/2} . \tag{4.20}$$

4.3.1 A general example

As a general example, we consider the case of a database composed of different and independent subsets and with a total of n experimental points, having both statistical and uniformly distributed systematic uncertainties (scaling factors), independent of each other. The true value $\mathcal{E}_i$ of each experimental point can then be written as:

$$\mathcal{E}_i = E_i \pm \sigma_i^{\text{exp}} \pm \Delta E_i^{\text{sys}} \tag{4.21}$$

where σ_i^{exp} is the standard deviation of the Gaussian statistical uncertainty and ΔE_i^{sys} is the half width of the uniform systematic uncertainty[2]. Such an artificial "measurement" is assumed to be Gaussian distributed around each experimental data point, with a standard deviation given by its statistical fluctuation. Then, a shift equal to the estimated systematic uncertainty is applied to all the points of every subset, independently one from each other. This last property is crucial, because it reflects the independence of different experimental setups. If we define a *cycle* as when the number of bootstrapped points are equal to the total number of points in the considered experimental set, the bootstrap sampling can be finally described as:

$$\mathcal{B}_{ij} = (1 + \delta_{ij})(E_i + \gamma_{ij}\sigma_i), \tag{4.22}$$

[1] We assume, for now, that the probability distribution of the measured value is known for every i; we will be back on this point later in the chapter.

[2] These distributions are just reasonable choices and they can be easily changed to cope with every specific situation.

where $\mathcal{B}_{ij}$ is a generic bootstrapped point with the index i running over the number of data points (n) and the index j indicates the j^{th} bootstrap cycle. The γ_{ij} parameters are sampled from the standard Gaussian distribution $\mathcal{N}[0,1]$, while the δ_{ij} are random numbers uniformly distributed, in each subset, as $\mathcal{U}[-\Delta_k, +\Delta_k]$, being $\pm\Delta_k$ the percentage systematic uncertainty of each subset k (k runs from 1 to the number of the different data subsets n_s). If only statistical uncertainties have been taken into account, the systematic sources can be easily excluded from this procedure by just imposing $\delta_{ij} \equiv 0$. After a complete cycle and once defined the rescaled statistical uncertainty $\sigma_{ij} \equiv (1 + \delta_{ij})\sigma_i$, the minimization procedure is performed on the function:

$$\chi^2_j = \sum_{i=1}^{n} \left(\frac{\mathcal{B}_{ij} - T_i(\boldsymbol{\theta})}{\sigma_{ij}} \right)^2, \tag{4.23}$$

and all the fit results are stored.

We will show in detail the big advantages of the bootstrap-based technique. Already at this point, we can notice that, for instance, the systematic errors can be very easily included in the minimization procedure, thus allowing us to reduce the overall number of free parameters (see Eq. (4.3), and comments therein). Furthermore, any kind of uncertainty distributions of the experimental data can be easily implemented on the basis of Eq. (4.22). In addition, Eq. (4.20) shows that this technique is able to provide reliable estimates of the fitting parameter uncertainties, even if the minimization algorithm does not give them explicitly. This is, for instance, the case of the simplex, as pointed out in Sec. 4.2.2. Moreover, the probability distribution of the fitted parameters is not assumed to be a-priori Gaussian, but it is reconstructed from the probability distribution assigned to every experimental data point.

If we consider the more complicated situation in which there are some additional model parameters $\boldsymbol{\theta}_f$, as shown in Sec. 4.1, the sampling itself and the cyclic structure of this algorithm prove useful. If we know the probability distributions $g(\boldsymbol{\theta}_f, \boldsymbol{\sigma}_f)$, based on the statistical uncertainty $\boldsymbol{\sigma}_f$, we can add a sampling from $g(\boldsymbol{\theta}_f, \boldsymbol{\sigma}_f)$ at every bootstrap cycle, thus modifying the minimization function of Eq. (4.23) according to

$$\chi^2_{b,j} = \sum_{i=1}^{n} \left(\frac{\mathcal{B}_{ij} - T_i(\boldsymbol{\theta}_{f,j}, \boldsymbol{\theta})}{\sigma_{ij}} \right)^2, \tag{4.24}$$

whose minimum value can be written as

$$\hat{\chi}^2_{b,j} = \sum_{i=1}^{n} \left(\frac{\mathcal{B}_{ij} - T_i(\boldsymbol{\theta}_{f,j}, \hat{\boldsymbol{\theta}}_j)}{\sigma_{ij}} \right)^2. \tag{4.25}$$

Once more, this fitting technique is very adaptable to each specific configuration like, for instance, additional correlated model parameters. In such a situation, a correlated sampling from $g(\boldsymbol{\theta}_f, \boldsymbol{\sigma}_f)$ could be performed, with no modifications to the algorithm itself.

4.4 The relation with a traditional χ^2

The value of $\hat{\chi}^2_{b,j}$ given in Eq. (4.25) cannot be treated as the standard $\hat{\chi}^2$ value commonly used to assess the goodness of a fit in the standard procedure, i.e.

$$\hat{\chi}^2 = \sum_{i=1}^{n_{data}} \left(\frac{E_i - T_i(\boldsymbol{\theta}_f, \hat{\boldsymbol{\theta}})}{\sigma_i} \right)^2 , \tag{4.26}$$

due to the artificial statistical fluctuations inherent to each bootstrapped sampling. Nevertheless, a connection between $\hat{\chi}^2_{b,j}$ and $\hat{\chi}^2$ should exist, being the $\mathcal{B}_{ij}$ point obtained from the E_i measurements.

In order to more easily find the desired connection between $\hat{\chi}^2_{b,j}$ and $\hat{\chi}^2$, the following definitions are useful:

$$\begin{aligned} \epsilon_{ij} &\equiv \frac{1}{\sigma_i} \left[T_i(\boldsymbol{\theta}_f, \hat{\boldsymbol{\theta}}) - \frac{T_i(\boldsymbol{\theta}_f, \hat{\boldsymbol{\theta}}_j)}{1+\delta_{ij}} \right], \\ \eta_{ij} &\equiv \frac{1}{(1+\delta_{ij})\sigma_i} \left[T_i(\boldsymbol{\theta}_f, \hat{\boldsymbol{\theta}}_j) - T_i(\boldsymbol{\theta}_{f,j}, \hat{\boldsymbol{\theta}}_j) \right]. \end{aligned} \tag{4.27}$$

They allow us to write the $T_i(\boldsymbol{\theta}_{f,j}, \hat{\boldsymbol{\theta}}_j)$ terms of Eq. (4.25) as

$$T_i(\boldsymbol{\theta}_{f,j}, \hat{\boldsymbol{\theta}}_j) = (1+\delta_{ij}) \left[T_i(\boldsymbol{\theta}_f, \hat{\boldsymbol{\theta}}) - \sigma_i(\epsilon_{ij} + \eta_{ij}) \right], \tag{4.28}$$

thus yielding to the decomposition

$$\hat{\chi}^2_{b,j} = \hat{\chi}^2 + \sum_i \gamma^2_{ij} + \sum_i \epsilon^2_{ij} + \sum_i D_{ij} + \sum_i \Phi_{ij}, \tag{4.29}$$

where

$$D_{ij} \equiv 2 \left[\epsilon_{ij}\gamma_{ij} + \frac{1}{\sigma_i}(\epsilon_{ij} + \gamma_{ij})(E_i - T_i(\boldsymbol{\theta}_f, \hat{\boldsymbol{\theta}})) \right], \tag{4.30}$$

$$\Phi_{ij} \equiv \eta^2_{ij} + 2\eta_{ij} \left[(\epsilon_{ij} + \gamma_{ij}) + \frac{1}{\sigma_i}(E_i - T_i(\boldsymbol{\theta}_f, \hat{\boldsymbol{\theta}})) \right]. \tag{4.31}$$

The sum $\sum_i \epsilon_{ij}$ quantifies the difference between the model evaluated at the global best values of the fitting parameters $\hat{\boldsymbol{\theta}}$ and the model evaluated at the j^{th} best values of $\boldsymbol{\theta}$ (i.e., $\hat{\boldsymbol{\theta}}_j$), taking into account both the statistical and systematic uncertainties. The η_{ij} term is related to the effect introduced by the uncertainties of the additional parameter set $\boldsymbol{\theta}_f$ on the model evaluation of the generic observable E_i.

The expression in Eq. (4.29) gives a crucial cross-check about the self-consistency of the fitting method, since the value obtained by the difference

$$\hat{\chi}^2_{b,j} - \left(\sum_i \gamma^2_{ij} + \sum_i \epsilon^2_{ij} + \sum_i D_{ij} + \sum_i \Phi_{ij} \right) \tag{4.32}$$

has to be identical, within the small numerical approximations introduced by the Monte-Carlo procedure, to the value calculated from Eq. (4.26). If not, there could be some mistakes in the sampling or in the generation of the random numbers.

4.5 Evaluation of the expected goodness-of-fit distribution

We could wonder which is the *goodness-of-fit distribution* of the $\hat{\chi}^2$ variable obtained in the bootstrap framework. Usually, it is assumed to be a χ^2 or, equivalently, the term $[E_i - T_i(\boldsymbol{\theta}_f, \hat{\boldsymbol{\theta}})]/\boldsymbol{\sigma}_i$ is assumed to be Gaussian distributed as $\mathcal{G}[0,1]$. However, this is a very strong statement, since we are forcing all the experimental points to be Gaussian distributed around the model results obtained with the best estimate of the parameters, i.e. $E_i \in \mathcal{G}[T_i(\boldsymbol{\theta}_f, \hat{\boldsymbol{\theta}}), \boldsymbol{\sigma}_i^2]$.

In our approach, we do not make any assumptions on the distribution of the measured values around our model results, but we analyze an ideal experiment in which all the points are *exactly* the values predicted by our model. The sampling shown in Eq. (4.22) can be performed replacing each experimental data with $T_i(\boldsymbol{\theta}_f, \hat{\boldsymbol{\theta}})$, thus obtaining

$$\mathcal{M}_{ij} = (1 + \delta_{ij})(T_i(\boldsymbol{\theta}_f, \hat{\boldsymbol{\theta}}) + \gamma_{ij}\sigma_i). \tag{4.33}$$

Based on this new sampling, the minimization function and its minimum (at every j^{th} bootstrap cycle) can be respectively defined as

$$\chi^2_{th,j} = \sum_{i=1}^{n} \left(\frac{\mathcal{M}_{ij} - T_i(\boldsymbol{\theta}_{f,j}, \boldsymbol{\theta})}{\sigma_{ij}} \right)^2, \tag{4.34}$$

$$\hat{\chi}^2_{th,j} = \sum_{i=1}^{n} \left(\frac{\mathcal{M}_{ij} - T_i(\boldsymbol{\theta}_{f,j}, \hat{\boldsymbol{\theta}}'_j)}{\sigma_{ij}} \right)^2. \tag{4.35}$$

The sampled parameters $\boldsymbol{\theta}_{f,j}$ are exactly the same as in Eq. (4.24), while the fit values of the parameters at every bootstrap cycle are, in general, different from the ones obtained from the fit of the bootstrapped data: for this reason we use $\hat{\boldsymbol{\theta}}'_j$ instead of $\hat{\boldsymbol{\theta}}_j$.

Following the steps described in Sec. 4.4, we can introduce the variables:

$$\begin{aligned}
\epsilon'_{ij} &\equiv \frac{1}{\sigma_i}\left[T_i(\boldsymbol{\theta}_f, \hat{\boldsymbol{\theta}}) - \frac{T_i(\boldsymbol{\theta}_f, \hat{\boldsymbol{\theta}}'_j)}{1 + \delta_{ij}} \right], \\
\eta'_{ij} &\equiv \frac{1}{(1 + \delta_{ij})\sigma_i}\left[T_i(\boldsymbol{\theta}_f, \hat{\boldsymbol{\theta}}'_j) - T_i(\boldsymbol{\theta}_{f,j}, \hat{\boldsymbol{\theta}}'_j) \right], \\
D'_{ij} &\equiv 2\epsilon'_{ij}\gamma_{ij}, \\
\Phi'_{ij} &\equiv {\eta'_{ij}}^2 + 2\eta'_{ij}\left(\epsilon'_{ij} + \gamma_{ij}\right),
\end{aligned} \tag{4.36}$$

which give the following decomposition of the $\hat{\chi}^2_{th,j}$ variable

$$\hat{\chi}^2_{th,j} = \hat{\chi}^2_{th} + \sum_i \gamma^2_{ij} + \sum_i {\epsilon'_{ij}}^2 + \sum_i D'_{ij} + \sum_i \Phi'_{ij}. \tag{4.37}$$

Here, $\hat{\chi}^2_{th}$ is defined as in Eq. (4.26), replacing E_i with $T_i(\boldsymbol{\theta}_f, \hat{\boldsymbol{\theta}})$. This parameter is equal to zero by construction, but we explicitly leave this decomposition as a cross-check[3] since, within the small numerical approximations introduced by the procedure itself, we should obtain:

$$0 = \hat{\chi}^2_{th,j} - \left[\sum_i \gamma^2_{ij} + \sum_i {\epsilon'_{ij}}^2 + \sum_i D'_{ij} + \sum_i \Phi'_{ij} \right]. \tag{4.38}$$

All the sensitivity of the theoretical model on the additional parameter set $\boldsymbol{\theta}_f$ is confined in the Φ'_{ij} term, that will play an important role as a cross-check of the fitting procedure as well as in the determination of the goodness-of-fit distribution. In the $\hat{\chi}^2$ variable, there is no dependence on the additional model parameters, thus convincing us that the most realistic distribution for the quality of the fit can be defined as

$$\chi^2_{u,j} = \sum_{i=1}^{n} \left(\frac{\mathcal{M}_{ij} - T_i(\boldsymbol{\theta}_f, \boldsymbol{\theta})}{\sigma_{ij}} \right)^2, \tag{4.39}$$

with a minimum at

$$\hat{\chi}^2_{u,j} = \sum_{i=1}^{n} \left(\frac{\mathcal{M}_{ij} - T_i(\boldsymbol{\theta}_f, \hat{\boldsymbol{\theta}}'_j)}{\sigma_{ij}} \right)^2 = \hat{\chi}^2_{th,j} - \sum_i \Phi'_{ij}. \tag{4.40}$$

Thus, the additional model parameters affect the determination of the $\hat{\boldsymbol{\theta}}$ vector, but they do not introduce any bias in the probability distribution which the variable $\hat{\chi}^2$ belongs to. This new parameter $\hat{\chi}^2_{u,j}$ is independent on any model or assumption about the probability distribution functions of the experimental data. Furthermore, when the systematic uncertainties are not included in the analysis and when the Φ'_{ij} term can be neglected, the expression in Eq. (4.40) is basically determined by the pure χ^2 contribution, given by the sum of squared Gaussian variables $\sum_i \gamma^2_{ij}$. This is a consequence of the bootstrap sampling, which is simplified as $\mathcal{B}_{ij} \in \mathcal{G}[\, T_i(\boldsymbol{\theta}_f, \hat{\boldsymbol{\theta}}), \sigma_i^2]$. The small additional corrections due to the $\sum_i {\epsilon'_{ij}}^2$ and $\sum_i D'_{ij}$ terms can introduce a tiny model-dependent distortion to this simple picture, as it will be discussed later.

On the other hand, when systematic errors are included in the data analysis, the sampled points are generated from the convolution $\mathcal{U}[-\Delta_i, \Delta_i] * \mathcal{G}[\, T_i(\boldsymbol{\theta}_f, \hat{\boldsymbol{\theta}}), \sigma_i^2]$. As a consequence, the terms $\sum_i {\epsilon'_{ij}}^2$ and $\sum_i D'_{ij}$ cannot be

[3] We will discuss this point in the comments related to Table 4.2 later in the text.

neglected, and a distortion is introduced to the standard χ^2-distribution. We can summarize these considerations as:

$$\begin{aligned}
\text{without systematics: } \hat{\chi}^2_{u,j} &= \sum_i \gamma^2_{ij} + \sum_i {\epsilon'_{ij}}^2\Big|_{\delta_{ij}=0} + \sum_i D'_{ij}\Big|_{\delta_{ij}=0} \sim \sum_i \gamma^2_{ij}, \\
\text{with systematics: } \hat{\chi}^2_{u,j} &= \sum_i \gamma^2_{ij} + \sum_i {\epsilon'_{ij}}^2\Big|_{\delta_{ij}\neq 0} + \sum_i D'_{ij}\Big|_{\delta_{ij}\neq 0}. \qquad (4.41)
\end{aligned}$$

Some other useful quantities that will be discussed later in this chapter are the terms of Eq. (4.29) and Eq. (4.41), divided by the number of degrees of freedom n_{dof}, i.e.

$$\begin{aligned}
\hat{\chi}^2_r &= \frac{1}{n_{dof}}\left\{\hat{\chi}^2_{b,j} - \left[\sum_i \gamma^2_{ij} + \sum_i \epsilon^2_{ij} + \sum_i D_{ij} + \sum_i \Phi_{ij}\right]\right\}, \\
\hat{\chi}^2_{th,r} &= \frac{1}{n_{dof}}\left\{\hat{\chi}^2_{th,j} - \left[\sum_i \gamma^2_{ij} + \sum_i {\epsilon'_{ij}}^2 + \sum_i D'_{ij} + \sum_i \Phi'_{ij}\right]\right\}, \\
\gamma^2_r &\equiv \frac{1}{n_{dof}}\sum_i \gamma^2_{ij}, \quad \epsilon^2_r \equiv \frac{1}{n_{dof}}\sum_i \epsilon^2_{ij}, \quad D_r \equiv \frac{1}{n_{dof}}\sum_i D_{ij}, \\
\Phi_r &\equiv \frac{1}{n_{dof}}\sum_i \Phi_{ij}, \quad {\epsilon'}^2_r \equiv \frac{1}{n_{dof}}\sum_i {\epsilon'_{ij}}^2, \quad D'_r \equiv \frac{1}{n_{dof}}\sum_i D'_{ij}, \\
\Phi'_r &\equiv \frac{1}{n_{dof}}\sum_i \Phi'_{ij}, \quad \chi^2_b = \gamma^2_r + \epsilon^2_r + D^2, \quad \chi^2_{th} = \gamma^2_r + {\epsilon'}^2_r + {D'_r}^2.
\end{aligned} \qquad (4.42)$$

Provided that the number of bootstrap replicas is sufficiently high, the $\hat{\chi}^2_{u,j}$ entries reconstruct the goodness-of-fit distribution $p(\chi^2_{th})$, from which we can obtain the p-value associated to the variable $\hat{\chi}^2_r$ from the two-sided χ^2 test:

$$p\text{-value} = \begin{cases} CDF(\mathbb{X}), & \text{if } CDF(\mathbb{X}) < 0.5, \\ 1 - CDF(\mathbb{X}), & \text{if } CDF(\mathbb{X}) \geq 0.5, \end{cases}$$

where $\mathbb{X}$ is the value of the $\hat{\chi}^2_r$ value obtained at the end of the fit and

$$CDF(\mathbb{X}) = \int_{-\infty}^{\mathbb{X}} p(\chi^2_{th}) d\chi^2_{th}. \qquad (4.43)$$

In the following, we will omit the $\mathbb{X}$ dependence in the cumulative distribution functions (CDFs).

4.6 A toy model to describe the new method

In order to deeper analyze all the features related to the bootstrap-based fitting technique, we implement a toy model, simulating random data from a Breit-Wigner (BW) distribution. The choice of this function is related both to the

important role that it plays in physics (it is commonly used for the description of resonance phenomena) and to the strong non linearity in the parameter space. This mathematical feature will turn out to be useful in the application of the fitting technique, making the toy model not too trivial. The BW function is then defined as

$$BW(x; I, \mu, \Gamma) = \frac{I}{\pi\Gamma} \frac{\Gamma^2}{(x-\mu)^2 + \Gamma^2}, \tag{4.44}$$

where, I is an overall scale factor, μ is the peak position and Γ specifies the half-width at half-maximum.

The simulated data are obtained by the cumulative inversion method, which is based on the fact that every CDF is uniformly distributed as $\mathcal{U}[0,1]$. Thus, we can sample a variable $\xi \in \mathcal{U}[0,1]$ and then consider is as an outcome of the BW cumulative distribution, i.e.

$$\xi = \frac{1}{\pi} \arctan\left[\frac{x-\mu}{\Gamma}\right] + \frac{1}{2}. \tag{4.45}$$

Thus, the x variable is distributed according to Eq. (4.44), provided that we impose $I \equiv 1$. Repeating this procedure for a large number of times, we can simulate the experimental measurements from the standard BW distribution. We then have the freedom to rescale the BW function, changing all of its parameters at will. Our chosen values for the μ, Γ, and I parameters of Eq. (4.44) are:

$$\mu_0 = 0, \quad \Gamma_0 = 1, \quad I_0 = 250. \tag{4.46}$$

Using this procedure, we generate 30000 events, collecting those that fall in the x range $[-4, 4]$ and diving them into 3 different subsets. We then build a 100-bin histogram, in order to simulate a counting-event experiment, obtaining the result shown in Fig. 4.2. For each subset, we can denote the content and the statistical fluctuation of the i^{th} histogram bin by B_i and $\sigma_{B,i}$, respectively. The bootstrapped data are obtained from Eq. (4.22), i.e.

$$\mathcal{B}_{ij} = (1 + \delta_{ij}) \left[B_i + \gamma_{ij}\sigma_{B,i}\right]. \tag{4.47}$$

Once the sampling is performed, we need to establish the fitting conditions that can better test the fitting procedure. Our choice is to perform the fit under the following configurations:

* Fit_{3p}: 3 fit parameters (I, μ and Γ);
* Fit_{2p+1f}: 2 fit parameters (I and Γ), and one fixed parameter ($\mu = \mu_0$);
* Fit_{2p+1s}: 2 fit parameters (I and Γ), and one sampled parameter ($\mu \in \mathcal{G}[\mu_0, \sigma^2_{\mu_0}]$). The σ_{μ_0} term is chosen as $k/100$, with $k = \{3, 20\}$ in such a way to investigate how the size of the uncertainties on $\boldsymbol{\theta}_f$ affects the fit results.

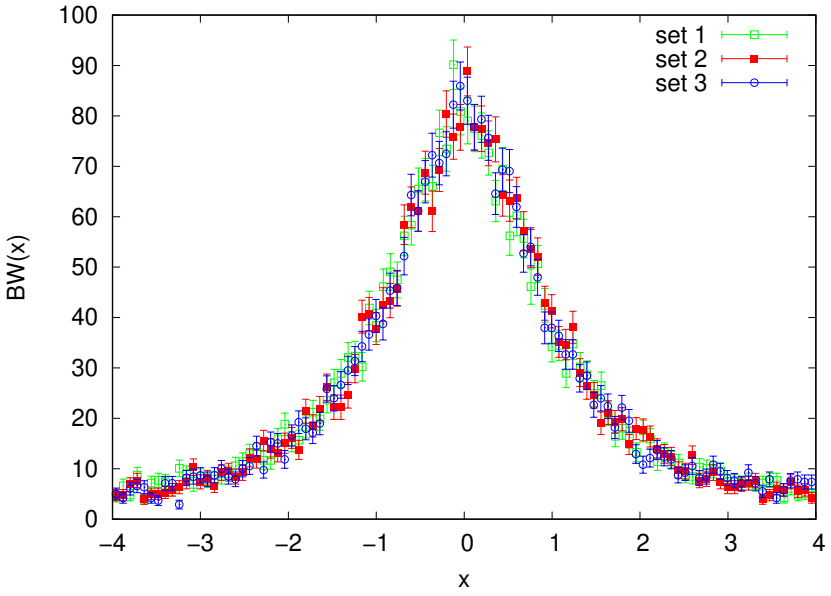

Figure 4.2: Simulated data from the Breit-Wigner distribution. They are separated into the three subsets denoted by the different colors.

In order to simulate a systematic offset to our toy data, we assume that each subset is affected by a box distributed systematic scale uncertainty with: $\Delta_1 = 0.04$, $\Delta_2 = 0.06$ and $\Delta_3 = 0.03$.

For each condition, the fit is performed with 10000 bootstrap replicas both with and without the inclusion of the systematic uncertainties. In this last case, we add the superscript $'$ to every fit label.

4.6.1 Fit results

We collect all the fit results, obtained under the different configurations, in Table 4.1, while the probability distributions of the fitted parameters are given in Figs. 4.3 and 4.4. In Table 4.2, we list also the expected values of the contributions of $\hat{\chi}^2_{b,j}$ (see Eq. (4.29)) and of $\hat{\chi}^2_{th,j}$ (see Eq. (4.37)), labeled as $\mathbb{E}[\dots]$ and divided by n_{dof}. Their probability distributions are shown in Figs. 4.6 and 4.9. Furthermore, the CDFs of the goodness-of-fit distributions are displayed in Figs. 4.10 and 4.11.

In order to provide a more schematic analysis of our fitting technique, we devote the next subsections to the discussion of each fitting condition one-by-one.

$\mathbf{Fit}_{3p}$

Before discussing our results, an important cross-check is in order. In the bootstrap framework, if only statistical uncertainties are included, the fit results should be the same as one would obtain with the standard fit procedure using

DATA						
Fitting conditions	I	μ (10^{-3})	Γ (10^{-1})	$\hat{\chi}^2_r$	p-value	Symbol
Fit_{3p}	$247.0^{+1.4}_{-1.5}$	$1.8^{+7.1}_{-7.6}$	9.8 ± 0.1	0.98	45%	○
Fit'_{3p}	$247.0^{+4.0}_{-4.2}$	$1.8^{+7.1}_{-7.7}$	9.8 ± 0.1	0.98	35%	○
Fit_{2p+1f}	$247.0^{+1.4}_{-1.5}$	fixed	9.8 ± 0.1	0.98	43%	⬠
Fit'_{2p+1f}	$247.0^{+4.0}_{-4.2}$	fixed	9.8 ± 0.1	0.98	34%	⬠
Fit_{2p+1s} (3%)	$247.0^{+1.4}_{-1.5}$	sampled	9.8 ± 0.1	0.98	43%	□
Fit'_{2p+1s} (3%)	$247.0^{+3.9}_{-4.3}$	sampled	9.8 ± 0.1	0.98	34%	□
Fit_{2p+1s} (20%)	$243.0^{+4.2}_{-5.0}$	sampled	$10.0^{+0.2}_{-0.3}$	1.05	25%	△
Fit'_{2p+1s} (20%)	$242.0^{+5.9}_{-6.2}$	sampled	$10.0^{+0.2}_{-0.3}$	1.05	19%	△

Table 4.1: Results from the fit applied to the toy data in the different conditions described in the text. Each p-value is calculated from the expected goodness-of-fit distribution, which is reconstructed in the framework of the bootstrap technique. The different symbols refer to the point styles of Figs. 4.3 and 4.4.

Eq. (4.1) and Eq. (4.2). In this case we obtain

$$\begin{aligned} I &= 247.0 \pm 1.5, \quad \mu = (1.7 \pm 7.4) \cdot 10^{-3}, \\ \Gamma &= (9.8 \pm 0.1) \cdot 10^{-1}, \quad \hat{\chi}^2 = 0.98, \end{aligned} \tag{4.48}$$

which are in (almost) perfect agreement with the values given in Table 4.1 and corresponding to the Fit_{3p} condition. The only tiny difference is the asymmetry of the bootstrapped 1-σ range for I and μ, which is completely absent in the standard minimization procedure. This feature can be explained by considering that (I) the standard fitting technique assume a-priori Gaussian distributed parameters, (II) the finite number of replicas introduces a small bias and (III) the number of bins used for the histograms introduces a numerical approximation in the evaluation of the CDFs, from which the 1-σ range is computed. We can reduce this difference by increasing both the number of replicas and the binning for the histograms. For instance, with 100000 replicas and 200-bin histograms, we obtain a completely symmetric range for all the fitted parameters.

The approximations introduced in our procedure can be kept under control by examining the reconstructed probability distribution and fitting it to a Gaussian distribution. In the left panel of Fig. 4.5, we show that the fitted results obtained in the Fit_{3p} configuration (black dots) are in excellent agreement with the expected Gaussian shape, according to Ref. [71].

The different contributions of $\hat{\chi}^2_{b,j}$ (see Eq. (4.29)), corresponding to the Fit_{3p} condition, are given in the first line of Table 4.2 (upper part) and in Fig. 4.6 (black curves). We can notice that for the $\hat{\chi}^2_{th,j}$ variable (see Eq. (4.37) and Fig. 4.7), the term $\mathbb{E}\left[\hat{\chi}^2\right]$ is numerically very close to zero (see Table 4.2), as expected. Furthermore, its distribution is basically a pure reduced χ^2 distribution, as previously discussed in Eq. (4.41) and shown in the left plot of Fig. 4.10, due to the quite small and almost opposite values of $\mathbb{E}\left[\epsilon'\right]$ and $\mathbb{E}\left[D'_r\right]$.

DATA

Fitting conditions	$\mathbb{E}[\hat{\chi}^2_r]$	$\mathbb{E}[\gamma^2_r]$	$\mathbb{E}[\epsilon^2_r]$	$\mathbb{E}[D]$	$\mathbb{E}[\Phi]$	Symbol
Fit_{3p}	0.98	1.01 ± 0.08	$(9.92 \pm 8.18) \cdot 10^{-3}$	$(-2.0 \pm 11.6) \cdot 10^{-2}$	0	○
Fit'_{3p}	0.98	1.01 ± 0.08	$(5.55 \pm 3.67) \cdot 10^{-2}$	$(-2.0 \pm 11.9) \cdot 10^{-2}$	0	○
Fit_{2p+1f}	0.98	1.01 ± 0.08	$(6.59 \pm 6.65) \cdot 10^{-3}$	$(-1.3 \pm 11.5) \cdot 10^{-2}$	0	⬠
Fit'_{2p+1f}	0.98	1.01 ± 0.08	$(5.20 \pm 3.63) \cdot 10^{-2}$	$(-1.3 \pm 11.8) \cdot 10^{-2}$	0	⬠
Fit_{2p+1s} (3%)	0.98	1.01 ± 0.08	$(6.76 \pm 6.70) \cdot 10^{-3}$	$(-1.2 \pm 11.5) \cdot 10^{-2}$	$(5.32 \pm 7.99) \cdot 10^{-2}$	□
Fit'_{2p+1s} (3%)	0.98	1.01 ± 0.08	$(5.15 \pm 3.58) \cdot 10^{-2}$	$(-1.2 \pm 11.8) \cdot 10^{-2}$	$(5.32 \pm 7.99) \cdot 10^{-2}$	□
Fit_{2p+1s} (20%)	1.05	1.01 ± 0.08	$(11.3 \pm 32.4) \cdot 10^{-2}$	$(-1.5 \pm 20.4) \cdot 10^{-2}$	2.00 ± 2.47	△
Fit'_{2p+1s} (20%)	1.05	1.01 ± 0.08	$(15.6 \pm 32.2) \cdot 10^{-2}$	$(-1.8 \pm 20.9) \cdot 10^{-2}$	2.00 ± 2.47	△

MODEL

Fitting conditions	$\mathbb{E}[\hat{\chi}^2_{th}]$	$\mathbb{E}[\gamma^2_r]$	$\mathbb{E}[\epsilon'^2_r]$	$\mathbb{E}[D'_r]$	$\mathbb{E}[\Phi']$	Symbol
Fit_{3p}	$\mathcal{O}(10^{-6})$	1.01 ± 0.08	$(9.96 \pm 8.20) \cdot 10^{-3}$	$(-1.99 \pm 1.64) \cdot 10^{-2}$	0	●
Fit'_{3p}	$\mathcal{O}(10^{-4})$	1.01 ± 0.08	$(5.66 \pm 3.75) \cdot 10^{-2}$	$(-2.00 \pm 3.02) \cdot 10^{-2}$	0	●
Fit_{2p+1f}	$\mathcal{O}(10^{-7})$	1.01 ± 0.08	$(6.61 \pm 6.67) \cdot 10^{-3}$	$(-1.32 \pm 1.33) \cdot 10^{-2}$	0	⬟
Fit'_{2p+1f}	$\mathcal{O}(10^{-4})$	1.01 ± 0.08	$(5.32 \pm 3.71) \cdot 10^{-2}$	$(-1.34 \pm 2.86) \cdot 10^{-2}$	0	⬟
Fit_{2p+1s} (3%)	$\mathcal{O}(10^{-5})$	1.01 ± 0.08	$(6.78 \pm 6.72) \cdot 10^{-3}$	$(-1.34 \pm 1.33) \cdot 10^{-2}$	$(5.46 \pm 8.16) \cdot 10^{-2}$	■
Fit'_{2p+1s} (3%)	$\mathcal{O}(10^{-4})$	1.01 ± 0.08	$(5.26 \pm 3.67) \cdot 10^{-2}$	$(-1.39 \pm 2.83) \cdot 10^{-2}$	$(5.46 \pm 8.15) \cdot 10^{-2}$	■
Fit_{2p+1s} (20%)	$\mathcal{O}(10^{-1})$	1.01 ± 0.08	$(11.0 \pm 31.6) \cdot 10^{-2}$	$(-1.6 \pm 16.4) \cdot 10^{-2}$	1.97 ± 2.43	▲
Fit'_{2p+1s} (20%)	$\mathcal{O}(10^{-1})$	1.01 ± 0.08	$(15.4 \pm 31.4) \cdot 10^{-2}$	$(-1.9 \pm 17.0) \cdot 10^{-2}$	1.97 ± 2.43	▲

Table 4.2: The expected values of the different components of $\hat{\chi}^2_{b,j}$ (upper panels) and $\hat{\chi}^2_{th,j}$ (lower panels), as shown in Eq. (4.42). The different symbols refer to the point styles in Figs. 4.3–4.5 and 4.10–4.12.

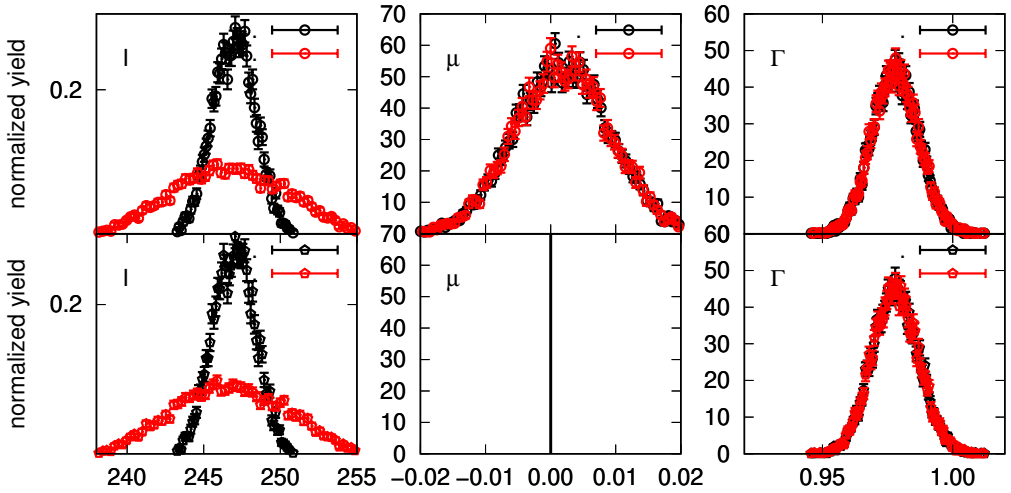

Figure 4.3: Probability distributions for the fit parameters I (left panels), μ (central panels) and Γ (right panels) for the Fit_{3p} (upper panels) and Fit_{2p+1f} (lower panels) configurations. The red (black) points correspond to the results with (without) the inclusion of the systematic uncertainties in the fit procedure. In the Fit_{2p+1f} case, the mean value μ is not fitted but kept fixed at zero.

These properties fully confirm the considerations outlined in Sec. 4.4 and Sec. 4.5 and point out that, when only statistical uncertainties are included in the data analysis, the goodness-of-fit distribution related to the $\hat{\chi}^2_r$ variable is almost a pure χ^2.

Fit'_{3p}

Due to the mathematical expression of the BW distribution in Eq. (4.44), the only parameter that is affected by the inclusion of a common scale factor is I, while μ and Γ remain almost the same: this feature is clearly visible from the second line of Table 4.1 and from the top panel of Fig. 4.3. The results obtained under this configuration can be compared with the ones obtained using the χ^2_{mod} defined in Eq. (4.3), leaving the normalization factors for each subset as additional free parameters:

$$\chi^2_{mod} = \sum_k \left\{ \left[\sum_{i \in \text{ set k}} \left(\frac{f_k E_i - T_i}{f_k \sigma_i} \right)^2 \right] + \left(\frac{f_k - 1}{\sigma_k^{sys}} \right)^2 \right\}, \tag{4.49}$$

where $\sigma_k^{\text{sys}} = \Delta_k/\sqrt{3}, k = 1, 2, 3$. In this case we obtain the values

$$\begin{aligned} I &= 246.7 \pm 3.5, \quad \mu = (1.7 \pm 7.5) \cdot 10^{-3}, \\ \Gamma &= (9.8 \pm 0.1) \cdot 10^{-1}, \quad \hat{\chi}^2 = 0.99, \end{aligned} \tag{4.50}$$

which are very similar to the results shown in Table 4.1 and referred to the Fit'_{3p} configuration. The slightly smaller uncertainty on I is (at least partially)

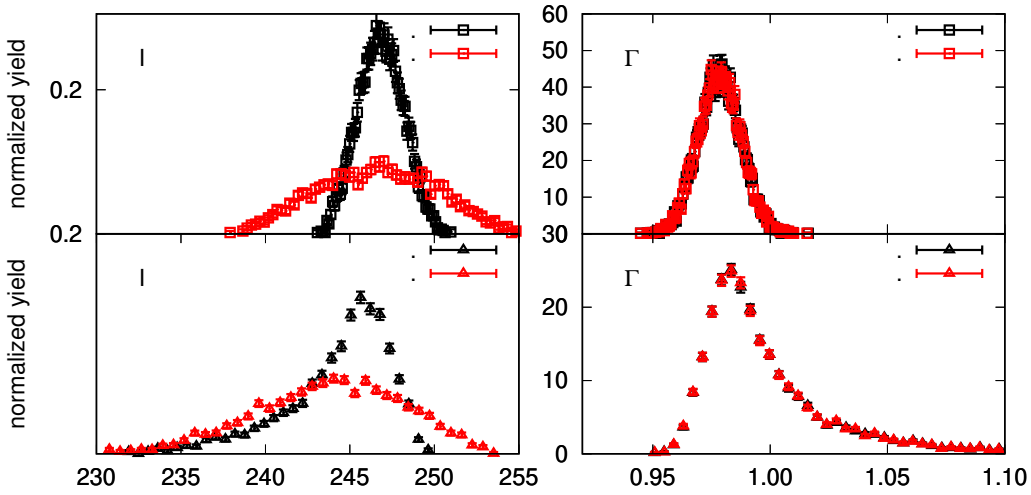

Figure 4.4: Probability distributions for the fit parameters I (left panels), μ (central panels) and Γ (right panels) Fit_{2p+1s} (3%) (upper panels) and Fit_{2p+1s} (20%) (lower panels) configurations. The red (black) points correspond to the results with (without) the inclusion of the systematic uncertainties in the fit procedure. The mean value μ is not shown here, being sampled from its known value μ_0.

due to the additional fit parameters that are present in Eq. (4.49) with respect to the bootstrap case. As a cross-check, we consider only one data set and we compare the modified χ^2 approach with the bootstrap one: the two results are identical and yield to $I = 243.8 \pm 6.2$.

We stressed in Sec. 4.5 that, when systematic errors are included in the data analysis, the goodness-of-fit distribution is not a proper χ^2. This is clearly visible from the $\hat{\chi}^2_{b,j}$ decomposition (red lines in the upper panel of Fig. 4.6), where we can notice an increased dispersion of the ϵ^2_r distribution (see also Table 4.2). However, the $\mathbb{E}\left[\hat{\chi}^2\right]$ value is the same as the one obtained in the Fit_{3p} configuration, and it is also in agreement with the results given by the χ^2_{mod} procedure. This means that, even if the value of the reduced χ^2 obtained at the end of the fit is the same, the inclusion of systematic errors can provide a different statistical significance. As a matter of fact, the p-value given in Table 4.1 is reduced by 10% with respect to the one obtained considering only statistical fluctuations.

We can examine the goodness-of-fit distribution in more detail. The CDF reconstructed by our technique is shown by the red dots of Fig. 4.10 (left panel) and it is quite far from the reduced χ^2-function. This feature is caused by the correlations between the data caused by the systematic uncertainties and it can be more thoroughly analyzed by looking at the plots in Fig. 4.7 (red curves): there, both the ϵ'^2_r and the D'_r term give a significant contribution to $\hat{\chi}^2_{th,j}$, thus distorting the effect of the predominant γ^2_r term. The size of the distortion depends both on the magnitude of the systematic bias and on the

analytical structure of the model T.

Furthermore, we could wonder what are the probability distributions of the fitted parameters: we do not expect a Gaussian shape, due to the correlation effects introduced by the systematic uncertainties. In Fig. 4.5, we show the probability distributions of the I parameter. The distributions are reconstructed under the Fit'_{3p} condition by using 100000 replicas (central panel), in order to increase the precision. To investigate the effect of the bias, we also increased the scaling factor by a factor 3 (right panel). In both cases, we notice a strong deviation from the Gaussian shape, which becomes even more pronounced when the systematic biases increase. This behavior can be qualitatively explained by the fact that, given the sampling defined by Eq. (4.22), the distribution of the I parameter results from the convolution of a uniform and a Gaussian function and its shape depends on the Δ/σ_i ratio.

We stress that all these statistical features would not be noticed in the framework given by the χ^2_{mod} function, where the goodness-of-fit distribution is assumed to be a Gaussian and no distortion in the fitted parameters distribution is observed.

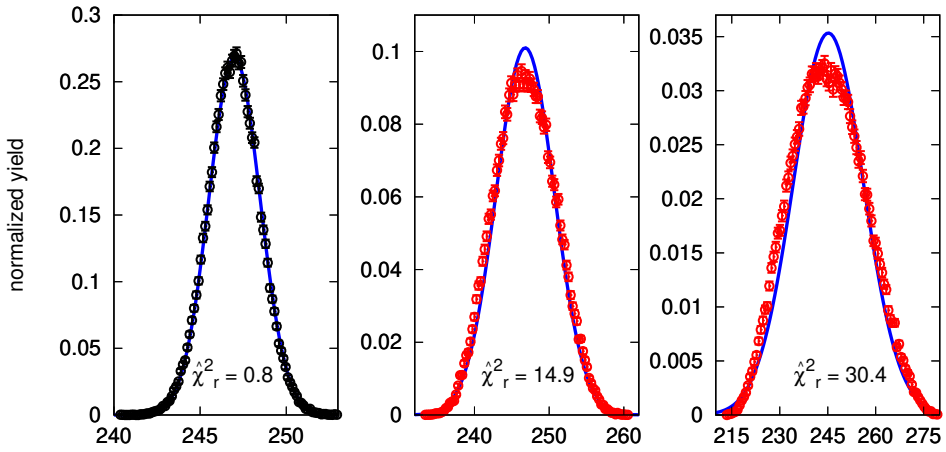

Figure 4.5: Probability distributions for the fitted parameter I, obtained with 100000 bootstrap cycles and 100 histogram bins under the Fit_{3p} (left panel), Fit'_{3p} (central panel) and Fit'_{3p} with $3 \cdot \Delta_k$ (right panel) configurations. These distributions are compared to the best-fit Gaussian curves (blue solid curves). At the bottom of each plot are also quoted the corresponding $\hat{\chi}^2_r$ values.

Fit_{2p+1f}

The results obtained under this configuration are almost identical to the ones from $\text{Fit}^{(\prime)}_{3p}$ conditions, as can be seen from Table 4.1 and Table 4.2. We just use them as a benchmark to compare the results of the $\text{Fit}^{(\prime)}_{2p+1s}$ conditions, where the uncertainty of the non-fitted parameter is included in the bootstrap sampling.

Fit$_{2p+1s}$

Under this fitting configuration, we analyze the effect of the uncertainties of the non-fitted parameter on the fitted results. If the uncertainty is small ($\sigma_{\mu_0} = 3\%$), we obtain almost the same values as in the Fit$^{(\prime)}_{2p+1f}$ configuration, as can be seen by looking at Table 4.1 and Table 4.2, and at Figs. 4.8 and 4.11 (left panels). Also the probability distributions of the fit parameters I and Γ are still compatible with a Gaussian function. This feature is ensured by the small value of $\mathbb{E}[\Phi]$, which is now non-zero by definition. As a matter of fact, if we increase σ_{μ_0} up to 20%, the $\mathbb{E}[\Phi]$ term increases and causes huge differences with respect to the Fit$^{(\prime)}_{2p+1f}$ condition. The outputs are shown in Table 4.1 and Table 4.2, while the decomposition of the $\hat{\chi}^2_{th,j}$ variable is shown in Fig. 4.9. Now, the Φ'_r term gives a sizable distortion with respect to a pure reduced χ^2 and basically overwhelms the effect due to the systematic errors, as can be seen in Fig. 4.11. Furthermore, the fitted parameters are definitely non-Gaussian distributed, as shown by the lower panels of Fig. 4.4.

All these features can be used to validate the choice of fixing the μ_0 parameter rather than fit it. With such a big uncertainty σ_{μ_0}, both the parameters distributions and the $\hat{\chi}^2_{th,j}$ CDF suggest that this configuration shows huge drawbacks.

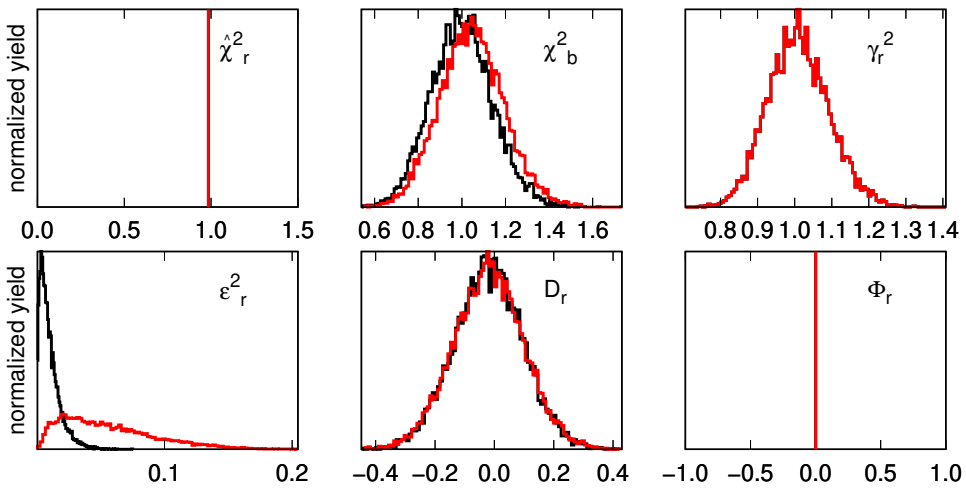

Figure 4.6: Decomposition of the $\hat{\chi}^2_{b,j}$ parameter in the Fit$_{3p}$ configuration when systematic uncertainties are excluded (black curves) and included (red curves). Upper panels (from left to right): $\hat{\chi}^2$, χ^2_b and γ^2_r components. Lower panels (from left to right): ϵ^2_r, D_r and Φ_r components. See Eq. (4.42) for the notation.

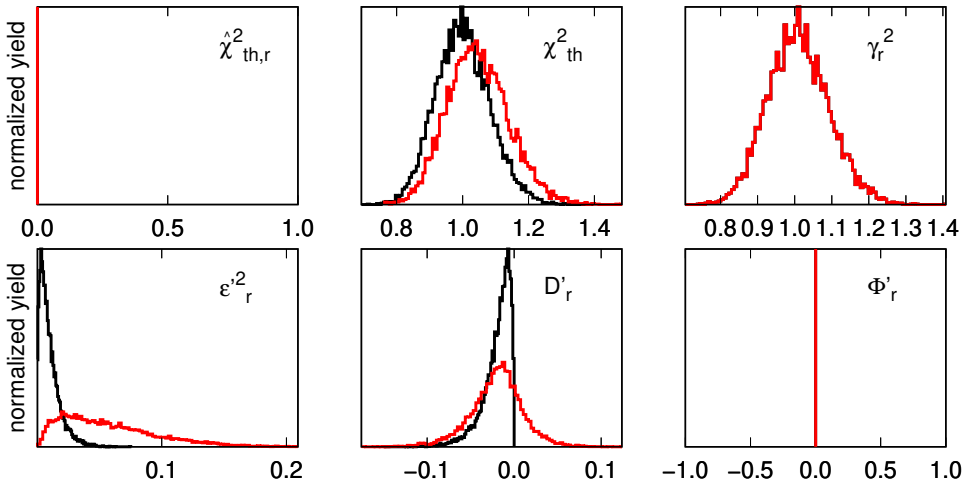

Figure 4.7: Decomposition of the $\hat{\chi}^2_{th,j}$ parameter in the Fit$_{3p}$ configuration when systematic uncertainties are excluded (black curves) and included (red curves). Upper panels (from left to right): $\hat{\chi}^2_{th,r}$, χ^2_{th} and γ^2_r components. Lower panels (from left to right): ϵ'^2_r, D'_r and Φ'_r components. See Eq. (4.42) for the notation.

4.7 A more realistic situation: data with a systematic offset

Up to now we have shown how to deal with systematic uncertainties by the bootstrap sampling. However, the simulated data are not affected by any intrinsic bias, thus not reflecting a more realistic experimental situation where all the data are shifted by some unknown quantity .

In order to take into account these aspects, we assume that each data set has a multiplicative offset δ_k^* lying inside the estimated uncertainty range $[-\Delta, \Delta]$. For our purposes, we fix $\delta_1^* = 3\%$, $\delta_2^* = 4\%$ and $\delta_3^* = -2\%$, and rescale all the points and their corresponding statistical uncertainties as $E_i^* = (1+\delta_k^*)E_i$ and $\sigma_i^* = (1+\delta_k^*)\sigma_i$, respectively.

We now apply the bootstrap sampling of Eq. (4.22), replacing E_i and σ_i with E_i^* and σ_i^*, respectively, and perform the fit under the Fit$_{3p}$ and Fit$'_{3p}$ conditions. Our results are:

$$\begin{aligned} \text{Fit}_{3p}\text{: } I &= 250.7^{+1.4}_{-1.5}, \quad \mu = (1.9 \pm 7.4)\cdot 10^{-3}, \quad \Gamma = (9.8 \pm 0.1)\cdot 10^{-1}, \\ \hat{\chi}^2 &= 1.07, \quad p-\text{value} \simeq 20\%, \end{aligned} \tag{4.51}$$

$$\begin{aligned} \text{Fit}'_{3p}\text{: } I &= 250.7 \pm 4.0, \quad \mu = (1.9^{+7.2}_{-7.6})\cdot 10^{-3}, \quad \Gamma = (9.8 \pm 0.1)\cdot 10^{-1}, \\ \hat{\chi}^2 &= 1.07, \quad p-\text{value} \simeq 30\%. \end{aligned} \tag{4.52}$$

We can see that both the central values and the uncertainties of the fit parameters are very similar to the previous results given in Table 4.1; however, the $\hat{\chi}^2$ increased and the goodness-of-fit distribution, even when the systematic errors

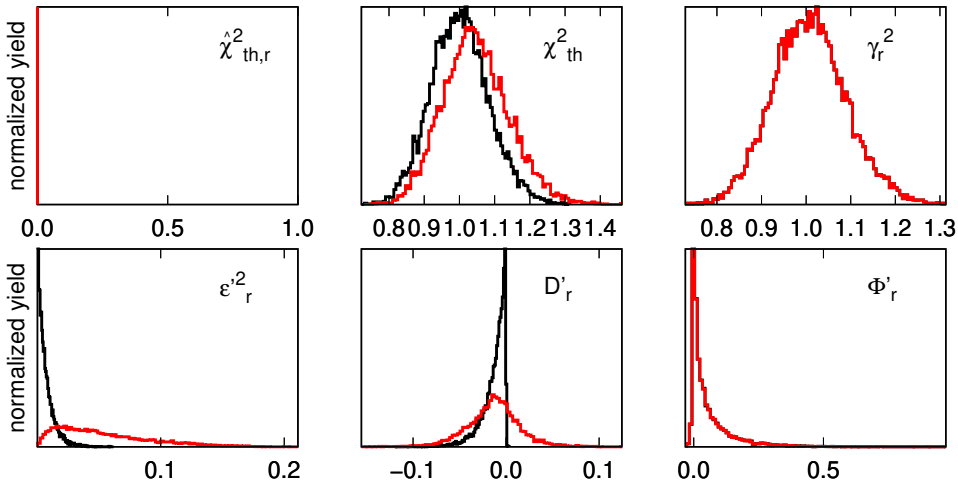

Figure 4.8: Decomposition of the $\hat{\chi}^2_{th,j}$ parameter in the Fit_{2p+1s} (3%) configuration when systematic excluded (black curves) and included (red curves). Upper panels (from left to right): $\hat{\chi}^2_{th,r}$, χ^2_{th} and γ^2_r components. Lower panels (from left to right): ϵ'^2_r, D'_r and Φ' components. See Eq. (4.42) for the notation.

are not included in the data analysis, is not a pure reduced χ^2-distribution. This effect is already visible in Fig. 4.12 and, as expected, the discrepancy increases with $|\delta^*_k|$.

4.7.1 Estimate of the systematic bias

The bootstrap framework can also provide a technique for the estimate of the "unknown" data offset. Using our toy model, we can apply the bootstrap fit in the Fit_{3p} condition and let the parameter δ_{ij} span a range at least as wide as[4] $[-\Delta, \Delta]$ only for one chosen set, while we assume that all other data sets are not affected by any systematic offset. This choice is justified when the considered data set is made by several (and independent) subsets, since, in such situation, the cumulative effect of all the biases should be small because of statistical compensation.

Under this configuration, we study the behavior of the $\hat{\chi}^2_{b,j}$ parameter as a function of δ_{ij}, in order to find the value $\tilde{\delta}$ where $\hat{\chi}^2_{b,j}$ has a minimum. We define 100 bins in the δ_{ij} domain, thus obtaining for each of them the expected value $\mathbb{E}\left[\hat{\chi}^2_{b,j}(\delta_{ij})\right]$ and its statistical fluctuation. Then, we choose a fourth-order polynomial to fit the $\hat{\chi}^2_{b,j}$ function: this is a particular choice, but the determination of the minimum itself is very robust and is not influenced by the specific choice of the fitting function. Once all these steps are well under control, we can repeat the procedure for all the subsets, one-by-one, and

[4] In our case, we fix $\delta_{ij} \in \mathcal{U}[-1/2, 1/2]$.

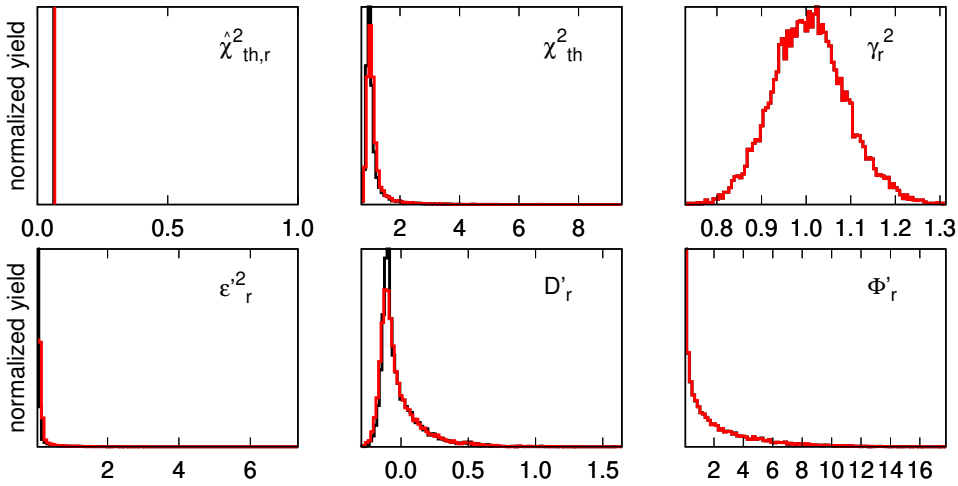

Figure 4.9: Decomposition of the $\hat{\chi}^2_{th,j}$ parameter for the Fit_{2p+1s} (20%) configuration when systematic excluded (black curves) and included (red curves). Upper panels (from left to right): $\hat{\chi}^2_{th,r}$, χ^2_{th} and γ^2_r components. Lower panels (from left to right): ϵ'^2_r, D'_r and Φ' components. See Eq. (4.42) for the notation.

evaluate all the $\tilde{\delta}_k$ values.

This strategy, when considering the offset only on set 1, yields to the results shown in Fig. 4.13, i.e. $\tilde{\delta} = -3.1\% \simeq -\delta_1^*$. Due to the high statistics, the uncertainty on the determination of the minimum is $\mathcal{O}(10^{-7})$ and it can be neglected[5]. The estimate of the bias relies on the idea that, if we want to "force" all the points of set 1 to be in good agreement with the other subsets, we need to shift each datum back to its starting value or, in other words, we should rescale every point by a factor $-\delta_1^*$.

If we use the χ^2_{mod} framework and we consider only set 1 as affected by an offset, we should write

$$\chi^2_{mod,1} = \left[\sum_{\text{set 1}} \left(\frac{f_1 E_i - T_i}{f_1 \sigma_i}\right)^2\right] + \left[\sum_{\text{set 2,set 3}} \left(\frac{E_i - T_i}{\sigma_i}\right)^2\right] + \left(\frac{f_1 - 1}{\sigma_1^{sys}}\right)^2, \quad (4.53)$$

where the additional fit parameter f_1 plays the role of a rescaling factor. Indeed, we expect that the $1 - f_1$ term is as close as possible to δ_1^*; after the minimization of the $\chi^2_{mod,1}$ function, we obtain $1 - f_1 = (2.60 \pm 1.16)\% \simeq \delta_1^*$, as expected. We can apply this strategy also to the subsets 2 and 3, thus obtaining the results shown in Fig. 4.13 and listed in Table 4.3. Our term of comparison is given, again, by the χ^2_{mod} framework, where we can fit the f_k parameters one by one or simultaneously, as shown in Eq. (4.49).

[5]In the most general case, such uncertainty can be computed with the standard error propagation applied to the function chosen to fit the data of Fig. 4.13.

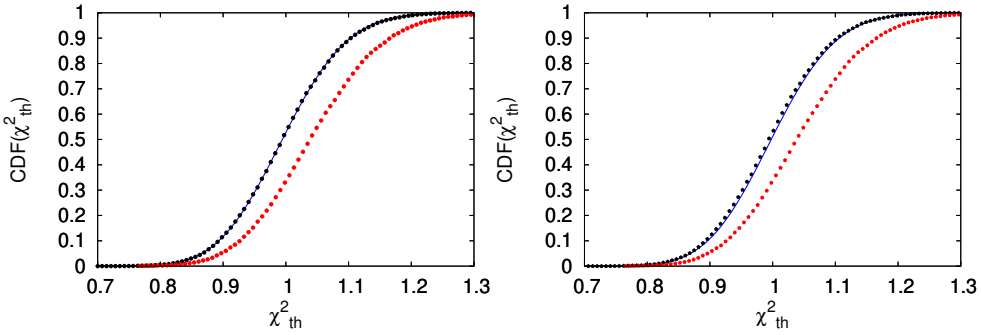

Figure 4.10: CDFs for the χ^2_{th} in the Fit_{3p} (left panel) and Fit_{2p+1f} condition (right panel), when systematic uncertainties are included (red points) or discarded (black points). The solid blue line is the CDF of the reduced χ^2-distribution.

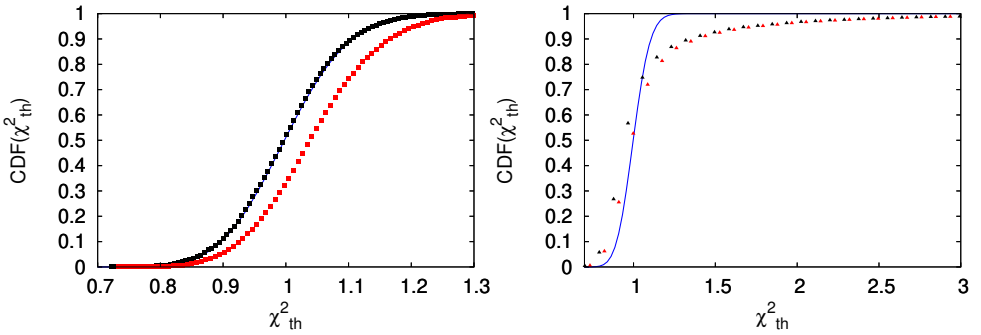

Figure 4.11: CDFs for the χ^2_{th} in the Fit_{2p+1s} condition (3%, left panel) and (20%, right panel), when systematic uncertainties are included (red points) or discarded (black points). The solid blue line is the CDF of a reduced χ^2 distribution.

We can notice that, when we apply Eq. (4.49), the central value of the rescaling factors f_k well reproduces the δ^* offset, but their uncertainties become significantly large. This reduces the accuracy of any estimate of the systematic offset in this framework. Nevertheless, the fitted parameters obtained from the minimization of the χ^2_{mod} function, i.e.

$$\begin{aligned} I &= 247.7 \pm 3.6, \quad \mu = (1.7 \pm 7.5) \cdot 10^{-3}, \\ \Gamma &= 0.98 \pm 0.01, \quad \hat{\chi}^2_{mod} = 1.01, \end{aligned} \tag{4.54}$$

are, within their estimated uncertainties, in agreement with the Fit'_{3p} results shown in Table 4.1. However, the correlation introduced to the data by the systematic errors causes a distortion in the goodness-of-fit distribution with respect to a reduced χ^2 function. In other words, the χ^2_{mod} is not the sum of squared and independent Gaussian variables, and we are not able to assign a reliable p-value to the fitted results.

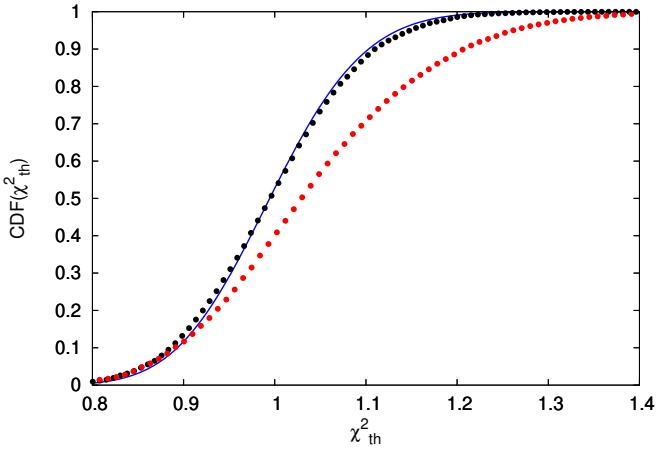

Figure 4.12: CDFs for the χ^2_{th} in the Fit'_{3p} condition (red points) and Fit_{3p} condition (black points). The solid blue line is the CDF of a reduced χ^2 distribution.

The bootstrap-based estimate of the bias seems to fail for set 3, while it works well for the other two subsets. The reason for this behavior is that, when we try to estimate δ_3^*, we are implicitly assuming that the other two subsets are not affected by any systematics, while they are both rescaled by positive numbers, δ_1^* and δ_2^* respectively. On contrary, when only set 1 or 2 are affected by the offset, the other two subsets are rescaled by factors of opposite signs, thus introducing a compensation that allow us to correctly determine the values of the offsets. With more than three sets and considering realistic situations, the true (and unknown) offsets are more likely to be random distributed and the cancellation effects should be more relevant. Once we collected all the

set number	known sys.	bootstrap	χ^2_{mod} (one-by-one)	χ^2_{mod} (simultaneous)
	δ_k^* (%)	$-\tilde{\delta}_k$ (%)	$1-f_k$ (%)	$1-f_k$ (%)
1	3.0	3.1	2.2 ± 1.1	2.6 ± 1.5
2	4.0	3.8	3.2 ± 1.1	3.3 ± 1.6
3	-2.0	-6.2	-4.1 ± 1.0	-2.1 ± 1.4

Table 4.3: Estimated offset values for each subset. Results from the bootstrap (third column) and from the χ^2_{mod} when the normalization factors f_k are fitted one-by one (fourth column) or simultaneously (last column). The known values are given in the second column, while the sets labels are in the first column.

estimates of the real systematic offsets, we can include them in the fitting procedure by rescaling all the data points and their statistical uncertainties by a factor $(1+\tilde{\delta}_k)$. At this stage, we could perform a traditional χ^2 minimization[6],

[6]The systematic offsets have already taken into account, thus we only deal with the statistical fluctuations.

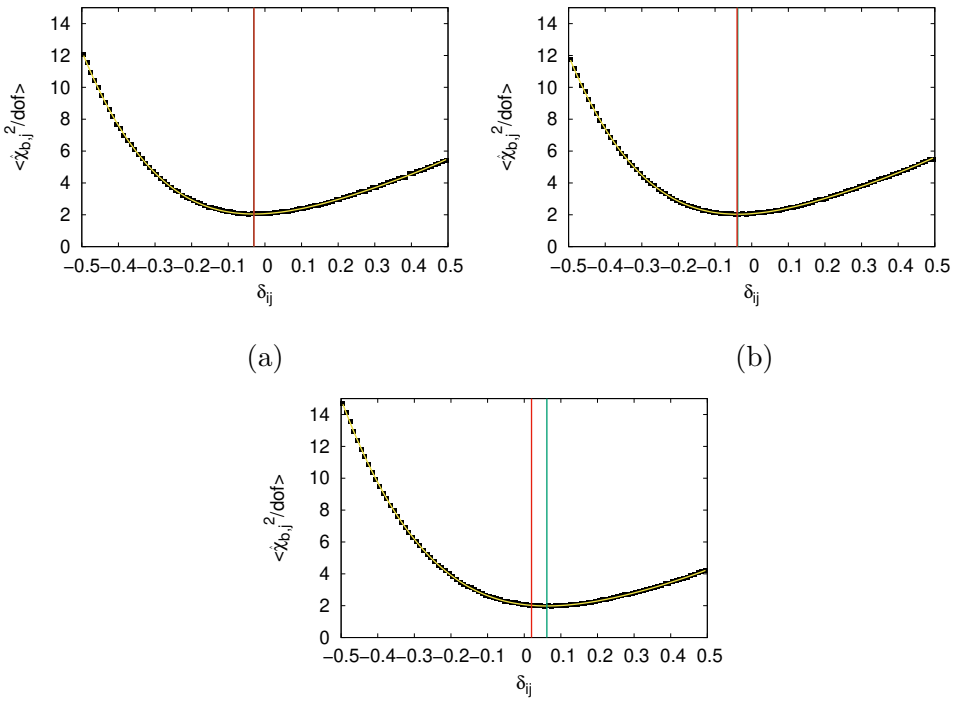

(a) (b)

(c)

Figure 4.13: The $\mathbb{E}\left[\hat{\chi}^2_{b,j}\right]$ value as a function of δ_{ij}. The black points are from the bootstrap technique, fitted with a fourth-order polynomial fit (yellow curve). The value $\tilde{\delta}$ is represented by the vertical green line, compared with the known $-\delta^*$ (red line). The numerical results are given for subset 1 (a), 2 (b) and subset 3 (c).

obtaining the results

$$\begin{aligned} I &= 250.1 \pm 1.5, \quad \mu = (1.4 \pm 7.5) \cdot 10^{-3}, \\ \Gamma &= (9.8 \pm 0.1) \cdot 10^{-1}, \quad \hat{\chi}^2_{mod} = 1.01, \quad p\text{-value} = 46\%. \end{aligned} \tag{4.55}$$

Alternatively, we can apply the bootstrap-fit by setting $\delta_{ij} = 0$ in Eq. (4.22), thus obtaining almost the same fitting results

$$\begin{aligned} I &= 250.1 \pm 1.5, \quad \mu = (1.6 \pm 7.4) \cdot 10^{-3}, \\ \Gamma &= (9.8 \pm 0.1) \cdot 10^{-1}, \quad \hat{\chi}^2_{mod} = 1.01, \quad p\text{-value} = 45\%. \end{aligned} \tag{4.56}$$

Even if the results of this technique are promising, we do not recommend to use this algorithm for the ultimate estimate of the real systematic offset, because we would introduce a strong model dependence. The working principle of this procedure can be summarized as the trial of "forcing" all the points to be in very good agreement with the model on which the χ^2 is built. Thus, we suggest using the bootstrap-based estimate of the real bias just as a cross-check for the stability of the fit or for the self-consistency of a given data set.

Chapter 5

Extraction of the dipole scalar static polarizabilities from proton real Compton scattering data

In this chapter, we show the results of the extraction of the static dipole scalar polarizabilities of the proton, i.e. α_{E1} and β_{M1}, from the available real Compton scattering data below pion production threshold. The theoretical framework is given by the fixed-t subtracted DRs, described in Ch. 3, while the fitting strategy follows the method outlined in Ch. 4.

We focus our attention on the data analysis, including all the sources of uncertainties and propagating the errors on the input used in the DRs framework. Furthermore, we discuss in detail the quality of the present data set and the dependence of the fit results from different theory inputs, notably, DRs and chiral perturbation theory.

Our analysis, within the fixed-t sDR framework, yields $\alpha_{E1} = (12.03^{+0.48}_{-0.54}) \times 10^{-4} fm^3$ and $\beta_{M1} = (1.77^{+0.52}_{-0.54}) \times 10^{-4} fm^3$, with p-value = 12%.

The contents of this chapter are mainly based on our works of Refs. [68, 72].

5.1 Sensitivity to the dipole scalar polarizabilities

As shown in Ch. 2 and Ch. 3, the RCS amplitudes in the subtracted DR formalism are given in terms of six subtraction constants, related to the leading-order static polarizabilities and dispersion integrals. The dispersion integrals can be evaluated with good accuracy using as input the experimental information from other scattering processes (notably, pion photoproduction), while

the remaining unknown static polarizabilities can be fitted directly to RCS data.

In order to check the sensitivity of the unpolarized differential cross section to the static polarizabilities, we first try to follow the scheme shown in Ref. [73], thus defining the derivative term

$$\frac{d\mathbb{O}}{d\mathbb{p}}, \tag{5.1}$$

where $\mathbb{O}$ is the experimental observable and $\mathbb{p}$ labels each of the six static polarizabilities.

As a matter of fact, this term can be numerically computed, since we can make the approximation

$$\frac{d\mathbb{O}(\mathbb{p})}{d\mathbb{p}} \simeq \frac{\mathbb{O}(\mathbb{p}+\delta\mathbb{p}) - \mathbb{O}(\mathbb{p})}{\delta\mathbb{p}}. \tag{5.2}$$

However, the electric and magnetic polarizability sum and difference, i.e. $\alpha_{E1} \pm \beta_{M1}$, are expressed in different units from the four spin polarizabilities. Thus, the derivative term introduced in Eq. (5.1) does not have the same units for all the static polarizabilities, making difficult any direct sensitivity comparison.

In order to overcome this problem, we propose to introduce the sensitivity parameter R, defined as

$$R = 100 \times \frac{\mathbb{O}(\mathbb{p}+\delta\mathbb{p}) - \mathbb{O}(\mathbb{p})}{\mathbb{O}(\mathbb{p})}, \tag{5.3}$$

where one polarizability at a time is varied. The R value is a pure number, thus allowing a very simple comparison among the sensitivity of the observable to different polarizabilities. Once the test-parameter R is defined, we need to fix the amount of the variation $\delta\mathbb{p}$: we assume $\delta\mathbb{p} = 0.05\mathbb{p}$, i.e. a variation of the polarizability by 5%.

By looking at the behavior of R as function of the kinematical variables, we can investigate the sensitivity of the observable to each polarizability and decide, on this basis, which of them should be used as free parameter in a fit. Furthermore, we could introduce a modification of the R parameter, i.e.

$$R_{exp} = 100 \times \frac{\mathbb{O}(\mathbb{p}+\Delta\mathbb{p}) - \mathbb{O}(\mathbb{p})}{\mathbb{O}(\mathbb{p})}, \tag{5.4}$$

where $\Delta\mathbb{p}$ labels the experimental uncertainty related to the polarizability $\mathbb{p}$. This parameter can be used to estimate the necessary accuracy in the measurements of the observables to improve the precision in the extraction of the polarizabilities.

We use both the expressions in Eqs. (5.3) and (5.4), applied to the unpolarized differential cross section and referred to the polarizability set $\alpha_{E1} + \beta_{M1}$, $\alpha_{E1} - \beta_{M1}$, γ_π, γ_0, γ_{E1E1} and γ_{M1M1}. The values of the uncertainties $\Delta\mathbb{p}$ are

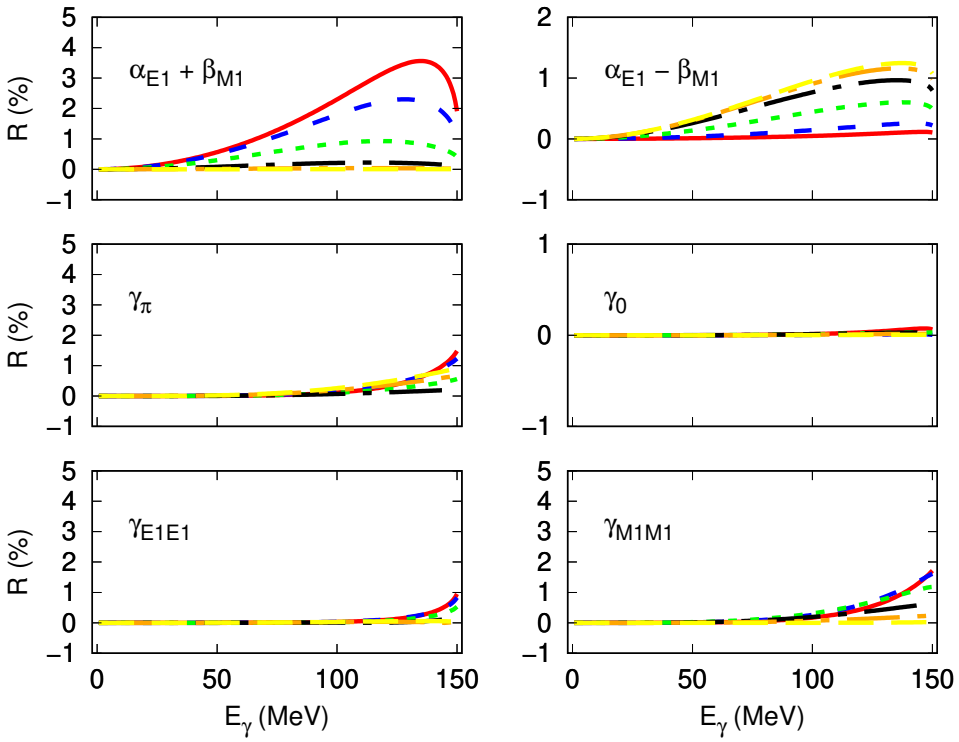

Figure 5.1: Ratio R as function of the photon energy E_γ, referred to the individual leading-order static polarizabilities and at different values of the scattering angle θ_{lab}: 45° (red solid curve), 60° (blue dashed curve), 85° (green dotted curve), 112° (black dash-dotted curve), 135° (orange dash-dot-dotted curve), 155° (yellow dashed curve).

given in the next section, for each of the six static polarizabilities. By looking at Figs. 5.1 and 5.2, we notice that the sensitivity of the RCS differential cross section to $\alpha_{E1} + \beta_{M1}$ is higher in the forward region, while $\alpha_{E1} - \beta_{M1}$ contributes more in the backward region, even if the absolute values of R for the two combinations of polarizabilities indicates a quite low sensitivity to the difference $\alpha_{E1} - \beta_{M1}$. Moreover, in the scattering region $\theta_{lab} \leq 60°$, the sensitivity to $\alpha_{E1} - \beta_{M1}$ is very close to zero, thus suggesting that the data below such scattering angle are not that much sensitive to this polarizability difference, as we shall check later in this chapter.

Furthermore, the sensitivity to every spin polarizability is low and increases as soon as we approach the pion-production threshold. The forward spin polarizability γ_0 gives an almost negligible contribution to the differential cross section. On the other hand, in the backward scattering angle region, the differential cross section becomes as sensitive to the backward spin polarizability γ_π as to $\alpha_{E1} - \beta_{M1}$.

However, if we look at the behavior of R_{exp}, we can make some important remarks. Apart from γ_0 (whose contribution to the differential cross section is negligible also in this case), the three spin polarizabilities γ_{E1E1}, γ_{M1M1} and γ_π

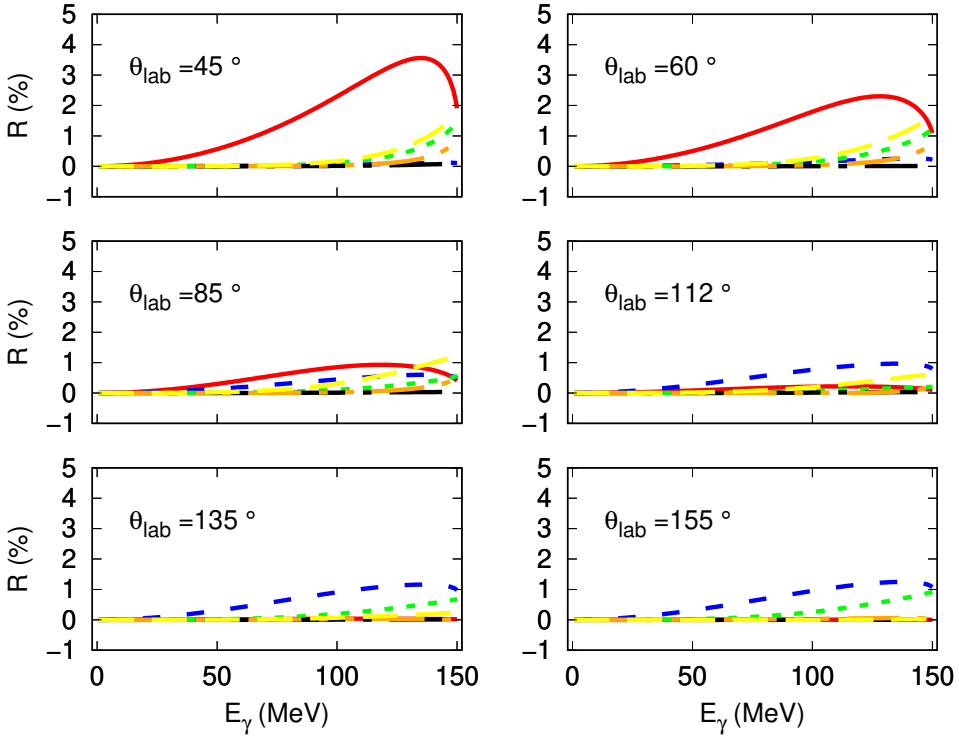

Figure 5.2: Ratio R as function of the photon energy E_γ for each static polarizability: $\alpha_{E1} + \beta_{M1}$ (red solid curve), $\alpha_{E1} - \beta_{M1}$ (blue dashed curve), γ_π (green-dotted curve), γ_0 (black dash-dotted curve), γ_{E1E1} (orange dash-dot-dotted curve) and γ_{M1M1} (yellow dashed curve). R is shown for different values of the scattering angle θ_{lab}.

become much more relevant, especially in the energy regions where $E_\gamma \gtrsim 100$ MeV. This feature stresses that the experimental uncertainties related to those three spin polarizabilities is much higher than the ideal one (namely, about 5% of the measured value), thus "artificially" increasing the sensitivity of the differential cross section to them. On the other hand, the comparison between R and R_{exp} for $\alpha_{E1} \pm \beta_{M1}$ shows that the experimental uncertainties of those two polarizabilities is close to the lowest value that could be appreciated by analyzing the RCS data.

These preliminary sensitivity tests convinced us that the spin polarizabilities input play a significant role even in the extraction of the static scalar dipole polarizabilities, thus implying a very careful choice of the input values used in the data analysis. Moreover, their statistical fluctuations are not negligible at all, thus suggesting us that we would better include them in a fit to the proton RCS data. Furthermore, the considerations made on the sensitivity to γ_π, suggest that the backward spin polarizability could be fitted simultaneously with the difference $\alpha_{E1} - \beta_{M1}$. We will come back to this point in Sec. 5.3, where we will define our fitting conditions.

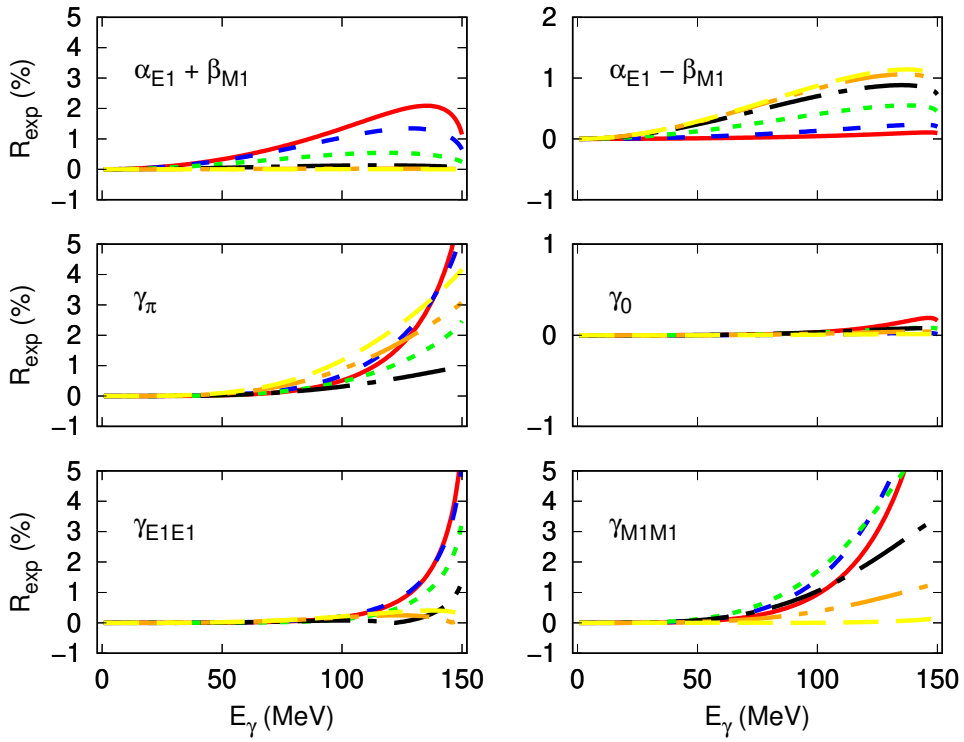

Figure 5.3: As in the caption of Fig. 5.1, but related to R_{exp}.

5.2 Discussion on the proton real Compton scattering database

As pointed out in Ref. [74], the values obtained for α_{E1} and β_{M1} from a fit of the unpolarized differential cross section strongly depend on the choice of the data set. Indeed, the scientific community has not reach so far a common agreement on the definition of the data set of the proton RCS unpolarized cross section below pion-production threshold [20, 59, 74].

For this reason, an in-depth discussion on the quality of the experimental data is in order. In Table 5.1, we list all the available data sets for RCS in the energy range below pion production threshold ($\sim$ 150 MeV in lab frame). Note that for the sets [75–77] and [78], we use the Baranov data-selection [79]. Furthermore, as done also in Refs. [8, 20], we discard the data from Table I in the Hallin paper [80], because it is not clear if they are really independent from the data given in Table II of the same work. The data sets we are going to discuss are labeled as:

- FULL, which includes all the available data sets below pion-production threshold listed in Table 5.1, for a total of 150 data points.

- SELECTED, which is based on the data selection proposed in Refs. [8, 20], corresponding to the FULL data set except for the data from Refs. [75, 81, 82], a single point ($\theta_{\rm lab} = 133°$, $E_\gamma = 108$ MeV) from Ref. [35] and

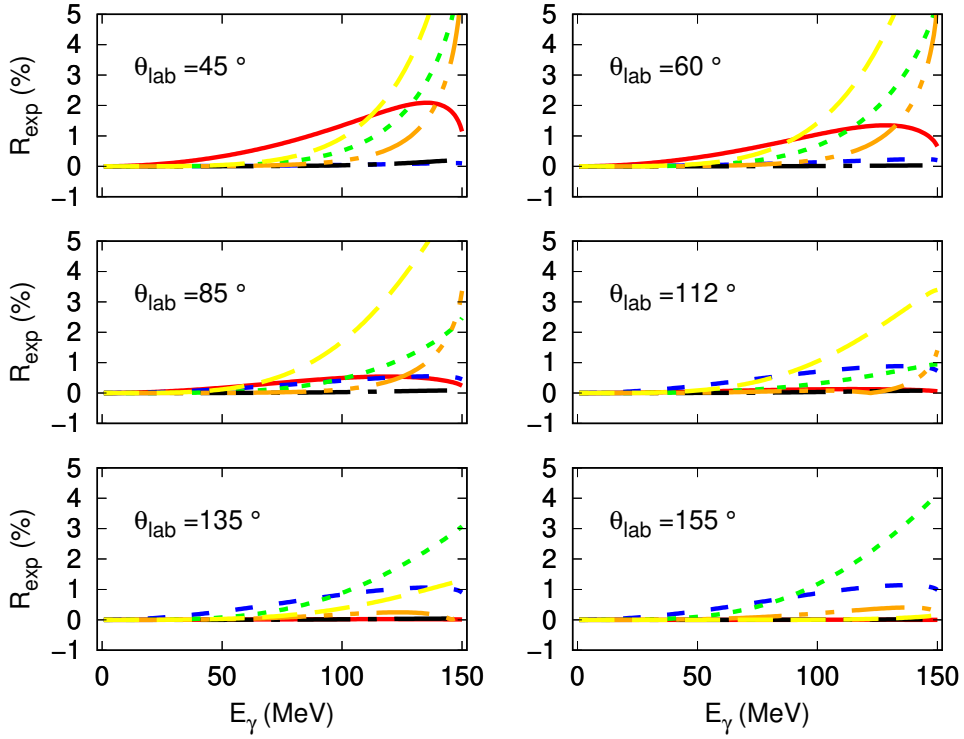

Figure 5.4: As in the caption of Fig. 5.2, but related to R_{exp}.

a single point ($\theta_{\rm lab} = 135°$, $E_\gamma = 44$ MeV) from Ref. [34], for a total of 137 data points.

- TAPS, which is the most comprehensive available subset with 55 data points below pion-production threshold [35].

We divide sets 6 and 7 from Refs. [82, 83] (and sets 11 and 12 from Ref. [33] as well), even if they are from the same experimental measurements, because they differ for the values of the systematic errors. The goal of our analysis is to perform some consistency checks of the data set and to look for the possible occurrence of outliers. In order to do so, we apply a traditional χ^2 minimization, using the gradient technique described in Sec. 4.2.1, thus not including the systematic errors in our tests. This choice is motivated by the aim of investigating the pure statistical features of the experimental data and to work in a well-established fitting condition.

From here on, the scalar dipole electric and magnetic polarizabilities are expressed in 10^{-4} fm^3 units, while the four leading-order spin-dependent polarizabilities are given in 10^{-4} fm^4 units. For all the tests shown in this section, we impose the constraint of the Baldin sum rule $\alpha_{E1} + \beta_{M1} = 13.8 \pm 0.4$, as evaluated in Ref. [21], and also adopted in the fit of Refs. [8, 35, 36]. The remaining parameters of fixed-t subtracted DRs are taken from the experimental values extracted from double-polarization RCS [36], i.e. $\gamma_{E1E1} = -3.5 \pm 1.2$ and $\gamma_{M1M1} = 3.16 \pm 0.85$, and from the GDH experiments [85, 86], i.e. $\gamma_0 =$

set label	Ref.	first author	points number	$\theta_{\rm lab}$ (°)	E_γ (MeV)	symbol
1	[75]	Oxley	4	$70-150$	$\simeq 60$	
2	[76]	Hyman	12	$50, 90$	$55-95$	
3	[77]	Goldansky	5	$75-150$	$55-80$	
4	[81]	Bernardini	2	$\simeq 135$	$\simeq 140$	
5	[78]	Pugh	16	$50-135$	$40-120$	
6	[82, 83]	Baranov	3	$90, 150$	$80-110$	
7	[82, 83]	Baranov	4	$90, 150$	$80-110$	
8	[34]	Federspiel	16	$60, 135$	$30-90$	
9	[84]	Zieger	2	180	$100, 130$	
10	[80]	Hallin	13	$45-135$	$130-150$	
11	[33]	MacGibbon	8	$90, 135$	$95-145$	
12	[33]	MacGibbon	10	$90, 135$	$95-145$	
13	[35]	Olmos de Leon	55	$60-155$	$60-150$	

Table 5.1: Angular and energy coverage of the available experimental data on unpolarized cross section for proton RCS.

$-1.01\pm0.08\pm0.10$ [1]. For the backward spin polarizability, we take the weighted average of the values extracted at MAMI [13], i.e. $\gamma_\pi = -8.0 \pm 1.8$. Here and in the following, we used the standard convention to exclude the t-channel π^0-pole contribution from the spin polarizabilities. These contributions amount to ${\gamma_\pi}^{\pi^0-\rm pole} = -46.7$ [16], $\gamma_{M1M1}^{\pi^0-\rm pole} = -\gamma_{E1E1}^{\pi^0-\rm pole} = \frac{1}{4}{\gamma_\pi}^{\pi^0-\rm pole}$, while they vanish in the case of the forward spin polarizability.

The statistical fluctuation related to $\alpha_{E1} + \beta_{M1}$ is taken into account as $\epsilon_{\alpha_{E1},\beta_{M1}} = \sqrt{(\epsilon^2_{\alpha_{E1}+\beta_{M1}} + \epsilon^2_{\alpha_{E1}-\beta_{M1}})/2}$. This fitting condition will be labeled as *test-fit*.

The result of the test-fit applied to the FULL data set leads to the best values

$$\alpha_{E1} = 11.99 \pm 0.31, \quad \beta_{M1} = 1.81 \pm 0.31, \quad \hat{\chi}^2 = 1.25, \tag{5.5}$$

which are, within the error bars, in good agreement with the ones given in Ref. [89].

As mentioned in Sec. 5.1, the sensitivity of the differential cross section to the difference $\alpha_{E1} - \beta_{M1}$ is basically negligible for $\theta_{lab} \leq 60°$, thus suggesting that the data in that region are not contributing to the determination of the $\alpha_{E1} - \beta_{M1}$ value. If we then exclude the data in the region where $\theta_{lab} \leq 60°$ (thus reducing the amount of data to 115 points), we do not expect different fitted values with respect to the result obtained using the FULL data set in the analysis. The result obtained with the angular-reduced data set are then

$$\alpha_{E1} = 11.95 \pm 0.30, \quad \beta_{M1} = 1.86 \pm 0.30, \quad \hat{\chi}^2 = 1.60, \tag{5.6}$$

which are almost identical to the ones given in Eq. (5.5). The main effect of the exclusion of the forward-angle data is the increasing of the reduced χ^2 value,

[1] This value is consistent with the fitting conditions adopted for the extraction of the spin polarizability in Ref. [36]. We note that recent reevaluations [87, 88] of γ_0 give a slightly smaller central values, with uncertainties consistent with the value used in Ref. [36].

which loses statistical significance as soon as we omit the data with $\theta_{lab} \leq 60°$. As a consequence, it is advisable to include also the forward scattering data in the analysis, even if the sensitivity of the unpolarized differential cross section to $\alpha_{E1} - \beta_{M1}$ is very small in this angular region.

5.2.1 The Jackknife resampling

In order to discuss the consistency of the data set, one can resort to a particular case of the non-parametric bootstrap technique, i.e. the Jackknife. If we consider a data set $D = \{d_i\}, i = 1, \ldots, n$, composed by n points, we can define n data subsets by removing one datum at a time, i.e. $D_k = D \setminus \{d_k\}$, where $k = 1, \ldots, n$. We then perform a fit of the model $T(\boldsymbol{\theta})$ to every D_k data set, thus obtaining a best value of the parameters $\hat{\boldsymbol{\theta}}$ for each set: from the n-tuple of $\hat{\boldsymbol{\theta}}_k$, we can compute the average $\hat{\boldsymbol{\theta}}_{Jack}$ and its sample standard deviation $\boldsymbol{\sigma}_{Jack}$. An outlier k is expected to give a result far from the average value, i.e. $|\frac{\hat{\boldsymbol{\theta}}_k - \hat{\boldsymbol{\theta}}_{Jack}}{\boldsymbol{\sigma}_{Jack}}| \gg 1$. Instead, if there are no evident outliers, we expect that all the variables $\hat{\boldsymbol{\theta}}_k$ follow, at least approximately, Gaussian confidence levels [90]. In this way, we can identify possible deviations of a data subset from the other ones.

If we now apply the Jackknife to the FULL, TAPS and SELECTED data sets previously defined, we can infer some information on the self-consistency of those data sets. In Fig. 5.5, we show the best values of α_{E1} and β_{M1} versus the index k of the excluded point in each subset. In the case of the FULL data set, we note that the statistical fluctuations are well in agreement with the expected Gaussian confidence levels ($\sim$ 95% of the occurrences within the 2σ range), thus allowing us to conclude that there is no clear evidence of outliers. On the other hand, in the case of the SELECTED data set, we obtain very similar results, with less pronounced fluctuations ($\sim$ 98% of the occurrences within the 2σ range). This does not necessarily imply that there is an improvement in the data set. Instead, this behavior may simply reflect the fact that the data points excluded from the set are not "close enough to" the model predictions.

The same test applied to the TAPS data set shows a clear dependence of the values of α_{E1} and β_{M1} on the scattering angle. This feature is due to the fact that the data are ordered by increasing scattering angles and that the sensitivity of the unpolarized RCS cross section to $\alpha_{E1} - \beta_{M1}$ is higher in the backward scattering region (see the discussion in Sec. 5.1): when a single datum is removed in the backward region, the value of β_{M1} decreases and α_{E1} increases.

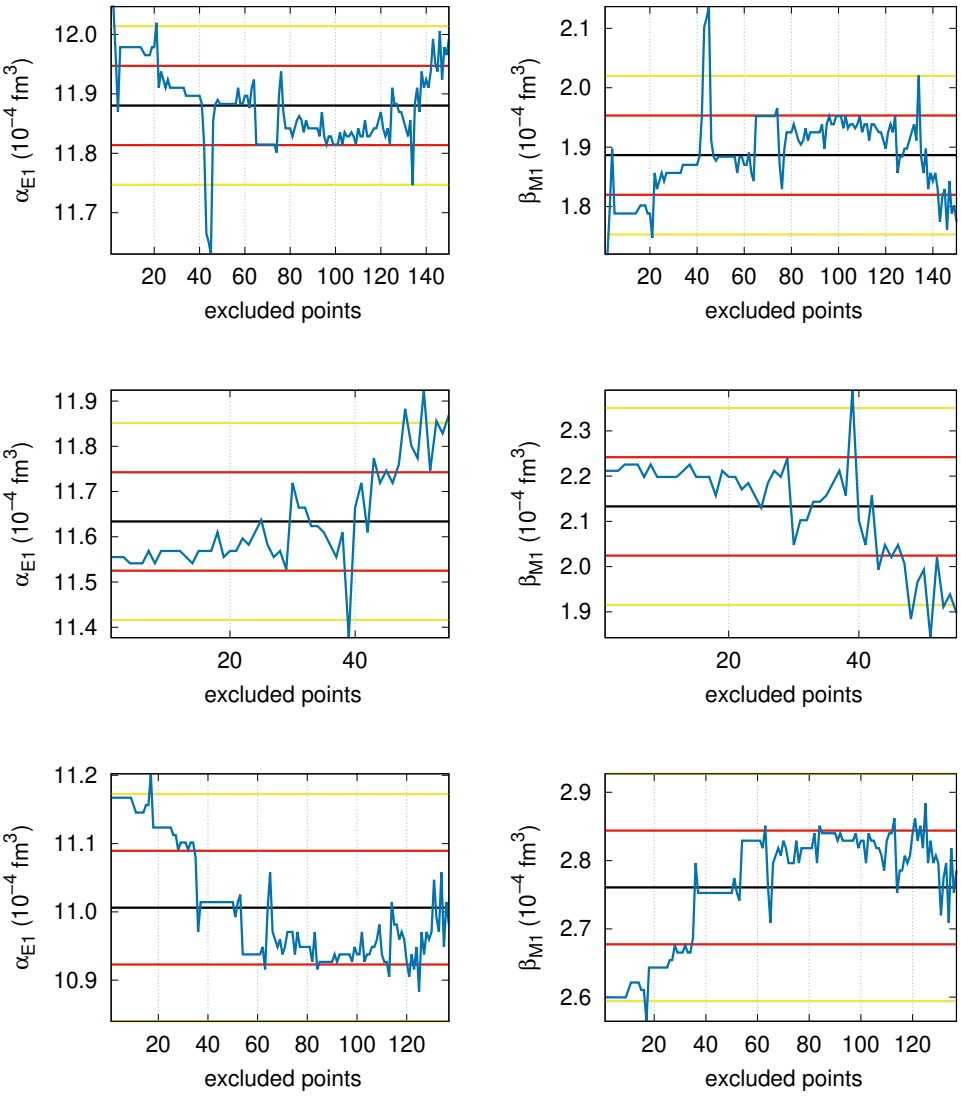

Figure 5.5: Results from the Jackknife (blue curve) for α_{E1} (left panels) and β_{M1} (right panels). The red (yellow) lines correspond to the 1-σ (2-σ) sample standard deviations. From top to bottom: results for the FULL data set, TAPS data set and the SELECTED data set.

5.2.2 Residual analysis

Another possible test is the analysis of the residuals, defined as

$$\xi_i \equiv \frac{E_i - \hat{T}_i}{\sigma_i}, \tag{5.7}$$

where E_i is the i^{th} experimental datum with the uncertainty σ_i and $\hat{T}_i$ is the model prediction obtained with the best values of the fitted parameters. If the model is able to correctly describe the experimental data, each value E_i can be considered a possible outcome of the probability distribution of T_i. In this case, the variable ξ_i defined in Eq. (5.7), is standard-Gaussian distributed as $\mathcal{G}[0,1]$. Note that this property is rigorously true if only statistical errors are included in the data analysis, otherwise there would be no reason for the experimental points to be Gaussian distributed around the theoretical model.

The results of the residual analyses applied to the FULL and SELECTED data sets are shown in left panels of Fig. 5.6, where we can observe that the ξ_i variable has mean value and standard deviation in fairly good agreement with the expectations. In the right panels of Fig. 5.6, we show also a q-q plot, which represents the CDF(ξ_i) compared to the expected CDF(z), where z is a Gaussian distributed variable according to $\mathcal{N}[0,1]$. The straight blue line is given by CDF(z) vs CDF(z), while the blue error bands show the 1σ (or 2σ) uncertainty regions due to the data set dimension.

In the case of the SELECTED data set, we observe again less pronounced statistical fluctuations mostly due to the exclusions of the subsets 1 [75] and 7 [82]. This is shown also by the fact that the CDF(ξ_i) for the SELECTED data set approaches the maximum value of unity faster than in the case of the FULL data set. If we look at the FULL data set more carefully, we note that there are three points lying outside the 3σ range: this configuration can happen with a 1% probability, if we assume only Gaussian fluctuations. Such a value, even if not extremely low, points to possible outliers inside the data set. On the other hand, the SELECTED data set has only 2 points outside the 2σ range; in this case the associated probability is $\simeq 3\%$. This probability is comparable with the previous one, thus suggesting that the exclusion of some data points does not really improve the data set or, in other words, that at least some of the discarded points are not definitely outliers.

The residual analysis thus let us to state that the FULL and SELECTED data sets have a very similar statistical significance: this ambiguity can be only resolved with new sets of precise and accurate data [48]. In the mean time, since there is not a clearly identified source of possible experimental problems that could affect the data that have been excluded from the SELECTED data base, we prefer not to discard any point to keep the highest sensitivity to $\alpha_{E1} - \beta_{M1}$. Instead, we suggest to treat the suspicious points with the approach outlined below.

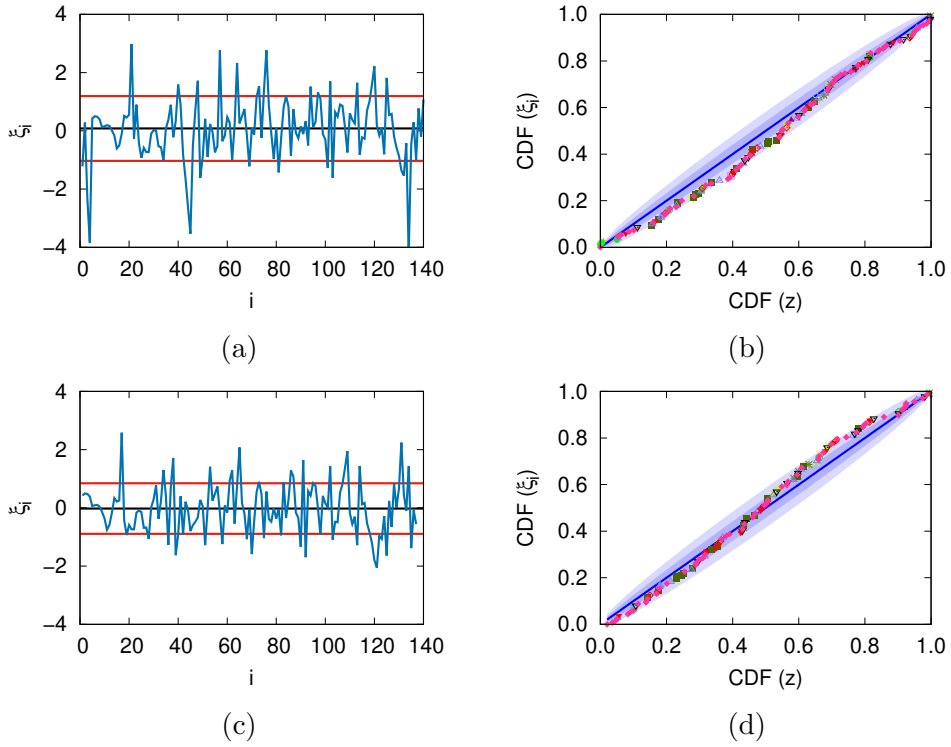

Figure 5.6: Residual analysis applied to the FULL (top panels) and SELECTED (lower panels) data set. The left panels show the values of ξ_i (blue curves), with their mean value (black curves) and their sample standard deviation band (red curves). The right panels are the q-q plots of ξ_i compared with the results expected in the case of a normal distribution (diagonal blue line). The dark (light) blue band shows the 1σ (2σ) uncertainty region due to the data set dimension. The labels of the data sets are described in Table 5.1.

5.2.3 The χ^2 per set

Another useful indicator is given by the "χ^2 per set" variable, i.e.

$$\chi^2_{set} \equiv \frac{1}{n_{set}} \sum_{i=1}^{n_{set}} \left(\frac{E_i - \hat{T}_i}{\sigma_i} \right)^2 , \tag{5.8}$$

where n_{set} is the number of points for each subset. If the model $\hat{T}_i$ is able to well describe the data, all the χ^2_{set} values should be fairly close to one. However, if $\chi^2_{set} \gg 1$, we would not be allowed to exclude all the points of such subset, being the parameter χ^2_{set} strongly model-dependent.

The numerical results of this test, applied to the FULL data set, are shown in Fig. 5.7, where we can notice that most of the subsets has $\chi^2_{set} \approx 1$, while the subsets 1 [75] and 7 [82] give higher χ^2_{set} values. As mentioned before, these subsets are indeed excluded in the definition of the SELECTED data set. However, the small number of points (4 for each subset) does not allow us to exclude the occurrence of pure statistical fluctuations. Instead of discarding

some data, we could follow the suggestion given in Ref. [91], where the statistical errors are rescaled by a factor $\sqrt{\chi^2_{set}}$, which is different for every subset, and the traditional χ^2 minimization is performed. The validity of this method relies on the assumption that a large χ^2_{set} value may suggest underestimated measurement uncertainties, that should be, in principle, equally attributed to all the points of a given subset. The result of the fit is a new set of best values for the fitted parameters ($\hat{\boldsymbol{\theta}}'$), while the minimum of the χ^2 function is equal to 1, by construction.

This strategy is again model dependent, but it can be used as an indication for the identification of outliers. If there are no data subsets that behave as outliers and then could determine very different values for the fitted parameters, we would expect that $\hat{p}' \simeq \hat{p}$. In our case, the values of the fitted parameters obtained from the FULL data set with and without rescaling of the statistical errors are consistent within the (large) fit errors, i.e.

$$\text{no rescaling}: \qquad \alpha_{E1} - \beta_{M1} = 10.17 \pm 0.47, \tag{5.9}$$

$$\sqrt{\chi^2_{set}}\ \text{rescaling}: \qquad \alpha_{E1} - \beta_{M1} = 9.36 \pm 0.50. \tag{5.10}$$

If, as a cross-check, we exclude both subsets 1 and 7 from the data analysis, and we perform a test-fit, we obtain $\alpha_{E1} - \beta_{M1} = 9.01 \pm 0.50$, which is very similar to the result shown in Eq. (5.10), obtained with the rescaling method. The two values are so similar because the rescaling method strongly reduces the impact of all the data points belonging to subsets with a relatively high χ^2_{set}. On the other hand, the rescaling procedure does not improve the accuracy of the extraction, since the error bars in Eqs. (5.9) and (5.10) are very similar. Furthermore, the difference between the central values in Eqs. (5.9) and (5.10) can be related to the angular distribution of the experimental data of sets 1 and 7, which is mainly in the backward scattering region, where the sensitivity to $\alpha_{E1} - \beta_{M1}$ is higher, as shown in Sec. 5.1.

In summary, also the χ^2 per set analysis let us to conclude once more that there is no clear evidence of outliers that should be excluded from the fit.

5.2.4 Behavior of the minimization function

A further test can be performed by examining the behavior of the minimization function in the parameter space. If some outliers are excluded from a given data set, we would expect that the minimum of the χ^2 function is more pronounced and closer to 1, i.e. the fitted parameters are known with higher precision. In Fig. 5.8 we show the χ^2 function of the test-fit versus the fit parameters α_{E1} and β_{M1} for the FULL data set (with and without rescaling the statistical error by a factor $\sqrt{\chi^2_{set}}$), for the TAPS data set and for the SELECTED data set [20]. In the case of the SELECTED data set, we indeed observe that the minimum value of the reduced χ^2 function is closer to 1, but the shape of the minimization function is the same as in the case of the FULL data set, i.e. the errors on the fitted parameters remain ultimately the same. Also this

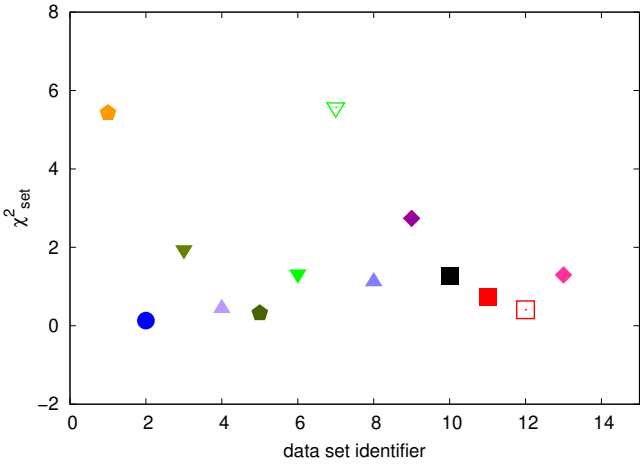

Figure 5.7: χ^2_{set} term for each data subset of the FULL set. The labels of the data sets are described in Table 5.1.

test provides an additional indication of the non-clear presence of outliers, thus convincing us once more that there are no strong enough motivation for the exclusion of some data points from the FULL data set.

5.2.5 Summary of the tests

All the previous consistency tests led us to the conclusion that there are no strong motivations for the exclusion of any data point from the global RCS data set below pion-production threshold, even though we observed significant deviations for a few data points at the backward scattering angles.

From the residual analysis we learn that the FULL and the SELECTED data sets have almost the same statistical significance, thus implying very similar error bars for the fitted parameters. We showed a possible strategy that allows one to deal with some suspicious points, by the use of the $\sqrt{\chi^2_{set}}$; however, we do not recommend to use this technique for a conclusive fit of α_{E1} and β_{M1}. Our choice is to intensively use the new fitting technique, shown in Ch. 4, based on the parametric bootstrap. In the next sections of this chapter, we will discuss all the information that can be inferred by using this technique.

5.3 The extraction of the dipole static scalar polarizabilities

The tests shown in the previous section suggested that the systematic uncertainties are likely to be relevant in the extraction of α_{E1} and β_{M1}. For all the reasons described in Ch. 4, our choice for the data analysis is to use the bootstrap-based fitting technique.

Thus, we fit the static scalar dipole polarizabilities in the framework of

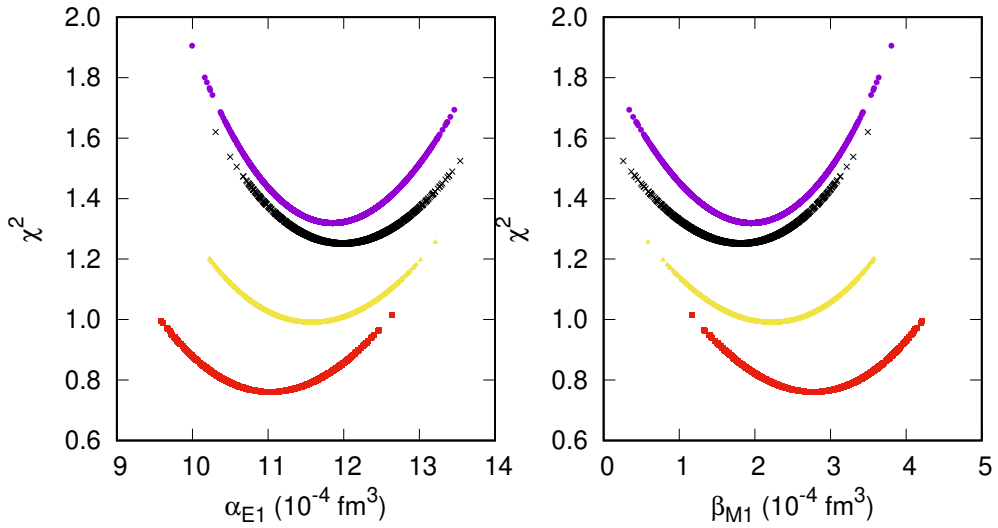

(a) (b)

Figure 5.8: The χ^2 profile as function of α_{E1} (a) and β_{M1} (b). The black curves are the results for the original FULL data set, while the yellow curves correspond to the results for the FULL data set with the $\sqrt{\chi^2_{set}}$ rescaling of the statistical errors. The purple and red curves show, respectively, the results for the TAPS and the SELECTED data set.

subtracted fixed$-t$ DRs, where the static polarizabilities enter through the a_i coefficients defined in Eq. (2.31) as subtraction constants. We apply the bootstrap-based fitting technique described in Ch. 4 under different fitting conditions, switching on/off the systematic errors and using two sets of free parameters: *i)* the scalar dipole polarizabilities, with and without the constraint of the Baldin sum rule for the polarizability sum $\alpha_{E1}+\beta_{M1}$, and *ii)* the scalar dipole polarizabilities constrained by the Baldin sum rule along with the backward spin polarizability γ_π.

Thanks to the bootstrap samplings, we are able to provide realistic probability distributions and p-values for the fitted parameters. The technique described in Ch. 4 is thus performed using $N = 10000$ bootstrap replicas and including the propagation of the statistical uncertainties related to those polarizabilities that are not treated as free parameters in the fit. In particular, we take[2] $\gamma_0 \in \mathcal{G}[-1.01, 0.13^2]$ from Ref. [85, 86], $\gamma_{E1E1} \in \mathcal{G}[-3.5, 1.2^2]$ from Ref. [36] and $\gamma_{M1M1} \in \mathcal{G}[3.16, 0.85^2]$ from Ref. [36]. When keeping fixed the backward spin polarizability, we propagate the error of γ_π using $\gamma_\pi \in \mathcal{G}[8.0, 1.8^2]$ from Ref. [13]. Furthermore, the Baldin sum rule constraint is implemented using $\alpha_{E1}+\beta_{M1} \in \mathcal{G}[13.8, 0.4^2]$ from Refs. [8, 21, 35, 36]. The uncertainties on the fitted α_{E1} and β_{M1} thus automatically include the prop-

[2]The uncertainty value 0.13^2 is the sum of the squares of the statistical and systematic errors.

agation of the errors of the spin polarizabilities and the Baldin sum rule. The statistical and systematic uncertainties of the experimental data are taken into account as described in Sec. 4.4, except for the TAPS data points [35]. As discussed in Ref. [20], they are affected by a 5% point-to-point systematic error, and, accordingly, the statistical error of each point is modified as follows

$$\sigma_{i,TAPS} \to \left[\sigma^2_{i,TAPS} + \left(\frac{5}{100} E_{i,TAPS}\right)^2\right]^{1/2} . \tag{5.11}$$

5.3.1 Results and discussion

As mentioned in Sec. 5.3, we perform the fit of α_{E1} and β_{M1} under different configurations, that are labeled as follows:

* Fit 1: with Baldin sum rule, and systematic errors excluded: $\alpha_{E1} - \beta_{M1}$ as free parameter;
* Fit 1′: like Fit 1, but with systematic errors included;
* Fit 2: without Baldin sum rule, and systematic errors excluded: $\alpha_{E1} + \beta_{M1}$ and $\alpha_{E1} - \beta_{M1}$ as free parameters;
* Fit 2′: like Fit 2, but with systematic errors included;
* Fit 3: with Baldin sum rule, and systematic errors excluded: $\alpha_{E1} - \beta_{M1}$ and γ_π as free parameters;
* Fit 3′: like Fit 3, but with systematic errors included.

We fit both the FULL and the TAPS data sets, in order to analyze the most comprehensive data set (FULL) and the biggest subset (TAPS) in the energy region below the pion-production threshold. Our numerical results are shown in Table 5.2, while the probability distributions for the fitted parameters are given in Figs. 5.9, 5.10 and 5.11.

Even if the best values of α_{E1} and β_{M1} strongly depend on the choice of the data set, they are all consistent within the uncertainties, giving confidence in the stability of our results. Furthermore, the values of α_{E1} and β_{M1} from the Baldin-unconstrained fit are well compatible with the Baldin sum rule value: for instance, in the Fit 2′ condition applied to the FULL data set, the fitting result gives $\alpha_{E1} + \beta_{M1} = 13.40 \pm 1.71$.

As extensively discussed in Ch. 4, the inclusion of systematic errors does not really change the central values of the fitted parameters, but increases their uncertainties. This effect is mostly visible for the TAPS data set, fitted in the Fit 2 and Fit 2′ conditions, while it is reduced for the FULL data set, where the effects of the systematic errors in the different subsets are, at least partially, compensated (see Figs. 5.9-5.11). Apart from the larger errors on the fitted parameters, the most important effect of the inclusion of systematic

errors is the increasing of the p-values. By looking at Table 5.2, we can notice that for the FULL data set the p-values are always increased as soon as the systematic errors are included in the data analysis, while the central values of the $\hat{\chi}^2/dof$ do not change. This feature means that higher values of $\hat{\chi}^2/dof$ are more likely to occur when systematic errors are included in the data analysis, as is clearly visible from the CDFs of $\hat{\chi}^2$ shown in Figs. 5.12 and 5.13. This effect is mostly absent when we fit the TAPS data set by itself: in this case, the systematic errors become a common scale factor for all the data points. As a consequence, the p-values are essentially unaffected while the uncertainties in the fitted parameters become bigger (see Fig. 5.11). Furthermore, we note that under the Fit 1 condition, taking into account only the statistical (Gaussian) errors, the p-value of the fit is about 3%, which is very close to the 1% occurrence probability discussed in Sec. 5.2.2. However, when the systematic errors are included in the fitting procedure (Fit 1′), the statistical significance strongly increases (12%). This indicates that the occurrence probability of the FULL data set is higher, when taking properly into account all the data error sources. In summary, the analysis with and without the systematic errors convinced us once more that the identification of outliers in the FULL data set should not be done on the basis of only statistical errors.

As outlined in Sec. 5.1, the sensitivity of the RCS differential cross section to γ_π is high enough to encourage a fit of the backward spin polarizability as well. In the Fit 3′ condition, we both propagate the uncertainty of the unfitted polarizabilities and include the systematic errors. Our best value for γ_π, once the π^0-pole contribution is summed as $\gamma_\pi^{\rm tot} = \gamma_\pi + \gamma_\pi^{\pi^0-{\rm pole}}$, is in very good agreement with the values extracted within the fixed-t unsubtracted DR analysis [13, 35, 92, 93]:

$$\begin{aligned}
\text{LARA [92]} &: \quad \gamma_\pi^{\rm tot} = -40.9 \pm 0.4 \pm 2.2, \\
\text{SENECA [93]} &: \quad \gamma_\pi^{\rm tot} = -39.1 \pm 1.2 \pm 0.8 \pm 1.5, \\
\text{TAPS [35]} &: \quad \gamma_\pi^{\rm tot} = -35.9 \pm 2.3, \\
\text{Fit 3′(FULL)} &: \quad \gamma_\pi^{\rm tot} = -38.11^{+2.85}_{-2.94}.
\end{aligned} \tag{5.12}$$

Note that the results of Refs. [92, 93] are obtained using data above the pion-production threshold, while the result of Ref. [35] is extracted from the complete TAPS data set, ranging up to photon energies of 165 MeV.

From all the results discussed in this section, and recalling the conclusions on the bootstrap method of Ch. 4, we can conclude that the inclusion of the systematic errors is crucial in the analysis of the RCS data since, at least for the FULL data set, the p-values change significantly (see Fig. 5.12). We want to stress that this behavior can be observed only thanks to the bootstrap method, since it is not possible to compute the correct p-values without resorting to the Monte Carlo replicas, once the systematic errors are included. A more detailed discussion of this feature is addressed in the next section.

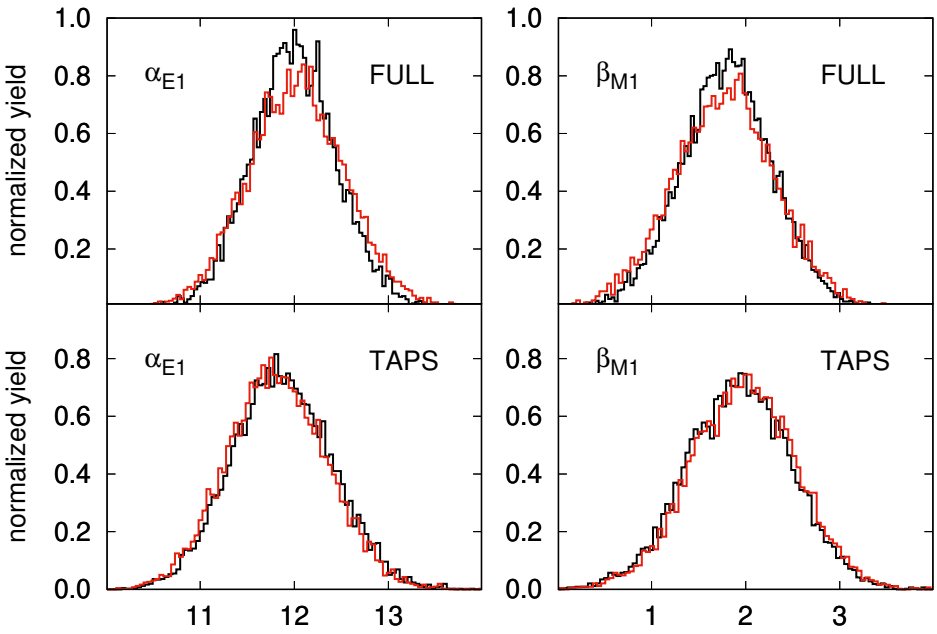

Figure 5.9: Probability distributions of the fitted scalar dipole static polarizabilities α_{E1} (left panels) and β_{M1} (right panels) in the Fit 1 (black curve) and Fit 1′ (red curve) conditions. The results are obtained using the FULL data set (upper panels) and the TAPS data set (lower panels).

5.3.2 Goodness-of-fit distributions

We discuss here the goodness-of-fit distributions related to the Fit 1 and Fit 1′ conditions, as well as the χ^2 decomposition, using the same procedure and notation described in Ch. 4. For the quantities shown in Eq. (4.42), we can evaluate both the expected values (Table 5.3) and the probability distributions (Fig. 5.15). From the numerical values of Table 5.3, we can conclude that: (I) the errors on the fitted parameters cannot be small, due to the relatively big values of the $\mathbb{E}\left[\epsilon'^2\right]$ and $\mathbb{E}\left[D'\right]$ terms, (II) the systematic errors could be relevant in the data analysis, being the $\mathbb{E}\left[\epsilon'^2\right]$ term increased by a factor 5 as soon as the systematic errors are included in the data analysis and (III) the sampling of the unfitted parameters is under control, given that the $\mathbb{E}\left[\Phi\right]$ is small. Furthermore, it we do not propagate the uncertainties of the unfitted polarizabilities, the goodness-of-fit distributions shown in Fig. 5.11 (black curves) get closer to a proper reduced χ^2, thus enlightening once more the role of the sampling for the fixed polarizabilities. All these considerations are in perfect agreement with the discussion of the results in Sec. 5.3.1.

The goodness-of-fit CDFs are shown in Fig. 5.14, and the distortion effect caused by the systematic errors is clearly visible. Unlike the behavior presented by the toy model of Ch. 4, when the systematic errors are excluded, the limit probability distribution for the $\hat{\chi}^2$ variable is not so close to a proper χ^2.

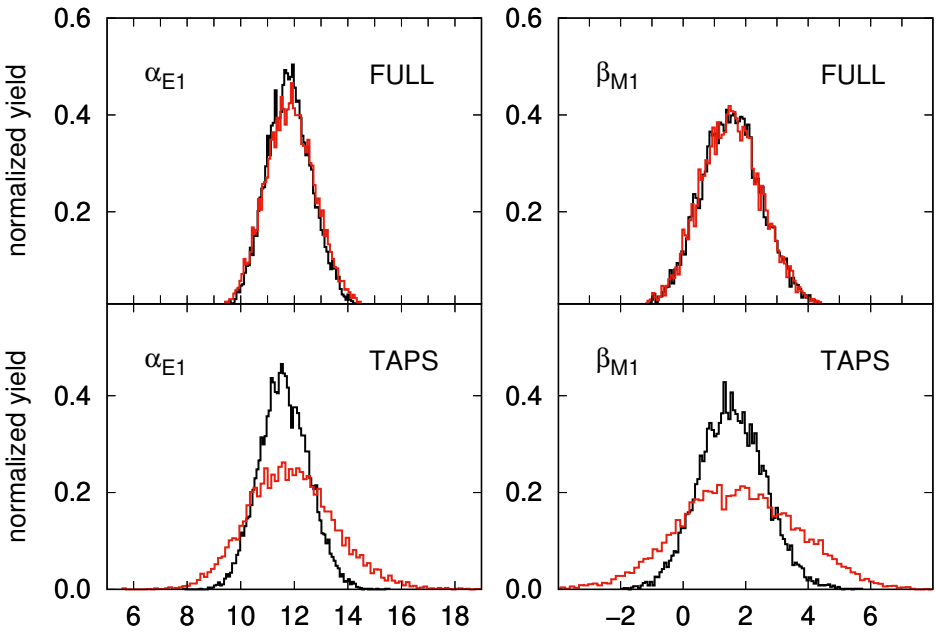

Figure 5.10: Probability distributions of the fitted scalar dipole static polarizabilities α_{E1} (left panels) and β_{M1} (right panels) in the Fit 2 (black curve) and Fit 2′ (red curve) conditions. The results are obtained using the FULL data set (upper panels) and the TAPS data set (lower panels).

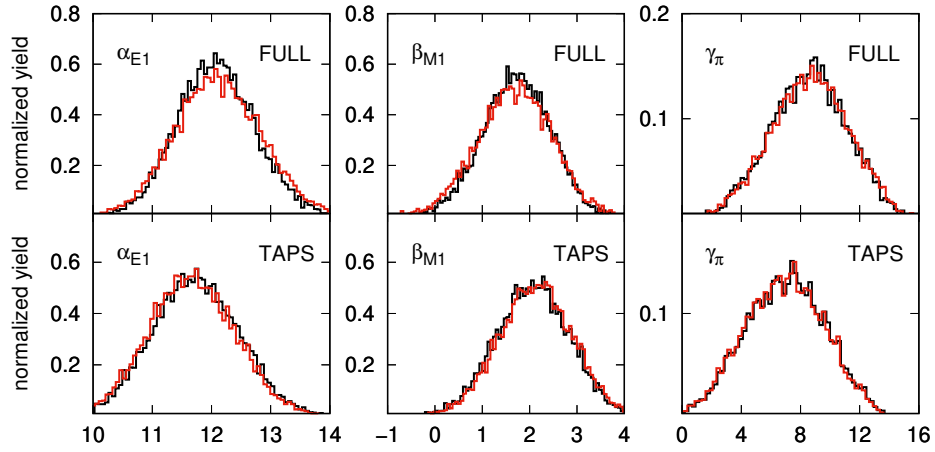

Figure 5.11: Probability distributions of the fitted static polarizabilities α_{E1} (left panels) and β_{M1} (central panels) and the backward spin polarizability γ_π (right panels) in the Fit 3 (black curve) and Fit 3′ (red curve) conditions. The results are obtained using the FULL data set (upper panels) and the TAPS data set (lower panels).

This feature is related to the analytical structure of the fitted model, to the sensitivity on the fitting parameter and to the presence of some offsets in the

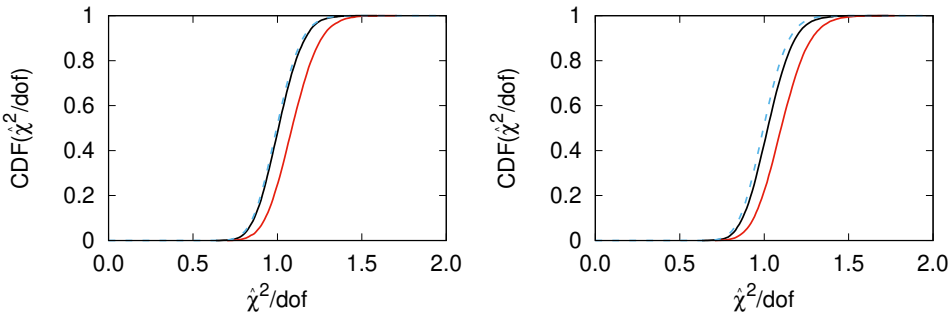

(a) (b)

Figure 5.12: Cumulative distribution functions for the variable $\hat{\chi}^2/dof$ in the case of Fit 1 (left panel, black curve), Fit 1′ (left panel, red curve), Fit 3 (right panel, black curve), Fit 3′ (right panel, red curve), using the FULL data set. The dashed-blue curves are the cumulative distribution functions of a pure reduced χ^2.

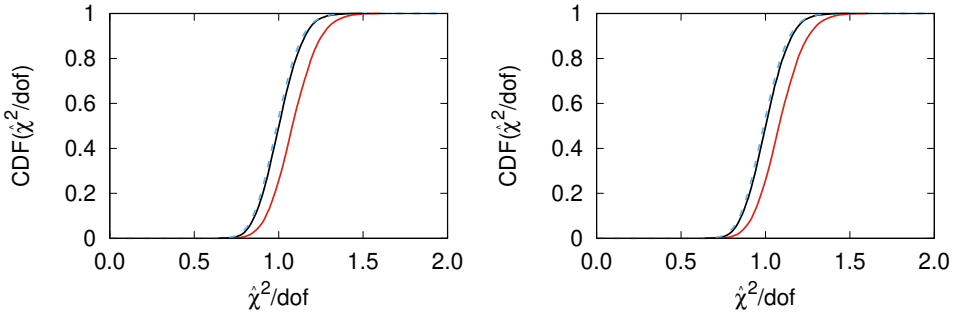

(a) (b)

Figure 5.13: The same as in Fig. 5.12 but neglecting the errors on the polarizability values not treated as free parameters in the fit procedure.

experimental data[3]; it can be quantified also with the $\mathbb{E}\left[\epsilon'^2\right]$ and $\mathbb{E}\left[D'\right]$ terms, which are not so small to be discarded even when only the statistical errors are included in the analysis. This difference with the expected χ^2 distribution is indeed not a surprise, but it is well explained by the decomposition given in Eq. (4.41) and it is clearly visible in Figs. 5.12 and 5.13.

5.3.3 Correlation coefficients among fit parameters

In the bootstrap framework, the correlation coefficients ρ among the fit parameters are obtained from the reconstructed probability distribution in the parameter space. In Table 5.4, we list these coefficients for all the different fitting conditions used in this work. In the Baldin-constrained fits, we do not

[3]This behavior was already observed for the toy model analysis in Ch. 4.

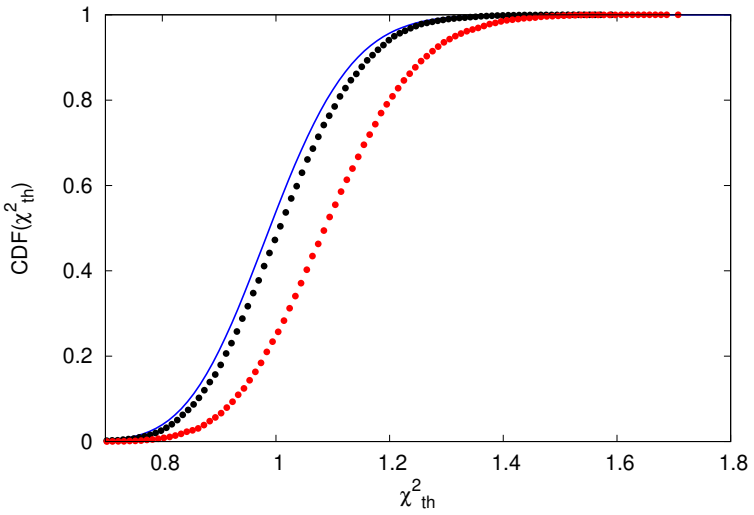

Figure 5.14: CDFs for the χ^2 in the Fit 1 (black points) and Fit 1′ (red points) conditions,compared to the expected error function (solid blue curve).

obtain $\rho_{\alpha_{E1}-\beta_{M1}} = -1$, due to the fact that $\alpha_{E1}+\beta_{M1}$ is not fixed to its central value, but is sampled within its uncertainty with a Gaussian distribution.

5.3.4 The fitted differential cross section

Another advantage provided by our fitting technique, is that we are able to compute the probability distribution of every function of the fitted parameters. If we consider a generic function ϕ of the parameters set $\boldsymbol{\theta}$, we can reconstruct the probability distribution $p(\phi)$ by collecting $\phi_j \equiv \phi(\hat{\boldsymbol{\theta}}_j)$, i.e. the function evaluated on the best values of $\boldsymbol{\theta}$ at every bootstrap cycle, labeled with j. In this way, all the possible correlations among the parameters are automatically taken into account, with no need to use the (approximated) propagation of the uncertainties. If we apply this procedure to the differential cross section, we can compute a realistic n-σ error band. In Fig. 5.16, we show the results for the RCS differential cross section obtained in the Fit 1′ configuration as function of the lab photon energy E_γ and the lab scattering angle θ_{lab}, in comparison with the experimental data of the FULL data set. The orange (gray) bands correspond to the 2-σ (1-σ) error range, computed in the bootstrap framework.

Furthermore, we can cross-check the stability of our fitted results in terms of the experimental observable. This can be done by comparing the differential cross section evaluated at the best values of the fitted parameters ($d\sigma/d\Omega(\hat{\alpha}_{E1}, \hat{\beta}_{M1})$) with the mean value of the differential cross section (for fixed value of angle and energy) as obtained from the reconstructed probability distribution, i.e.

$$\mathbb{E}\left[d\sigma/d\Omega\right] \equiv \mathbb{E}_j\left[d\sigma/d\Omega(\hat{\alpha}_{E1,j}, \hat{\beta}_{M1,j})\right]. \tag{5.13}$$

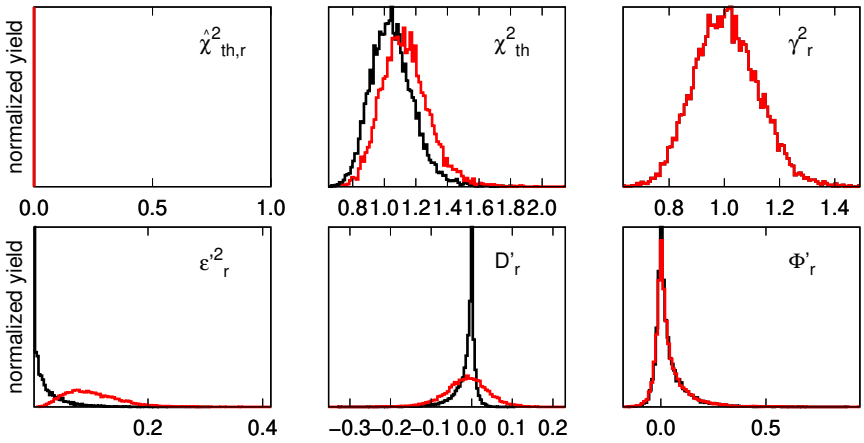

Figure 5.15: Decomposition of the $\hat{\chi}^2_j$ variable for the Fit 1 (black curves) and Fit 1′ (red curves) conditions, applied to the model. Upper panels (from left to right): $\hat{\chi}^2$, χ^2_b and γ^2. Lower panels (from left to right): ϵ^2, the D term and Φ. See Eq. (4.42) for the notation.

If these two values are almost identical (as it happens in our case), the fitted results are stable, and we are formally allowed to compare $(d\sigma/d\Omega(\hat{\alpha}_{E1}, \hat{\beta}_{M1}))$ to the experimental data. As a further cross-check, we show also the differential cross section at forward angle $\theta_{\rm lab} = 0^o$ from our analysis (red band) in comparison with the results obtained with the empirical forward RCS amplitudes of Refs. [88, 94] (blue band). The last ones are evaluated from dispersive sum rules, using as input the total photo-absorption cross sections fitted to the available experimental data. In particular, we used the empirical amplitudes from the fit I of Refs. [88, 94], that are tabulated from $E_\gamma = 50$ MeV and correspond to $\alpha_{E1} + \beta_{M1} = 14.29 \pm 0.27$ and $\gamma_0 = -0.929 \pm 0.105$. The two different curves are almost in perfect agreement, thus confirming again the stability of the fit and the robustness of the adopted dispersive framework.

5.3.5 Comparison with other extractions of the static dipole scalar polarizabilities

We show in Fig. 5.18 the available results for the extraction of the scalar dipole static polarizabilities from RCS at low energies. Numerically, our results read

$$\begin{aligned} &\alpha_{E1} = 12.03^{+0.48}_{-0.53}, \qquad \beta_{M1} = 1.77^{+0.52}_{-0.54}, \\ &\rho_{\alpha_{E1}-\beta_{M1}} = -0.72, \quad \hat{\chi}^2 = 1.25, \quad p\text{-value} = 12\%, \end{aligned} \tag{5.14}$$

and are shown by the red solid curve. The ellipse in the α_{E1} vs β_{M1} plane is obtained by the approximation for the 1-σ range of a 2-dimensional Gaussian, even if we could have obtained the 68% area directly from the bootstrap

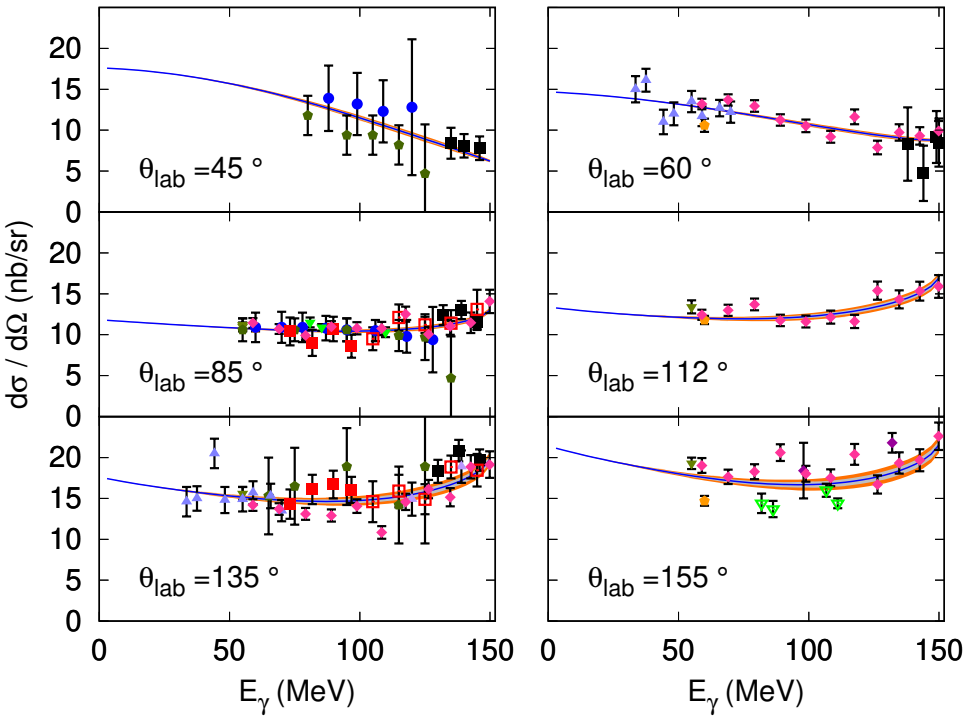

Figure 5.16: The RCS differential cross section (blue curve), evaluated with the scalar dipole polarizabilities of Eq. (5.14) and the experimental values of Ref. [36] for the leading-order spin polarizabilities, as function of the lab photon energy (E_γ) and lab scattering angle ($\theta_{\rm lab}$). The orange (gray) bands correspond to the 2-σ (1-σ) error band obtained in the bootstrap framework (see text for more detail). The experimental data are from the FULL data set, with the labels reported in Table 5.1. In the last figure for $\theta_{\rm lab} = 155°$, we show also the two data points at $\theta_{\rm lab} = 180°$ of Ref. [84] .

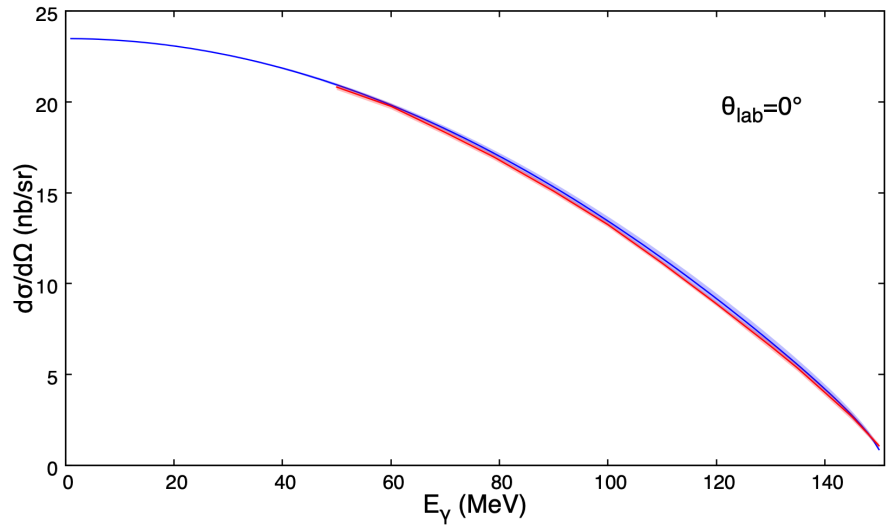

Figure 5.17: Results for the differential cross section at forward angle as function of the photon lab energy, obtained from the empirical amplitudes of Refs. [88, 94] (blue band) and our analysis (red band).

technique[4]. Thus, the red ellipse of Fig. 5.18 is obtained according to

$$\frac{1}{1-\rho^2_{\alpha_{E1}-\beta_{M1}}}\left[u^2_{\alpha_{E1}} - 2\rho_{\alpha_{E1}-\beta_{M1}} u_{\alpha_{E1}} v_{\beta_{M1}} + v^2_{\beta_{M1}}\right] = 1, \tag{5.15}$$

where we defined

$$u_{\alpha_{E1}} = \frac{\alpha_{E1} - \hat{\alpha}_{E1}}{\sigma_{\alpha_{E1}}}, \quad v_{\beta_{M1}} = \frac{\beta_{M1} - \hat{\beta}_{M1}}{\sigma_{\beta_{M1}}}. \tag{5.16}$$

Here, the superscript $\hat{}$ is used for the best value, while $\sigma_{...}$ are the uncertainties of the fitted parameters.

We remark that our results include both the propagation of the statistical errors of the fixed polarizabilities $\alpha_{E1}+\beta_{M1}$, γ_0, γ_π, γ_{E1E1} and γ_{M1M1} and the effects introduced by the systematic errors.

The results in Eq. (5.14) are in very good agreement with the ones obtained using a traditional χ^2 fitting procedure in a fixed-t subtracted DRs framework [17]. In Fig. 5.18, the fits shown by black curves have been obtained within unsubtracted DRs [33–35], while the experimental constraint on the difference $\alpha_{E1} - \beta_{M1}$ from Zieger et al. [84] is shown by the light-green band. Two results from the χPT framework are shown: the BχPT predictions of Ref. [9] (green solid curve) and the 68% ellipse of the Baldin constrained fit of Ref. [8, 37], using the SELECTED data set and the HBχPT framework. These last results are in excellent agreement also with the fit within BχPT of Ref. [38]. Finally, the Baldin sum rule is represented by the orange band,

[4]The two different results are almost identical, but the output from the bootstrap does not have a regular boundary, because of the numerical approximations of the method.

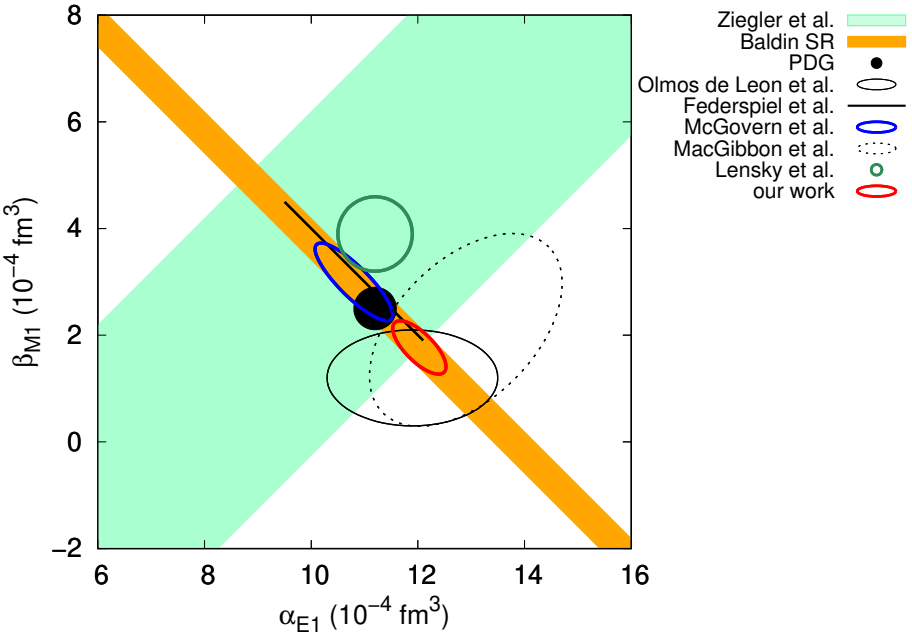

Figure 5.18: Results for α_{E1} vs β_{M1} obtained in different frameworks. The light-green band shows the experimental constraint on the difference $\alpha_{E1} - \beta_{M1}$ from Zieger et al. [84], while the orange band is the average over the available Baldin sum rule evaluations [21]. The experimental extractions are from Federspiel et al. [34] (straight black line), obtained from the fit of $\alpha_{E1} - \beta_{M1}$ constrained by $\alpha_{E1} + \beta_{M1} = 14.0$; MacGibbon et al. [33] (short-dashed black curve, unconstrained fit); TAPS [35] (solid black curve, unconstrained fit). The green solid curve is the BχPT prediction from Ref. [9], while the blue solid curve shows the fit with the constraint $\alpha_{E1} + \beta_{M1} = 13.8 \pm 0.4$ within HBχPT from Refs. [8, 37]. The solid black circle shows the PDG results [89]. The solid red curve is the extraction from this work (Fit 1′), using fixed-t subtracted DRs.

while the latest value from the PDG [89] is shown in a solid black disk and it correspond to[5]

$$\alpha_{E1} = 11.2 \pm 0.4, \quad \beta_{M1} = 2.5 \pm 0.4. \tag{5.17}$$

We note that there is a discrepancy between the values obtained in the framework of effective field theories [8, 9, 20] and the results obtained using DRs, even if they are compatible within the 2σ-range. In order to shed some light on the origin of the difference between the results from the extraction within HBχPT and fixed-t subtracted DRs, we performed some test-fits, in the condition described in Sec. 5.2, using fixed-t subtracted DRs with input from the central values of HBχPT predictions for the spin polarizabilities.

[5]They differ from the 2012 and earlier editions by inclusion of the data fit analysis within HBχPT [8].

The results for the leading-order spin polarizabilities in HBχPT read [8, 37] $\gamma_{E1E1} = -1.1 \pm 1.9$, $\gamma_{M1M1} = 2.2 \pm 0.5(\text{stat}) \pm 0.6$, $\gamma_0 = -2.6 \pm 0.5(\text{stat}) \pm 1.8$, and $\gamma_\pi = 5.6 \pm 0.5(\text{stat}) \pm 1.8$, and are quite different from the experimental values used in our DR analysis. Furthermore, we noticed a different evaluation for the π^0-pole contribution calculated in Ref. [8], which is -45.9 for γ_π. In Table 5.5, we compare the test-fit values for α_{E1} and β_{M1} in the case we use the results of the spin polarizabilities and the π^0pole from the experimental extraction [36] or the corresponding values from HBχPT [8, 37], with the π^0-pole contribution reported in [8] (results in brackets). This analysis has been performed for both the FULL and SELECTED data sets, in order to investigate the dependence of the results not only on the values of the spin polarizabilities, but also on the choice of the data set. If we focus on the central values of β_{M1}, we notice that the different input for the spin polarizabilities affects the results by 20-30%, while the choice of the data set leads to a 40-50% increase. It is certainly too simplistic to estimate the model dependence of the two extractions with the different values of the spin polarizabilities. However, in the energy range below pion production threshold, this gives a rather good indication of the main effects due to the model dependence.

5.4 Estimate of the real bias

We want also to discuss the possible estimate of the experimental bias, following the procedure described in Sec. 4.7. In Figs. 5.19 and 5.20 we show the results applied to the RCS data base, under the Fit 1 condition in the bootstrap framework[6]. From this test we can notice that the sets with a small number of experimental points show a flat χ^2 profile, thus signaling that the evaluation of the systematic error would not have a strong influence on the final-fit result. Furthermore, the estimated bias lies perfectly in the published range for the most of subsets, thus confirming the validity of the method.

Once the $\tilde{\delta}_k$ parameters are determined for all the subsets (see Table 5.6), we can rescale all the experimental points according to

$$E_i' = (1 + \tilde{\delta_k})E_i, \quad \sigma_i' = (1 + \tilde{\delta_k})\sigma_i, \tag{5.18}$$

where both the measured values and their statistical fluctuations are rescaled by the same quantity. We can now perform a traditional χ^2 minimization (test-fit condition), thus obtaining

$$\alpha_{E1} = 12.08 \pm 0.24, \quad \beta_{M1} = 1.69 \pm 0.24, \quad \hat{\chi}^2 \sim 0.9, \tag{5.19}$$

which are in perfect agreement with the values that can be obtained from a fit in which the systematic errors are not included, as shown in Eq. (5.5):

$$\alpha_{E1} = 11.99 \pm 0.31, \quad \beta_{M1} = 1.81 \pm 0.31, \quad \hat{\chi}^2 \sim 1.25. \tag{5.20}$$

[6]In this framework, the values of the unfitted polarizabilities are taken as described in Sec. 5.2.

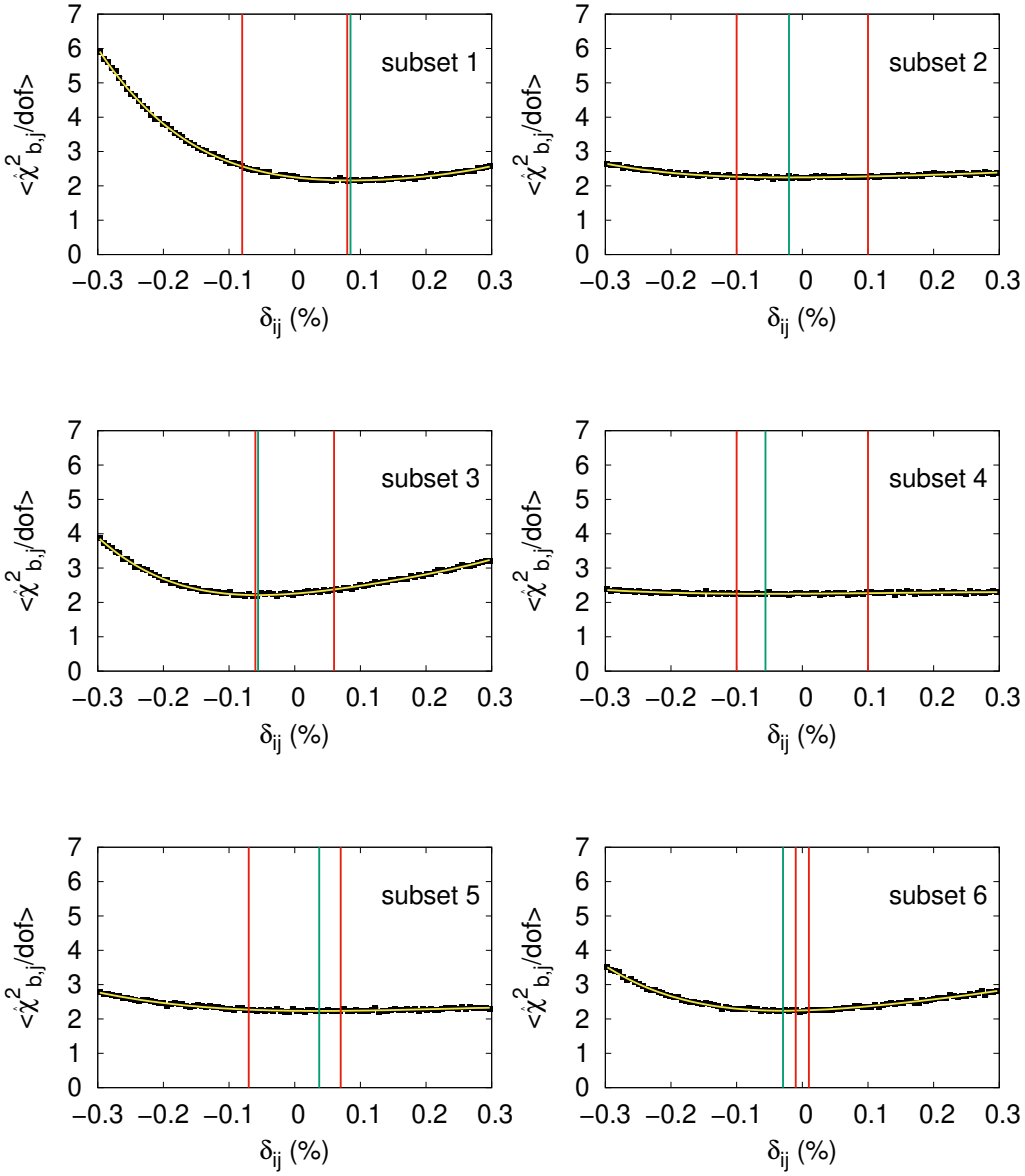

Figure 5.19: Estimate of $\hat{\delta_k}$ for the data subsets from 1 to 6: black points are the results of the preliminary bootstrap cycle, the yellow curve is the 4^{th}-order polynomial fit described in Sec. 4.7.1, the red lines are at the fixed values $\pm\Delta_k$ and the green line is fixed at $\hat{\delta_k}$.

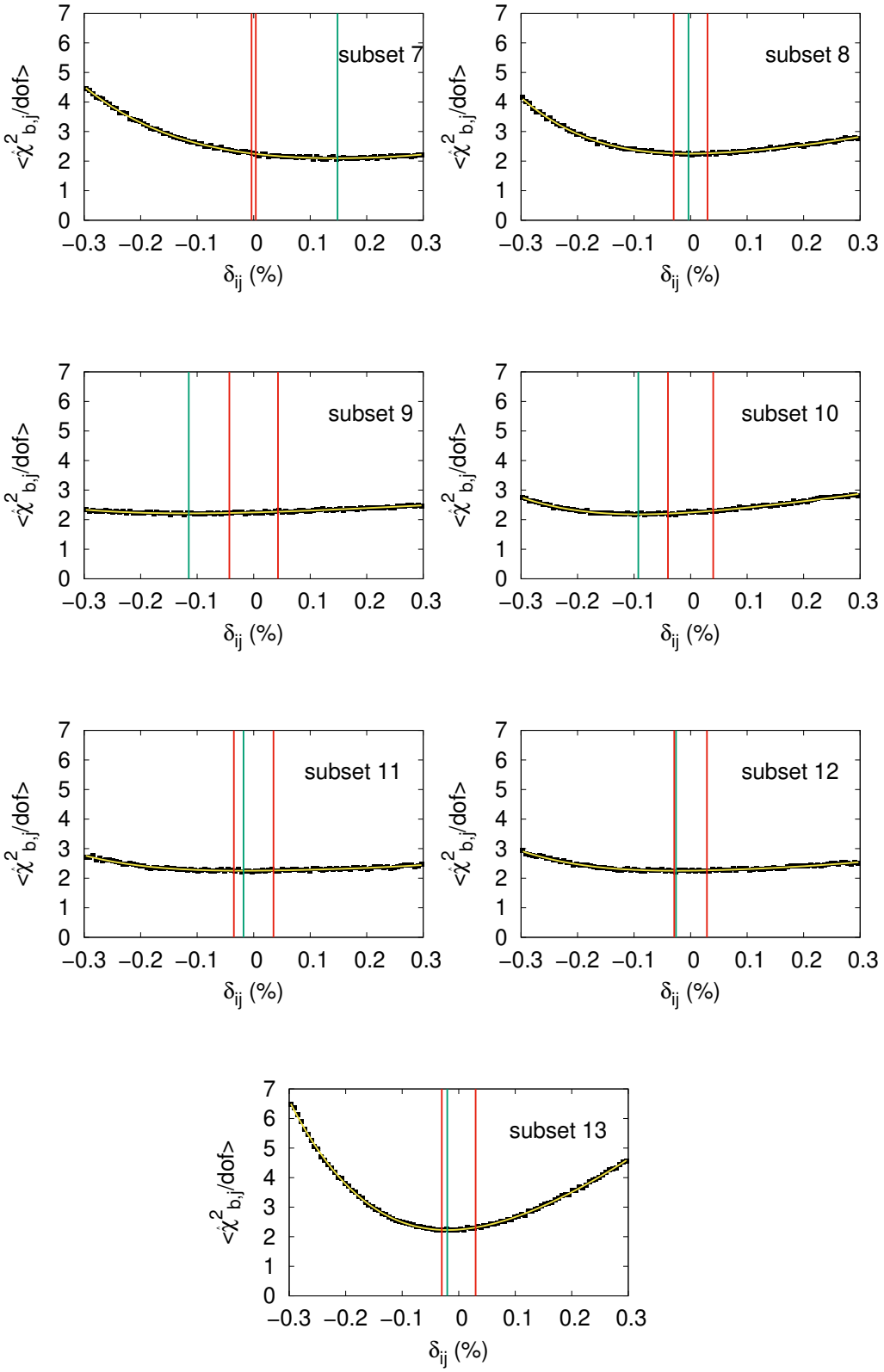

Figure 5.20: As in Fig. 5.19, but referred to the data from subsets 7-13.

If, on the other hand, we minimize the χ^2_{mod} given in Eq. (4.4), we obtain

$$\alpha_{E1} = 11.94 \pm 0.40, \quad \beta_{M1} = 1.86 \pm 0.40, \quad \hat{\chi}^2 \sim 1.26, \tag{5.21}$$

which are, again, almost identical to the results of Eq. (5.5), where no systematic errors are included.

The normalization factors[7] f_k can be compared with the estimate of the systematic errors obtained in the bootstrap framework, as shown in Table 5.6. As noticed in Sec. 4.7.1, the estimate of the realistic systematic errors is more reliable due to the high number of data subsets. The values obtained with the two methods are, almost in all cases, in very good agreement. Another possibility is to introduce the rescaled bootstrap sampling, i.e.

$$\mathcal{S}_{ij} = (1 + \tilde{\delta}_k)(E_i + \gamma_{ij}\sigma_i), \tag{5.22}$$

where the only random number are the Gaussian variables γ_{ij}, since the offsets are not known and can be fixed once for all before performing the global fit. The results obtained in this way are identical to the ones given in Eq. (5.19), as expected.

It is noteworthy to compare the statistical significance of the results given in Eq. (5.19) with the ones given in Eq. (5.5): the former ones have a p-value $\simeq 20\%$, while the latter ones have a p-value $\simeq 2\%$. As already discussed in this work, the inclusion of the systematic errors is crucial in the determination of the correct statistical significance.

5.5 The data above the pion-production threshold

We restricted the analysis of the unpolarized differential cross section to the energy region below the pion production threshold, where the A_i amplitudes are real. However, the fixed-t subtracted DRs can be successfully applied up to $E_\gamma \simeq 300$ MeV, as pointed out in Ref. [17], thus suggesting us to include also the experimental data collected for 150 MeV $\leq E_\gamma \leq 300$ MeV in the fit of α_{E1} and β_{M1}. As a first step, we would like to compare the existing data with the predictions given by DRs, using as inputs the values quoted in Ref. [89] for α_{E1} and β_{M1} and we fix the spin polarizabilities to the experimental extractions quoted in Sec. 5.3. The results of this comparison is shown in Figs. 5.21 and 5.22, from which we can see that the energy behavior of the experimental differential cross section is well reproduced by the theoretical curves. On this basis, we can perform a test-fit of $\alpha_{E1} - \beta_{M1}$, using the traditional χ^2

[7] We recall that, in the χ^2_{mod} framework, the normalization factors are free parameters and their values, together with their uncertainties, are related to the estimate of the realistic systematic error for each subset.

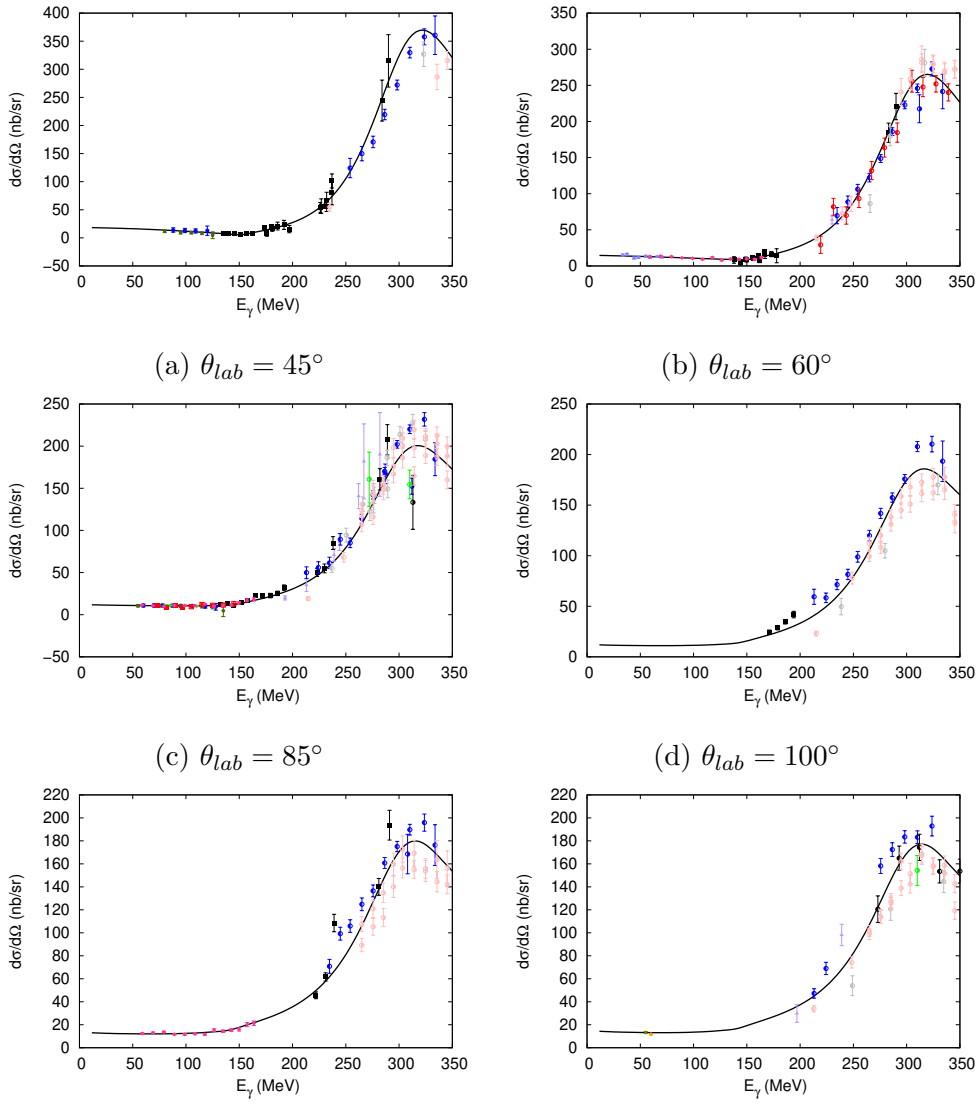

(a) $\theta_{lab} = 45°$ (b) $\theta_{lab} = 60°$

(c) $\theta_{lab} = 85°$ (d) $\theta_{lab} = 100°$

(e) $\theta_{lab} = 110°$ (f) $\theta_{lab} = 120°$

Figure 5.21: The RCS differential cross section (solid black curve), evaluated with the scalar dipole polarizabilities of Ref. [89] and the experimental values of Ref. [36] for the leading-order spin polarizabilities, as function of the lab photon energy (E_γ) and lab scattering angle ($\theta_{\rm lab}$). The experimental data are labeled according to Table 5.1 and Table 5.7.

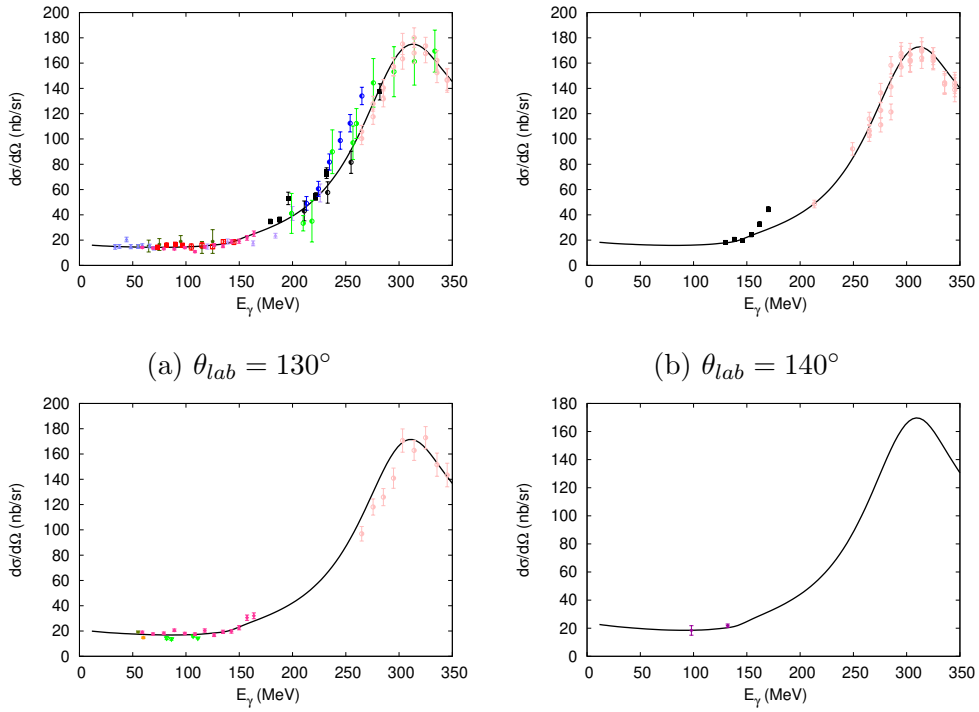

(a) $\theta_{lab} = 130°$ (b) $\theta_{lab} = 140°$

(c) $\theta_{lab} = 150°$ (d) $\theta_{lab} = 180°$

Figure 5.22: The RCS differential cross section (solid black curve), evaluated with the scalar dipole polarizabilities of Ref. [89] and the experimental values of Ref. [36] for the leading-order spin polarizabilities, as function of the lab photon energy (E_γ) and lab scattering angle ($\theta_{\rm lab}$). The experimental data are labeled according to Table 5.1 and Table 5.7.

minimization and not including the systematic errors in the analysis. Our numerical values are

$$\alpha_{E1} = 11.01 \pm 0.24, \quad \beta_{M1} = 2.80 \pm 0.24, \quad \hat{\chi}^2 \sim 3.3, \tag{5.23}$$

which are quite different from the ones shown in Eq. (5.20). However, the high value of the reduced $\hat{\chi}^2$ suggest that a very low statistical significance can be assigned to the fit result. Furthermore, the uncertainties of the fitted polarizabilities in Eqs. (5.20) and (5.23) are almost of the same size, thus suggesting that the accuracy in the extraction of α_{E1} and β_{M1} does not improve. As a

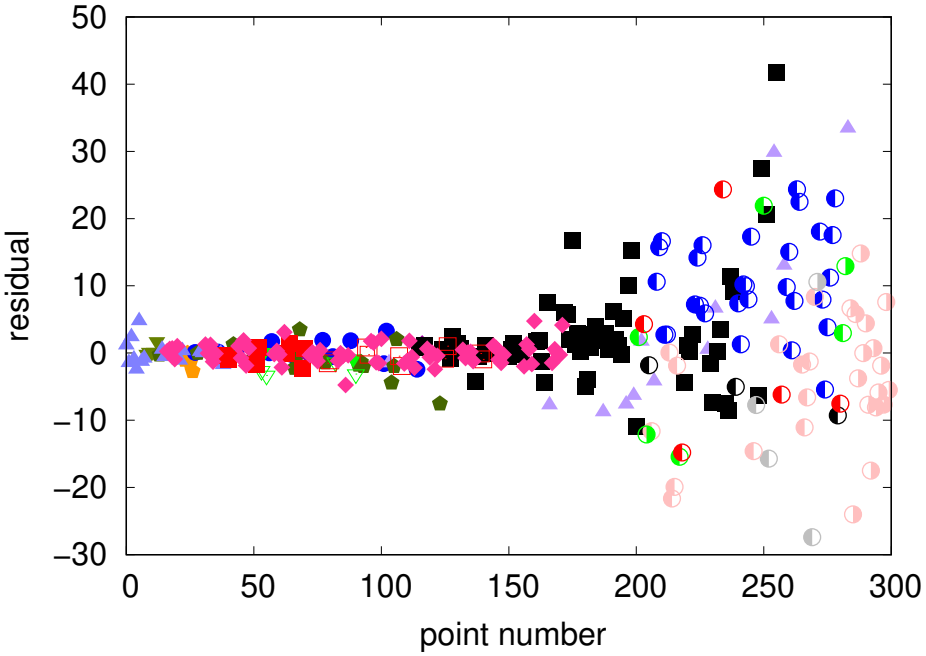

Figure 5.23: Residues obtained with the values of Eq. (5.23) as function of the photon energy in the lab frame. The colors and the type of each point follows the same nomenclature as in Fig. 5.21.

consistency-test on the experimental data above the pion-production threshold, we can compute the residues evaluated with the best-fit values of Eq. (5.23) and plot them as a function of E_γ. The results are shown in Fig. 5.23, where we can notice that, as soon as we cross the pion-production threshold, the statistical fluctuations strongly increase, suggesting some inconsistency of the data-base. A further cross-check can be performed on the χ^2 value, using a variant of the Jackknife sampling described in Sec. 5.2.1. Given a data set $D = \{d_i\}, i = 1, \ldots, n$, composed by n points, we can define n data subsets by adding one datum at a time, i.e. $D_k = \{d_j\}$, where $j = 1, \ldots, k$ and $k = 1, \ldots n$, for increasing values of energy. We then apply a test-fit to every D_k data set and look at the reduced χ^2 as function of the energy E_γ: the results are shown in Fig. 5.24. We can notice that, increasing the number of data points to

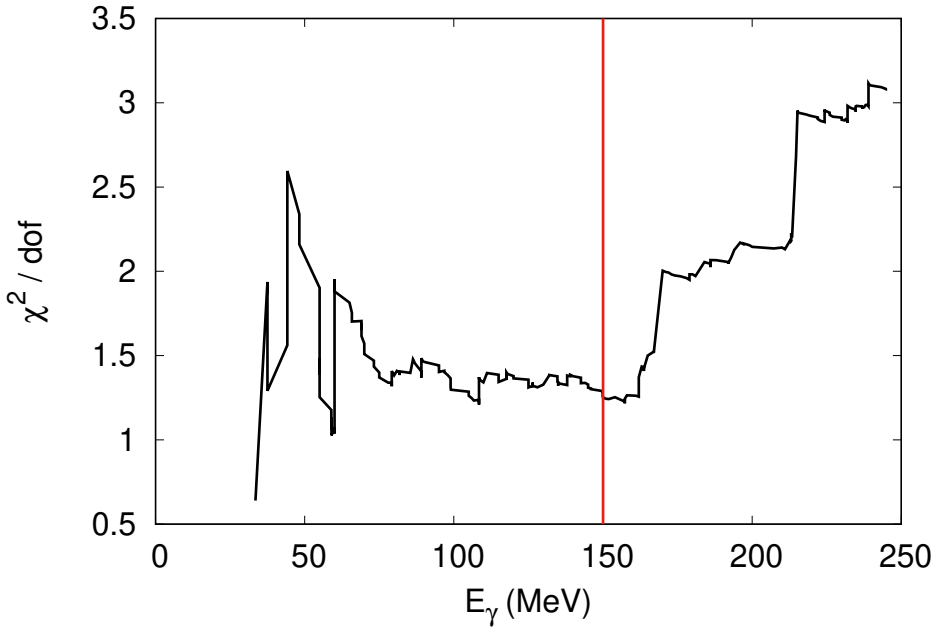

Figure 5.24: Reduced χ^2 (solid black curve) obtained from the fit of all the D_k data sets as function of the photon energy in the lab frame. The vertical red line is the pion-production threshold.

be fitted, the χ^2 tends to converge toward a stable number (1.25, as given in Eq. (5.5)), which is reached at the pion-production threshold. As soon as the threshold is crossed, the χ^2 value tends to increase and do not seem to reach a plateau for higher energy.

According to the results shown in this section, we have decided not to include the data above the pion-production threshold in the extraction of the scalar dipole polarizabilities α_{E1} and β_{M1}.

FULL data set				
fit conditions	α_{E1}	β_{M1}	γ_π	$\hat{\chi}^2/dof$ (p-value)
Fit 1	$12.00^{+0.41}_{-0.47}$	$1.80^{+0.46}_{-0.48}$	fixed	1.25 (3%)
Fit 1′	$12.03^{+0.48}_{-0.54}$	$1.77^{+0.52}_{-0.54}$	fixed	1.25 (12%)
Fit 2	$11.82^{+0.81}_{-0.91}$	$1.54^{+0.95}_{-1.00}$	fixed	1.26 (4%)
Fit 2′	$11.86^{+0.93}_{-0.99}$	$1.54^{+0.95}_{-1.05}$	fixed	1.26 (13%)
Fit 3	$12.08^{+0.61}_{-0.64}$	$1.71^{+0.70}_{-0.75}$	$8.52^{+2.72}_{-2.93}$	1.26 (4%)
Fit 3′	$12.12^{+0.68}_{-0.77}$	$1.68^{+0.77}_{-0.79}$	$8.59^{+2.85}_{-2.94}$	1.26 (13%)
TAPS data set				
fit conditions	α_{E1}	β_{M1}	γ_π	$\hat{\chi}^2/dof$ (p-value)
Fit 1	$11.87^{+0.50}_{-0.54}$	$1.93^{+0.52}_{-0.56}$	fixed	1.32 (7%)
Fit 1′	$11.82^{+0.50}_{-0.55}$	$1.98^{+0.52}_{-0.56}$	fixed	1.32 (7%)
Fit 2	$11.62^{+0.86}_{-0.96}$	$1.57^{+1.01}_{-1.04}$	fixed	1.34 (8%)
Fit 2′	$11.89^{+1.50}_{-1.67}$	$1.76^{+1.83}_{-2.00}$	fixed	1.34 (8%)
Fit 3	$11.74^{+0.68}_{-0.78}$	$2.06^{+0.77}_{-0.84}$	$6.95^{+2.81}_{-3.09}$	1.34 (9%)
Fit 3′	$11.67^{+0.68}_{-0.77}$	$2.12^{+0.76}_{-0.78}$	$6.85^{+2.83}_{-3.07}$	1.34 (9%)

Table 5.2: Results of the fits for the static polarizabilities α_{E1}, β_{M1} and γ_π using the FULL and TAPS data sets and different fit conditions, together with the corresponding $\hat{\chi}^2/dof$ and p-values.

fitting conditions	Fit 1	Fit 1′
$\mathbb{E}\left[\hat{\chi}^2\right]$	10^{-6}	10^{-6}
$\mathbb{E}\left[\gamma^2\right]$	1.01 ± 0.11	1.01 ± 0.11
$\mathbb{E}\left[\epsilon'^2\right]$	$(2.09 \pm 2.97) \cdot 10^{-2}$	$(10.3 \pm 4.8) \cdot 10^{-2}$
$\mathbb{E}\left[D'\right]$	$(-1.30 \pm 2.75) \cdot 10^{-2}$	$(-1.35 \pm 5.36) \cdot 10^{-2}$
$\mathbb{E}\left[\Phi\right]$	$(3.62 \pm 7.66) \cdot 10^{-2}$	$(3.62 \pm 7.86) \cdot 10^{-2}$
Symbol	●	●

Table 5.3: Decomposition of the bootstrap χ^2, with the notation of Eq. (4.42), referred to the analysis of RCS proton data [72].

FULL data set			
fit conditions	$\rho_{\alpha_{E1}-\beta_{M1}}$	$\rho_{\alpha_{E1}-\gamma_\pi}$	$\rho_{\beta_{M1}-\gamma_\pi}$
Fit1	-0.64	$--$	$--$
Fit $1'$	-0.72	$--$	$--$
Fit 2	0.59	$--$	$--$
Fit $2'$	0.52	$--$	$--$
Fit 3	-0.84	0.86	-0.88
Fit $3'$	-0.87	0.84	-0.86
TAPS data set			
fit conditions	$\rho_{\alpha_{E1}-\beta_{M1}}$	$\rho_{\alpha_{E1}-\gamma_\pi}$	$\rho_{\beta_{M1}-\gamma_\pi}$
Fit 1	-0.74	$--$	$--$
Fit $1'$	-0.74	$--$	$--$
Fit 2	0.47	$--$	$--$
Fit $2'$	0.23	$--$	$--$
Fit 3	-0.85	0.82	-0.84
Fit $3'$	-0.86	0.81	-0.83

Table 5.4: Correlation coefficients ρ among the fit parameters in the different fitting conditions described in Sec. 5.3.1. The columns 2-4 correspond, from the left to the right, to the correlation coefficients between α_{E1} and β_{M1}, α_{E1} and γ_π, β_{M1} and γ_π.

	FULL		SELECTED	
α_{E1}	11.99 ± 0.31	(11.47 ± 0.30)	11.02 ± 0.33	(10.46 ± 0.32)
β_{M1}	1.81 ± 0.31	(2.33 ± 0.30)	2.78 ± 0.33	(3.34 ± 0.32)

Table 5.5: Results for α_{E1} and β_{M1} from the test-fit of the FULL and the SELECTED data set, and taking different values for the leading-order spin polarizabilities: the experimental results from Ref. [36] and the values predicted in HBχPT [20] (results in brackets).

k	$f_k - 1$ (%)	$\tilde{\delta}_k$ (%)	k	$f_k - 1$ (%)	$\tilde{\delta}_k$ (%)
1	7.5 ± 2.3	8.6	8	0.0 ± 1.9	-0.4
2	-0.6 ± 4.8	-2.0	9	-4.7 ± 3.6	-11.6
3	-4.5 ± 2.1	-5.6	10	-5.7 ± 2.5	-9.2
4	-2.5 ± 6.5	-5.6	11	-0.4 ± 2.8	-1.7
5	3.0 ± 4.3	3.7	12	-0.7 ± 2.4	-2.6
6	-0.3 ± 0.9	-2.9	13	-0.1 ± 1.3	-2.1
7	7.5 ± 2.4	14.8			

Table 5.6: Estimate of the realistic systematic errors in the RCS analysis for each data subset (labeled with k): results from the χ^2_{mod} method $(1 - f_k)$ compared with the results of the bootstrap framework $(\tilde{\delta}_k)$.

set label	Ref.	first author	points number	θ_{lab} (°)	E_γ (MeV)	symbol
4	[81]	Bernardini	15	$\simeq 60 - 135$	$\simeq 160 - 280$	▲
10	[80]	Hallin	64	$25 - 135$	$150 - 290$	■
13	[35]	Olmos de Leon	10	$60 - 155$	$155, 165$	◆
14	[95]	DeWire	77	$50 - 130$	$210 - 335$	◐
15	[96, 97]	Nagashima	8	130	$200 - 335$	◐
16	[98, 99]	Baranov	8	$120 - 130$	$210 - 350$	◐
17	[96]	Gray	12	$60 - 65$	$205 - 340$	◐
18	[97]	Genzel	14	$45 - 120$	$235 - 335$	◐
19	[100, 101]	Peise	12	$45 - 140$	$210, 150$	◐
20	[101, 102]	Molinari	4	$60 - 110$	$280, 310$	◑
21	[103]	Wissmann	5	$75 - 135$	$210 - 310$	◑
22	[92, 104]	Wolf	2	75	$310, 350$	◑
23	[105]	Blanpied	9	~ 75	$250 - 350$	◑
24	[93]	Camen	182	$50 - 150$	$265 - 345$	◑

Table 5.7: Angular and energy coverage of the available experimental data on unpolarized cross section for proton RCS in the energy region above the pion-production threshold.

Chapter 6

Scalar dipole dynamical polarizabilities from proton real Compton scattering data

In this chapter, we show the results of the extraction of the scalar dipole dynamical polarizabilities (DDPs) of the proton, i.e. $\alpha_{E1}(\omega)$ and $\beta_{M1}(\omega)$, from the available RCS data below the pion-production threshold. We show some preliminary tests, which can be used for a critical analysis of the sensitivity of the differential cross section to the DDPs.

The global results of the fit are obtained from the bootstrap-based fitting technique shown in Ch. 4, within the theoretical framework of the fixed-t sDR framework described in Ch. 3. This chapter is mainly based on our work [59], which represents the first extraction of the DDPs from the proton RCS data.

6.1 Parametrization of the scalar dipole dynamical polarizabilities

In Sec. 2.3.2 we presented the multipole expansion of the RCS amplitudes. The sums performed over the angular momentum l given in Eq. (2.37) are supposed, in principle, to go until infinity. However, they have in practice to be truncated at some finite value l_{max}. As already stated, the convergence for the multipole expansion is rather fast in the energy range below pion-production threshold, and it is basically reached for $l_{max} = 3$, as shown in Fig. 6.1. It is also true that the main contribution is given by the $l = 1$ terms, which are the ones that can be related to the DDPs through Eq. (2.39). On the other hand, the sensitivity to the higher angular momentum multipoles is suppressed. This makes us confident that it is possible to extract the scalar DDPs $\alpha_{E1}(\omega)$ and $\beta_{M1}(\omega)$ from the experimental data below the pion-production threshold, by assuming that the contribution from higher multipoles can be calculated within sDRs

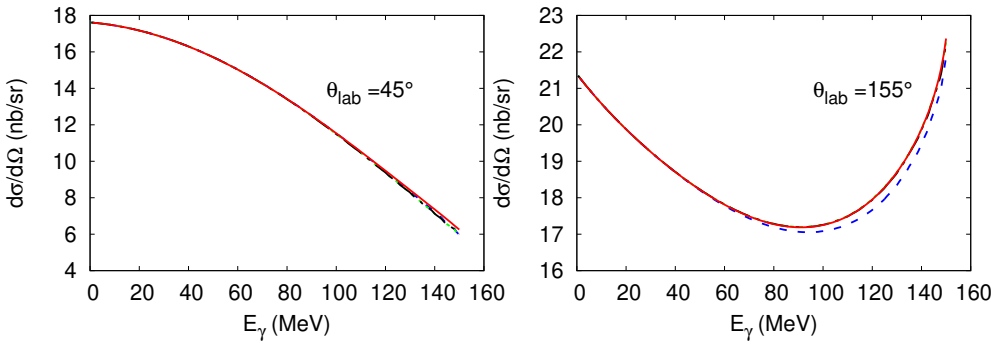

(a) (b)

Figure 6.1: Differential cross section as function of the photon lab energy. Multipole expansion for $l_{max} = 1$ (dashed blue curve), $l_{max} = 2$ (dotted green curve) and $l_{max} = 3$ (dashed-dotted black curve) are compared to the sDRs calculation (solid red curve), with the same input values for the static polarizabilities. The results are shown for $\theta_{lab} = 45°$ (left panel) and for $\theta_{lab} = 155°$ (right panel).

with a minimum of model dependence.

In Ch. 2, we have derived the LEX of the DDPs, corresponding to expressing the DDPs as polynomials of the form $\sum_{k=0}^{k_{max}} p_k \omega^k$, where the p_k coefficients are combinations of the static polarizabilities. The results in Eqs. (2.43) and (2.44) can be conveniently rewritten as

$$
\begin{aligned}
\alpha_{E1}^{\mathrm{LEX}}(\omega) &= \alpha_{E1} + \frac{\beta_{M1}}{M_N}\omega + \left(\alpha_{E1,\nu} + \frac{5\alpha_{E1} - 2\beta_{M1}}{8M_N^2}\right)\omega^2 \\
&+ \left(\frac{8\alpha_{E1,\nu} + \alpha_{E2} + 12\beta_{M1,\nu}}{8M_N} + \frac{\gamma_{M1E2} - \gamma_{M1M1}}{8M_N^2} + \frac{\beta_{M1} - 2\alpha_{E1}}{8M_N^3}\right)\omega^3 \\
&+ \Big[\alpha_4^{\mathrm{L}} + \frac{1}{480M_N^4}(-72\alpha_{E1} - 57\beta_{M1} + 6M_N(25\gamma_{E1E1} - 25\gamma_{E1M2} \\
&+ 39(\gamma_{M1E2} - \gamma_{M1M1})) + M_N^2(1248\alpha_{E1,\nu} + 95\alpha_{E2} + 540\beta_{M1,\nu} + 26\beta_{M2}) \\
&- 12M_N^3(15\gamma_{E1E1,\nu} - 15\gamma_{E1M2,\nu} - 69\gamma_{E2E2} + 12\gamma_{E2M3} + 25\gamma_{M1E2,\nu} \\
&- 25\gamma_{M1M1,\nu} - 12\gamma_{M2E3} + 51\gamma_{M2M2}))\Big]\omega^4 \\
&+ \Big[\alpha_5^{\mathrm{L}} + \frac{1}{2400M_N^5}(15\alpha_{E1} + 5M_N^2(612\alpha_{E1,\nu} + 38\alpha_{E2} + 1008\beta_{M1,\nu} + 89\beta_{M2}) \\
&- 210\beta_{M1} + 15M_N(-46\gamma_{E1E1} + 46\gamma_{E1M2} + 33(\gamma_{M1M1} - \gamma_{M1E2})) \\
&+ 12M_N^3(55\gamma_{E1E1,\nu} - 55\gamma_{E1M2,\nu} - 6(35\gamma_{E2E2} - 22\gamma_{E2M3} + 5\gamma_{M1E2,\nu} \\
&- 5\gamma_{M1M1,\nu} + 38\gamma_{M2E3}) + 555\gamma_{M2M2}))\Big]\omega^5, \qquad (6.1)
\end{aligned}
$$

$$
\beta_{M1}^{\mathrm{LEX}}(\omega) = \beta_{M1} + \frac{\alpha_{E1}}{M_N}\omega + \left(\frac{5\beta_{M1} - 2\alpha_{E1}}{8M_N^2} + \beta_{M1,\nu}\right)\omega^2
$$

$$
\begin{aligned}
&+ \left(\frac{\alpha_{E1}-2\beta_{M1}}{8M_N^3}+\frac{8\beta_{M1,\nu}+\beta_{M2}+12\alpha_{E1,\nu}}{8M_N}+\frac{\gamma_{E1M2}-\gamma_{E1E1}}{8M_N^2}\right)\omega^3\\
&+ \Big[\beta_4^{\mathrm{L}}+\frac{1}{480M_N^4}(-72\beta_{M1}+M_N^2(1248\beta_{M1,\nu}+95\beta_{M2}+540\alpha_{E1,\nu}+26\alpha_{E2})\\
&- 57\alpha_{E1}+6M_N(25\gamma_{M1M1}-25\gamma_{M1E2}+39(\gamma_{E1M2}-\gamma_{E1E1}))\\
&- 12M_N^3(15\gamma_{M1M1,\nu}-15\gamma_{M1E2,\nu}-69\gamma_{M2M2}+12\gamma_{M2E3}+25\gamma_{E1M2n}\\
&- 25\gamma_{E1E1,\nu}-12\gamma_{E2M3}+51\gamma_{E2E2}))\Big]\omega^4\\
&+ \Big[\beta_5^{\mathrm{L}}+\frac{1}{2400M_N^5}(15\beta_{M1}+5M_N^2(612\beta_{M1,\nu}+38\beta_{M2}+1008\alpha_{E1,\nu}+89\alpha_{E2})\\
&- 210\alpha_{E1}+15M_N(-46\gamma_{M1M1}+46\gamma_{M1E2}+33(\gamma_{E1E1}-\gamma_{E1M2}))\\
&+ 12M_N^3(55\gamma_{M1M1,\nu}-55\gamma_{M1E2,\nu}-6(35\gamma_{M2M2}-22\gamma_{M2E3}+5\gamma_{E1M2,\nu}\\
&- 5\gamma_{E1E1,\nu}+38\gamma_{E2M3})+555\gamma_{E2E2}))\Big]\omega^5, \qquad (6.2)
\end{aligned}
$$

where we follow the notation used in Ref. [59].

In Eqs. (6.1) and (6.2), the terms with even power of ω contain both retardation effects and recoil terms. The terms with odd powers of ω are recoil contributions, which, in addition to the contributions from the static polarizabilities of lower orders, can include terms with the static scalar and spin-dependent polarizabilities of higher multipolarity.

In particular, the first dispersive contributions enter at $\mathcal{O}(\omega^2)$ and correspond to the static polarizabilities $\alpha_{E1,\nu}$ and $\beta_{M1,\nu}$. The recoil terms at $\mathcal{O}(\omega^3)$ are given in terms of the static dipole scalar and spin polarizabilities, the fourth-order dipole scalar polarizabilities $\alpha_{E1,\nu}$ and $\beta_{M1,\nu}$ and the quadrupole scalar polarizabilities α_{E2} and β_{M2}. In particular, $\alpha_{E1,\nu}$, $\beta_{M1,\nu}$ and the quadrupole polarizabilities enter as recoil terms with the same suppression factor in $1/M$. The static spin dipole polarizabilities enter with a coefficient in $1/M^2$ and the static scalar dipole polarizabilities enter with a factor in $1/M^3$.

At $\mathcal{O}(\omega^4)$, the recoil terms contain different combinations of the same polarizabilities entering at $\mathcal{O}(\omega^3)$, weighed with an additional power in $1/M$. Furthermore, they involve the higher-order spin polarizabilities defined in Ref. [15], with a coefficient in $1/M$, and the dispersive coefficients α_4^{L} and β_4^{L} corresponding to sixth-order scalar polarizabilities, which have never been defined in literature. Following Ref. [12], we can write them as combinations of the second-order derivatives of the non-Born contribution to the Lorentz invariant amplitudes A_i, i.e.

$$
a_{i,\nu\nu}=\left.\frac{\partial^2 A_i^{\mathrm{NB}}}{\partial\nu^4}\right|_{\nu^2=t=0},\quad a_{i,\nu t}=\left.\frac{\partial^2 A_i^{\mathrm{NB}}}{\partial\nu^2\partial t}\right|_{\nu^2=t=0},\quad a_{i,tt}=\left.\frac{\partial^2 A_i^{\mathrm{NB}}}{\partial t^2}\right|_{\nu^2=t=0}, \qquad (6.3)
$$

with $i=1,\ldots,6$.

At $\mathcal{O}(\omega^5)$, one finds a recoil contribution in $1/M$ given by combinations of these 18 constants, which correspond to a combination of the dispersive effects of the sixth-order scalar polarizabilities entering at $\mathcal{O}(\omega^4)$ and new

scalar sixth-order polarizabilities, which have never been discussed so-far in the literature. These terms are collectively indicated with the α_5^{L} and β_5^{L} coefficients in Eqs. (6.1) and (6.2), respectively.

The convergence radius of such a Taylor expansion is limited by the first singularity, which is set by the pion-production branch cut. In particular, the LEX of $\alpha_{E1}(\omega)$ fails to reproduce the non-analytical behavior of the polarizability when approaching the pion-production threshold. This behavior is clearly visible in Fig. 6.2, where we show both $\alpha_{E1}^{\mathrm{LEX}}(\omega)$ and $\beta_{M1}^{\mathrm{LEX}}(\omega)$ as a function of the cm energy ω up to $\mathcal{O}(\omega^5)$. The contribution beyond the LEX in Eqs. (2.43) and (2.44) can be taken into account by introducing two residual functions $\tilde{f}$ defined by

$$\alpha_{E1}(\omega) = \alpha_{E1}^{\mathrm{LEX}}(\omega) + \tilde{f}_\alpha(\omega), \quad \beta_{M1}(\omega) = \beta_{M1}^{\mathrm{LEX}}(\omega) + \tilde{f}_\beta(\omega). \tag{6.4}$$

The two functions $\tilde{f}_\alpha(\omega)$ and $\tilde{f}_\beta(\omega)$ can be calculated using DRs, and the results from DRs can be parametrized using the following functional form $\tilde{f}_\alpha(\omega) = \tilde{\alpha}_4\omega^4 + \tilde{\alpha}_5\omega^5$ and $\tilde{f}_\beta(\omega) = \tilde{\beta}_4\omega^4 + \tilde{\beta}_5\omega^5$. This particular choice allows us to merge the α_4^{L}, α_5^{L}, β_4^{L} and β_5^{LL} coefficients in Eqs. (2.43) and (2.44) with the polynomial coefficients of $\tilde{f}_{\alpha,\,\beta}(\omega)$ and to write the whole energy dependence of the scalar DDPs as

$$\alpha_{E1}(\omega) = \alpha_{E1}^{\mathrm{L_0}}(\omega) + f_\alpha(\omega), \quad \beta_{M1}(\omega) = \beta_{M1}^{\mathrm{L_0}}(\omega) + f_\beta(\omega), \tag{6.5}$$

where

$$\begin{aligned} \alpha_{E1}^{\mathrm{L_0}}(\omega) &\equiv \alpha_{E1}^{\mathrm{LEX}}(\omega)|_{\alpha_4^{\mathrm{L}}=\alpha_5^{\mathrm{L}}=0}, \quad f_\alpha(\omega) \equiv \alpha_4\omega^4 + \alpha_5\omega^5, \\ \beta_{M1}^{\mathrm{L_0}}(\omega) &\equiv \beta_{M1}^{\mathrm{LEX}}(\omega)|_{\beta_4^{\mathrm{L}}=\beta_5^{\mathrm{L}}=0}, \quad f_\beta(\omega) \equiv \beta_4\omega^4 + \beta_5\omega^5. \end{aligned} \tag{6.6}$$

with

$$\alpha_{4,5} \equiv \alpha_{4,5}^{\mathrm{L}} + \tilde{\alpha}_{4,5}, \quad \beta_{4,5} \equiv \beta_{4,5}^{\mathrm{L}} +, \tilde{\beta}_{4,5}. \tag{6.7}$$

The analytical expressions for the scalar DDPs in Eqs. (6.5) are the same as in Eqs. (6.1) and (6.2), provided that the $(\alpha,\beta)_{4,5}^{\mathrm{L}}$ coefficients are replaced by the coefficients $(\alpha,\beta)_{4,5}$ in Eqs. (6.7).

In Fig. 6.3, we show the predictions for the scalar DDPs from the full DR calculation, without LEX, in comparison with the results obtained from Eq. (6.5), using the predictions from DRs for all the static polarizabilities entering the $\alpha_{E1}^{\mathrm{L_0}}(\omega)$ and $\beta_{M1}^{\mathrm{L_0}}(\omega)$ contributions and the results from the fit to the DR calculation for the residual functions $f_\alpha(\omega)$ and $f_\beta(\omega)$. We note that the parametrization in Eq. (6.5) is able to reproduce the full energy dependence of the scalar DDPs in the energy range below the pion-production threshold[1] very well, giving us confidence that it can be conveniently adopted for our fitting procedure of the scalar DDPs to the Compton scattering data.

[1] We tried also different parameterizations, which worked very well and led us to the same considerations explained in this paragraph.

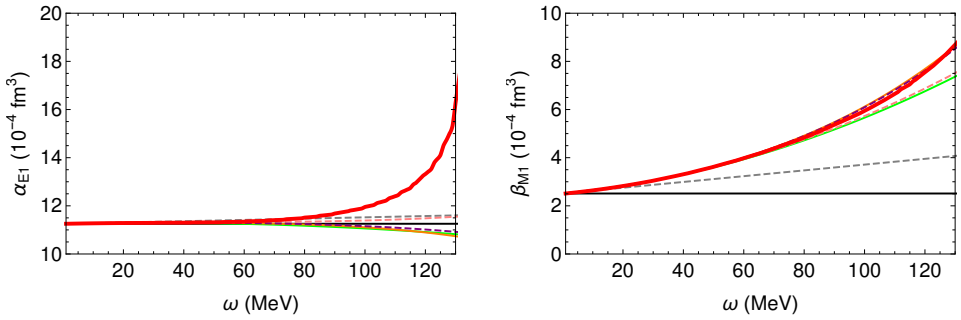

(a) (b)

Figure 6.2: Convergence of $\alpha_{E1}^{\mathrm{LEX}}(\omega)$ and $\beta_{M1}^{\mathrm{LEX}}(\omega)$ as function of the center-of-mass energy ω: expansions up to $\mathcal{O}(\omega^0)$ (black solid curve), $\mathcal{O}(\omega)$ (dashed gray curve), $\mathcal{O}(\omega^2)$ (full green curve), $\mathcal{O}(\omega^3)$ (dashed pink curve), $\mathcal{O}(\omega^4)$ (full orange curve) and $\mathcal{O}(\omega^5)$ (dashed purple curve) are compared with the $\alpha_{E1}(\omega)$ and $\beta_{M1}(\omega)$ functions (full red curve), respectively.

6.2 Sensitivity of the unpolarized real Compton scattering cross section to the scalar dipole dynamical polarizabilities

As already done for the extraction of the static dipole polarizabilities α_{E1} and β_{M1}, some sensitivity tests can be useful before performing the fit of the DDPs to the proton RCS data. In order to do so, we label as $(d\sigma)/(d\Omega)^{(2)}$ the differential cross section in which $\beta_{M1}(\omega) \equiv 0$. From this quantity we can check the sensitivity to $\alpha_{E1}(\omega)$. Similarly, the sensitivity to $\beta_{M1}(\omega)$ is tested by $(d\sigma)/(d\Omega)^{(3)}$ (where we set $\alpha_{E1}(\omega) \equiv 0$). If we set both the DDPs to zero, the resulting differential cross section is named $(d\sigma)/(d\Omega)^{(8)}$. Another interesting test is given by the analysis of the contribution of the static polarizabilities α_{E1} and β_{M1} to the DDPs. As a first check, we can set $\alpha_{E1}(\omega) \equiv \alpha_{E1}$ and $\beta_{M1}(\omega) \equiv \beta_{M1}$, thus suppressing the energy dependence of the DDPs and studying the sensitivity of the differential cross section to the higher-order coefficients of the polynomial expansion in Eqs. (6.1) and (6.2) (this condition is labeled as $(d\sigma)/(d\Omega)^{(9)}$). We can also modify this configuration, by imposing $\alpha_{E1}(\omega) \equiv \alpha_{E1}$ and $\beta_{M1}(\omega) \equiv \beta_{M1}$ just one at a time, thus testing the impact of the higher order terms of one DDP per time and obtaining $(d\sigma)/(d\Omega)^{(4)}$ and $(d\sigma)/(d\Omega)^{(5)}$, respectively. Furthermore, we can also investigate the sensitivity of the differential cross section to those recoil terms in Eqs. (6.1) and (6.2) that depend on the static scalar polarizabilities, α_{E1} and β_{M1}. Setting to zero all terms but α_{E1} in Eq. (6.1), we obtain $(d\sigma)/(d\Omega)^{(6)}$. Applying the same prescription for the contribution from $\beta_{M1}(\omega)$, we can label the corresponding differential cross section as $(d\sigma)/(d\Omega)^{(7)}$.

The results of these sensitivity tests are shown from Fig. 6.4 to Fig. 6.7, as

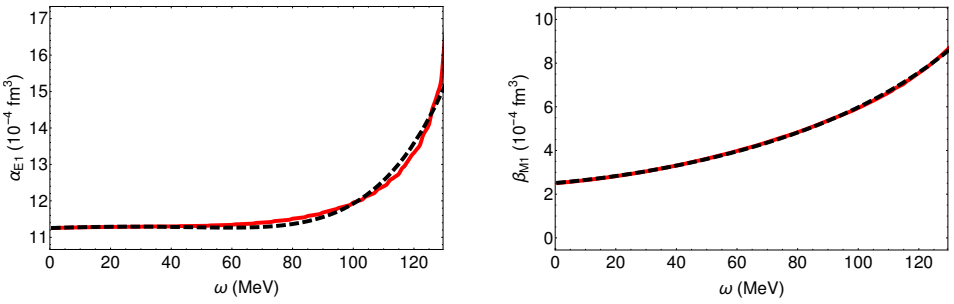

(a) (b)

Figure 6.3: The scalar DDPs $\alpha_{E1}(\omega)$ (left panel) and $\beta_{M1}(\omega)$ (right panel) as function of the center of mass energy ω. The solid red curves show the results from the DR calculation, with the full energy dependence. The dashed black curves are the results from Eq. (6.5), using the predictions from DRs for all the static polarizabilities entering the $\alpha_{E1}^{\mathrm{Lo}}(\omega)$ and $\beta_{M1}^{\mathrm{Lo}}(\omega)$ contributions and the results from the fit to the DR calculation for the residual functions $f_\alpha(\omega)$ and $f_\beta(\omega)$.

function of the lab photon energy E_γ and for 6 values[2] of the scattering angle θ_{lab}. From Fig. 6.4, we notice that $\alpha_{E1}(\omega)$ by itself gives a sizable contribution to the differential cross section, especially for $\theta_{lab} \sim 90°$, while the cross section obtained with only the contribution from $\beta_{M1}(\omega)$ deviates appreciably from the complete result. On the other hand, the static polarizability α_{E1} dominates the energy dependence of $\alpha_{E1}(\omega)$, as can be seen from Fig. 6.5, while the recoil terms embedded in $(d\sigma)/(d\Omega)^{(6)}$ have an almost negligible contribution to the differential cross section. Similarly, the terms in $(d\sigma)/(d\Omega)^{(7)}$ do not contribute appreciably, and the static β_{M1} is clearly not representing the main contribution in $\beta_{M1}(\omega)$, as can be observed from Fig. 6.6. Finally, by analyzing the results shown in Fig. 6.7, we can conclude that the scalar DDPs play a very important role in the determination of the differential cross section (by comparing $(d\sigma)/(d\Omega)^{(8)}$ with the complete calculation of the differential cross section). Moreover, the main contribution to the DDPs is given by both α_{E1} and β_{M1}, being $(d\sigma)/(d\Omega)^{(9)}$ very close to the complete $\frac{d\sigma}{d\Omega}$. This indicates a small sensitivity of the unpolarized cross section to dispersive terms in the scalar DDPs.

From this study, we can infer that a fit of the energy dependence of the scalar DDPs to the proton RCS data could be very challenging. Nevertheless, we succeeded in extracting for the first time the dipole dynamical scalar polarizabilities from the RCS data [59]. The results there obtained are shown in the next sections of this chapter.

[2]The values of θ_{lab} are related to the proton RCS data base, as described in Table 5.1.

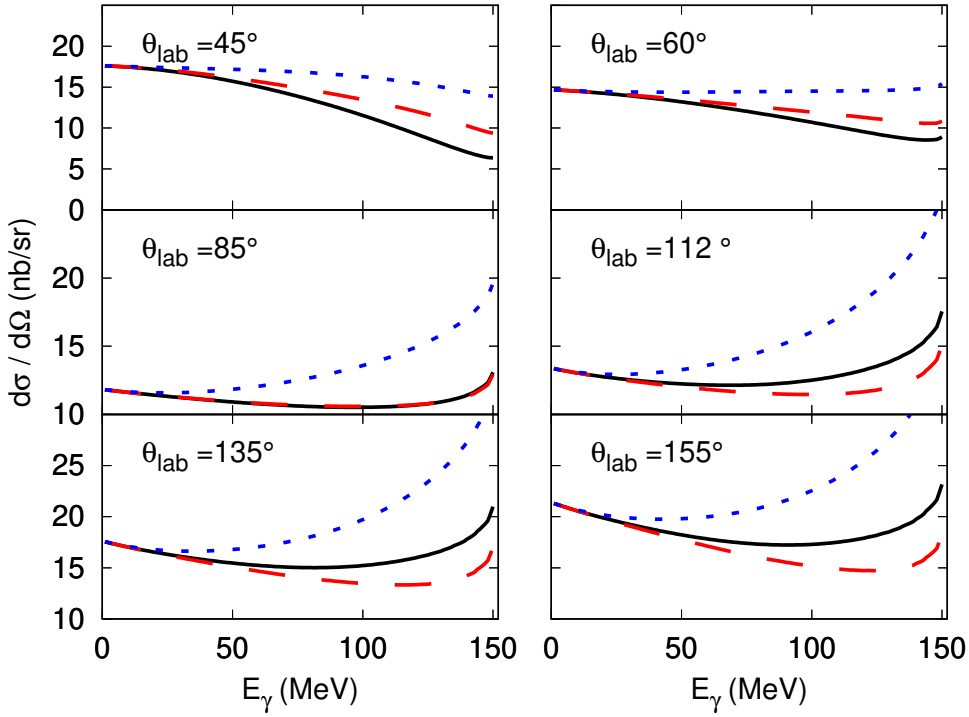

Figure 6.4: Sensitivity of the unpolarized differential cross section $d\sigma/d\Omega$ to the dipole dynamical polarizabilities $\alpha_{E1}(\omega)$ and $\beta_{M1}(\omega)$ as function of the lab energy E_γ: $d\sigma/d\Omega$ (black solid curve) compared to $(d\sigma)/(d\Omega)^{(2)}$ (red dashed curve) and to $(d\sigma)/(d\Omega)^{(3)}$ (blue dotted curve). See text for explanation.

6.3 A first fit of the scalar dipole dynamical polarizabilities

Before resorting to the bootstrap-based technique described in Ch. 4 for the fit of the DDPs from the RCS data, an internal cross-check about the approximation introduced by the LEX and the multipole expansion is in order. If all polarizabilities but α_{E1} and β_{M1} are fixed to the DR predictions or to the experimental measurements (as described in Ch. 5) and the bootstrap-based technique described in Ch. 4 is applied, we expect to find a result that is in very good agreement with the one obtained directly fitting the static electric and magnetic polarizabilities using the full DR calculation, as done in Ch. 5. Recalling the bootstrap sampling introduced in Eq. (4.22), i.e. $\mathcal{B}_{ij} = (1+\delta_{ij})(E_i + \gamma_{ij}\sigma_i)$, and fixing $\delta_{ij} = 0$, the results of this cross-check are:

$$\alpha_{E1} = 11.8 \pm 0.2, \quad \beta_{M1} = 2.0 \mp 0.2, \tag{6.8}$$

which are almost identical[3] to the values shown in Eq. (5.5). Note that the same results can be obtained by the traditional χ^2 minimization through the gradient

[3]In this case, no error on the Baldin sum rule is included in the data analysis.

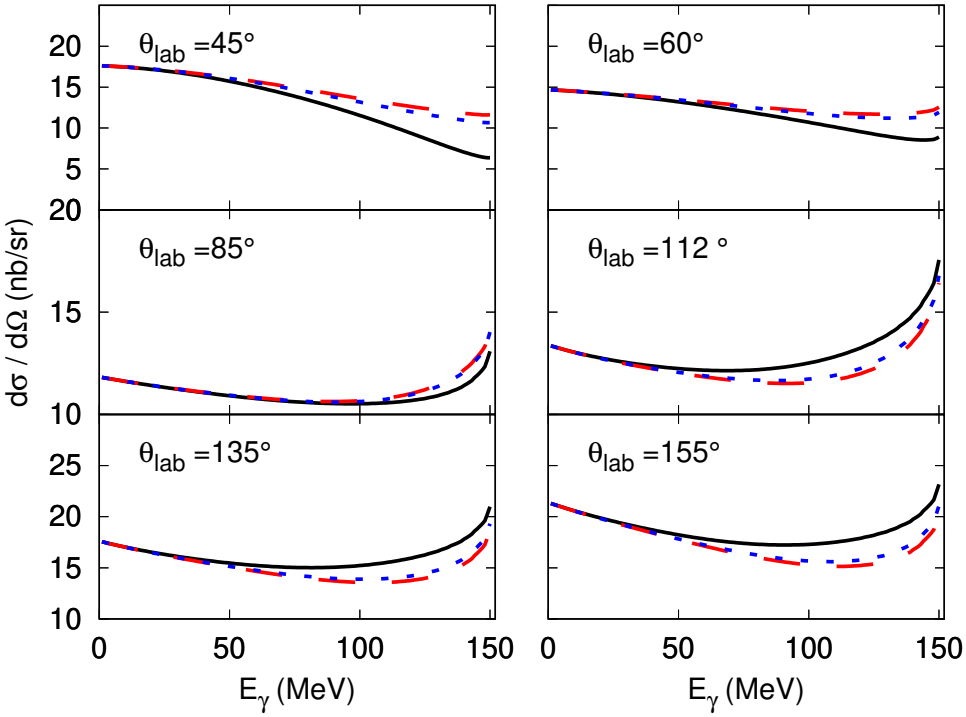

Figure 6.5: Sensitivity of the unpolarized differential cross section $d\sigma/d\Omega$ to the dipole dynamical polarizabilities $\alpha_{E1}(\omega)$ and $\beta_{M1}(\omega)$ as function of the lab energy E_γ: $d\sigma/d\Omega$ (black solid curve) compared to $(d\sigma)/(d\Omega)^{(4)}$ (red dashed curve) and to $(d\sigma)/(d\Omega)^{(6)}$ (blue dotted curve). See text for explanation.

method. This cross-check gives us confidence on the theoretical framework we implemented to fit the energy dependence of the DDPs.

As a first step, we try to fit the complete energy-dependence of the scalar DDPs from the RCS data. In order to do so, we fixed the recoil contributions from the static leading-order spin polarizabilities to the experimental values of Ref. [36], and the recoil terms from higher-order spin polarizabilities as well as from quadrupole scalar polarizabilities to the values predicted by the subtracted DRs [15]. The remaining polarizabilities – that enter the fit as free parameters – are: α_{E1}, β_{M1}, $\alpha_{E1,\nu}$, $\beta_{M1,\nu}$ and the four coefficients of the residual functions $f_{\alpha,\beta}(\omega)$ defined in Eq. (6.6), i.e. α_4, α_5, β_4 and β_5. In the most generic situation, we do not impose the Baldin sum rule, thus leaving both the electric and the magnetic polarizabilities as free parameters, for a total of 8 independent fitting parameters. The systematic errors as well as the point-to-point bias for the TAPS [35] dataset are here not included in the data analysis. The numerical results from the eight-parameter fit, both to the FULL and to the TAPS datasets, are shown in Table 6.1. We notice that the higher-energy coefficients have huge uncertainties and thus can be extracted only with a very low accuracy. This feature is mainly caused by the low sensitivity of the RCS differential cross section to them (see Fig. 6.7, for instance) and by the

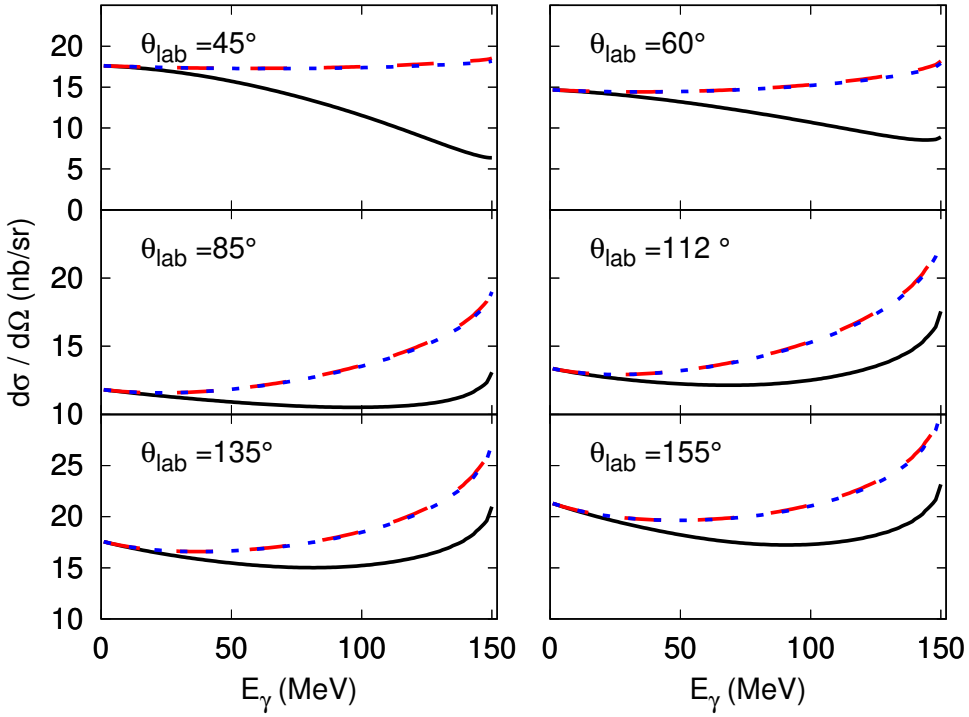

Figure 6.6: Sensitivity of the unpolarized differential cross section $d\sigma/d\Omega$ to the dipole dynamical polarizabilities $\alpha_{E1}(\omega)$ and $\beta_{M1}(\omega)$ as function of the lab energy E_γ: $d\sigma/d\Omega$ (black solid curve) compared to $(d\sigma)/(d\Omega)^{(5)}$ (red dashed curve) and to $(d\sigma)/(d\Omega)^{(7)}$ (blue dotted curve). See text for explanation.

high correlations among the fitting parameters. We could also wonder how the uncertainties of the fitted parameters in Table 6.1 affect the DDPs calculation. Using the standard error propagation, we obtain the results shown in Figs. 6.8 and 6.9, for the FULL and the TAPS dataset, respectively. In both cases, we observe that the 1-σ error band (in yellow) is huge.

6.4 Scalar dipole dynamical polarizabilities from the real Compton scattering data: results and discussion

As shown in the previous section, the attempt to fit the complete energy dependence of the DDPs fails due to the low sensitivity of the differential cross section to the higher-order coefficients of the expressions defined in Eq. (6.5). For this reason, we adopt a different strategy: we fix $f_\alpha(\omega)$ and $f_\beta(\omega)$ from the DR predictions, as well as the higher-order terms in the DDPs expressions. Thus, the number of fitting parameters are reduced to four: the static dipole α_{E1} and β_{M1}, together with their dispersive corrections $\alpha_{E1,\nu}$ and $\beta_{M1,\nu}$. Fur-

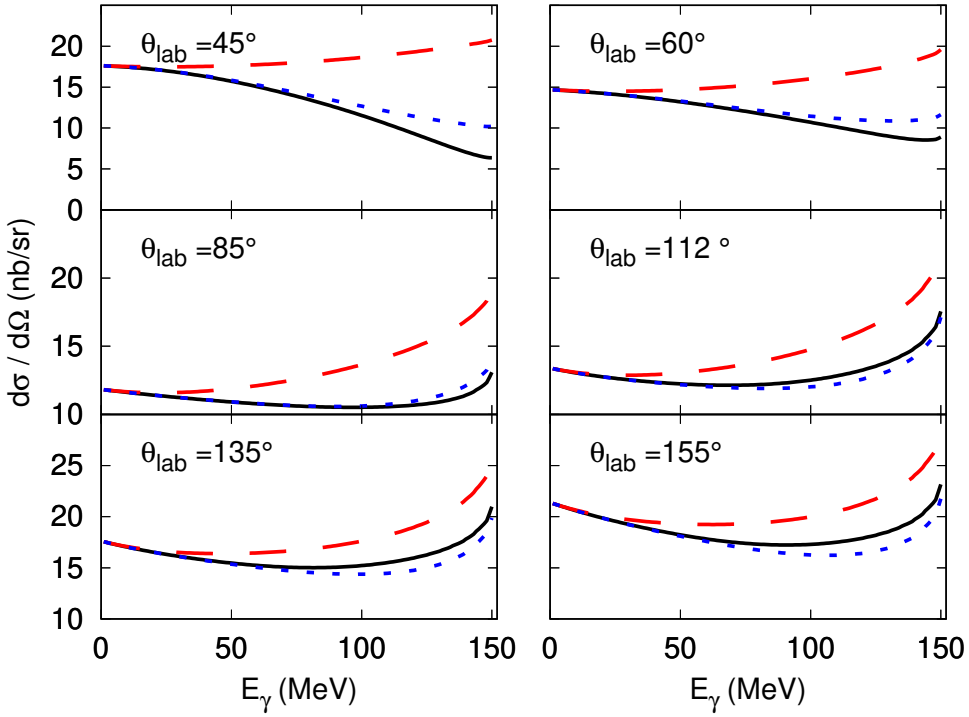

Figure 6.7: Sensitivity of the unpolarized differential cross section $d\sigma/d\Omega$ to the dipole dynamical polarizabilities $\alpha_{E1}(\omega)$ and $\beta_{M1}(\omega)$ as function of the lab energy E_γ: $d\sigma/d\Omega$ (black solid curve) compared to $(d\sigma)/(d\Omega)^{(8)}$ (red dashed curve) and to $(d\sigma)/(d\Omega)^{(9)}$ (blue dotted curve). See text for explanation.

thermore, by imposing the constraint of the Baldin sum rule, the number of fit parameters reduces to three.

Moreover, the bootstrap framework gives us the possibility of automatically include the error of non-fitted parameters on the fit results, as described in Ch. 4 and already used in Ch. 5. In this framework, we include only the propagation of the Baldin[4] uncertainty, while all the other polarizabilities are assumed to be known with no uncertainty. The results of the fit performed under this configuration are shown in Table 6.2, both for the FULL and the TAPS dataset. The corresponding probability distributions are shown in Fig. 6.10, as a result of the bootstrap-based fitting technique. As already stressed, no a-priori Gaussian assumption is performed here, while the entire probability distributions (as well as the correlation terms, shown in Fig. 6.11) are obtained from the sampling of Eq. (4.22). As a matter of fact, the traditional χ^2 minimization (through the gradient method) works quite well with three fit parameters, but the covariance matrix (see Eq. (4.16), for instance) is forced to be positive definite, thus casting some doubts on the validity of the procedure even if the fitted parameter estimates turned out to be close to those given in Table 6.2. As already noticed for the extraction of the static scalar dipole

[4]As done in Ch. 5, we take the value 13.8 ± 0.4.

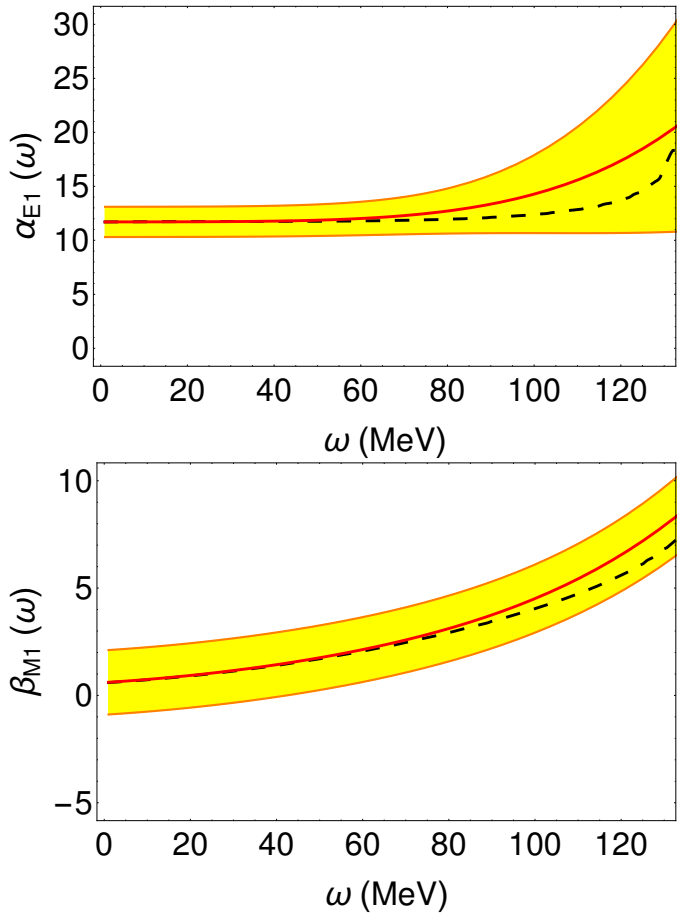

Figure 6.8: Results from the fit of the scalar DDPs (red solid curve) in the 8 parameter framework and for the FULL dataset: $\alpha_{E1}(\omega)$ on the top and $\beta_{M1}(\omega)$ on the bottom. The 68% CL area (filled in yellow) is obtained by the standard error propagation. The dashed curves are the predictions from DRs [30].

polarizabilities, the FULL dataset could include some inconsistent data, but the fine analysis performed in Ch. 5 made us concluding that there are no strong enough motivations to exclude any of those data points. Furthermore, the central values of the fitted parameters shown in Table 6.2 from the fit with the FULL and the TAPS datasets are different, even if still compatible within the errors[5]. This difference could be related to the correlation between the different angular distributions of the two datasets and the varying sensitivity to α_{E1} and β_{M1} in different angular regions, as shown in Sec. 5.1.

Furthermore, the fitting parameters turn out to be strongly correlated, as clearly visible from Fig. 6.11: there, the two-dimensional joint probability dis-

[5]If, as an example, we consider the SELECTED dataset defined in [8, 20] and in Ch. 5, we obtain for the fitted polarizabilities the following values: $\alpha_{E1} = (10.8 \pm 0.9) \cdot 10^{-4}\,\mathrm{fm}^3$, $\alpha_{E,1\nu} = (-2.6 \pm 2.7) \cdot 10^{-4}\,\mathrm{fm}^5$, $\beta_{M1} = (2.9 \pm 1.0) \cdot 10^{-4}\,\mathrm{fm}^3$ and $\beta_{M1,\nu} = (6.2 \pm 3.0) \cdot 10^{-4}\,\mathrm{fm}^5$. These values are compatible, within two standard deviations, with the ones given in Table 6.2.

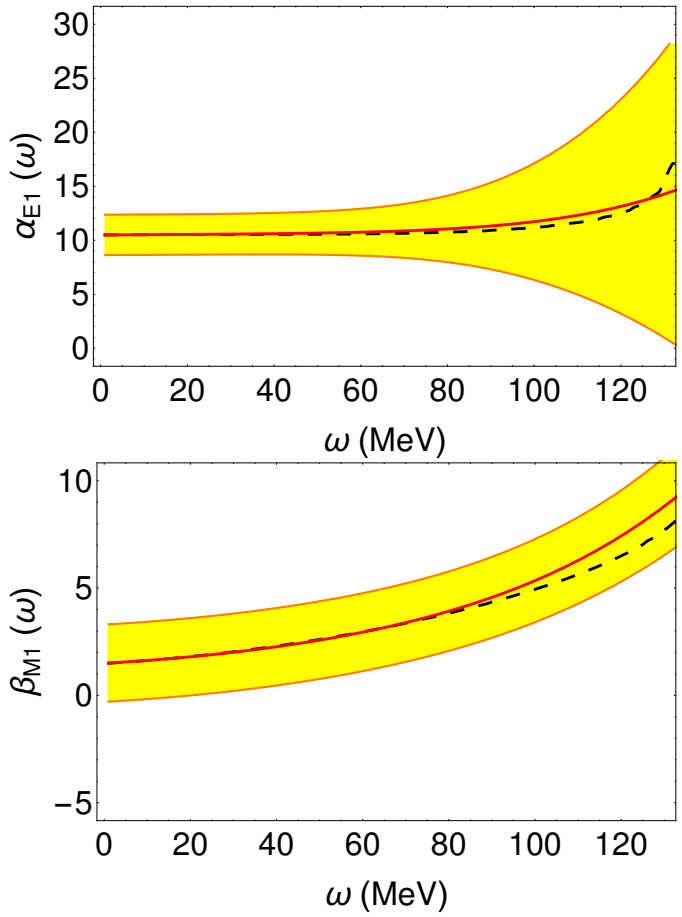

Figure 6.9: Results from the fit of the scalar DDPs (red solid curve) in the 8 parameter framework and for the TAPS dataset: $\alpha_{E1}(\omega)$ on the top and $\beta_{M1}(\omega)$ on the bottom. The 68% CL area (filled in yellow) is obtained by the standard error propagation. The dashed curves are the predictions from DRs [30].

tributions are shown for $\alpha_{E1}, \beta_{M1}, \alpha_{E1,\nu}$ and $\beta_{M1,\nu}$. We would expect that the correlation coefficient between α_{E1} and β_{M1} is -1, due to the Baldin constraint: however, thanks to the uncertainty propagation performed at every bootstrap cycle, the result is -0.89. Besides this expected high (and negative) value, the correlations between the static dipole polarizabilities and their respective dispersive corrections are also very high (top left and bottom right panels of Fig. 6.11, respectively).

As already shown in Sec. 5.3.4, the bootstrap-based framework provides the automatic calculation of the uncertainty of every function of the fitted parameters, with the considerable advantage that all the correlation terms are straightforwardly included. Thus, for fixed value of the cm energy ω, we can compute the probability distribution of the DDPs of Eqs. (6.1) and (6.2) and from there we we can estimate the uncertainties at any confidence level (CL). In Fig. 6.12, we show our fit results for the scalar DDPs, extracted from the FULL and TAPS dataset, as function of the cm energy ω and with the

		FULL	TAPS
α_{E1}	(10^{-4}fm^3)	11.7 ± 1.4	10.5 ± 1.8
$\alpha_{E1,\nu}$	(10^{-4}fm^5)	-0.7 ± 5.7	0.4 ± 10.1
β_{M1}	(10^{-4}fm^3)	0.6 ∓ 1.5	1.5 ∓ 1.8
$\beta_{M1,\nu}$	(10^{-4}fm^5)	7.9 ± 7.2	7.3 ± 10.1
α_4	(10^{-4}fm^7)	-16.9 ± 44.7	-10.2 ± 65.1
α_5	(10^{-4}fm^8)	32.0 ± 70.1	33.8 ± 99.4
β_4	(10^{-4}fm^7)	-1.2 ± 11.9	-4.4 ± 20.5
β_5	(10^{-4}fm^8)	17.3 ± 35.6	11.6 ± 28.2

Table 6.1: Values of the LEX coefficients of the scalar DDPs from the fit to the FULL and TAPS datasets in the eight-parameter case.

		FULL	TAPS
α_{E1}	(10^{-4}fm^3)	13.3 ± 0.8	11.6 ± 1.1
$\alpha_{E1,\nu}$	(10^{-4}fm^5)	-8.8 ± 2.5	-3.2 ± 3.1
β_{M1}	(10^{-4}fm^3)	0.4 ∓ 0.9	2.2 ∓ 1.1
$\beta_{M1,\nu}$	(10^{-4}fm^5)	10.8 ± 2.8	5.1 ± 3.7

Table 6.2: Values of the LEX coefficients of the scalar DDPs from the fit to the FULL and TAPS datasets in the three-parameter fit.

corresponding 68% and 95% CL uncertainty bands. They are compared with the subtracted DR predictions, obtained with the values of the static dipole polarizabilities from the fit to the FULL and the TAPS datasets in Table 6.2. The DR results for both the scalar DDPs are within the 68% confidence area of the fit results just for $\omega \lesssim 60$ MeV. At higher energy, the DR predictions for $\beta_{M1}(\omega)$ remain within the 95% CL region, while for $\alpha_{E1}(\omega)$ we observe deviations from the fit results in the case of the FULL dataset and a very good agreement, within the 68% confidence area, in the case of the TAPS dataset. This different behavior can be again a hint of inconsistencies between the two datasets. The larger relative error in the case of $\beta_{M1}(\omega)$ also reflects the lower sensitivity of the unpolarized RCS data to the magnetic polarizability than to the electric polarizability.

6.5 Comparison with the fit of the scalar static polarizabilities

We have shown in this chapter how the DDPs can be extracted from the proton RCS data. In our framework, this can be done by a three-parameter fit, with the results shown in Table 6.2. If we compare them with the values

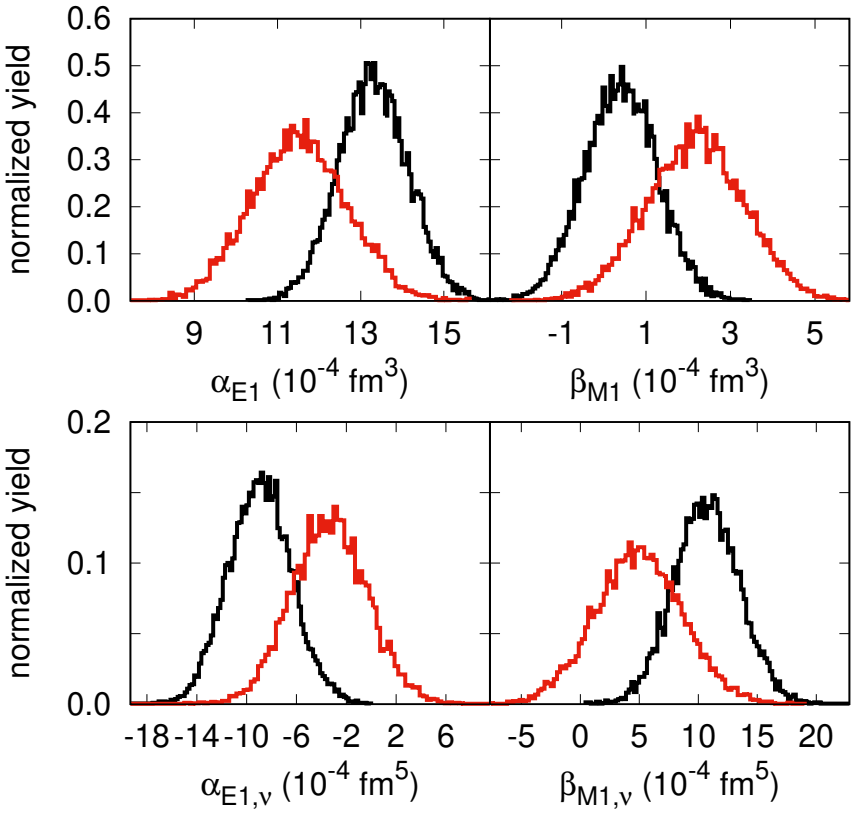

Figure 6.10: Probability distributions of the fit parameters, with 100 bins per histogram, from the bootstrap analysis of the FULL (black curves) and TAPS datasets (red curves): static polarizabilities α_{E1} (top-left) and β_{M1} (top-right) and dispersive polarizabilities $\alpha_{E1,\nu}$ (bottom-left) and $\beta_{M1\nu}$ (bottom-right).

of α_{E1} and β_{M1} obtained in Ch. 5 and listed in Table 5.2, we notice that they are compatible within the intersection of the 1-σ uncertainty band, even if the central values are quite different. This feature can be related to the high correlations among the fit parameters of the DDPs: for instance, the fitted value of $\alpha_{E1,\nu}$ has a quite strong effect in the determination of α_{E1}, being their correlation coefficient quite close to -1.

The dispersive polarizabilities that we fitted in the DDP framework, on the other hand, can be compared with the values predicted within unsubtracted [12] and subtracted [15] DRs, as well as baryon χPT [9]. Our results are, within the very large error bars, consistent with these theoretical predictions and cannot discriminate between them.

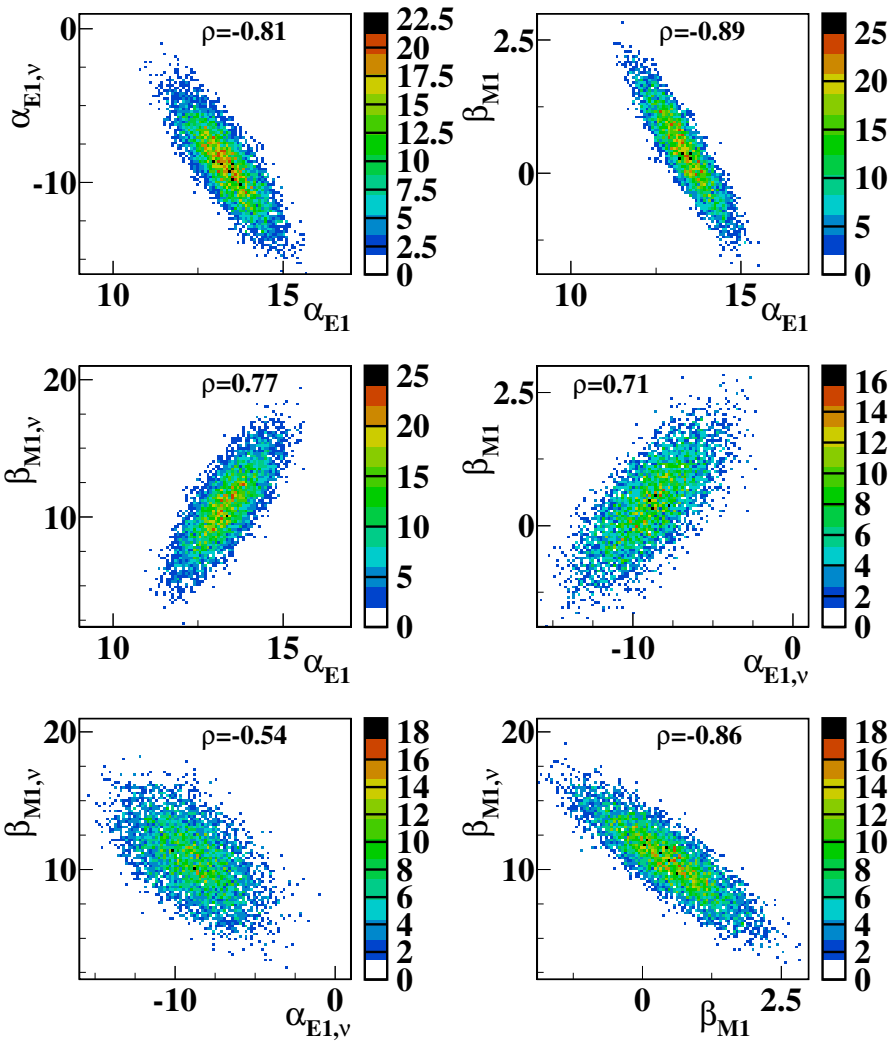

Figure 6.11: Joint probability distributions and correlation coefficients ρ for α_{E1}, β_{M1}, $\alpha_{E1,\nu}$, and $\beta_{M1,\nu}$ for the three-parameter fit of the FULL data base. The scales on the axes are different for each plot.

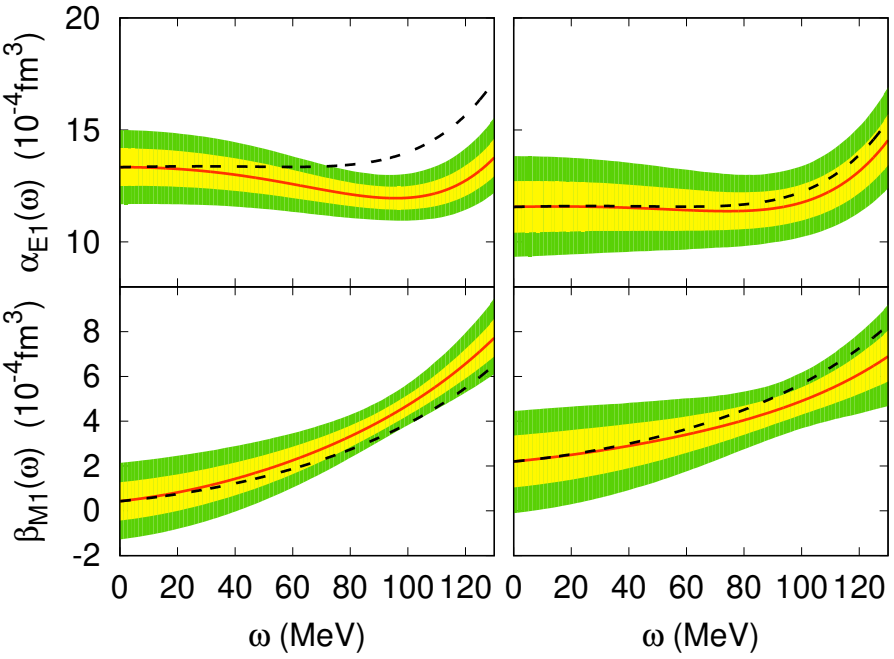

Figure 6.12: Results from the fit of the scalar DDPs (solid curve) for the FULL and TAPS datasets: $\alpha_{E1}(\omega)$ on the top and $\beta_{M1}(\omega)$ on the bottom. The 68% (yellow) and 95% (green) CL areas include all the correlations between the parameters. The dashed curves are the predictions from DRs [30].

Chapter 7

The beam asymmetry and the total photo absorption cross sections

In this chapter, we analyze the sensitivity of the beam asymmetry Σ_3 to the dipole scalar polarizabilities α_{E1} and β_{M1}. This preliminary study can serve as guideline to establish both the accuracy that can be achieved in the extraction of the scalar polarizabilities from this observable and which of the leading-order static polarizabilities should be used as fit parameters. We then give an estimate of α_{E1} and β_{M1}, combining in the data analysis also the experimental measurements of Σ_3 and the unpolarized differential cross section.

The second part of this chapter is devoted to a preliminary analysis of the unpolarized and the helicity-difference of total photo-absorption cross sections, introduced in Sec. 3.2.1. We evaluate the GDH integral, the GGT sum rule for the forward spin polarizability and the Baldin sum rule, using a model independent approach to calculate the propagation of the statistical uncertainties of the experimental data.

7.1 The beam asymmetry

As shown in Sec. 2.3.3, we can identify 11 independent observables for the RCS process, as listed in Table 2.1. As already stated in Ch. 2, we decided to focus our attention mainly on the unpolarized differential cross section ($d\sigma/d\Omega$), devoting some attention also on the beam asymmetry (Σ_3). In Ch. 5 and Ch. 6, we focused on the unpolarized differential cross section $d\sigma/d\Omega$ and we used available experimental data to extract both the static and dynamical scalar polarizabilities. As discussed in Sec. 2.3.3, the analysis of Ref. [47] pointed out that the beam asymmetry Σ_3 is a promising observable to extracting the magnetic polarizability β_{M1} with better precision. Based on this work, new experimental data from MAMI [40] have been recently analyzed for a new

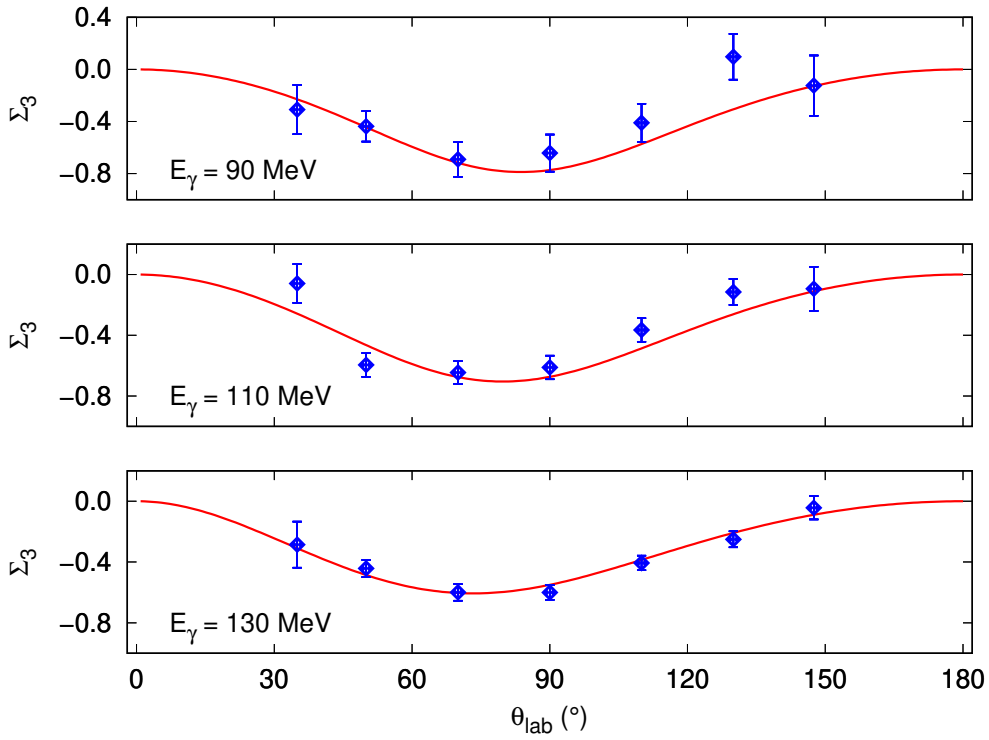

Figure 7.1: The DR predictions for the beam asymmetry Σ_3 (red solid curve) as a function of the scattering angle θ_{lab}, evaluated for $E_\gamma = 90$ MeV (upper panel), 110 MeV (middle panel) and 130 MeV (lower panel). The experimental data from Ref. [40] are shown with their statistical uncertainty.

evaluation of the magnetic polarizability. These data are shown in Fig. 7.1, together with the DR predictions obtained using the PDG values for α_{E1} and β_{M1} and the values of the spin polarizabilities given in Sec. 5.2. The data have been collected for three energy bins, $E_\gamma = \{90, 110, 130\}$ MeV, and are presented as a function of the scattering angle θ_{lab}. Following the steps described in Ch. 5, we fit Σ_3 data within the DR framework and use the bootstrap-based technique with the goal to determine β_{M1} with a better accuracy. However, as done in Ch. 5, some sensitivity tests are required to establish which of the six leading-order static polarizabilities can be used as fit or fixed parameters. For this purpose, we follow the sensitivity study described in Sec. 5.1, and here applied to the beam asymmetry Σ_3. Our results are shown in Fig. 7.2 for each of the six leading-order static polarizabilities, as function of the scattering angle and the incoming photon energy. As additional and complementary information, we show in Fig. 7.3 the R parameter defined in Eq. (5.3) at fixed values of the photon energy. The same results are shown in Figs. 7.4 and 7.5 for the R_{exp} parameter defined in Eq. (5.4).

The information that we obtain from these sensitivity tests is very similar to the ones related to the unpolarized cross section and collected in Sec. 5.1: also the beam asymmetry Σ_3 turns out to be almost insensitive to the spin

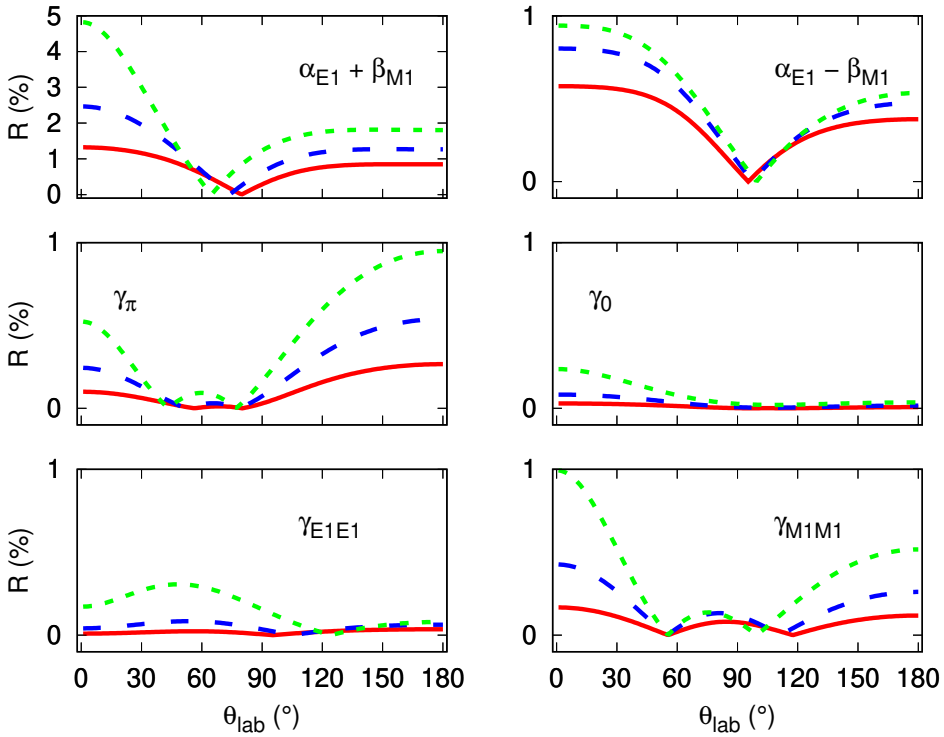

Figure 7.2: Ratio R as function of the scattering angle θ_{lab} and at different values of the photon energy E_γ: 90 MeV (red solid curve), 110 MeV (blue dashed curve) and 130 MeV (green dotted curve).

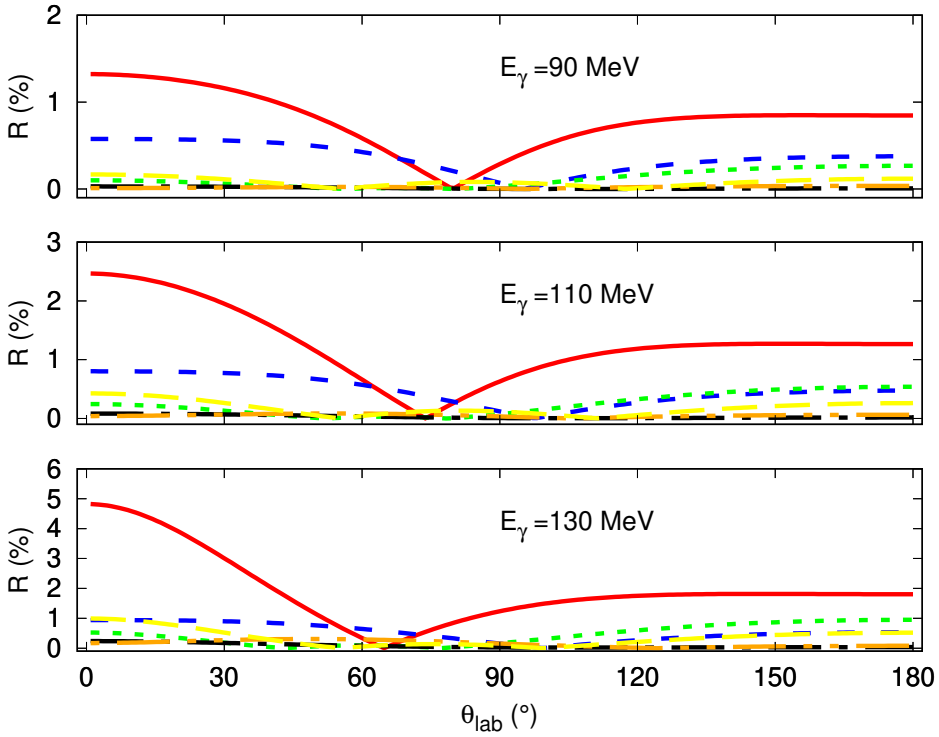

Figure 7.3: Ratio R as function of the scattering angle θ_{lab} for each static polarizability: $\alpha_{E1} + \beta_{M1}$ (red solid curve), $\alpha_{E1} - \beta_{M1}$ (blue dashed curve), γ_π (green-dotted curve), γ_0 (black dash-dotted curve), γ_{E1E1} (orange dash-dot-dotted curve) and γ_{M1M1} (yellow dashed curve). The results are for different values of the photon energy E_γ.

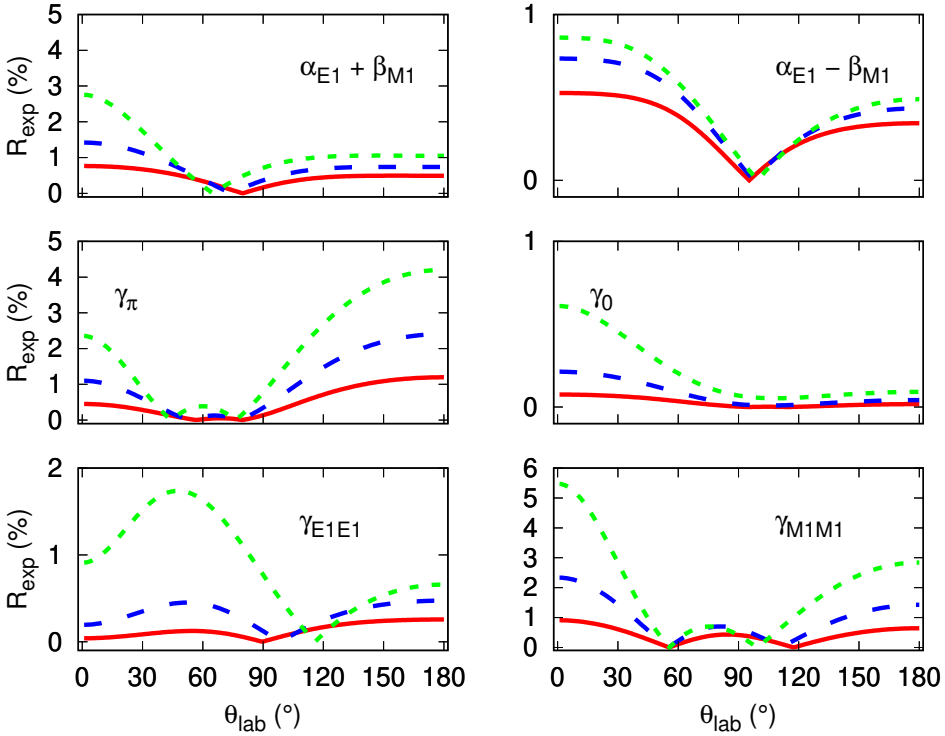

Figure 7.4: The same as in Fig. 7.2, but for R_{exp}.

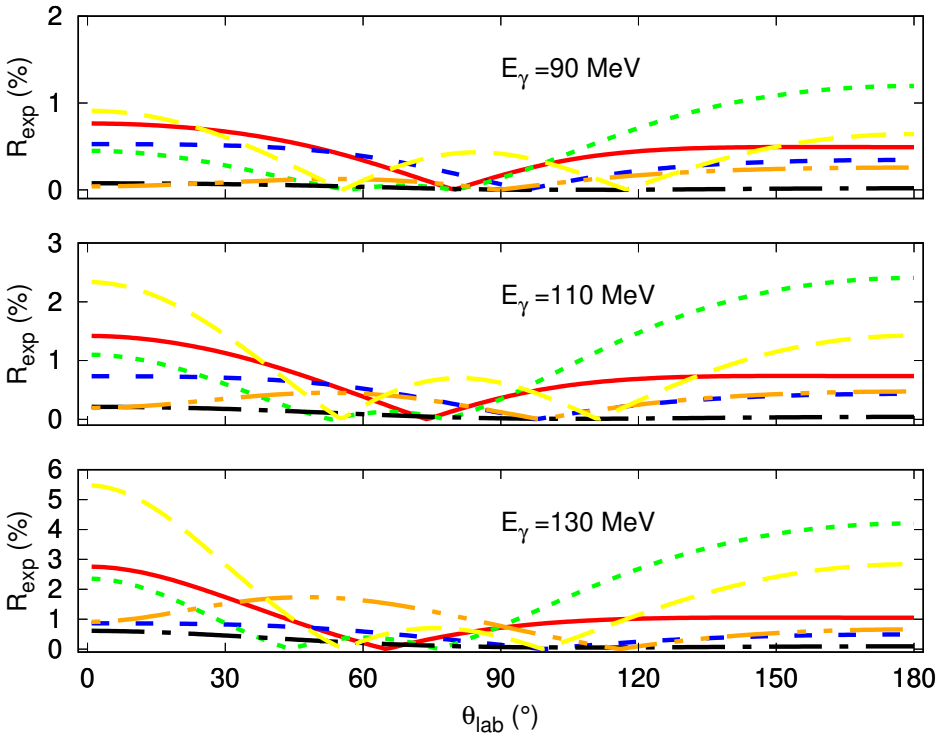

Figure 7.5: The same as in Fig. 7.3, but for R_{exp}.

polarizabilities. However, their relatively big statistical uncertainties increase the value of the R_{exp} parameter (as can be seen comparing Fig. 7.2 with Fig. 7.4, for instance), thus making non-negligible the effects due to γ_{M1M1} and γ_π. On the other hand, the accuracy under which the dipole scalar polarizabilities α_{E1} and β_{M1} are known is quite close to their limit value. This feature is clearly visible by comparing Fig. 7.2 with Fig. 7.4: the results for the sum $\alpha_{E1} + \beta_{M1}$ and the difference $\alpha_{E1} - \beta_{M1}$ are almost identical in the two cases.

From these tests, we learn that the beam asymmetry has the highest sensitivity to the three parameters γ_π and $\alpha_{E1} \pm \beta_{M1}$. However, as a preliminary look at the Σ_3 data, we just tried to fit $\alpha_{E1} - \beta_{M1}$, and fix all the other polarizabilities at the values used in Ch. 5, following the scheme of Ref. [40].

7.1.1 A test-fit of the scalar dipole static polarizabilities

Once the fit parameters are established, we can perform the fit in the test-fit condition described in Ch. 5. We first fit the data of the beam asymmetry Σ_3 shown in Fig. 7.1, thus obtaining

$$\alpha_{E1} = 11.03 \pm 1.97, \quad \beta_{M1} = 2.77 \pm 1.97, \quad \hat{\chi}^2 = 1.09. \tag{7.1}$$

These numerical values are quite different from the ones obtained by a test-fit of the unpolarized differential cross section (see Eq. (5.5), for instance), even if they are compatible within the very large error bars. The best fit of Σ_3 is then shown in Fig. 7.6 together with its 1-σ error band. These results are compared with the calculation performed as described at the beginning of this chapter. The two different curves (black solid and red solid, respectively) are very similar, thus confirming the very low sensitivity of the beam asymmetry to the difference $\alpha_{E1} - \beta_{M1}$. In order to improve the statistical significance of the fit, we could simultaneously fit both the beam asymmetry and the unpolarized differential cross section. As a first step, we use the data given in Ref. [40] and the FULL data set, described in Ch. 5. The fitted results are

$$\alpha_{E1} = 11.93 \pm 0.30, \quad \beta_{M1} = 1.87 \pm 0.30, \quad \hat{\chi}^2 = 1.37, \tag{7.2}$$

and the corresponding best evaluation of Σ_3 is shown in Fig. 7.7. These numerical values are almost identical to the ones given in Eq. (5.5), thus confirming once more the very low sensitivity of the beam asymmetry to $\alpha_{E1} - \beta_{M1}$.

However, from a simulation we checked that the uncertainty in Eq. (7.1) could be reduced by a factor two by doubling both the number and the precision of the data points. This accuracy level should be reached by the incoming results from MAMI [48, 49], thus leading us to a much more precise result for the extraction of β_{M1} from Σ_3. However, even in this optimal situation, the statistical fluctuation of the fit results would be much greater than the actual uncertainty quoted by the PDG [89], thus suggesting that a simultaneous fit of Σ_3 and the unpolarized cross section would be recommended.

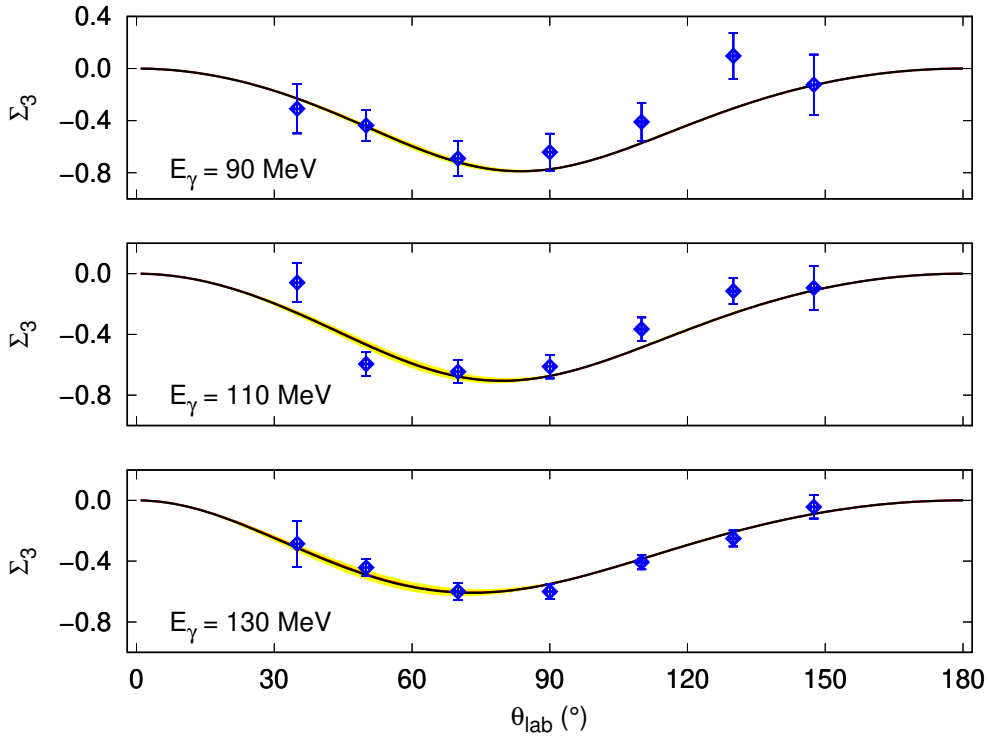

Figure 7.6: The DR fitted results for the beam asymmetry Σ_3 (black solid curve) as function of the scattering angle θ_{lab}, evaluated for $E_\gamma = 90$ MeV (upper panel), 110 MeV (middle panel) and 130 MeV (lower panel). The experimental data from Ref. [40] are shown with their statistical uncertainty. The yellow band is the 1-σ interval as obtained from the standard error propagation. The red curve corresponds to the results shown in Fig. 7.1, obtained with the PDG values of the scalar polarizabilities and the values of the spin polarizabilities given in Sec. 5.2.

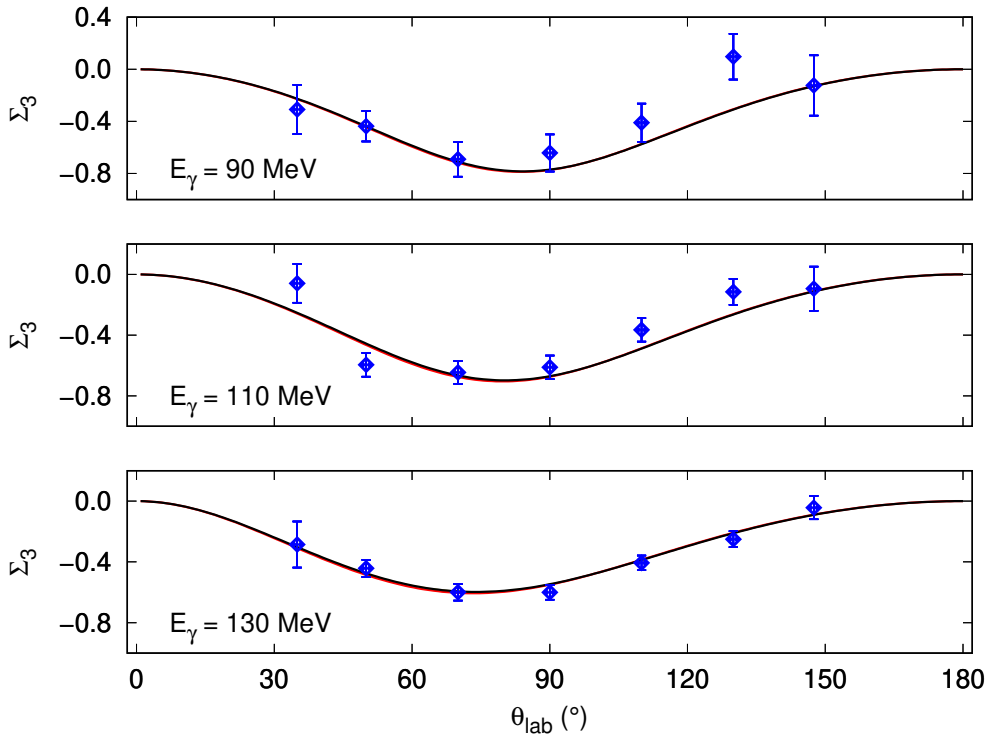

Figure 7.7: The DR fitted results for the beam asymmetry Σ_3 (black solid curve) as function of the scattering angle θ_{lab}, evaluated for $E_\gamma = 90$ MeV (upper panel), 110 MeV (middle panel) and 130 MeV (lower panel). The experimental data from Ref. [40] are shown with their statistical uncertainty. Also the unpolarized data were included in the analysis, as described in the text. The yellow band is the 1-σ interval as obtained from the standard error propagation. The red curve corresponds to the results shown in Fig. 7.1, obtained with the PDG values of the scalar polarizabilities and the values of the spin polarizabilities given in Sec. 5.2.

7.2 Sum rules evaluation from the data of photo absorption

As shown in Sec. 3.2.1, the optical theorem allows us to relate the imaginary part of the forward Compton scattering amplitudes $f(\nu)$ and $g(\nu)$ to the unpolarized ($\sigma(\nu)$) and the helicity-difference ($\Delta\sigma(\nu)$) cross sections of total photo-absorption, respectively. The available experimental data of $\sigma(\nu)$ [106–111] and $\Delta\sigma(\nu)$ [85, 86, 112, 113] are shown in Figs. 7.8 and 7.9, respectively, while the imaginary parts of the scattering amplitudes $f(\nu)$ and $g(\nu)$, defined in Eq. (3.18), are computed from the experimental data, with the results shown in Figs. 7.10 and 7.11.

The goal of this section is to give a first estimate of the sum rules in Eqs. (3.28)-(3.30), i.e. the Baldin, the GDH and the GGT sum rules. We follow the steps described in Refs. [88, 94], but with a key difference: instead of using a parametrization for the cross section fitted to the data, we evaluate the integrals with the experimental data as input, propagating the corresponding statistical uncertainties.

Before performing the integration, we divide the ν domain into three regions:

1. *low-ν*: $\nu \in [\nu_0, \nu_L)$, where $\nu_0 = 0.145$ GeV is the single-pion production threshold in the lab-frame, while ν_L is the lowest ν value of the available experimental data;

2. *data-ν*: $\nu \in [\nu_L, \nu_H]$, where ν_H is the highest ν value of the available experimental data;

3. *high-ν*: $\nu \in (\nu_H, \nu_T)$, where ν_T is the upper limit of integration.

In the *low-ν* region we use the MAID input [63] for the total photo-absorption cross sections, while for the *high-ν* region we follow the parameterization of Refs. [88, 94], given in terms of Regge trajectories.

The integrals of Eqs. (3.28) and (3.29) can be shortly written as

$$I_\nu \equiv C \int_{\nu_0}^{\infty} d\nu \frac{\mathcal{E}(\nu)}{\nu^n}, \tag{7.3}$$

where we label with $\mathcal{E}(\nu)$ both the unpolarized and the helicity-difference photo-absorption cross sections.

In order to perform the integrals directly from the experimental data, we need to bin the ν axis: if we label as ν_k the ν value at which the k^{th} experimental datum was measured, we can define the upper and lower limits of each bin as

$$\begin{aligned} \nu_k^{(B)} &= \frac{\nu_{k-1} + \nu_k}{2}, \quad k = 2, \ldots, N, \\ \nu_1^{(B)} &= \frac{3\nu_1 - \nu_2}{2}, \quad \nu_{N+1}^{(B)} = \frac{3\nu_N - \nu_{N-1}}{2}, \end{aligned} \tag{7.4}$$

where N is the number of experimental data. In this way, each bin is centered on the experimental value ν_k and its width is symmetric for every k. Now, we can write the discretization of the integrals in Eq. (7.3), i.e.

$$I_\nu^{disc} = C \sum_{k=1}^{N} \int_{\nu_k^{(B)}}^{\nu_{k+1}^{(B)}} d\nu \frac{\mathcal{E}(\nu)}{\nu^n}. \tag{7.5}$$

As a first attempt for the evaluation of the sum rules, we introduce an approximation: we assume that $\mathcal{E}(\nu) = \mathcal{E}(\nu_k)$ in the k^{th} bin. This is just one of the possible approximations that can be assumed in a numerical evaluation of integrals, but it is suitable for our purposes. Under this assumption, the expression in Eq. (7.5) can be rewritten as

$$I_\nu^{disc} \approx C \sum_{k=1}^{N} \mathcal{E}(\nu_k) \int_{\nu_k^{(B)}}^{\nu_{k+1}^{(B)}} d\nu \frac{1}{\nu^n}. \tag{7.6}$$

The main advantage of this approximation is that we can analytically evaluate the integrals in Eq. (7.6), i.e. $I_k = \int_{\nu_k^{(B)}}^{\nu_{k+1}^{(B)}} d\nu \frac{1}{\nu^n}$, thus strongly simplifying the calculation. Finally, we can write the discretized version of the integrals in Eq. (7.3) as

$$I_\nu^{disc} = C \sum_{k=1}^{N} \mathcal{E}(\nu_k) I_k. \tag{7.7}$$

If we want to propagate the experimental uncertainties of the measured values of $\mathcal{E}(\nu)$, we can apply the traditional error propagation, which yields to an estimate of the 1-σ uncertainty for the I_ν^{disc} value, i.e.

$$\sigma_I = C \left[\sum_{k=1}^{N} \left(\mathcal{E}(\nu_k) I_k \right)^2 \right]^{1/2}. \tag{7.8}$$

We stress that, just as a first step of this evaluation, we include only the statistical fluctuations of the measured values involved in the integral calculations.

Our numerical results for the sum rules given in Eqs. (3.28)-(3.30) read:

$$\begin{aligned} \alpha_{E1} + \beta_{M1} &= (13.93 \pm 0.05) \times 10^{-4} \text{ fm}^3, \\ I_{GDH} &= (224.15 \pm 5.45) \ \mu\text{b}, \\ \gamma_0 &= (-1.03 \pm 0.07) \times 10^{-4} \text{ fm}^4. \end{aligned} \tag{7.9}$$

Our value for the Baldin sum rule is in very good agreement with the one obtained in Ref. [94], as well as the value that we used in Ch. 5 and Ch. 6. Furthermore, both the GDH integral and the forward spin polarizability γ_0 are consistent with the values extracted in Ref. [88]. Our value for I_{GDH} is also in very good agreement with the one from Refs. [85, 86, 112–114], while our evaluation of γ_0 is almost identical to the value used in Ch. 5 and Ch. 6.

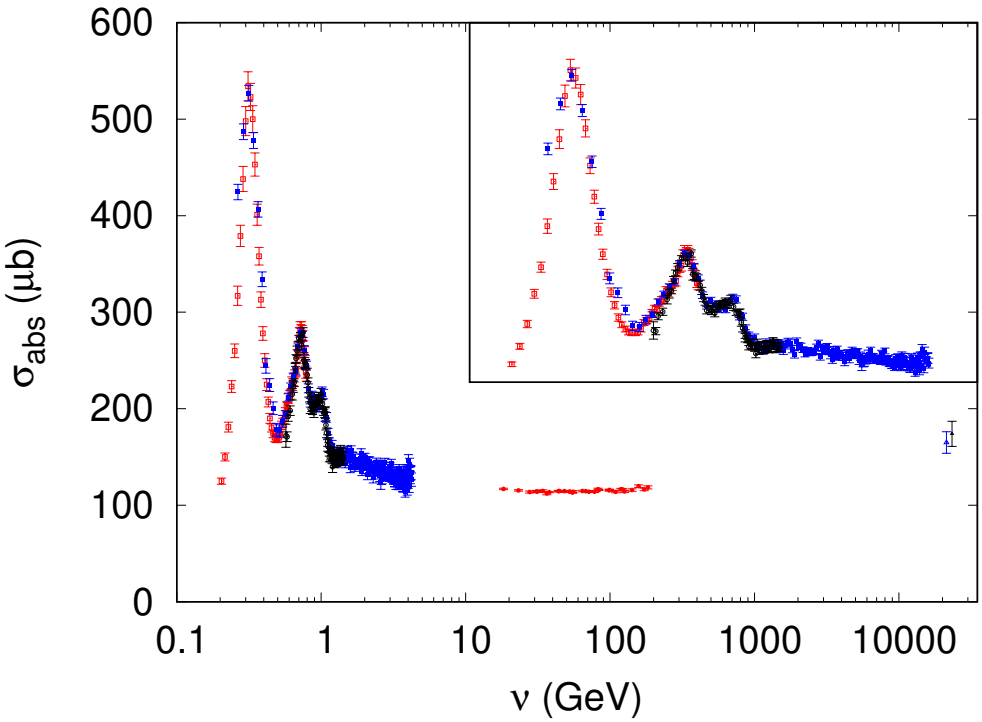

Figure 7.8: Experimental data of the unpolarized cross sections of total photo-absorption as function of the ν variable. They are taken from Ref. [106] (red empty squares), Ref. [107] (blue solid squares), Ref. [108] (black empty circles), Ref. [109] (red full circles), Ref. [110] (blue solid triangles), Ref. [111] (black solid triangle)

It is interesting to notice that the uncertainties on the sum rule values are mostly dominated by the systematic errors of the total photo-absorption cross section, as can be deduced from the very small errors quoted in Eq. (8.2). This feature is particularly true for $\alpha_{E1} + \beta_{M1}$, where the contribution coming from the statistical fluctuations of the experimental data in the determination of the uncertainty of the sum rule evaluation is about $\sim 10 \div 20\%$ of the PDG estimate. Also for the GDH integral, the main source of uncertainty is given by the effect of the systematic errors (~ 12 μb [115]), thus suggesting that a more refined analysis, which includes also the propagation of the systematic errors of the experimental data, should be recommended. Furthermore, we can look at the running values of the integrals in Eqs. (3.28)-(3.30), as function of the upper limit of integration in ν. The results for $\alpha_{E1} + \beta_{M1}$ are shown in Fig. 7.12, while the GDH and the GGT integrals are shown in Figs. 7.13 and 7.14, respectively. Due to the additional powers in ν at the denominators of the integrands for $\alpha_{E1} + \beta_{M1}$ and γ_0 with respect to I_{GDH}, the convergence shown in Figs. 7.12 and 7.14 is reached for relatively small values of ν: $\nu \simeq 10$ GeV and $\nu \simeq 1$ GeV, respectively. For I_{GDH}, on the other hand, the convergence is reached at ~ 100 GeV, thus requiring very accurate measurements also at

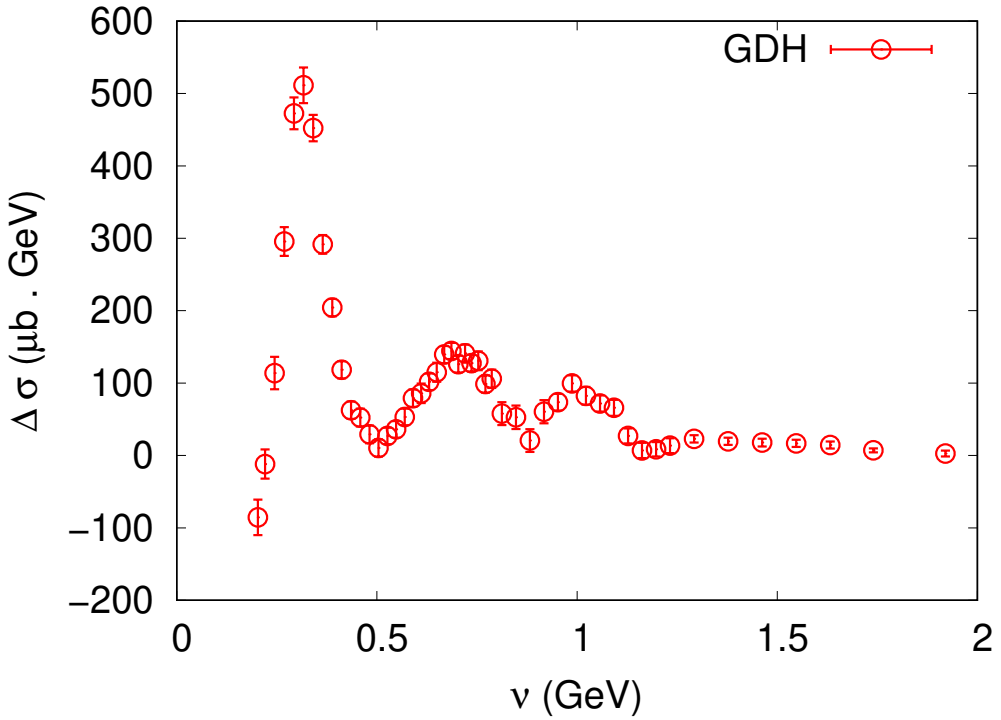

Figure 7.9: Experimental data of the helicity-difference cross sections of total photo-absorption as function of the ν variable. The data are from Refs. [85, 86, 112, 113].

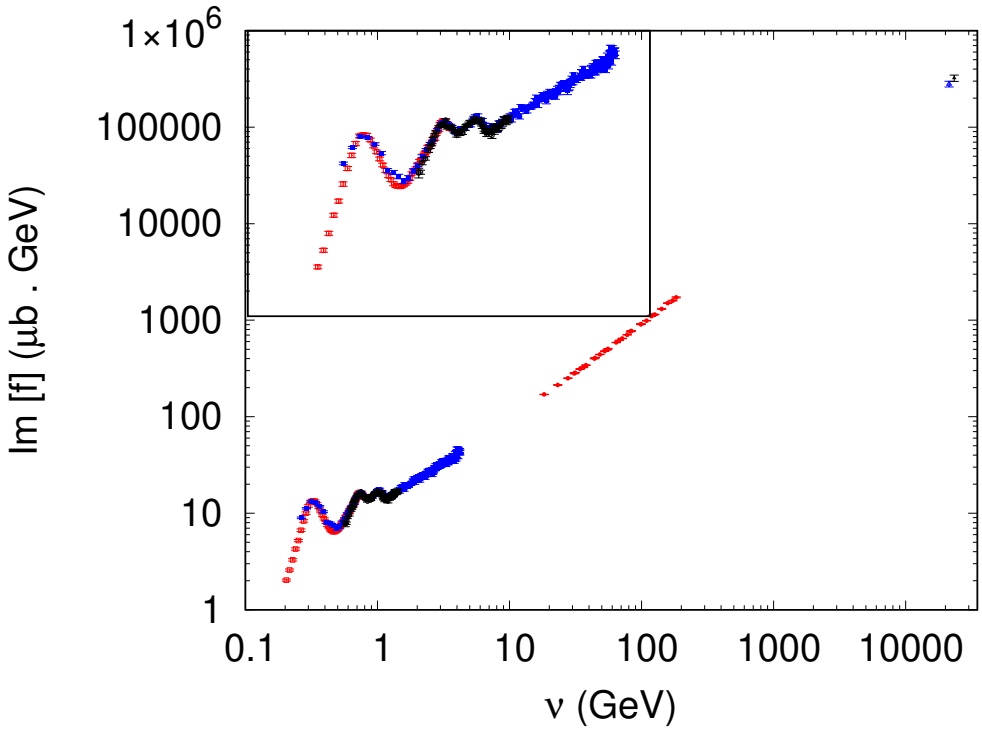

Figure 7.10: The imaginary part $\Im f(\nu)$ as obtained from the experimental data shown in Fig. 7.8, thanks to Eq. (3.21), as function of the ν variable. The labels of the data are the same as in Fig. 7.8.

.

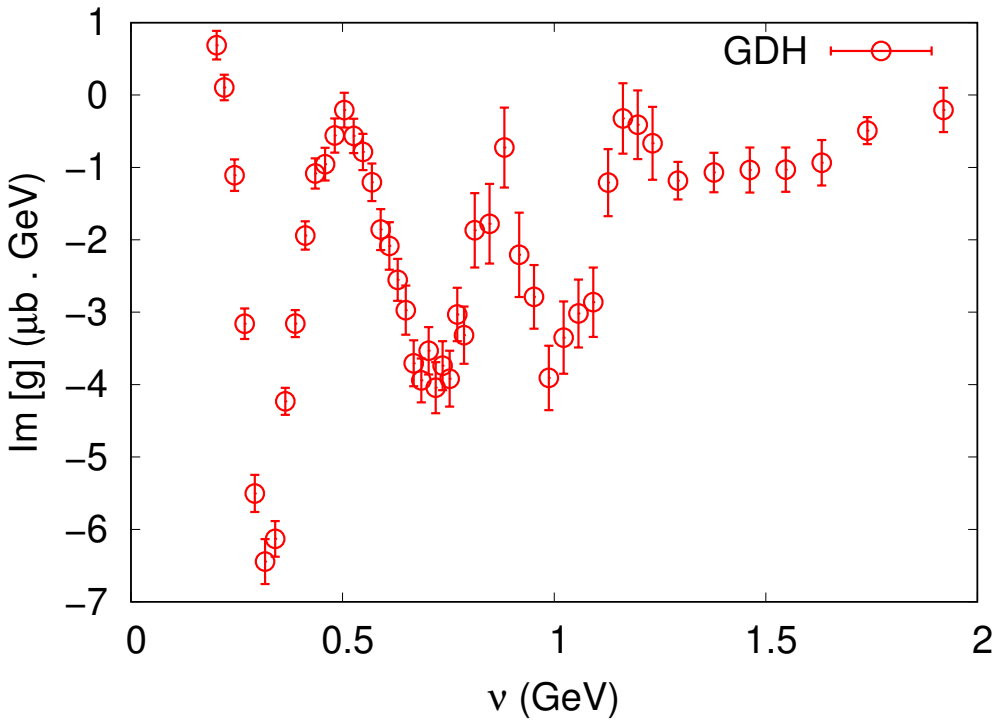

Figure 7.11: The imaginary part $\Im g(\nu)$ as obtained from the experimental data shown in Fig. 7.9, thanks to Eq. (3.21), as function of the ν variable. The labels of the data are the same as in Fig. 7.9.

high energy. We stress that the results shown in this section are not intended to be conclusive, but they should be looked as a first approach to a possible re-evaluation of the sum rules given in Eqs. (3.28)-(3.30), the intent of reducing as much as possible the model dependence of a parametrization fitted to the experimental data.

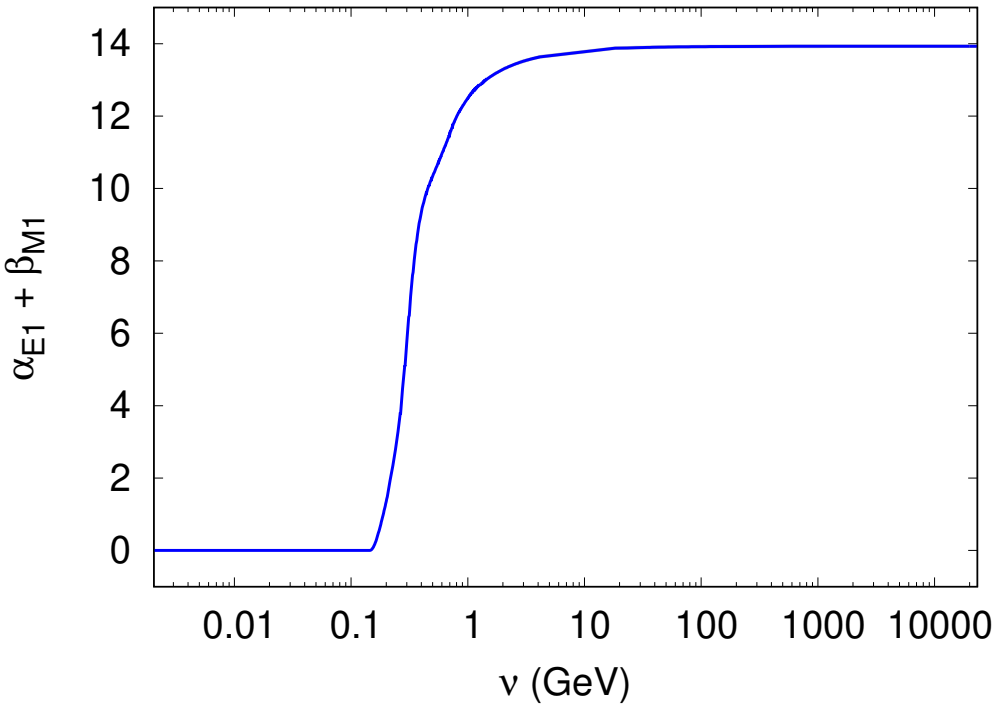

Figure 7.12: Running value of $\alpha_{E1} + \beta_{M1}$ (in 10^{-4} fm^3 units) from the Baldin sum rule as function of the upper limit of integration ν.

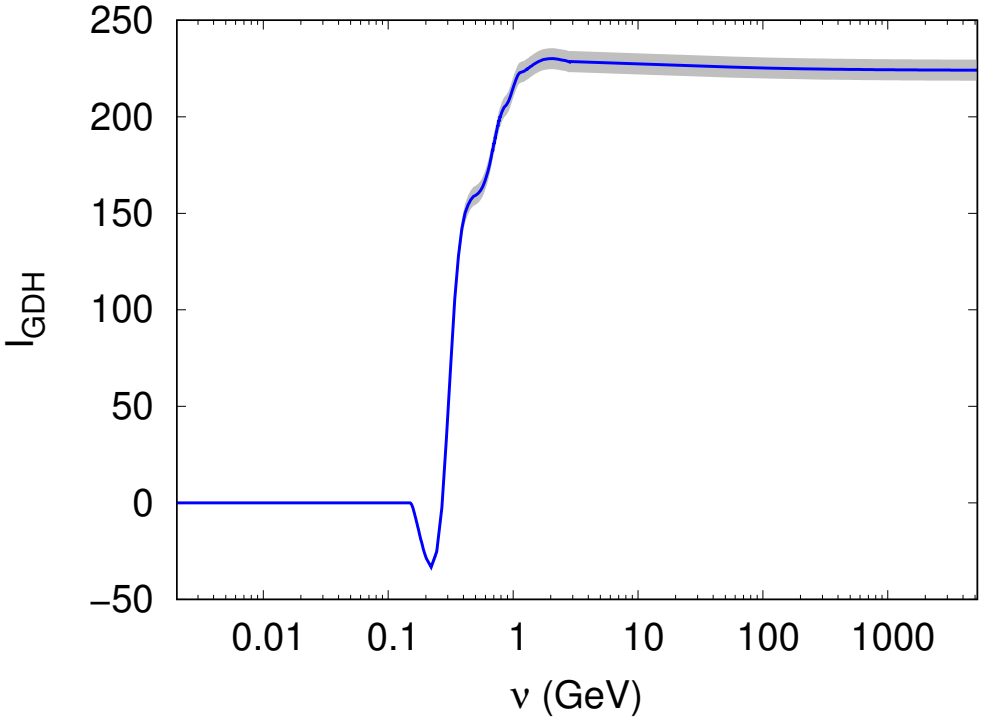

Figure 7.13: Running value of the GDH integral (in μb units) as function of the upper limit of integration ν.

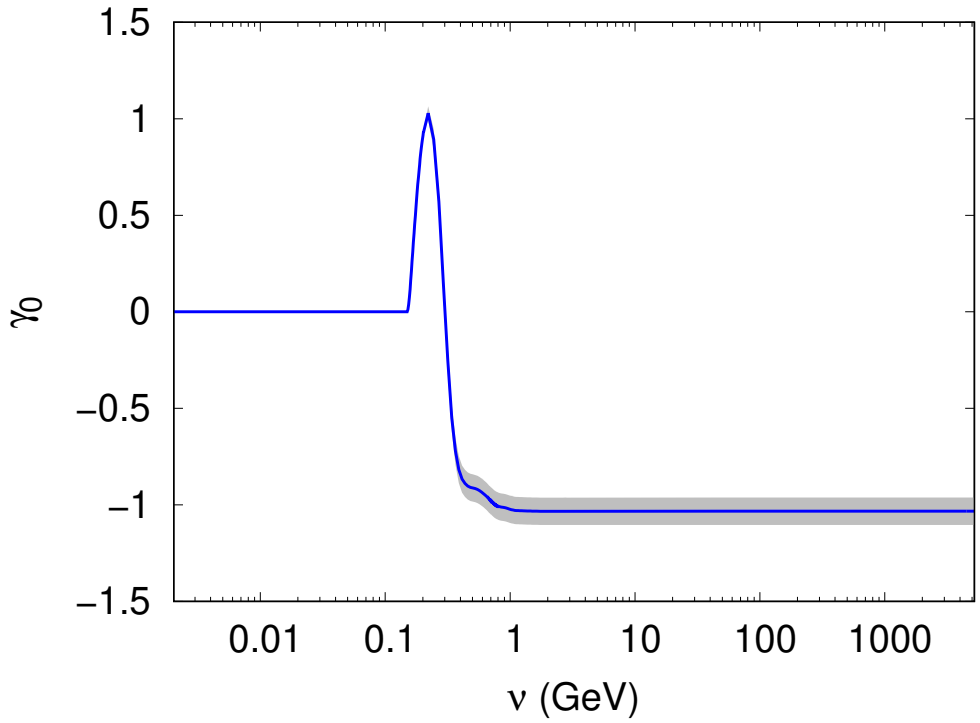

Figure 7.14: Running value of γ_0 from the GGT sum rule (in 10^{-4} fm^4 units) as function of the upper limit of integration ν.

Chapter 8

Conclusions and outlooks

In this thesis, we have extracted the scalar dipole (static and dynamical) polarizabilities from the proton data of real Compton scattering (RCS) unpolarized differential cross sections below the pion-production threshold. Our results have been obtained within the framework of fixed-t subtracted dispersion relations (DRs) [14]. With respect to existing extractions in literature, the DR analysis has the merit to reduce the model dependence, being based on experimental inputs from other processes. For the data analysis, we used a new bootstrap-based fitting technique, thus making a step forward with respect to the state of the art, from both a theoretical and a phenomenological point of view.

We thoroughly analyzed the application of the parametric bootstrap in the fitting procedure. Within this framework, we showed how the systematic errors can be included in the data analysis with no modification in the shape of the χ^2-like minimization function, but just assuming that each experimental measurement is a convolution of a Gaussian variable (completely determined by the data points and their pure statistical fluctuations) and a random shift caused by the systematic biases. Moreover, we discussed how to propagate on the fit results the uncertainties of those fixed parameters that serve as input for the theoretical model, without resorting to the standard, linear (and approximated) propagation. The more important result is the determination of the goodness-of-fit distribution also for those cases where the experimental points are neither independent, nor Gaussian distributed. This is, indeed, a common situation, mainly caused by systematic uncertainties and/or correlated errors. In our framework, no a priori assumptions are made on the probability distribution of the fit parameters, but all the conclusions derive directly from the bootstrap sampling. In this way, our method is very robust and flexible: the convolution with systematic errors can be easily modified (if there are some experimental motivations) or even suppressed in the case we would like to study only the pure statistical fluctuations.

Using this Monte-Carlo fitting technique, we gave our best estimate of both the electric and magnetic static polarizabilities, α_{E1} and β_{M1}, including in the

fit all the sources of systematic uncertainties and the statistical fluctuations of those static polarizabilities that enter the DR calculation of the differential cross section, but are not fitted. Furthermore, we performed several tests about the statistical significance of the proton RCS data base in the energy range below the pion-production threshold, giving our contribution in the debate about the data-set definition [20, 59, 72, 74]. Our evaluation of the electric and magnetic polarizabilities reads

$$\begin{aligned} \alpha_{E1} &= (12.03^{+0.48}_{-0.54}) \times 10^{-4}\text{fm}^3, \quad \beta_{M1} = (1.77^{+0.52}_{-0.54}) \times 10^{-4}\text{fm}^3, \\ \hat{\chi}^2 &= 1.25, \quad p\text{-value} = 12\%, \end{aligned} \tag{8.1}$$

where the statistical significance has been obtained from the bootstrap method.

We analyzed also the scalar dipole dynamical polarizabilities (DDPs) and we studied possible different strategies to fit them to the available data on the unpolarized RCS cross section. We extracted for the first time the scalar DDPs from the unpolarized RCS cross section below pion production threshold [59], including in our analysis the systematic errors of the experimental points, as well as the uncertainty of the Baldin sum rule [3] evaluation (which involves the sum of the electric and magnetic polarizabilities). Our results pointed out that the poor statistics of the data, combined with the strong correlations among the fitting parameters, makes a precise extraction of the DDPs quite challenging. Nevertheless, our work [59] represents a baseline for future extraction of the DDPs from data of RCS observables.

Moreover, we performed some preliminary analysis on the beam asymmetry (Σ_3) data, showing that this observable does not appreciably contribute in a more precise evaluation of β_{M1}. However, the new expected data on the unpolarized differential cross section from MAMI [48, 49] hold the promise of a much better accuracy in the experimental measurements, being thus able to reduce the uncertainty on β_{M1} up to a factor 2. Moreover, we performed a first re-evaluation of the Baldin sum rule, the Gerasimov [4], Drell and Hearn [5] (GDH) sum rule (involving the nucleon anomalous magnetic moment) and the Gell-Mann, Goldberger and Thirring [2, 41] (GGT) sum rule (for the forward spin polarizability γ_0), using a model independent approach to calculate the propagation of the statistical uncertainties of the experimental data. Our results, even if very preliminary, are quite encouraging and in very good agreement with the existing literature [21, 85, 86, 88, 94, 112–115], i.e.

$$\begin{aligned} \alpha_{E1} + \beta_{M1} &= (13.93 \pm 0.05) \times 10^{-4}\ \text{fm}^3, \\ I_{GDH} &= (224.15 \pm 5.45)\ \mu\text{b}, \\ \gamma_0 &= (-1.03 \pm 0.07) \times 10^{-4}\ \text{fm}^4. \end{aligned} \tag{8.2}$$

****

We list some possible outlooks for the future, concerning both the evaluation of the sum rules and the analysis of proton RCS data.

* In order to perform a more accurate evaluation of the sum rules, also the systematic errors of the experimental data should be included in the

computation of the uncertainty, being responsible for most of the error bands on the integral evaluations;

* Also the analysis of the expected RCS data from MAMI [48, 49] should be accurately performed; we encourage a wide use of the bootstrap-based fitting technique which is able, as already stressed, to correctly deal with the systematic errors and to assign the correct statistical significance to the fit results. Furthermore, one expects that the combined analysis of the beam asymmetry and the unpolarized differential cross section will help to reduce the uncertainty in the determination of α_{E1} and, especially, β_{M1};

* We could perform a combined analysis of all available unpolarized and polarized RCS data for a simultaneous extraction of all six leading-order static polarizabilities. Sofar, the double polarization measurements from MAMI have been analyzed [36, 116] to extract the spin polarizabilities, using as input the values of α_{E1} and β_{M1} extracted separately from the unpolarized and beam asymmetry RCS data;

* For the future, the estimate of the uncertainties related to the available phenomenological analysis for the pion photoproduction channel would be desirable in order to be able to quantify the corresponding theoretical uncertainties in the dispersion calculation of RCS;

* As pointed out in Ref. [117], the formalism of fixed-t subtracted DRs adopted in this thesis could be profitably extended to analyze the nucleon virtual Compton scattering at low energies, in order to directly fit the six leading-order generalized polarizabilities from the data.

Appendix A

Relations between the A_i and R_i amplitudes

In this appendix, we give the relation between the R_i amplitudes (defined in the c.m. reference frame) and the invariant amplitudes A_i, whose low-energy expansion has been explicitly formulated in the lab reference frame, as shown in Ch. 2. According to Ref. [12], the R_i amplitudes can be related to the A_i as

$$\begin{aligned}
R_1 &= C\left[c_1\left(-A_1-\frac{W^2}{M_N^2}A_3\right)-\frac{\nu}{M_N}c_2A_5-\frac{W}{M_N}c_3A_6\right],\\
R_2 &= C\left[c_1\left(A_1-\frac{W^2}{M_N^2}A_3\right)+\frac{\nu}{M_N}c_2A_5-\frac{W}{M_N}c_3A_6\right],\\
R_3 &= C\left[(W-m)^2\left((x-1)A_1+(1+x)\frac{W^2}{M_N^2}A_3\right)-\frac{\nu}{M_N}c_3A_5-\frac{W}{M_N}c_2A_6\right],\\
R_4 &= C\left[(W-m)^2\left((1-x)A_1+(1+x)\frac{W^2}{M_N^2}A_3\right)+\frac{\nu}{M_N}c_3A_5-\frac{W}{M_N}c_2A_6\right],\\
R_5 &= C\left[(W-m)^2\left(-A_1-\frac{W^2}{M_N^2}A_3\right)+(W^2-M_N^2)\left(A_2+\frac{W^3}{M_N^3}A_4\right)\right.\\
&+ \left.2(W-m)\left(-\nu A_5+\frac{W^2}{M_N}A_6\right)\right],\\
R_6 &= C\left[(W-m)^2\left(A_1-\frac{W^2}{M_N^2}A_3\right)+(W^2-M_N^2)\left(-A_2+\frac{W^3}{M_N^3}A_4\right)\right.\\
&+ \left.2(W-m)\left(\nu A_5+\frac{W^2}{M_N}A_6\right)\right],
\end{aligned} \tag{A.1}$$

where $x=\cos\theta_{c.m.}$ and

$$\begin{aligned}
C &= \frac{(s-M_N^2)^2}{64\pi s^2}, \quad c_1=4mW+(W-m)^2(1-x),\\
c_2 &= 4W(W-m)-(W-m)^2(1-x),\\
c_3 &= 4W^2-(W-m)^2(1-x).
\end{aligned} \tag{A.2}$$

The R_i amplitudes can be expanded in multipole amplitudes, and from them one can define the dynamical polarizabilities. If we look at α_{El} and β_{Ml}, we would like to be able to associate to them all the nucleon-structure effects in the T_{fi} amplitude that are even function in the photon energy or momentum and that do not depend on the nucleon spin. However, as noticed in Ref. [12], both the spin and the energy depend on the reference frame. As soon as we change the frame, the energy is Lorentz transformed and the Pauli spinors are Wigner rotated. Thus, if the contribution of T_{fi} related to α_{El} and β_{Ml} is chosen to be spin-independent, for instance, in the c.m. frame, it would be spin-dependent in other frames. Moreover, the electric and magnetic fields are not invariant under Lorentz transformations, thus making the splitting into effects due to α_{El} or β_{Ml} frame-dependent.

Furthermore, neither the center of mass, nor the lab reference frame have the same symmetry properties of the scattering amplitude T_{fi}, while in the Breit reference frame, where the nucleon is at rest on average, both time reversal and crossing symmetry are fulfilled. For instance, the terms in T_{fi} that are related to the dipole scalar polarizabilities α_{E1} and β_{M1} can be correctly defined only in the Breit frame, where one has

$$T_{fi,B}^{(\alpha_{E1},\beta_{M1})} \equiv 4\pi\omega_B^2 \bar{u}' u \left[\boldsymbol{\epsilon}_B'^{*} \cdot \boldsymbol{\epsilon}_B \alpha_{E1} + \boldsymbol{s}_B'^{*} \cdot \boldsymbol{s}_B \beta_{M1}\right], \tag{A.3}$$

and where both the polarization vectors and the energy are in the Breit frame. By comparing the spin-independent part of Eq. (2.26) written in the Breit frame and the expression defined in Eq. (A.3), we obtain the following relations:

$$A_1^{(\alpha_{E1},\beta_{M1})} = -2\pi(\alpha_{E1} - \beta_{M1}), \quad A_3^{(\alpha_{E1},\beta_{M1})} = -\frac{2\pi(\alpha_{E1} + \beta_{M1})}{1 - t/4M_N^2} \tag{A.4}$$

If we now plug-in these results into the spin-independent part of T_{fi} given in Eq. (2.26), we obtain an equation that corresponds to Eq. (A.3), this time expressed in the lab reference frame, i.e.

$$\begin{aligned} T_{fi,lab}^{\alpha_{E1},\beta_{M1}} &= \frac{8\pi M_N E_\gamma E'_\gamma}{N(t)} \bar{u}' u \Big[\boldsymbol{\epsilon}'^{*} \cdot \boldsymbol{\epsilon} \alpha_{E1} + \boldsymbol{s}'^{*} \cdot \boldsymbol{s} \beta_{M1} \\ &- \frac{t}{4M_N^2} (\boldsymbol{\epsilon}'^{*} \cdot \boldsymbol{\epsilon} - \boldsymbol{s}'^{*} \cdot \boldsymbol{s})(\alpha_{E1} - \beta_{M1})\Big], \end{aligned} \tag{A.5}$$

where the recoil terms $\sim t/4M_N^2$ are effects of the non-recoil ansatz of Eq. (A.3). These terms contribute at higher order than $\mathcal{O}(\omega\omega')$ in the LEX of the spin-independent part of T_{fi} and therefore generate relativistic recoil corrections in the definition of the higher-order scalar polarizabilities.

Appendix B

Low energy expansion of the real Compton scattering observables

In this appendix, we give the explicit expressions of the higher-order terms entering the LEX of the W_{00} and W_{03} functions that parametrize the unpolarized differential cross section and the beam asymmetry. At order $\mathcal{O}(E_\gamma E'_\gamma)^2$, the $U_{00}^{(4)}$ and $U_{03}^{(4)}$ terms in Eq. (2.49) read [12]:

$$\begin{aligned}
\frac{1}{(8\pi M_N)^2}\,U_{00}^{(4)} &= \frac{1}{2}(1+z^2)(\alpha_{E1}^2+\beta_{M1}^2)+2z\alpha_{E1}\beta_{M1}+\frac{r_0}{4M_N^2}(1-z)\times \\
&\quad\Big[(1+z)(\kappa_N^2+2q\kappa_N)(\alpha_{E1}+z\beta_{M1})+2q^2(2z\alpha_{E1}+(1+z^2)\beta_{M1})\Big] \\
&\quad - r_0q^2\Big[(1+z^2)\alpha_{E1,\nu}+2z\beta_{M1,\nu}+\frac{z^3}{6}\alpha_{E2}+\frac{3z^2-1}{12}\beta_{M2}\Big] \\
&\quad + \frac{r_0}{2M_N}P(z), \\
\frac{1}{(8\pi M_N)^2}\,U_{03}^{(4)} &= (1-z^2)\Big\{-\frac{1}{2}(\alpha_{E1}^2-\beta_{M1}^2) \\
&\quad - \frac{r_0}{4M_N^2}(\kappa_N^2+2q\kappa_N)(\alpha_{E1}+z\beta_{M1}) \\
&\quad + r_0q^2\Big[\alpha_{E1,\nu}+\frac{z}{6}\alpha_{E2}-\frac{1}{12}\beta_{M2}\Big]+\frac{r_0}{2M_N}R\Big\}.
\end{aligned} \tag{B.1}$$

Here $r_0 = e^2/4\pi M_N$ and $P(z)$ and R are polynomials in z of the third and zero order, respectively, which are determined by the spin polarizabilities as follows:

$$\begin{aligned}
P(z) &= \Big[q^2(1+2z-3z^2)-2q\kappa_N(1-z)^2+2\kappa_N^2 z\Big]\gamma_{E1E1} \\
&+ \Big[(q^2+2q\kappa_N)(3-2z-z^2)+\kappa_N^2(3-z^2)\Big]\gamma_{M1M1}
\end{aligned}$$

$$
\begin{aligned}
&+ \quad \Big[-q^2(1-3z^2+2z^3) - 2q\kappa_N(1+z-3z^2+z^3) \\
&+ \quad \kappa_N^2(3z^2-1)\Big]\gamma_{M1E2} \\
&+ \quad \Big[-q^2(1-z)^2 + 4q\kappa_N(z-z^2) + 2\kappa_N^2 z\Big]\gamma_{E1M2}, \qquad \text{(B.2)}
\end{aligned}
$$

and

$$
R = q^2(\gamma_{E1E1} - \gamma_{E1M2}) - (\kappa_N + q)^2(\gamma_{M1M1} - \gamma_{M1E2}). \qquad \text{(B.3)}
$$

Bibliography

[1] A. H. Compton, Phys. Rev. **14**, 20 (1919).

[2] M. Gell-Mann, M. L. Goldberger, and W. E. Thirring, Phys. Rev. **95**, 1612 (1954).

[3] A. Baldin, Nuclear Physics **18**, 310 (1960).

[4] S. B. Gerasimov, Sov. J. Nucl. Phys. **2**, 430 (1966), [Yad. Fiz.2,598(1965)].

[5] S. D. Drell and A. C. Hearn, Phys. Rev. Lett. **16**, 908 (1966).

[6] V. Bernard, N. Kaiser, and U.-G. Meissner, Int. J. Mod. Phys. **E4**, 193 (1995).

[7] S. R. Beane, M. Malheiro, J. A. McGovern, D. R. Phillips, and U. van Kolck, Phys. Lett. **B567**, 200 (2003), [Erratum: Phys. Lett.B607,320(2005)].

[8] J. A. McGovern, D. R. Phillips, and H. W. Griesshammer, Eur. Phys. J. A **49**, 12 (2013).

[9] V. Lensky, J. McGovern, and V. Pascalutsa, Eur. Phys. J. C **75**, 604 (2015).

[10] V. Lensky and V. Pascalutsa, Eur. Phys. J. **C65**, 195 (2010).

[11] A. I. L'vov, V. A. Petrun'kin, and M. Schumacher, Phys. Rev. C **55**, 359 (1997).

[12] D. Babusci, G. Giordano, A. L'vov, G. Matone, and A. Nathan, Phys. Rev. C **58**, 1013 (1998).

[13] M. Schumacher, Prog. Part. Nucl. Phys. **55**, 567 (2005).

[14] D. Drechsel, M. Gorchtein, B. Pasquini, and M. Vanderhaeghen, Phys. Rev. C **61**, 015204 (1999).

[15] B. R. Holstein, D. Drechsel, B. Pasquini, and M. Vanderhaeghen, Phys. Rev. C **61**, 034316 (2000).

[16] B. Pasquini, D. Drechsel, and M. Vanderhaeghen, Phys. Rev. C **76**, 015203 (2007).

[17] D. Drechsel, B. Pasquini, and M. Vanderhaeghen, Phys. Rept. **378**, 99 (2003).

[18] B. Pasquini and M. Vanderhaeghen, Ann. Rev. Nucl. Part. Sci. **68**, 75 (2018).

[19] V. Gribov, *Strong Interactions of Hadrons at High Energies: Gribov Lectures on Theoretical Physics*Cambridge Monographs on Particle Physics, Nuclear Physics and Cosmology (Cambridge University Press, 2008).

[20] H. W. Griesshammer, J. A. McGovern, D. R. Phillips, and G. Feldman, Prog. Part. Nucl. Phys. **67**, 841 (2012).

[21] F. Hagelstein, R. Miskimen, and V. Pascalutsa, Prog. Part. Nucl. Phys. **88**, 29 (2016).

[22] K. Pachucki, Physical Review A - Atomic, Molecular, and Optical Physics **60**, 3593 (1999).

[23] C. E. Carlson and M. Vanderhaeghen, (2011), arXiv:1109.3779.

[24] A. Walker-Loud, C. E. Carlson, and G. A. Miller, Phys. Rev. Lett. **108**, 232301 (2012).

[25] W. Cottingham, Annals of Physics **25**, 424 (1963).

[26] M. A. Maize and J. J. Smetanka, European Journal of Physics **29**, 497 (2008).

[27] C. Kittel, *Introduction to Solid State Physics* (Wiley, New York, 1996).

[28] R. M. Glover and F. Weinhold, J. Chem. Phys.F **66**, 191 (1977).

[29] H. W. Griesshammer and T. R. Hemmert, Phys. Rev. C **65**, 045207 (2002).

[30] R. P. Hildebrandt, H. W. Griesshammer, T. R. Hemmert, and B. Pasquini, Eur. Phys. J. A **20**, 293 (2004).

[31] A. Aleksejevs and S. Barkanova, Nucl. Phys. Proc. Suppl. **245**, 17 (2013).

[32] A. Aleksejevs and S. Barkanova, J. Phys. G **38**, 035004 (2011).

[33] B. E. MacGibbon *et al.*, Phys. Rev. C **52**, 2097 (1995).

[34] F. J. Federspiel *et al.*, Phys. Rev. Lett. **67**, 1511 (1991).

[35] V. Olmos de Leon *et al.*, Eur. Phys. J. A **10**, 207 (2001).

[36] P. P. Martel *et al.*, (A2 Coll. at MAMI), Phys. Rev. Lett. **114**, 112501 (2015).

[37] H. W. Griesshammer, J. A. McGovern, and D. R. Phillips, Eur. Phys. J. **A52**, 139 (2016).

[38] V. Lensky and J. A. McGovern, Phys. Rev. **C89**, 032202 (2014).

[39] A. C. Davison and D. V. Hinkley, *Bootstrap Methods and their Application* (Cambridge University Press, 1997).

[40] V. Sokhoyan *et al.*, Eur. Phys. J. **A53**, 14 (2017).

[41] M. Gell-Mann and M. L. Goldberger, Phys. Rev. **96**, 1433 (1954).

[42] S. Kondratyuk and O. Scholten, Phys. Rev. **C64**, 024005 (2001).

[43] A. M. Gasparyan, M. F. M. Lutz, and B. Pasquini, Nucl. Phys. **A866**, 79 (2011).

[44] M. Moinester and S. Scherer, International Journal of Modern Physics A **34**, 1930008 (2019).

[45] L. I. Lapidus and C. K. Chao, Sov. Phys. JETP **14**, 210 (1961).

[46] A. P. Contogouris, Il Nuovo Cimento **25**, 104 (1962).

[47] N. Krupina and V. Pascalutsa, Phys. Rev. Lett. **110**, 262001 (2013).

[48] E. J. Downie and et al., Proposal MAMI-A2/04-16 (2016).

[49] E. Mornacchi, EPJ Web Conf. **199**, 05020 (2019).

[50] H. A. Kramers, Atti Cong. Intern. Fisica (Transactions of Volta Centenary Congress) Como **2**, 545 (1927).

[51] R. de L. Kronig, J. Opt. Soc. Am. **12**, 547 (1926).

[52] M. L. Goldberger, Phys. Rev. **97**, 508 (1955).

[53] F. E. Low, Phys. Rev. **96**, 1428 (1954).

[54] H. D. I. Abarbanel and M. L. Goldberger, Phys. Rev. **165**, 1594 (1968).

[55] A. Klein, Phys. Rev. **99**, 998 (1955).

[56] T. Akiba and I. Sato, Progr. Theoret. Phys. **19**, 93 (1958).

[57] L. I. Lapidus and K.-C. Chou, Soviet Phys.-JETP **11**, 147 (1960).

[58] D. Holliday, Ann. Phys. (N.Y.) **24**, 319 (1963).

[59] B. Pasquini, P. Pedroni, and S. Sconfietti, Phys. Rev. **C98**, 015204 (2018).

[60] J. R. Cudell, V. Ezhela, K. Kang, S. Lugovsky, and N. Tkachenko, Phys. Rev. D **61**, 034019 (2000).

[61] R. L. Workman, W. J. Briscoe, M. W. Paris, and I. I. Strakovsky, Phys. Rev. C **85**, 025201 (2012).

[62] O. Hanstein, D. Drechsel, and L. Tiator, Nuclear Physics A **632**, 561 (1998).

[63] D. Drechsel, S. S. Kamalov, and L. Tiator, Eur. Phys. J. A **34**, 69 (2007).

[64] R. A. Arndt, R. L. Workman, Z. Li, and L. D. Roper, Phys. Rev. C **42**, 1853 (1990).

[65] I. Guiasu and E. E. Radescu, Annals Phys. **122**, 436 (1979).

[66] I. Guiaşu and E. Radescu, Annals of Physics **120**, 145 (1979).

[67] G. Höhler, *Pion Nucleon Scattering. Part 2: Methods and Results of Phenomenological Analyses* (Springer Berlin Heidelberg, Berlin, Heidelberg, 1983).

[68] P. Pedroni and S. Sconfietti, (2019), arXiv:1909.03885.

[69] G. D'Agostini, Nucl. Instrum. Meth. A **346**, 306 (1994).

[70] F. James and M. Roos, Comput. Phys. Commun. **10**, 343 (1975).

[71] F. James, *Statistical methods in experimental physics* (Hackensack, USA: World Scientific, 2006).

[72] B. Pasquini, P. Pedroni, and S. Sconfietti, J. Phys. G **46**, 104001 (2019).

[73] H. W. Griesshammer, J. A. McGovern, and D. R. Phillips, The European Physical Journal A **54**, 37 (2018).

[74] N. Krupina, V. Lensky, and V. Pascalutsa, Phys. Lett. B **782**, 34 (2018).

[75] C. L. Oxley, Phys. Rev. **110**, 733 (1958).

[76] L. G. Hyman, R. Ely, D. H. Frisch, and M. A. Wahlig, Phys. Rev. Lett. **3**, 93 (1959).

[77] V. Goldansky, O. Karpukhin, A. Kutsenko, and V. Pavlovskaya, Nuclear Physics **18**, 473 (1960).

[78] G. E. Pugh, R. Gomez, D. H. Frisch, and G. S. Janes, Phys. Rev. **105**, 982 (1957).

[79] P. S. Baranov, A. I. L'vov, V. A. Petrunkin, and L. N. Shtarkov, Phys. Part. Nucl. **32**, 376 (2001), [Fiz. Elem. Chast. Atom. Yadra32,699(2001)].

[80] E. L. Hallin *et al.*, Phys. Rev. C **48**, 1497 (1993).

[81] G. Bernardini *et al.*, Nuovo Cim. **18**, 1203 (1960).

[82] P. S. Baranov *et al.*, Yad. Fiz. **21**, 689 (1975).

[83] P. Baranov *et al.*, Phys. Lett. B **52**, 122 (1974).

[84] A. Zieger *et al.*, Phys. Lett. B **278**, 34 (1992).

[85] J. Ahrens *et al.*, GDH and A2 Collaborations, Phys. Rev. Lett. **87**, 022003 (2001).

[86] H. Dutz *et al.*, GDH Coll., Phys. Rev. Lett. **91**, 192001 (2003).

[87] B. Pasquini, P. Pedroni, and D. Drechsel, Phys. Lett. B **687**, 160 (2010).

[88] O. Gryniuk, F. Hagelstein, and V. Pascalutsa, Phys. Rev. D **94**, 034043 (2016).

[89] C. Patrignani *et al.*, Particle Data Group, Chin. Phys. C **40**, 100001 (2016).

[90] D. V. Hinkley, Biometrika **64**, 21 (1977).

[91] R. T. Birge, Phys. Rev. **40**, 207 (1932).

[92] S. Wolf *et al.*, Eur. Phys. J. A **12**, 231 (2001).

[93] M. Camen *et al.*, Phys. Rev. C **65**, 032202 (2002).

[94] O. Gryniuk, F. Hagelstein, and V. Pascalutsa, Phys. Rev. D **92**, 074031 (2015).

[95] J. W. DeWire, M. Feldman, V. L. Highland, and R. Littauer, Phys. Rev. **124**, 909 (1961).

[96] E. R. Gray and A. O. Hanson, Phys. Rev. **160**, 1212 (1967).

[97] H. Genzel, M. Jung, R. Wedemeyer, and H. J. Weyer, Z. Phys. A **279**, 399 (1976).

[98] P. S. Baranov, L. I. Slovokhotov, G. A. Sokol, and L. N. Shtarkov, Sov. Phys. JETP **23**, 242 (1966), [Zh. Eksp. Teor. Fiz.50,364(1966)].

[99] P. S. Baranov, V. A. Kuznetsova, L. I. Slovokhotov, G. A. Sokol, and L. N. Shtarkov, Sov. J. Nucl. Phys. **3**, 791 (1966), [Yad. Fiz.3,1083(1966)].

[100] J. Peise and M. Schumacher, Phys. Lett. B **384**, 37 (1996).

[101] A. Hünger *et al.*, Nucl. Phys. A **620**, 385 (1997).

[102] C. Molinari *et al.*, Phys. Lett. B **371**, 181 (1996).

[103] F. Wissmann *et al.*, Nucl. Phys. A **660**, 232 (1999).

[104] G. Galler *et al.*, Phys. Lett. B **503**, 245 (2001).

[105] G. Blanpied *et al.*, Phys. Rev. C **64**, 025203 (2001).

[106] M. MacCormick *et al.*, Phys. Rev. C **53**, 41 (1996).

[107] T. Armstrong *et al.*, Physics Letters B **34**, 535 (1971).

[108] O. Bartalini *et al.*, Physics of Atomic Nuclei **71**, 75 (2008).

[109] D. O. Caldwell *et al.*, Phys. Rev. Lett. **40**, 1222 (1978).

[110] H1 Coll. *et al.*, Z. Phys. C **69**, 27 (1995).

[111] S. Chekanov *et al.*, Nuclear Physics B **627**, 3 (2002).

[112] J. Ahrens *et al.*, GDH and A2 Collaborations, Phys. Rev. Lett. **84**, 5950 (2000).

[113] H. Dutz *et al.*, GDH Coll., Phys. Rev. Lett. **93**, 032003 (2004).

[114] B. Pasquini, P. Pedroni, and D. Drechsel, Phys. Lett. B **687**, 160 (2010).

[115] K. Helbing, Prog. Part. Nucl. Phys. **57**, 405 (2006).

[116] D. Paudyal *et al.*, (A2 Coll. at MAMI), (2019), arXiv:1909.02032.

[117] H. Fonvieille, B. Pasquini, and N. Sparveris, (2019), arXiv:1910.11071.

List of publications

* **Papers in peer-reviewed journals:**:

[1] B. Pasquini, P. Pedroni and S. Sconfietti, *First extraction of the scalar proton dynamical polarizabilities from real Compton scattering data*, Phys. Rev. C **98**, no. 1, 015204 (2018), [arXiv:1711.07401 [hep-ph]].

[2] B. Pasquini, P. Pedroni and S. Sconfietti, *Proton scalar dipole polarizabilities from real Compton scattering data, using fixed-t subtracted dispersion relations and the bootstrap method*, J. Phys. G **46**, no. 10, 104001 (2019), [arXiv:1903.07952 [hep-ph]].

[3] P. Pedroni and S. Sconfietti, *A new Monte Carlo-based fitting method*, arXiv:1909.03885 [physics.data-an], to be published in J. Phys. G.

* **Proceedings**:

[1] S. Sconfietti, B. Pasquini and P. Pedroni, *Scalar dipole dynamical polarizabilities from real Compton scattering data*, EPJ Web Conf. **199**, 05008 (2019)

[2] P. Pedroni, B. Pasquini and S. Sconfietti, *Extracting the scalar dynamical polarizabilities from real Compton scattering data*, PoS SPIN **2018**, 122 (2018)

[3] S. Sconfietti, B. Pasquini and P. Pedroni, *Statistical approach for the first extraction of dipole dynamical polarizabilities from proton real Compton scattering data*, Il Nuovo Cimento C **42** (2019) 113

[4] S. Sconfietti, B. Pasquini and P. Pedroni, *proceedings of MENU-2019* to appear in *AIP Conference Proceedings*

[5] S. Sconfietti, B. Pasquini and P. Pedroni, *proceedings of INPC 2019*, to appear in *Journal of Physics: Conference Series*

Greetings

I want to say *thank you* to a lot of people.

I would like to start with my supervisors, Barbara and Paolo. Barbara, working with you has been a honor, you are the teacher that all the students would like to meet during their career: your knowledge is wide, your behavior made me feel like at home during these years. Paolo, I'm still waiting for the day when I will ask you *a little test*, but I know it is just in my dreams: you taught me both statistics and, even more important, honesty in life and in making science. I want to acknowledge Dr. Marc Vanderhaeghen and Dr. Carl Carlson: during my period in Mainz you were always ready to correct my mistakes, from which I have learned so much. Thank you for your time and the small piece of knowledge that I could get from you.

Thank you to all the guys that I met in Mainz, that made memorable my visit there: Sasha girl, Slava, Daniel, Matthias and his crazy friends, Victor, Sasha boy, Oleksji, Misha, Vladimir and Vadim.

I want to say thank you to Edoardo, for the stimulating discussions and the friendship, as well as for the time we spent together in several conferences.

Thank you to all the HASQCD group in Pavia: Marco, Alessandro, Carlotta, Marco, Valerio, Giuseppe, Miguel and Francesco. I want to mention also Luca and Barbara, that were fundamental figures at the beginning of my PhD.

I want to thank also all the Professors that I met during my career and that contribute to shape the scientist I became: thank you all.

A special acknowledgment goes to Simone, who shared the office with me during almost all my PhD: thank you for the coffee, the friendship, the coffee, the Physics discussions, the coffee, the support while I was writing the thesis and the tea (because too much coffee is not healthy).

Thank you Ben, for all the nice time together in these (many many) years, for the friendship and the breaks. Thank you Mary, for our old and strong friendship: you are like a sister for me. Thank you Teo, even from far we are always friends and I am sure that this will last forever.

A special acknowledgment goes to my friend group, *I Vignaioli*, to whom I would like to remember that we will be forever like a big family, no adversity could stop us, nor rain or snow.

I want to thank my parents that allow me to reach this moment of my career at the University, and all my brothers and sisters: Monica, Andrea, Elena and Mitch. You are always with me, part of me: nothing in our lives can change this truth.

I want to thank my wife, Anastasia, for the love that constantly binds us. You have been always with me, you were with me also when I came back to my dear Physics Department, you are always with me: I could never become the person I am without you. Two years ago we started our biggest adventure together: being parents of our beloved Mia. She is the best event in our lives: I am proud of you and she, more and more.

Thank you all for this three-year adventure, it will be always part of my life.